2016

Materials Discovery by Crystal Growth: Synthesis, Structure Determination, Magnetic, and Optical Properties of Complex Lanthanide Containing Oxides, Oxyhydroxides, and Oxyfluorides

Allison Marie Latshaw
University of South Carolina

Materials Discovery by Crystal Growth: Synthesis, Structure Determination, Magnetic, and Optical Properties of Complex Lanthanide Containing Oxides, Oxyhydroxides, and Oxyfluorides

by

Allison Marie Latshaw

Bachelor of Science
Lebanon Valley College, May 2012

Submitted in Partial Fulfillment of the Requirements

For the Degree of Doctor of Philosophy in

Chemistry

College of Arts and Sciences

University of South Carolina

2016

Accepted by:

Hans-Conrad zur Loye, Major Professor

Daniel Reger, Chair, Examining Committee

Andrew Greytak, Committee Member

Harry Ploehn, Committee Member

Paul Allen Miller, Vice Provost and Interim Dean of Graduate Studies

Dedication

To my father, the one who inspired my love of chemistry

Acknowledgements

First, and foremost, I would like to thank my advisor Dr. Hans-Conrad zur Loye. I truly doubt that I can ever fully express my gratitude to you. I thank you for allowing me the privilege of being a student in your lab and allowing me numerous opportunities that I never dreamed possible. By believing that I was a good choice for your group and by constantly pushing me to apply to research activities, conferences, and for prestigious awards, you inspired a faith in myself that I will now take with me into the future.

In addition to my advisor, I would like to thank the other members of my committee, Dr. Daniel Reger, Dr. Andrew Greytak, and Dr. Harry Ploehn, for always being very flexible with scheduling despite your many commitments.

I would also like to thank the zur Loye group members, both past and present. Each and every one of you have taught me and helped me along this path. I would like to extend special thanks to Dr. W. Michael Chance and Dr. Gregory Morrison. Both of you have been my office mates and been there for me through difficult research times and personal struggles. Michael, I am truly indebted to you for the knowledge you passed on, the compassion you bestowed, and being more than willing to drop everything to help me. And Greg, you always had time to help me, whether or not you actually had the time and I thank you for helping me with crystallography and also for making every day fun.

I also owe huge thanks to Alexis Myers, Karl zur Loye, Kendall Hughey, and Branford Wilkins. To all of you, I thank you for your skills, personality, and willingness

to try anything. I know you will all go far and cannot wait to see the barriers you each break through.

To my mom and dad, I thank you for everything you have done for me. You have inspired me and always encouraged me to pursue my dreams. Thanks for always believing in me, even when I did not. Additionally, thank you Andrew. You are my little brother and my big cheerleader. Thank you for always thinking there was nothing I couldn't do. I love all of you and thank you for preparing me for this endeavor.

Jan, I am so grateful for everything you have done and continue to do. I love you so much and am so thankful that you and I are journeying through life together. You always support me and I know that having you by my side has made this pursuit easier. And Allan, while you are still too young to read this, I thank you for your constant smiles. I love coming home and seeing your face light up when you see me. I love you both so much.

Finally, I thank God. Without Him I would be nothing. It is amazing to see how He keeps orchestrating my life and how He continually made things come together in ways I never dreamed. I thank you for giving me the gifts I have used for the last four years and I can't wait to see where you take me next.

Thank you to the National Science Foundation for supporting the research presented here. Mary Anne Fitzpatrick, Dean, and the USC selection committee are also gratefully acknowledged for supporting me via a College of Arts and Sciences Dean's Dissertation Fellowship. In addition, thank to the USC Office of the Vice President for Research for the Support to Promote Advancement of Research and Creativity (SPARC) grant.

Abstract

Exploratory crystal growth is a versatile technique and one that can advance materials discovery. Through exploratory crystal growth, it is possible to synthesize many new materials that can have applications in many fields, including solid-state lighting. There exist many adaptations for exploratory crystal growth, including the use of alkali halide flux growth and hydroflux growth, both reported herein. By changing variants in these techniques like reactant ratios, temperature, reaction profile, and, most importantly here, the flux compositions, it is possible to change the products formed or fine tune reactions for product purity.

For solid-state lighting applications, compounds that adopt colorless frameworks, like tungstates, germanates, and silicates are of interest. Herein, we report on the synthesis, structure determination and physical property measurements of $Na_5Ln(OH)_6WO_4$ (*Ln* = Er, Tm, Yb), $Na_5Ln_4F[GeO_4]_4$ (*Ln* = Pr, Nd), $Na_xLn_{10-x}(SiO_4)_6O_{2-y}F_y$, $Ca_xLn_{10-x}(SiO_4)_6O_{2-y}F_y$ (*Ln* = Nd, Sm, Eu, Gd), $Gd_{9.34}(SiO_4)_6O_2$, $K_{1.32}Pr_{8.68}(SiO_4)_6O_{1.36}F_{0.64}$, $Na_5Ln_4F[SiO_4]_4$ (*Ln* = Pr, Nd, Sm-Tm), $K_5Pr_4F[SiO_4]_4$, $K_3LnSi_2O_7$ (*Ln* = Sm, Y), $Na_3LnSi_2O_7$ (*Ln* = Ho, Yb), $NaLnSiO_4$ (*Ln* = La, Yb), $K_5Ln_2Si_4O_{13}F$ (*Ln* = Y, Sc), and $Cs_3LnSi_4O_{10}F_2$ (*Ln* = Gd, Tb, Dy). These new compositions have been studied for magnetic properties, second harmonic generation, and optical properties, including fluorescence quantum yield, when practical.

Antiferromagnetic ordering has been observed in $Na_5Tb_4F[SiO_4]_4$ and $Na_5Dy_4F[SiO_4]_4$. The $Na_5RE_4F[SiO_4]_4$ (RE = Pr, Sm-Tm) series exhibits second harmonic generation and fluorescence has been observed in $NaEu_9(SiO_4)_6O_2$, $Na_{1.5}Eu_{8.5}(SiO_4)_6OF$, $Eu_{9.34}(SiO_4)_6O_2$, $Gd_{9.34}(SiO_4)_6O_2$, $Na_5Eu_4F[SiO_4]_4$, $Na_5Gd_4F[SiO_4]_4$, $Na_5Tb_4F[SiO_4]_4$, and $K_3YSi_2O_7$. Fluorescence quantum yield was measured on $Na_5Eu_4F[SiO_4]_4$, $Na_5Gd_4F[SiO_4]_4$, and $Na_5Tb_4F[SiO_4]_4$. The optical properties are exciting as they indicate that a silicate material, composed of the earth abundant element silicon, may be able to be used as a framework for new potential phosphor coatings for light emitting diodes (LEDs). Using silicate materials as new host structures could decrease the cost of LEDs.

Table of Contents

List of Tables

List of Figures

Chapter 1

Introduction to Materials Discovery of Complex Lanthanide Containing Oxides, Oxyhydroxides, and Oxyfluorides for Applications in Solid-State Lighting

In the field of solid-state lighting (SSL), especially light-emitting diode (LED) technology, the current drive is to find new LED lighting technology that continues to decrease energy consumption while fixing the current LED limitations of low color rendering and high color temperature.[1.1-1.3] Many different approaches have been proposed, however, in this research, the focus has been on synthesizing new, more efficient phosphor coating materials that address the current limitations of LEDs while also decreasing costs to consumers. This chapter will explore the progress of solid-state lighting technology, why this research is focused on rare earth containing tetragen materials, and highlight new findings of dual purpose materials that both luminesce and strongly scintillate.

During the last decade, LEDs have become competitive in the market due to the many improvements in the color rendering and color temperature, the increased push towards more energy efficient lighting, and the decrease in the cost of a LED light bulb.[1.3, 1.4] Despite the increase in LED sales, there are still many factors holding LED technology back from becoming the primary source of lighting.

True color rendering, or the ability of an artificial light to give the same coloring to an object that natural sunlight does,[1.5] is essential for widespread application and has steadily been improving in LED technology, however, while LEDs are now an 80 – 95 on a scale of 100 where 100 is ideal, incandescent light bulbs are a 98 – 100. In addition, the color temperature, which is best described as the cool (bluish) tint or warm (yellowish) tint of the light, is not as good in current generation LEDs as it needs to be. With an ideal range of 2,700 – 3,200 K (warm light) where lower numbers are warmer and higher numbers are cooler, LEDs range from 2,700 – 6,500 K and incandescent bulbs range

from 2,400 – 2,900 K. While LEDs are able to achieve the ideal color temperature range, those LED light bulbs are much more expensive than regular LED bulbs.

In order to convince consumers to switch their lighting from incandescent to a much more energy efficient LED source, which requires only about 16 % of the energy required for an incandescent, it is necessary for research to continue to improve the color rendering and color temperature while all the time decreasing the cost of the LED. One way to resolve this issue is to develop a better phosphor coating material.

LED lighting involves a semiconductor and a phosphor coating. The semiconductor is a p-n junction where when a voltage is applied, the electrons on the n side recombine with the holes on the p side and release photons of a certain color wavelength, usually blue.[1.6] These photons excite the phosphor coating, which is used to tune the light bulb emission wavelength. In the current commercial LED technology, there are two ways to achieve white light emission. A commercial LED standard such as InGaN can be used as the semiconductor, where the emission is in the blue region. This blue light can then excite red and/or yellow phosphor coatings to achieve white light, or three different LEDs, a green, red, and blue, can be used to provide white light emission.[1.1, 1.7] When searching for a new phosphor coating material, the goal would is to synthesize a material that, when excited by the blue emission from the semiconductor, tunes the emission to a warmer white light while still maintaining good color rendering. It is also important to make sure that this research focuses on using earth abundant materials.

Due to all of these considerations, this thesis research focused on the synthesis of new complex luminescent oxides. Complex luminescent oxides are materials with

oxygen as the primary anion component with at least one luminescent cation, one framework cation, and potentially, an alkali or alkaline earth metal cation. In the research presented here, sodium, potassium, cesium, and calcium are the alkali or alkaline earth metals, rare earths (the lanthanide row, yttrium, and scandium) are the luminescent center(s), silicon, germanium, or tungsten are the framework, and primarily oxygen, with the addition of some fluorine or hydroxide, are the anions. The framework components, especially silicon, are earth abundant and the rare earths provide strong luminescence that requires only small quantities to be included in the structure, in these cases, via doping onto a rare earth site. Additionally, the oxide frameworks are inert host lattices with good thermal stability compared to sulfides[1.8, 1.9] that have wide band gaps, making them better phosphors.[1.6] Therefore, these complex luminescent oxides are well suited to make strides in the improvement of current LED technology.

Silicon is one of the most abundant elements, by mass, on earth. Silicon is present in many naturally occurring minerals and usually occurs as a silicate, a family of materials that are based on the SiO_4^{4-} tetrahedral unit. Silicates create a very rigid and versatile framework that tends to easily incorporate other elements, such as rare earths and alkali or alkaline earth metal cations.[1.8, 1.10, 1.11] In addition to silicon, germanium,[1.10] another tetragen, and tungsten,[1.1] also comprise rigid frameworks, where rare earth elements can be incorporated. All three of these elements also tend to be colorless when in oxide frameworks, thus not interfering with luminescence in the visible range of the electromagnetic spectrum.

When considering silicates, it is important to look at the various framework possibilities. As previously mentioned, SiO_4^{4-} is the primary building block in silicate

structures. The primary silicate units include nesosilicates (isolated SiO_4^{4-}), sorosilicates ($Si_2O_7^{-6}$), cyclosilicates (rings including $Si_6O_{18}^{-12}$, $Si_3O_9^{-6}$, $Si_4O_{12}^{-8}$, and $Si_5O_{15}^{-10}$), inosilicates (single and double chain silicates such as $Si_4O_{13}^{-10}$), phyllosilicates (sheet silicates), and tectosilicates (framework silicates). With so many different arrangements of the primary silicate building block, it is easy to understand why there are so many different silicate materials known.[1.12, 1.13]

With a tetragen such as silicon or germanium as the primary framework unit of the complex oxide, the next consideration is the luminescent material. In LED technology, rare earth elements are still heavily relied on to provide the luminescent component.[1.8]

Rare earth and lanthanide elements were discovered relatively recently, with the first rare earth, yttrium, discovered in 1787, 15 others discovered between 1803 and 1907, and finally, radioactive promethium was discovered in 1947.[1.14] Rare earths were found to exhibit strong luminescence that is scarcely affected by the environment in which the rare earth is found. The 4*f* electrons in rare earth elements are shielded by the 5*s* and 5*p* orbitals, leading to very little interaction with the framework that the rare earth resides in. Within the 4*f* orbital there are electron-electron repulsions, known as the Coulombic interaction, that cause large term, energy state, separations, on the order of 10^4 cm^{-1}. These term separations lead to a split of several J-levels via spin-orbital coupling, which is also large due to the heavy nuclei of a rare earth ion, on the order of 10^3 cm^{-1}. If the rare earth element is in a coordinating environment, such as a crystalline lattice, the J-levels can be split even further by the electric field, or crystal field, of the lattice. This effect is known as crystal field splitting and is rather small in rare earth ions,

on the order of 10^2 cm^{-1}. Because the crystal field splitting in rare earths is small, and because the filled 5*s* and 5*p* orbitals shield the 4*f* electrons, the luminescent properties of rare earth elements are rather consistent and only slightly affected by their coordination environment in the framework.[1.15]

In addition to activated luminescence, when the rare earth center exhibits luminescence due to its valence *f* electrons, sometimes rare earths such as yttrium and lutetium, which have no valence *f* electrons when present as trivalent Y^{3+} and Lu^{3+}, exhibit intrinsic luminescence.[1.16, 1.17] In many cases the intrinsic luminescence appears to come from the yttrium environment, with examples such as Y_2SiO_5,[1.16] YF_3,[1.18] and Y_2SiO_5[1.19] previously reported in the literature.

Additionally, when studying luminescent compounds where the luminescence results from heavy rare earth elements, scintillation abilities should be tested. Scintillator materials are used to detect ionizing radiation.[1.20-1.22] In order to have a scintillator material, the compound must luminesce under usual UV excitation and contain heavy elements. Rare earth elements such as Eu^{3+}, Gd^{3+}, and Tb^{3+} are heavy and luminescent so when they are in structures, the potential of scintillation increases.[1.23, 1.24] Additionally, when a heavier element like potassium, or a very heavy element such as cesium is also in the structure, the potential for scintillation increases again. Finally, trivalent rare earth, specifically Ce^{3+}, doped silicates currently dominate the scintillator market because they have high chemical stability, high light yields, and fast decay times.[1.23]

Due to the framework and luminescent ions, rare earth silicates are strong candidates for new phosphor coating materials for LEDs and potential scintillator materials. Despite being extensively studied, new rare earth silicate phases are

continually being discovered. In this thesis research, the focus has been on a relatively unexplored phase space where exploratory flux crystal growth was carried out primarily using alkali halide eutectic fluxes.[1.25] Throughout this research, numerous new phases were synthesized. The choice of the alkali metal in the flux, in addition to the reaction conditions, appears to be very important in influencing the specific products formed.

When sodium halides were chosen as the flux, the primary phases synthesized were the apatite, $A_{10-x}Ln_x(SiO_4)_6O_{2-y}F_y$ (A = Na, K, Ca; *Ln* = Pr, Nd, Sm, Eu, Gd), family [1.26-1.39] and the $A_5Ln_4X[TO_4]_4$ (A = Na, K; *Ln* = Pr, Nd, Sm – Yb, Y) family.[1.40-1.43] **Chapters 2** and **3** present the apatite structures that were synthesized. In the apatite research the changes in the luminescence due to the presence or absence of fluorine and/or the alkali metal was explored. **Chapters 3 – 6** present the $A_5Ln_4X[TO_4]_4$ compositions that were synthesized. For A = Na and T = Si, a comparison between X = F and X = OH is discussed, where second harmonic generation, luminescence, fluorescence quantum yield, and magnetism were all collected for the comparison. It was observed that having X = F improves all properties tested. It was also determined that when using sodium halides as the flux and using larger and smaller lanthanide elements, La, Yb, and Sc different structures were formed. **Chapter 7** discusses the $NaLnSiO_4$[1.44-1.46] and the $Na_2RESiO_4(OH)$[1.47] structures that formed for La, Yb, and Sc under conditions that yielded the $A_5Ln_4X[TO_4]_4$ (A = Na, K; *Ln* = Pr, Nd, Sm – Yb, Y) family for the other lanthanides. The magnetism properties of these structures are discussed.

When potassium halides were chosen as the flux components, compositions differed from those formed when sodium was in the flux. A very stable phase is the $K_3LnSi_2O_7$ phase, which has been extensively studied in the literature.[1.48-1.52] **Chapters 8**

and **9** present additional aspects of the series of $K_3LnSi_2O_7$ and expand into some $Na_3LnSi_2O_7$ compositions. In this family, polymorphism is common and multiple polymorphs are reported. Additionally, it was found that $K_3YSi_2O_7$ exhibits intrinsic luminescence. It was found that the luminescence can be tuned to white luminescence through the addition of a red component, Eu^{3+}, and a yellow component, Dy^{3+}.[1.1, 1.53-1.55] With yttrium, an earth abundant element together with small levels of other rare earths, occupying the rare earth crystallographic site, promising luminescence is observed for this composition making it potentially suitable as a phosphor coating. In addition to the $K_3LnSi_2O_7$ phase, a second phase sometimes crystallized in the reactions. **Chapter 10** presents the $K_5RE_2FSi_4O_{13}$ (Sc, Y) phase.[1.56]

In addition to sodium and potassium flux reactions, recent research has expanded into using cesium halide fluxes. **Chapter 11** presents $Cs_3LnSi_4O_{10}F_2$, which is a new structure type. This is the first example of a composition with Si_3O_9 units connected through a fourth silicon tetrahedron. Specifically, three Si_3O_9 units are connected through the fourth silicon tetrahedron. In addition to being interesting as a new structure type and an uncommon example of cesium-rare-earth-silicate compositions, the Tb analogue exhibits intense luminescence and very strong scintillation on the laboratory X-ray diffractometer. Further research is ongoing.

Overall, this research has been driven by the goal to find new materials that can be used as phosphor coatings in solid-state lighting. Throughout this research, it has been observed that rare earth silicates exhibit strong luminescence that can be tuned and the presence of fluorine in a composition of complex luminescent oxides increases the brightness of the luminescence.[1.57] Future studies are ongoing to determine the strength

of potential scintillator materials, and how the presence of fluorine in the rare earth polyhedra and/or the presence of a heavier element such as cesium affect the scintillation behavior in addition to the overarching goal to continue to find a new phosphor coating for LED technology that can overcome the current limitations.

References

1.1 Liu, Y.; Liu, G.; Wang, J.; Dong, X.; Yu, W. *Inorg. Chem.* **2014**, *53*, 11457-11466.
1.2 Xia, Y.; Liu, Y.-G.; Huang, Z.; Fang, M.; Molokeev, M. S.; Mei, L. F. *J. Mater. Chem. C* **2016**, *4*, 4675-4683.
1.3 He, G.; Tang, J. *IEEE Photonics Technol. Lett.* **2014**, *26*, 1450-1453.
1.4 Lin, Z.; Lin, H.; Xu, J.; Huang, F.; Chen, H.; Wang, B.; Wang, Y. *J. Alloys Compd.* **2015**, *649*, 661-665.
1.5 Rea, M. S.; Freyssinier-Nova, J. P. *Color Res. Appl.* **2008**, *33*, 192-202.
1.6 McKittrick, J.; Shea-Rohwer, L. E. *J. Am. Ceram. Soc.* **2014**, *97*, 1327-1352.
1.7 Xu, C.; Poduska, K. M. *J. Mater. Sci: Mater. Electon* **2015**, *26*, 4565-4570.
1.8 Zhang, Y.; Li, G.; Geng, D.; Shang, M.; Peng, C.; Lin, J. *Inorg. Chem.* **2012**, *51*, 11655-11664.
1.9 Brgoch, J.; Borg, C. K. H.; Denault, K. A.; Mikhailovsky, A.; DenBaars, S. P.; Seshadri, R. *Inorg. Chem.* **2013**, *52*, 8010-8016.
1.10 Dawson, C. J.; Sanchez-Smith, R.; Rez, P.; O'Keeffe, M.; Treacy, M. M. J. *Chem. Mater.* **2014**, *26*, 1523-1527.
1.11 Yang, P.; Yu, X.; Yu, H.; Jiang, T.; Zhou, D.; Qiu, J. *J. Rare Earths* **2012**, *30*, 1208-1212.
1.12 Ananias, D.; Kostova, M.; Almeida Paz, F. A.; Ferreira, A.; Carlos, L. D.; Klinowski, J.; Rocha, J. *J. Am. Chem. Soc.* **2004**, *126*, 10410-10417.
1.13 Wanklyn, B. M.; Wondre, F. R.; Ansell, G. B.; Davison, W. *J. Mater. Sci.* **1974**, *9*, 2007-2014.
1.14 Eliseeva, S. V.; Bünzli, J.-C. G. *New J. Chem.* **2011**, *35*, 1165-1176.
1.15 Werts, M. H. V. *Sci. Prog.* **2005**, *88*, 101-131.
1.16 Ivanov, V. Y.; Shlygin, E. S.; Pustovarov, V. A.; Mazurenko, V. V.; Shul'gin, B. V. *Phys. Solid State* **2008**, *50*, 1692-1698.
1.17 Muresan, L. E.; Popovici, E. J.; Perhaita, I.; Indrea, E.; Oro, J.; Casan Pastor, N. *Luminescence* **2016**, *31*, 929-936.
1.18 Pankratov, V.; Kirm, M.; von Seggern, H. *J. Lumin.* **2005**, *113*, 143-150.
1.19 Zorenko, Y.; Zorenko, T.; Voznyak, T.; Sidletskiy, O. *J. Lumin.* **2013**, *137*, 204-207.
1.20 Horiai, T.; Kurosawa, S.; Murakami, R.; Pejchal, J.; Yamaji, A.; Shoji, Y.; Chani, V. I.; Ohashi, Y.; Kamada, K.; Yokota, Y.; Yoshikawa, A. *Opt. Mater. (Amsterdam, Neth.)* **2016**, Ahead of Print.
1.21 Martins, A. F.; Carreira, J. F. C.; Rodrigues, J.; Ben Sedrine, N.; Castro, I. F. C.; Correia, P. M. M.; Veloso, J. F. C. A.; Rino, L.; Monteiro, T. *Spectrochim. Acta, Part A* **2016**, Ahead of Print.
1.22 Yokota, Y.; Kurosawa, S.; Ohasi, Y.; Kamada, K.; Yoshikawa, A. *J. Cryst. Growth* **2016**, Ahead of Print.
1.23 Yanagida, T. *Opt. Mater.* **2013**, *35*, 1987-1992.
1.24 Yamaguchi, H.; Kamada, K.; Kurosawa, S.; Pejchal, J.; Shoji, Y.; Yokota, Y.; Ohashi, Y.; Yoshikawa, A. *Opt. Mater* **2016**, *In Press*.
1.25 Bugaris, D. E.; zur Loye, H.-C. *Angew. Chem. Int. Ed.* **2012**, *51*, 3780-3811.
1.26 Chiu, Y.-C. L., W.-R.; Yeh, Y.-T.; Jang, S.-M.; and Chen, T.-M. *J. Chem. Chem. Eng.* **2011**, *5*, 841-846.

1.27 Dong, Z.; White, T. J.; Wei, B.; Laursen, K. *J. Am. Ceram. Soc.* **2002**, *85*, 2515-2522.
1.28 Felsche, J. *J. Solid State Chem.* **1972**, *5*, 266-275.
1.29 Hopkins, R. H.; Melamed, N. T.; Henningsen, T.; Roland, G. W. *J. Cryst. Growth* **1971**, *10*, 218-222.
1.30 Leu, L.-C.; Thomas, S.; Sebastian, M. T.; Zdzieszynski, S.; Misture, S.; Ubic, R. *J. Am. Ceram. Soc.* **2011**, *94*, 2625-2632.
1.31 Maisonneuve, V.; Leduc, E.; Bohnke, O.; Leblanc, M. *Chem. Mater.* **2004**, *16*, 5220-5222.
1.32 Masubuchi, Y.; Higuchi, M.; Takeda, T.; Kikkawa, S. *Solid State Ionics* **2006**, *177*, 263-268.
1.33 Nakayama, S.; Highchi, M. *J. Mater. Sci. Lett.* **2001**, *20*, 913-915.
1.34 Nötzold, D.; Wulff, H. *Phys. Stat. Sol. (B)* **1998**, *207*, 271-282.
1.35 Sansom, J. E. H.; Richlings, D.; Slater, P. R. *Solid State Ionics* **2001**, *139*, 205-210.
1.36 Schroeder, L. W.; Mathew, M. *J. Solid State Chem.* **1978**, *26*, 383-387.
1.37 Shen, Y.; Tok, A.; Dong, Z. *J. Am. Ceram. Soc.* **2010**, *93*, 1176-1182.
1.38 Takahashi, M.; Uematsu, K.; Ye, Z.-G.; Sato, M. *J. Solid State Chem.* **1998**, *139*, 304-309.
1.39 Toumi, M.; Smiri-Dogguy, L.; Bulou, A. *Ann. Chim. Sci. Mat.* **2002**, *27*, 17-26.
1.40 Hughey, K.; Yeon, J.; zur Loye, H.-C. *J. Chem. Crystallogr.* **2014**, *44*, 376-379.
1.41 Malinovskii, Y. A. *Dokl. Akad. Nauk SSSR* **1984**, *274*, 75-78.
1.42 Merinov, B. V.; Maksimov, B. A.; Ilyukhin, V. V.; Belov, N. V. *Dokl. Akad. Nauk SSSR* **1980**, *255*, 348-351.
1.43 Schafer, M. C.; Schleid, T. *Z. Anorg. Allg. Chem.* **2010**, *636*, 2069.
1.44 Chichagov, A. V.; Ilyukhin, V. V.; Belov, N. V. *Dokl. Akad. Nauk SSSR* **1967**, *177*, 574.
1.45 Chichagov, A. V.; Belov, N. V. *Geochem. Int.* **1968**, *5*, 858.
1.46 Emirdag-Eanes, M.; Krawiec, M.; Kolis, J. W. *J. Chem. Crystallogr.* **2001**, *31*, 281-285.
1.47 Chiragov, M. I.; Mamedov, K. S. *Uch. zap. Azerb. un-t. Ser. geol.-geogr. n.* **1974**, *4*, 3-6.
1.48 Bondar, I. A.; Tenisheva, T. F.; Toropov, N. A.; Shepelev, Y. F. *Dokl. Akad. Nauk SSSR* **1965**, *160*, 1069-1071.
1.49 Hwang, M. S.; Hong, H. Y.-P. *Acta Crystallogr., Sect. C: Cryst. Struct. Commun.* **1987**, *43*, 1241-1243.
1.50 Napper, J. D.; Layland, R. C.; Smith, M. D.; zur Loye, H.-C. *J. Chem. Crystallogr.* **2004**, *34*, 347-351.
1.51 Tamazyan, R. A.; Malinovskii, Y. A.; Sirota, M. I.; Simonov, V. I. *Kristallografiya* **1988**, *33*, 1128-1133.
1.52 Vidican, I.; Smith, M. D.; zur Loye, H.-C. *J. Solid State Chem.* **2003**, *170*, 203-210.
1.53 Bharat, L. K.; Jeon, Y. I.; Yu, J. S. *Ceram. Int.* **2016**, *42*, 5677-5685.
1.54 Leng, Z.; Li, L.; Liu, Y.; Zhang, N.; Gan, S. *J. Lumin.* **2016**, *173*, 171-176.
1.55 Zhai, Y.; Wang, M.; Zhao, Q.; Yu, J.; Li, X. *J. Lumin.* **2016**, *172*, 161-167.
1.56 Chiang, P.-Y.; Lin, T.-W.; Dai, J.-H.; Chang, B. C.; Lii, K.-H. *Inorg. Chem.* **2007**, *46*, 3619-3622.
1.57 Kunkel, N.; Meijerink, A.; Kohlmann, H. *Inorg. Chem.* **2014**, *53*, 4800-4802.

Chapter 2

Photoluminescent and Magnetic Properties of Lanthanide Containing Apatites: $Na_xLn_{10-x}(SiO_4)_6O_{2-y}F_y$, $Ca_xLn_{10-x}(SiO_4)_6O_{2-y}F_y$ (*Ln* = Eu, Gd, and Sm), $Gd_{9.34}(SiO_4)_6O_2$, and $K_{1.32}Pr_{8.68}(SiO_4)_6O_{1.36}F_{0.64}$*

*Latshaw, A. M., Hughey, K. D., Smith, M. D., Yeon, J., zur Loye, H.-C. *Inorg. Chem.*, **2015**, *54* (3), 876-884.

Introduction

Apatite structures have long been studied for many potential applications ranging from electrolytes for solid fuel cells[2.1] to solid state laser hosts[2.2] to phosphors used in luminescent devices.[2.3] More recently, the potential applications of materials belonging to this extensive structural family in solid state lighting has further increased interest in exploring the apatite structure, and in preparing new rare earth containing compositions crystallizing in the apatite structure.

The apatite structure type is named after a class of minerals that have the composition $Ca_5(PO_4)_3X$, where X = F, Cl, or OH. The nomenclature within the apatite mineral class is extensive and overlapping. For this reason, we will apply the basic nomenclature when discussing apatite structures, and use the X component to distinguish the apatites; specifically, we will refer to a fluoroapatite when X = F, a chlorapatite when X = Cl, a hydroxyapatite when X = OH, and an oxyapatite when X =O.[2.4]

Within the extensive family of known apatites, many are reported using the composition $A_{10}(BO_4)_6X_2$, instead of $A_5(BO_4)_3X$. This doubled composition is helpful when sites A and X are occupied by two different cations or anions, as reported herein. In general, "apatite" is used to describe a material with the composition $A_{10}(BO_4)_6X_2$, where A is a large cation, such as an alkali, alkaline-earth, or lanthanide metal cation, or a mix of two of these, B is a smaller cation, such as arsenic ($Sr_{10}(AsO_4)_6Cl_2$),[2.5] boron, chromium ($Sr_{10}(CrO_4)_6F_2$),[2.6] germanium ($NaLa_9(GeO_4)_6O_2$),[2.7] phosphorous, silicon ($Na_{0.5}Nd_{4.5}(SiO_4)_3O$),[2.8] sulfur, or vanadium ($Ba_5(VO_4)_3OH$),[2.9] and X is an anion, such as fluorine, chlorine, or oxygen, or a combination of two of these.[2.10] For the compositions

reported herein it is best to think of the apatite composition as $AA'(BO_4)_6XY$, where A = Ca, K, or Na, A' = *Ln* (Eu, Gd, or Sm), B = Si, and X and Y = O or F.

The silicate apatite structure can act as a sensitizer by absorbing UV radiation and transmitting it to an activator, making it a good host structure for luminescence, as noted in the review by Waychunas in 2002.[2.11] It was also noted in the review that despite this ability, the silicate apatite structure has rarely been studied for its luminescent properties.

In this paper, we are reporting on our efforts to synthesize new rare earth containing silica based apatite materials and on our investigation of the luminescent and magnetic properties observed in silicate apatites. Herein, we present the crystal structures of seven new apatite oxides and oxyfluorides, along with the photoluminescence and magnetic properties of $NaEu_9(SiO_4)_6O_2$, $Na_{1.5}Eu_{8.5}(SiO_4)_6OF$, $Eu_{9.34}(SiO_4)_6O_2$, and $Gd_{9.34}(SiO_4)_6O_2$. The luminescence study indicates that lanthanide containing silicate apatites display luminescent properties that are essentially not affected by other cations or anions, making them good candidates in the search for new optical materials.

Experimental Section

Reagents

Eu_2O_3 (99.9 %), Gd_2O_3 (99.9 %), Sm_2O_3 (99.99 %), Pr_2O_3 reduced from Pr_6O_{11} (99.9 %), LiF (98+ %), $CaCO_3$ (99.95 %), $Na_2MoO_4 \bullet 2H_2O$ (99.5 – 103.0 %), KF (99 % min.), and NaF (99 % min.) were purchased from Alfa Aesar. Na_2CO_3 was purchased from Fisher Scientific, KCl (99.42 %) from Mallinckrodt, and SiO_2 (99.99 %) was purchased from Aldrich as fused pieces and ground to a powder in a ball mill.

Crystal Growth

The conditions described for the crystal growth of the various compositions are those found empirically to give the best yield and crystal quality. A compilation of the flux crystal growth reactions is given in **Table 2.1**.

Single crystals of $Na_{1.5}Eu_{8.5}(SiO_4)_6OF$, $NaEu_9(SiO_4)_6O_2$, and $Na_{1.62}Gd_{8.36}(SiO_4)_6O_{0.72}F_{1.28}$ were grown out of a sodium fluoride flux. Crystals of $Na_{1.5}Eu_{8.5}(SiO_4)_6OF$ were prepared by loading a 2:2:4 mmol ratio of Eu_2O_3:Na_2CO_3:SiO_2 into a platinum crucible. 5 grams of NaF flux were placed on top of the reactants, and a platinum lid was loosely fitted onto the crucible. The crucible was placed into a programmable furnace that was heated to 1150 °C over 1.5 h, allowed to dwell there for 12 h, and then slow cooled at a rate of 6 °C per hour to 1000 °C, after which the furnace was shut off. The flux was washed away using water, aided by sonication, and then the crystals were isolated by filtration.

$NaEu_9(SiO_4)_6O_2$ crystals were prepared by loading a 2:2:4 mmol ratio of Eu_2O_3:Na_2CO_3:SiO_2 into a silver crucible. 3.37g:3.11g of NaF:Na_2MoO_4 flux were placed on top of the reactants, and a silver lid was loosely fitted onto the crucible. The crucible was placed into a programmable furnace that was heated to 750 °C over 1.5 h, allowed to dwell there for 12 h, and then slow cooled at a rate of 6 °C per hour to 550 °C, after which the furnace was shut off. The flux was washed away using water, aided by sonication, and then the crystals were isolated by filtration.

$Na_{1.62}Gd_{8.36}(SiO_4)_6(O_{0.72}F_{1.28})$ crystals were prepared by loading a 1:2 mmol ratio of Gd_2O_3: SiO_2 into a silver crucible. 0.2519g:4.95g of NaF:Na_2MoO_4 flux were placed on top of the reactants, and a silver lid was loosely fitted onto the crucible. The crucible

was placed into a programmable furnace that was heated to 750 °C over 1.5 h, allowed to dwell there for 12 h, and then slow cooled at a rate of 6 °C per hour to 550 °C, after which the furnace was shut off. The flux was washed away using water, aided by sonication, and then the crystals were isolated by filtration.

Crystals of $Gd_{9.34}(SiO_4)_6O_2$ were prepared by loading a 1:2 mmol ratio of Gd_2O_3:SiO_2 into a silver crucible. 1.86g:2.97g of KF:KCl flux were placed on top of the reactants, and a silver lid was loosely fitted onto the crucible. The crucible was placed into a programmable furnace that was heated to 750 °C over 1.5 h, allowed to dwell there for 10 days, and then slow cooled at a rate of 6 °C per hour to 550 °C, after which the furnace was shut off. The flux was washed away using water, aided by sonication, and then the crystals were isolated by filtration.

Crystals of $Ca_{2.6}Eu_{7.4}(SiO_4)_6O_{1.4}F_{0.6}$ and $Ca_{4.02}Sm_{5.98}(SiO_4)_6F_2$ were prepared by loading a 2:1:1 mmol ratio of $CaCO_3$:SiO_2:Ln_2O_3 into a silver crucible. 1.85g:2.97g of KF:KCl flux were placed on top of the reactants, and a silver lid was loosely fitted onto the crucible. The crucible was placed into a programmable furnace that was heated to 750 °C over 1.5 h, allowed to dwell there for 24 h, and then slow cooled at a rate of 6 °C per hour to 550 °C, after which the furnace was shut off. The flux was washed away using water, aided by sonication, and then the crystals were isolated by filtration.

Crystals of $K_{1.32}Pr_{8.68}(SiO_4)_6O_{1.36}F_{0.64}$ were prepared by loading a 2:4 mmol ratio of Pr_2O_3:SiO_2 into a copper tube that was welded at one end. 5 g of KF was then loaded on top of the reactants, and the top of the tube was crimped shut. The reaction was loaded into a flow-through furnace, which contained an outer quartz tube with N_2 gas flowing through it, an inner copper tube to prevent any flux leaks from shattering the

outer quartz tube, and the reaction tube. The furnace was then programmed to heat to 1000 °C over 1.5 h, and held there for 24 h before slow cooling to 800 °C at a rate of 6 °C per hour and then shutting off the furnace. The flux was washed away using water, aided by sonication, and then the crystals were isolated by filtration.

Polycrystalline samples of $NaEu_9(SiO_4)_6O_2$, $Gd_{9.34}(SiO_4)_6O_2$, and $Eu_{9.34}(SiO_4)_6O_2$ were also synthesized via a solid state route. For $NaEu_9(SiO_4)_6O_2$, a stoichiometric ratio of Na_2CO_3 (0.125 mmol), SiO_2 (1.5 mmol), and Eu_2O_3 (1.125 mmol) was ground for 30 min and then transferred to an alumina crucible. The reaction was then heated to 900 °C with multiple heating/grinding cycles before the temperature was increased to 950 °C with multiple heating/grinding cycles. For $Gd_{9.34}(SiO_4)_6O_2$ and $Eu_{9.34}(SiO_4)_6O_2$, stoichiometric ratios of Gd_2O_3 or Eu_2O_3 (1.1675 mmol), and SiO_2 (1.5 mmol) were ground for 30 min and then transferred to an alumina crucible. The reactions were then heated to 900 °C with multiple heating/grinding cycles before the temperature was increased to 950 °C, with regrinding occurring after 48 h of heating. No change took place between 900 °C and 950 °C; therefore, the temperature was increased to 1000 °C with multiple heating/grinding cycles before the temperature was increased to 1050 °C and reground after 48 h, followed by a final heat treatment at 1100 °C, with regrinding after 100 h.

A polycrystalline sample of $Na_{1.5}Eu_{8.5}(SiO_4)_6OF$ was also synthesized via a solid state route. A stoichiometric ratio of Eu_2O_3 (2.125 mmol), Na_2SiO_3 (0.125 mmol), SiO_2 (2.875 mmol), and NaF (0.5 mmol) was ground for 30 min and then pressed into a pellet. The pellet was then loaded into a small copper tube that was crimped at both ends to avoid losing fluoride. The copper tube was loaded into a flow-through furnace purged

with N_2 gas. The reaction was heated to 850 °C, with regrinding occurring after 100 h of heating, before increasing the temperature to 900 °C, with multiple heating/grinding cycles until the pattern stopped changing.

Single Crystal X-ray Diffraction

Single crystal X-ray diffraction data were collected on all titled compounds. X-ray intensity data from a colorless needle crystal of $NaEu_9(SiO_4)_6O_2$ and colorless hexagonal rod crystals of $Na_{1.5}Eu_{8.5}(SiO_4)_6OF$, $Gd_{9.34}(SiO_4)_6O_2$, $Na_{1.62}Gd_{8.36}(SiO_4)_6O_{0.72}F_{1.28}$, $Ca_{2.6}Eu_{7.4}(SiO_4)_6O_{1.4}F_{0.6}$, $Ca_{4.02}Sm_{5.98}(SiO_4)_6F_2$, and $K_{1.32}Pr_{8.68}(SiO_4)_6O_{1.36}F_{0.64}$ were collected using a Bruker SMART APEX diffractometer (Mo Kα radiation, λ = 0.71073 Å).[2.12] The data collection covered 100 % of reciprocal space to $2\theta_{max}$ = 65.2 °, 56.6 °, 70.6 °, 70.1 °, 71.1 °, 70.1 °, and 56.58 °, respectively, with R_{int} = 0.036, 0.025, 0.036, 0.040, 0.040, 0.052, and 0.031 after absorption correction. The raw area detector data frames were reduced and corrected for absorption effects using the SAINT+ and SADABS programs.[2.12] Final unit cell parameters were determined by least-squares refinement of reflections from the data set. The initial structural model was obtained by direct methods using SHELXS.[2.13] Subsequent difference Fourier calculations and full-matrix least-squares refinement against F^2 were performed with SHELXL-2013/4[2], using the ShelXle interface.[2.14]

The compounds crystallize in the hexagonal space group $P6_3/m$, as determined by the pattern of systematic absences in the intensity data, and by the structure solution. These compounds adopt the fluoroapatite ($Ca_5(PO_4)_3F$) structure type. The apatite structure contains two unique lanthanide sites, where *Ln*(1) is located on a three-fold axis (Wyckoff symbol 4*f*, site symmetry 3), while *Ln*(2) is located on a mirror plane (site 6*h*,

site symmetry m). In $NaEu_9(SiO_4)_6O_2$, sodium mixes on the *Ln*(1) site, while in $Na_{1.5}Eu_{8.5}(SiO_4)_6OF$, $Gd_{8.36}Na_{1.62}(SiO_4)_6O_{0.72}F_{1.28}$, $Ca_{2.6}Eu_{7.4}(SiO_4)_6O_{1.4}F_{0.6}$, $Ca_{4.02}Sm_{5.98}(SiO_4)_6F_2$, and $K_{1.32}Pr_{8.68}(SiO_4)_6O_{1.36}F_{0.64}$, sodium or potassium mixes on both the *Ln*(1) and *Ln*(2) sites. For $Gd_{9.34}(SiO_4)_6O_2$, there is a partial vacancy on the *Ln*(1) site that matches what has been previously reported for the $Gd_{9.34}(SiO_4)_6O_2$ compound.[2.15] Atoms Si(1), O(1), and O(2) are located on mirror planes (site 6*h*, site symmetry *m*). Oxygen O(3) is located on a general position (site 12*i*), and oxygen O(4) is located on site 2*a* with -6 site symmetry. Site 2*a* is occupied either by O(4), in $NaEu_9(SiO_4)_6O_2$ and $Gd_{9.34}(SiO_4)_6O_2$, a mixing of O(4) and F(1), in $Na_{1.5}Eu_{8.5}(SiO_4)_6OF$, $Gd_{8.36}Na_{1.62}(SiO_4)_6O_{0.72}F_{1.28}$, $Ca_{2.6}Eu_{7.4}(SiO_4)_6O_{1.4}F_{0.6}$, and $K_{1.32}Pr_{8.68}(SiO_4)_6O_{1.36}F_{0.64}$, or only F(1), in $Ca_{4.02}Sm_{5.98}(SiO_4)_6F_2$. All atoms were refined with anisotropic displacement parameters. Final atomic coordinates were standardized with Structure Tidy.[2.16 2.17 2.18] Further details of the crystal structure investigation can be obtained from the Fachinformationszentrum Karlsruhe (e-mail: crystdata@fiz-karlsruhe.de) using the depository numbers 428482 for $Na_{1.64}Gd_{8.36}(SiO_4)_6O_{0.72}F_{1.28}$, 428483 for $K_{1.32}Pr_{8.68}(SiO_4)_6O_{1.36}F_{0.64}$, 428484 for $Na_{1.5}Eu_{8.5}(SiO_4)_6OF$, 428485 for $NaEu_9(SiO_4)_6O_2$, 428486 for $Ca_{2.6}Eu_{7.4}(SiO_4)_6O_{1.4}F_{0.6}$, 428487 for $Ca_{4.02}Sm_{5.98}(SiO_4)_6F_2$ and 428488 for $Gd_{9.34}(SiO_4)_6O_2$.

Powder X-ray Diffraction

The powder X-ray diffraction patterns for the polycrystalline samples from the solid state reactions $NaEu_9(SiO_4)_6O_2$, $Na_{1.5}Eu_{8.5}(SiO_4)_6OF$, $Gd_{9.34}(SiO_4)_6O_2$, and $Eu_{9.34}(SiO_4)_6O_2$ were collected using a Rigaku Dmax/2100 powder diffractometer using Cu Kα radiation. Data for $NaEu_9(SiO_4)_6O_2$, $Na_{1.5}Eu_{8.5}(SiO_4)_6OF$, and $Gd_{9.34}(SiO_4)_6O_2$

were collected using a step scan covering the 2-theta range of 5 – 65 ° in steps of 0.02 °. Data for the $Eu_{9.34}(SiO_4)_6O_2$ were collected using a step scan covering the 2-theta range of 5 – 120 ° in steps of 0.04 °. PXRD patterns were collected on the compounds grown by flux growth; $Na_{1.64}Gd_{8.36}(SiO_4)_6O_{0.72}F_{1.28}$, $Gd_{9.34}(SiO_4)_6O_2$, $Ca_{2.6}Eu_{7.4}(SiO_4)_6O_{1.4}F_{0.6}$, $Ca_{4.02}Sm_{5.98}(SiO_4)_6F_2$, and $K_{1.32}Pr_{8.68}(SiO_4)_6O_{1.36}F_{0.64}$, all of which contain small amounts of unreacted, water insoluble SiO_2, Gd_2O_3 (about 5 %), CaF_2 (about 10-16 %), as well as, in some cases, secondary phases like $K_3GdSi_2O_7$ (about 40 %), $Eu(AlO_3)$ (about 33 %), and another new praseodymium compound in the powder samples that cannot be removed by washing. Powder samples that included lanthanide containing secondary phases were not measured for luminescent properties because the impurities would affect the luminescence.

X-ray Photoelectron Spectroscopy

Survey and detailed scans of the polycrystalline sample of $Na_{1.5}Eu_{8.5}(SiO_4)_6OF$ were performed using X-ray Photoelectron Spectroscopy (XPS) on a Kratos AXIS Ultra DLD XPS system equipped with a monochromatic Al Kα. The Al Kα source had an operational level of 15 keV and 120 W, and the analyzer lens mode was hybrid. For the survey scan, the pass energy was fixed at 160 eV, the scan range was from 1350 eV to -0.8 eV, and the scan step was 400 meV with a dwell time of 500 ms. For the high-resolution XPS spectra acquisition, the pass energy was fixed at 40 eV; the scan range was chosen based on the interested elements, and the scan step was 60 meV with a dwell time of 2500 ms.

Luminescence

Emission and excitation spectra were collected on powders of $NaEu_9(SiO_4)_6O_2$, $Gd_{9.34}(SiO_4)_6O_2$, $Eu_{9.34}(SiO_4)_6O_2$, and $Na_{1.5}Eu_{8.5}(SiO_4)_6OF$ at room temperature using a Perkin Elmer LS 55 fluorescence spectrometer. Excitation and emission scans were performed in the 225 – 500 and 550 – 900 nm ranges, respectively. Luminescence data of the other compounds were not collected due to the presence of lanthanide containing secondary phases that would have affected the data collection.

Magnetic Property Measurements

The DC magnetizations of $NaEu_9(SiO_4)_6O_2$, $Gd_{9.34}(SiO_4)_6O_2$, $Eu_{9.34}(SiO_4)_6O_2$, and $Na_{1.5}Eu_{8.5}(SiO_4)_6OF$ were measured as a function of temperature using a Quantum Design Magnetic Property Measurement System (QD-MPMS3 SQUID VSM). These compounds were placed in gel capsules. The samples were then cooled to 2 K in zero-field cooled (zfc) conditions. Data was collected from 2 to 300 K with an applied magnetic field of 1000 Oe. Corrections for the radial offset and sample shape were applied to the magnetism with a fitting routine that involved data collected at 30 K under both DC and VSM modes.[2.19] Magnetic properties of the other compounds were not collected due to the presence of lanthanide containing secondary phases that would have affected the sample magnetization.

Results and Discussion

Powder X-ray Diffraction

The calculated and experimental PXRD patterns for the polycrystalline solid state reactions $NaEu_9(SiO_4)_6O_2$, $Na_{1.5}Eu_{8.5}(SiO_4)_6OF$, and $Gd_{9.34}(SiO_4)_6O_2$ are in excellent

agreement, as seen in **Figure 2.1**. $Eu_{9.34}(SiO_4)_6O_2$, which has been published previously as a polycrystalline powder,[2.20] was compared to $Gd_{9.34}(SiO_4)_6O_2$ (**Figure 2.2**). It was determined that there was a very small amount of Eu_2O_3 in the $Eu_{9.34}(SiO_4)_6O_2$ polycrystalline powder. The Eu_2O_3 can only been seen when zooming in on the powder pattern.

Crystal Structure

Alkali fluoride melts have been identified as good fluxes for the crystal growth of oxides,[2.21] and were used to grow crystals of the title compounds. In order to lower the temperatures of the fluxes to carry out the reactions in silver instead of platinum crucibles, eutectic compositions were used. The fluxes used include NaF (m.p. 993°), NaF(34%)/NaCl(66%) (m.p. 679°), NaF(20%)/Na_2MoO_4(80%) (m.p. 614°C), and KF(45%)/KCl(55%) (m.p. 606°C). Crystal growth reactions carried out in the NaF and NaF containing eutectic fluxes consistently resulted in sodium incorporation into the reaction products, while reactions carried out in KF based eutectics did not result in the incorporation of potassium into the crystals. Only when KF was used neat, did the potassium incorporate. All compounds crystallize in the hexagonal space group $P6_3/m$. The crystallographic data are compiled in **Table 2.2**.

Many of the known lanthanide silicate oxyapatites crystallize in the space group $P6_3/m$, as is the case for the title compounds; however, apatites are known to also crystallize in five other principle space groups including $P6_3$, P-3, P-6, $P2_1/m$ and $P2_1$.[2.3, 2.10, 2.22-2.31] All apatite structures contain columns consisting of distorted, face-sharing trigonal prisms as shown in **Figure 2.3**. In the case of apatites taking on the $P6_3/m$ space group, the $Ln(1)$ site occupies the cation sites in these columns. As the space group

changes to, for example, $P2_1/m$ or $P2_1$, there are either multiple cations occupying these columns, or the distortions of the columns, called the metaprism twist angles, grow larger or less uniform. In the $P6_3/m$ space group, the metaprism twist angles must be uniform, while for space groups $P2_1/m$ and $P2_1$, there can be multiple metaprism angles for each trigonal prism.[2.22]

As observed previously in the literature, in compounds with the composition $A_xLn_{10-x}(SiO_4)_6O_2$, where *A* is an alkali or alkaline earth metal cation, and *Ln* is a lanthanide, mixing of the *A* and *Ln* cations will only occur on the 4*f*, or *Ln*(1), site, leaving the 6*h*, or *Ln*(2), site fully occupied by the *Ln* cations. Compounds with compositions $A_xLn_{10-x}(SiO_4)_6OF$ or $A_xLn_{10-x}(SiO_4)_6F_2$, on the other hand, typically exhibit mixing of the *A* and *Ln* cations on both the 4*f* and 6*h* sites. [2.23] The 4*f* and 6*h* sites are shown in **Figure 2.4**.

In the $A_xLn_{10-x}(SiO_4)_6X_2$ apatite structure, there are two unique lanthanide polyhedra (*Ln*(1) and *Ln*(2)), an isolated SiO_4 tetrahedra, and an O(4) site that contains either O^{2-}, F^-, or a mix of O^{2-} and F^-. *Ln*(1) is located in a six coordinated twisted trigonal prism, *Ln*(2) is located in a seven-coordinated distorted pentagonal bipyramid, and Si(1) is located in an isolated tetrahedron. *Ln*(1) and *Ln*(2) form columns down the *c* axis. The *Ln*(1) columns are formed by face-shared stacking of distorted trigonal prisms, as shown in **Figure 2.3**. The *Ln*(2) columns are formed when three *Ln*(2) polyhedra in each layer corner share through the O(4)/F(1) site to form $Ln(2)_3O_{19}$ units, as depicted in **Figure 2.5**. The $Ln(2)_3O_{19}$ units are rotated by 60 ° (**Figure 2.5**) to form the *Ln*(2) polyhedra columns down the *c* axis (**Figure 2.6**). The lanthanide polyhedra are connected via edge sharing of the *Ln*(1) polyhedra with three of the *Ln*(2) columns. The isolated SiO_4 tetrahedra are

located between the *Ln*(1) and *Ln*(2) containing columns. The overall view of the structure down the *c* axis is shown in **Figure 2.7**. In all of the compounds reported herein, the average Si-O bond distance is 1.62 Å, the average *Ln*(1)-O interatomic distance is 2.55 Å, and the average *Ln*(2) – O interatomic distance is 2.42 Å. Selected interatomic distances are tabulated in **Table 2.3**.

The metaprism twist angles of the *Ln*(1) polyhedra for the seven compounds range from 22.43 – 22.23 °. These values fall into the range of twist angles of 5 – 25 °, which is expected for apatites crystallizing in the $P6_3/m$ space group. [2.32]

X-ray Photoelectron Spectroscopy

The preparation of oxyfluoride samples via the solid-state route readily leads to the desired composition and structure. However, since it is very difficult to differentiate between oxygen and fluorine by X-ray diffraction, and because of the possibility that fluorine might be lost during the synthesis, X-ray photoelectron spectroscopy was used to confirm the presence of fluorine in a polycrystalline sample of $Na_{1.5}Eu_{8.5}(SiO_4)_6OF$. The survey scan in **Figure 2.8** covered the entire sample surface and confirms the existence of Na, Eu, Si, O, and F elements. A high-resolution XPS spectrum covering the range of 705-670 eV revealed a peak at 685 eV (after a correction with C 1s, 284.6 eV), as shown in **Figure 2.8**, which conclusively indicates the presence of metal bound fluorine; it matches well with the metal bound F 1s peak ranges (684-685.8 eV) given in the Handbook of X-ray Photoelectron Spectroscopy.[2.33] These results confirm the presence of fluorine in the polycrystalline sample of $Na_{1.5}Eu_{8.5}(SiO_4)_6OF$ and its coordination nature.

Photoluminescence

Fluorescence data were collected on solid state powders of $NaEu_9(SiO_4)_6O_2$, $Na_{1.5}Eu_{8.5}(SiO_4)_6OF$, $Eu_{9.34}(SiO_4)_6O_2$, and $Gd_{9.34}(SiO_4)_6O_2$. The room temperature emission spectra for the europium containing compounds are shown in **Figure 2.9**, and the excitation spectra are shown in **Figure 2.10**. The emission spectra for the europium containing compounds were collected using an excitation wavelength of 230 nm, while the excitation spectra of the compounds were collected using an emission wavelength of 607 nm. The maximum emission peaks at 607 nm are typical for europium containing compounds.[2.34] In **Figure 2.10**, the excitation peaks of the europium containing compounds follow the expected set of peaks from 350 – 425 nm that indicate the transitions within the $4f^6$ configuration of the Eu^{3+} cation.

For the gadolinium compound, the excitation and emission spectra are displayed in **Figure 2.11**. The excitation wavelength was 250 nm, and the emission wavelength was 622 nm. The gadolinium compound exhibits excitation and emission spectra peaks consistent with expected values for gadolinium containing compounds.

A close look at the luminescence data for $NaEu_9(SiO_4)_6O_2$, $Na_{1.5}Eu_{8.5}(SiO_4)_6OF$, and $Eu_{9.34}(SiO_4)_6O_2$ demonstrates that the excitation and emission data are almost identical. This suggests that changing the ratio of the cation atoms on the *Ln* sites and of the anion atoms on the *X* site does not change the luminescence. This result supports the hypothesis that doping other luminescent cations onto the lanthanide site will allow tuning of the luminescence.

Magnetic Properties

The temperature dependencies of the magnetic susceptibilities of $NaEu_9(SiO_4)_6O_2$, $Na_{1.5}Eu_{8.5}(SiO_4)_6OF$, $Eu_{9.34}(SiO_4)_6O_2$, and $Gd_{9.34}(SiO_4)_6O_2$ were measured over the temperature range of 2-300 K and are shown in **Figures 2.12 – 2.13**. The europium containing compounds display van Vleck paramagnetism, while the gadolinium compound follows the Curie-Weiss law. The effective moment at 300 K was determined for the three europium compounds, $NaEu_9(SiO_4)_6O_2$, $Eu_{9.34}(SiO_4)_6O_2$, and $Na_{1.5}Eu_{8.5}(SiO_4)_6OF$, and found to be 3.40, 3.42, and 3.18 μ_B/Eu, which compares well with the generally accepted 300 K value for Eu^{3+} of 3.4 μ_B/Eu. The $Gd_{9.34}(SiO_4)_6O_2$ susceptibility data collected from 2 – 300 K, when fit to the Curie-Weiss law, yielded an effective moment of 7.86 μ_B/Gd and a Weiss constant of θ = 0.3 K, which compares well to the expected value of 7.94 μ_B/Gd.

Conclusion

Single crystals of compounds of the apatite structure type, $NaEu_9(SiO_4)_6O_2$, $Na_{1.5}Eu_{8.5}(SiO_4)_6OF$, $Na_{1.64}Gd_{8.36}(SiO_4)_6O_{0.72}F_{1.28}$, $Gd_{9.34}(SiO_4)_6O_2$, $Ca_{2.6}Eu_{7.4}(SiO_4)_6O_{1.4}F_{0.6}$, $Ca_{4.02}Sm_{5.98}(SiO_4)_6F_2$, and $K_{1.32}Pr_{8.68}(SiO_4)_6O_{1.36}F_{0.64}$, were synthesized in fluoride fluxes, and $NaEu_9(SiO_4)_6O_2$, $Na_{1.5}Eu_{8.5}(SiO_4)_6OF$, $Eu_{9.34}(SiO_4)_6O_2$, and $Gd_{9.34}(SiO_4)_6O_2$ were prepared as polycrystalline powders using solid state synthesis techniques. As previously reported, the mixing of the *Ln*(2) cation site is dependent upon substitution on the O(4) site with either F^- or OH^-. The luminescent properties of the silicon containing apatites indicate that these compounds may find potential applications in solid-state lighting, because the luminescence may be tunable.

References

2.1 Masubuchi, Y.; Higuchi, M.; Takeda, T.; Kikkawa, S. *Solid State Ionics* **2006**, *177*, 263-268.
2.2 Hopkins, R. H.; Melamed, N. T.; Henningsen, T.; Roland, G. W. *J. Cryst. Growth* **1971**, *10*, 218-222.
2.3 Ferdov, S.; Sa Ferreira, R.; Lin, Z. *Chem. Mater.* **2006**, *18*, 5958-5964.
2.4 Pasero, M.; Kampf, A. R.; Ferraris, C.; Pekov, I. V.; Rakovan, J.; White, T. J. *Eur. J. Mineral* **2010**, *22*, 163-179.
2.5 Henderson, C. M. B.; Bell, A. M. T.; Charnock, J. M.; Knight, K. S.; Wendlandt, R. F.; Plant, D. A.; Harrison, W. J. *Mineral Mag.* **2009**, *73*, 433-455.
2.6 Baikie, T.; Ahmad, Z.; Srinivasan, M.; Maignan, A.; Pramana, S. S.; White, T. J. *J. Solid State Chem.* **2007**, *180*, 1538-1546.
2.7 Takahashi, M.; Uematsu, K.; Ye, Z.-G.; Sato, M. *J. Solid State Chem.* **1998**, *139*, 304-309.
2.8 Latshaw, A. M.; Smith, M. D.; zur Loye, H.-C. *Solid State Sci.* **2014**, *35*, 28-32.
2.9 Mugavero, S. J., III; Bharathy, M.; McAlum, J.; zur Loye, H.-C. *Solid State Sci.* **2008**, *10*, 370-376.
2.10 Leu, L.-C.; Thomas, S.; Sebastian, M. T.; Zdzieszynski, S.; Misture, S.; Ubic, R. *J. Am. Ceram. Soc.* **2011**, *94*, 2625-2632.
2.11 Waychunas, G. A. *Rev. Mineral Geochem.* **2002**, *48*, 701-742.
2.12 SMART Version 5.630, SAINT+ Version 6.45 and SADABS Version 2.10. Bruker Analytical X-ray Systems, Inc., Madison, Wisconsin, USA, 2003.
2.13 Sheldrick, G. M. *Acta. Cryst.* **2008**, *A64*, 112-122.
2.14 Hübschle, C. B.; Sheldrick, G. M.; Bittrich, B. *J. Appl. Cryst.* **2011**, *44*, 1281-1284.
2.15 Smolin, Y. I.; Shepelev, Y. F. *Izv. Akad. Nauk SSSR, Neorg. Mater.* **1969**, *5*, 1823-1825.
2.16 Parthé, E.; Gelato, L. M. *Acta. Cryst.* **1984**, *A40*, 169-183.
2.17 Gelato, L. M.; Parthé, E. *J. Appl. Cryst.* **1987**, *20*, 139-143.
2.18 Hu, S.-Z.; Parthé, E. *Chinese J. Struct. Chem.* **2004**, *23*, 1150-1160.
2.19 Morrison, G.; zur Loye, H.-C. *J. Solid State Chem.*, **2015**, *221*, 334-337.
2.20 Felsche, J. *J. Solid State Chem.* **1972**, *5*, 266-275.
2.21 Bugaris, D. E.; zur Loye, H.-C. *Angew. Chem. Int. Ed.* **2012**, *51*, 2-34.
2.22 White, T.; Ferraris, C.; Kim, J.; Madhavi, S. *Rev. Mineral Geochem.* **2005**, *57*, 307-401.
2.23 Toumi, M.; Smiri-Dogguy, L.; Bulou, A. *Ann. Chim. Sci. Mat.* **2002**, *27*, 17-26.
2.24 Shen, Y.; Tok, A.; Dong, Z. *J. Am. Ceram. Soc.* **2010**, *93*, 1176-1182.
2.25 Schroeder, L. W.; Mathew, M. *J. Solid State Chem.* **1978**, *26*, 383-387.
2.26 Chiu, Y.-C. L., W.-R.; Yeh, Y.-T.; Jang, S.-M.; and Chen, T.-M. *J. Chem. Chem. Eng.* **2011**, *5*, 841-846.
2.27 Lu, W.; Jia, Y.; Lv, W.; Zhao, Q.; You, H. *New J. Chem.* **2013**, *37*, 3701-3705.
2.28 Nötzold, D.; Wulff, H. *Phys. Stat. Sol. (B)* **1998**, *207*, 271-282.
2.29 An, T.; Baikie, T.; Wei, F.; Pramana, S. S.; Schreyer, M. K.; Piltz, R. O.; Shin, J. F.; Wei, J.; Slater, P. R.; White, T. J. *Chem. Mater.* **2013**, *25*, 1109-1120.
2.30 Maisonneuve, V.; Leduc, E.; Bohnke, O.; Leblanc, M. *Chem. Mater.* **2004**, *16*, 5220-5222.

2.31 White, T. J.; ZhiLi, D. *Acta. Cryst.* **2003**, *B59*, 1-16.
2.32 Lim, S. C.; Baikie, T.; Pramana, S. S.; Smith, R.; White, T. J. *J. Solid State Chem.* **2011**, *184*, 2978-2986.
2.33 Wagner, C. D.; Riggs, W. M.; Davis, L. E.; Moulder, J. F. *Handbook of X-ray Photoelectron Spectroscopy*; Perkin-Elmer Corporation: Eden Prairie, MN, 1979; pp 169.
2.34 Blasse, G.; Grabmaier, B. C. *Luminescent materials*; Springer-Verlag: New York, 1994.

Table 2.1. Reaction conditions of the flux crystal growth syntheses of the titled compounds.

Compound	Reactants			Flux	Flux Melting Point	Dwell Temp. Time	Cooling Temp. Rate
$Na_{1.5}Eu_{8.5}(SiO_4)_6OF$	Eu_2O_3 2mmol	Na_2CO_3 2mmol	SiO_2 4mmol	NaF	993 °C	1150 °C 12 h	1000 °C 6 °C/h
$NaEu_9(SiO_4)_6O_2$	Eu_2O_3 2mmol	Na_2CO_3 2mmol	SiO_2 4mmol	$NaF:Na_2MoO_4$	614 °C	750 °C 12 h	550 °C 6 °C/h
$Na_{1.62}Gd_{8.36}(SiO_4)_6O_{0.72}F_{1.28}$	Gd_2O_3 1mmol		SiO_2 2mmol	$NaF:Na_2MoO_4$	614 °C	750 °C 12 h	550 °C 6 °C/h
$Gd_{9.34}(SiO_4)_6O_2$	Gd_2O_3 1mmol		SiO_2 2mmol	KF:KCl	606 °C	750 °C 10 days	550 °C 6 °C/h
$Ca_{2.6}Eu_{7.4}(SiO_4)_6O_{1.4}F_{0.6}$	Eu_2O_3 1mmol	$CaCO_3$ 2mmol	SiO_2 1mmol	KF:KCl	606 °C	750 °C 24 h	550 °C 6 °C/h
$Ca_{4.02}Sm_{5.98}(SiO_4)_6F_2$	Sm_2O_3 1mmol	$CaCO_3$ 2mmol	SiO_2 1mmol	KF:KCl	606 °C	750 °C 24 h	550 °C 6 °C/h
$K_{1.32}Pr_{8.68}(SiO_4)_6O_{1.36}F_{0.64}$	Pr_2O_3 2mmol		SiO_2 4mmol	KF	858 °C	1000 °C 24 h	800 °C 6 °C/h

Table 2.2. Crystallographic data for the reported compounds where all crystallize in the hexagonal crystal system.

Formula	$NaEu_9(SiO_4)_6O_2$	$Na_{1.5}Eu_{8.5}(SiO_4)_6OF$	$Na_{1.64}Gd_{8.36}(SiO_4)_6O_{0.72}F_{1.28}$	$Gd_{9.34}(SiO_4)_6O_2$
Formula weight	1975.18	1913.69	1940.02	2052.16
Temperature (K)	296(2)	296(2)	296(2)	296(2)
Crystal System	Hexagonal	Hexagonal	Hexagonal	Hexagonal
Space group	$P\,6_3/m$	$P\,6_3/m$	$P\,6_3/m$	$P\,6_3/m$
a (Å)	9.4434(1)	9.4492(4)	9.4257(2)	9.4366(2)
c (Å)	6.9150(2)	6.9155(7)	6.8850(2)	6.9345(2)
V (Å^3)	534.047(19)	534.74(6)	529.74(3)	534.78(3)
Z	2	2	2	2
Density (mg/m^3)	6.141	5.943	6.081	6.372
Absorption coefficient (mm^{-1})	26.481	25.021	26.259	28.953
Crystal size (mm^3)	0.12 × 0.04 × 0.04	0.09 × 0.04 × 0.04	0.08 × 0.06 × 0.04	0.10 × 0.06 × 0.05
2 theta range (°)	4.98 to 65.17	4.98 to 56.56	4.99 to 70.13	4.98 to 70.59
reflections collected	12296	7410	15179	14658
data/restraints/parameters	707 / 0 / 41	485 / 1 / 42	837 / 0 / 42	861 / 0 / 39
R (int)	0.0359	0.0250	0.0395	0.0360
GOF (F^2)	1.292	1.179	1.245	1.341
R indices (all data)	R_1 = 0.0228 wR_2 = 0.0482	R_1 = 0.0195 wR_2 = 0.0409	R_1 = 0.0265 wR_2 = 0.0562	R_1 = 0.0280 wR_2 = 0.0646

Table 2.2. (Continued)

Formula	$Ca_{4.02}Sm_{5.98}(SiO_4)_6F_2$	$Ca_{2.6}Eu_{7.4}(SiO_4)_6O_{1.4}F_{0.6}$	$K_{1.32}Pr_{8.68}(SiO_4)_6O_{1.36}F_{0.64}$
Formula weight	1650.98	1814.6	1861.17
Temperature (K)	296(2)	296(2)	294(2)
Crystal System	Hexagonal	Hexagonal	Hexagonal
Space group	*P* $6_3/m$	*P* $6_3/m$	*P* $6_3/m$
a (Å)	9.4792(6)	9.4515(2)	9.6103(2)
c (Å)	6.9358(8)	6.9181(3)	7.1367(2)
V (Å^3)	539.72(9)	535.20(3)	570.82(2)
Z	2	2	2
Density (mg/m^3)	5.079	5.630	5.414
Absorption coefficient (mm^{-1})	17.429	22.417	18.814
Crystal size (mm^3)	0.12 × 0.04 × 0.03	0.12 × 0.03 × 0.02	0.24 x 0.12 x 0.10
2 theta range (°)	4.96 to 70.12	4.98 to 71.16	4.90 to 56.58
reflections collected	12616	14418	5979
data/restraints/parameters	849 / 0 / 42	879 / 0 / 43	510 / 0 / 42
R (int)	0.0516	0.0396	0.0310
GOF (F^2)	1.314	1.291	1.299
R indices (all data)	R_1 = 0.0483	R_1 = 0.0268	R_1 = 0.0152
	wR_2 = 0.0808	*w*R_2 = 0.0583	*w*R_2 = 0.0356

Table 2.3. Selected Bond Distances (in Å) for $NaEu_9(SiO_4)_6O_2$, $Na_{1.5}Eu_{8.5}(SiO_4)_6OF$, $Na_{1.64}Gd_{8.36}(SiO_4)_6O_{0.72}F_{1.28}$, $Gd_{9.34}(SiO_4)_6O_2$, $Ca_{4.02}Sm_{5.98}(SiO_4)_6F_2$, $Ca_{2.6}Eu_{7.4}(SiO_4)_6O_{1.4}F_{0.6}$, and $K_{1.32}Pr_{8.68}(SiO_4)_6O_{1.36}F_{0.64}$.

	$NaEu_9(SiO_4)_6O_2$	$Na_{1.5}Eu_{8.5}(SiO_4)_6OF$	$Na_{1.64}Gd_{8.36}(SiO_4)_6O_{0.72}F_{1.28}$	$Gd_{9.34}(SiO_4)_6O_2$
Ln(1) – O(2) (x3)	2.382(3)	2.386(4)	2.373(3)	2.387(4)
Ln(1) – O(1) (x3)	2.456(3)	2.463(3)	2.449(3)	2.475(4)
Ln(1) – O(3) (x3)	2.813(4)	2.830(5)	2.803(4)	2.813(5)
Ln(2) – *X*	2.2431(3)	2.2646(3)	2.2532(3)	2.2254(3)
Ln(2) – O(3) (x2)	2.336(3)	2.331(4)	2.317(3)	2.346(4)
Ln(2) – O(1)	2.405(4)	2.393(5)	2.382(4)	2.401(5)
Ln(2) – O(3) (x2)	2.489(4)	2.484(4)	2.479(4)	2.473(4)
Ln(1) – O(2)	2.664(5)	2.654(5)	2.662(5)	2.648(7)
	$Ca_{4.02}Sm_{5.98}(SiO_4)_6F_2$	$Ca_{2.6}Eu_{7.4}(SiO_4)_6O_{1.4}F_{0.6}$	$K_{1.32}Pr_{8.68}(SiO_4)_6O_{1.36}F_{0.64}$	
Ln(1) – O(2) (x3)	2.384(4)	2.377(3)	2.467(2)	
Ln(1) – O(1) (x3)	2.441(5)	2.443(3)	2.535(2)	
Ln(1) – O(3) (x3)	2.820(7)	2.799(4)	2.870(3)	
Ln(2) – *X*	2.3287(6)	2.2465(3)	2.2814(2)	
Ln(2) – O(3) (x2)	2.325(5)	2.330(3)	2.429(3)	
Ln(2) – O(1)	3.386(7)	2.412(4)	2.462(3)	
Ln(2) – O(3) (x2)	2.505(5)	2.495(3)	2.550(2)	
Ln(1) – O(2)	2.680(8)	2.703(5)	2.684(4)	

X = O(4) or F(1), respectively

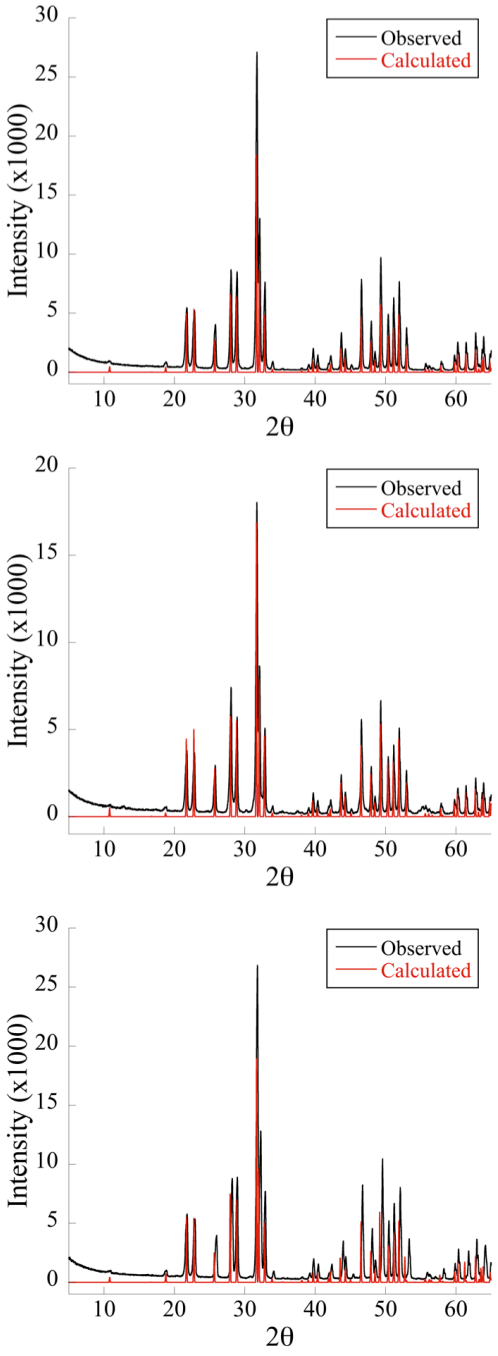

Figure 2.1. PXRD pattern of $NaEu_9(SiO_4)_6O_2$, $Na_{1.5}Eu_{8.5}(SiO_4)_6OF$, and $Gd_{9.34}(SiO_4)_6O_2$. The observed patterns are in good agreement with the calculated patterns.

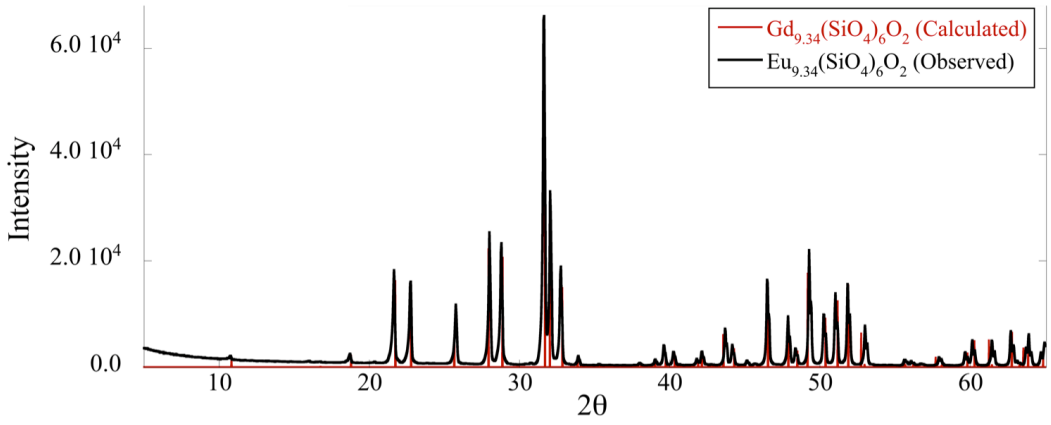

Figure 2.2. Powder diffraction of the polycrystalline sample of $Eu_{9.34}(SiO_4)_6O_2$ where the calculated powder diffraction pattern of $Gd_{9.34}(SiO_4)_6O_2$ is overlaid in red to indicate that $Eu_{9.34}(SiO_4)_6O_2$ was synthesized.

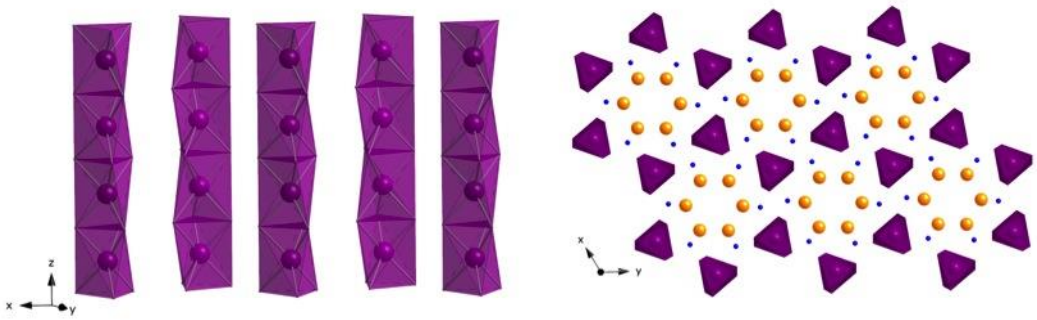

Figure 2.3. Crystal structure of $Na_{1.5}Eu_{8.5}(SiO_4)_6OF$, which is representative of the titled compounds. The left image represents the *Ln*(1) columns where the distortion of the columns can be seen, and the image on the right indicates the view of the *Ln*(1) columns shown down the *c* axis, where the purple polyhedra are the *Ln*(1) site, the orange spheres represent the *Ln*(2) site, and the blue spheres indicate the Si site.

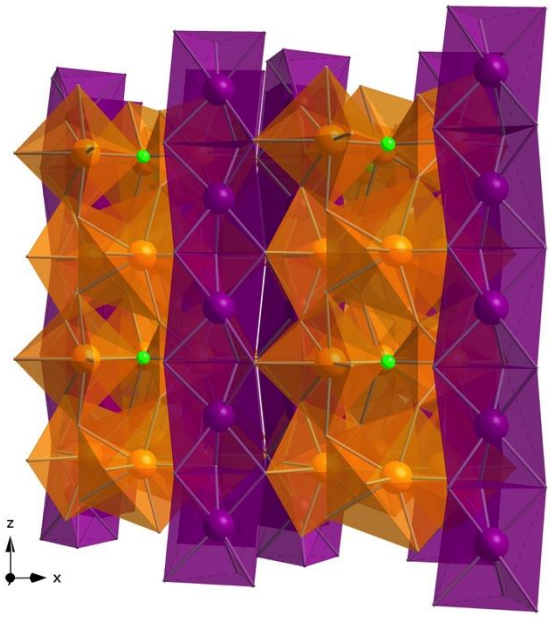

Figure 2.4. Crystal structure of $K_{1.32}Pr_{8.68}(SiO_4)_6O_{1.36}F_{0.64}$, which is representative of the titled compounds. The 4*f*, or *Ln*(1), site is shown as purple polyhedra, the 6*h* site is shown as orange polyhedra, and the O(4)/F(1) site is shown as green spheres.

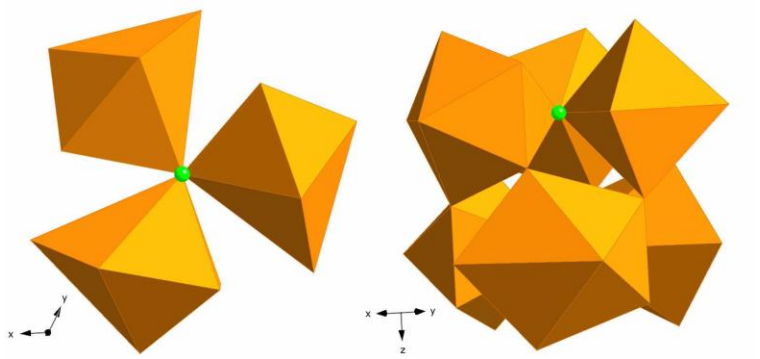

Figure 2.5. Crystal structure of $Na_{1.5}Eu_{8.5}(SiO_4)_6OF$, a representative structure of the titled compounds. The $Ln(2)_3O_{19}$ or $Ln(2)_3O_{18}F$ group is shown on the left, where the orange polyhedra indicate each $Ln(2)O_7$ or $Ln(2)O_6F$ unit, and the green atom is the O(4) or F(1) site. The image on the left represents the 60 ° rotation that occurs to the $Ln(2)_3O_{19}$ units to form the columns down the *c* axis.

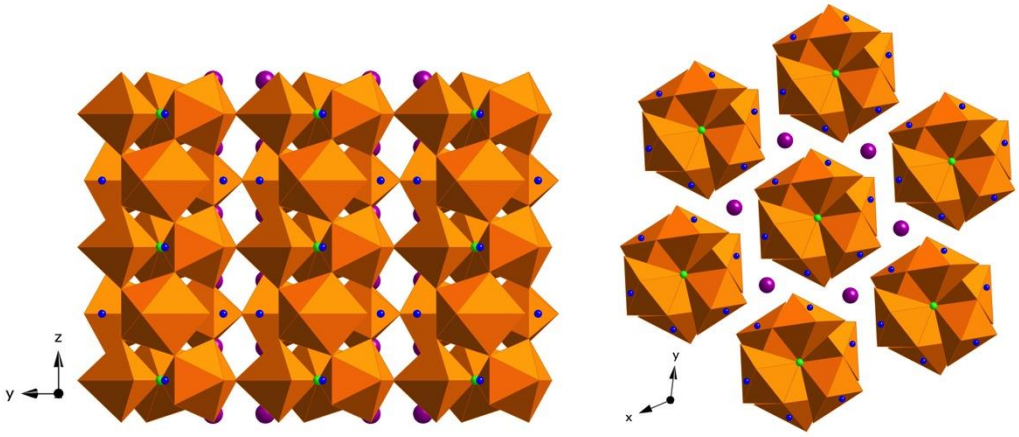

Figure 2.6. Crystal structure of $Na_{1.5}Eu_{8.5}(SiO_4)_6OF$, which is representative of the titled compounds. The image on the left shows the stacking of the $Ln(2)_3O_{19}$ units down the *a* axis, and the image on the right is the view of the columns down the *c* axis. The orange polyhedra represent the *Ln*(2) site, the purple spheres represent the *Ln*(1) site, the blue spheres represent the Si site, and the green spheres represent the O(4)/F(1) site.

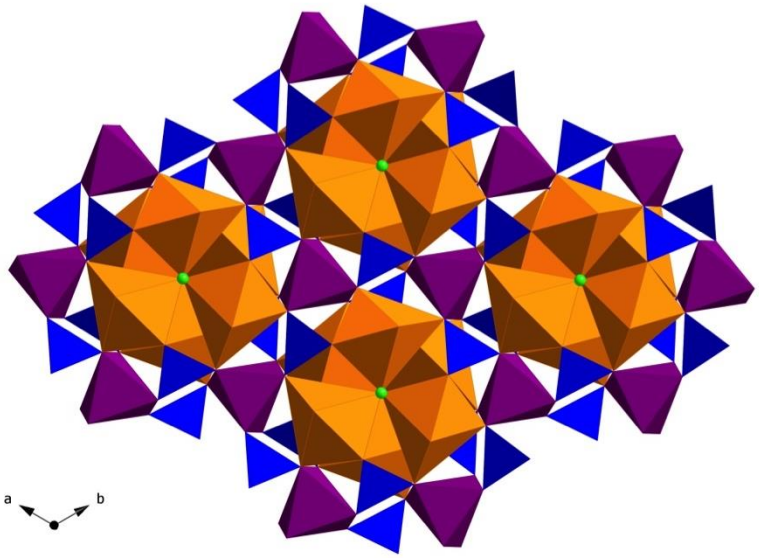

Figure 2.7. Crystal structure of $Na_{1.5}Eu_{8.5}(SiO_4)_6OF$, a representative structure of the titled compounds down the *c* axis, where the *Ln*(1) polyhedra are shown in purple, *Ln*(2) polyhedra are shown in orange, SiO_4 tetrahedra are shown in blue, and the O(4)/F(1) site is shown in green.

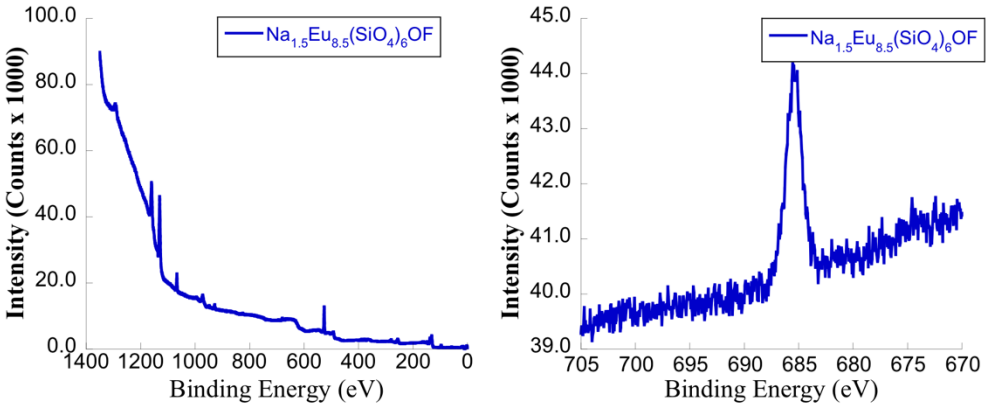

Figure 2.8. XPS data of $Na_{1.5}Eu_{8.5}(SiO_4)_6OF$. The image on the left depicts the survey scan that indicates the presence of Na, Eu, Si, O, and F, and the image on the right depicts the detailed scan of the region where the peak around 685 eV indicates the presence of metal fluoride bonding.

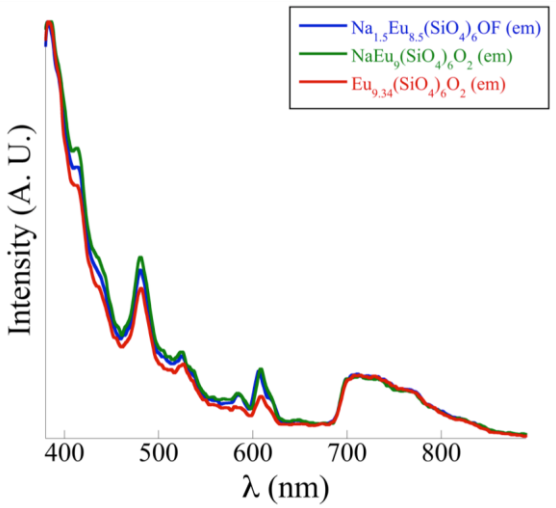

Figure 2.9. Emission spectra of $NaEu_9(SiO_4)_6O_2$, $Na_{1.5}Eu_{8.5}(SiO_4)_6OF$, and $Eu_{9.34}(SiO_4)_6O_2$.

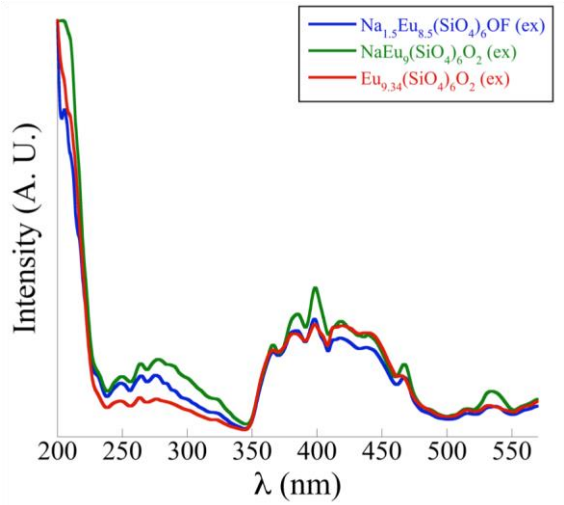

Figure 2.10. Excitation spectra of $NaEu_9(SiO_4)_6O_2$, $Na_{1.5}Eu_{8.5}(SiO_4)_6OF$, and $Eu_{9.34}(SiO_4)_6O_2$.

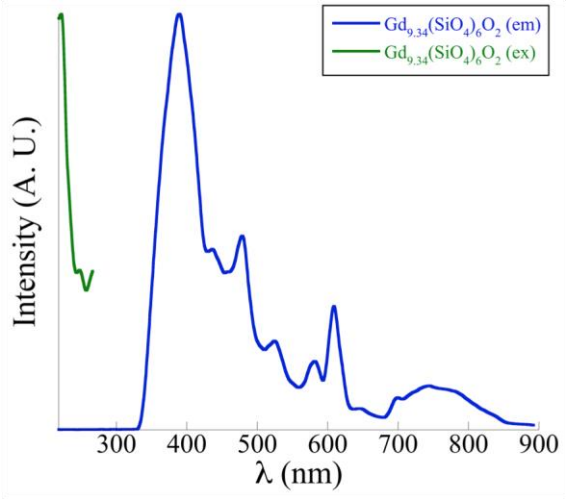

Figure 2.11. Emission and excitation spectra of $Gd_{9.34}(SiO_4)_6O_2$.

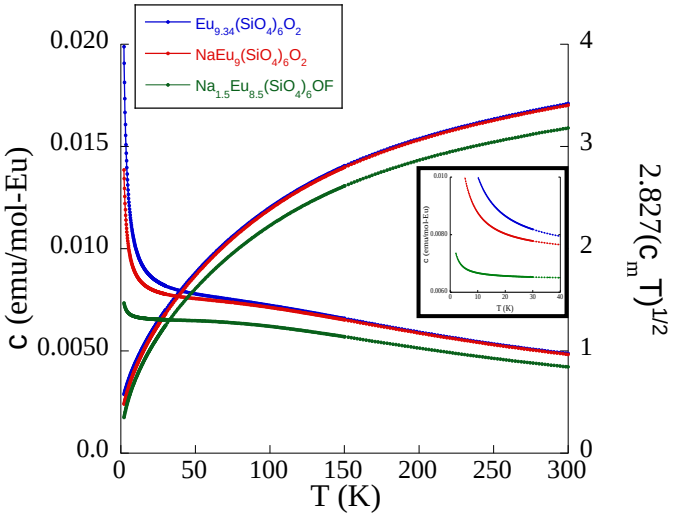

Figure 2.12. Temperature dependence of the magnetic susceptibility data and of the magnetic moments of $Eu_{9.34}(SiO_4)_6O_2$, $NaEu_9(SiO_4)_6O_2$, and $Na_{1.5}Eu_{8.5}(SiO_4)_6OF$.

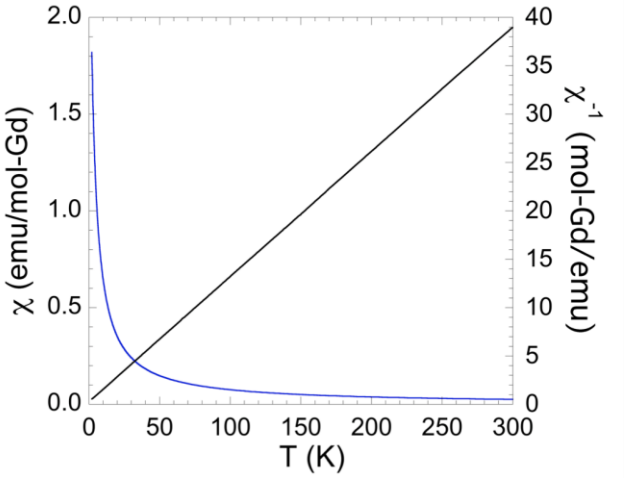

Figure 2.13. Temperature dependence of the magnetic susceptibility data and of the magnetic moment of $Gd_{9.34}(SiO_4)_6O_2$.

Chapter 3

Crystal Growth and Structure of Three New Neodymium Containing Silicates:

$Na_{0.5}Nd_{4.50}(SiO_4)_3O$, $Na_{0.63}Nd_{4.37}(SiO_4)_3O_{0.74}F_{0.26}$ and $Nd_{4.74}Nd_{4.26}(O_{0.52}F_{0.48})[SiO_4]_4$*

*Latshaw, A. M., Smith, M. D., zur Loye, H.-C. *Solid State Sci.*, **2014**, *35*, 28-32.

Introduction

Flux crystal growth has become a popular technique for obtaining new materials in single crystal form. As each system tends to be unique, different reaction conditions have to be explored and fluxes need to be chosen to match reactivity, melting points, and solubility of the reagents used in the synthesis.[3.1] Utilizing eutectic compositions of the flux components can lower the melting points of fluxes, for example the eutectic ratios of alkali fluorides used for the synthesis of the title compounds. A flux is deemed reactive when one or more of the elements present in the product crystals have originated in the flux. All three of the new neodymium silicate compositions discussed in this paper contain sodium and two of the three also contain fluorine, both of which originated in the NaF and KF flux mixture, making this a reactive flux crystal growth process.

Silver reaction vessels are used because of their inertness to fluoride melts; however, the melting point of NaF flux (mp 993 °C) is too high to be used with the silver reaction vessels (mp 962 °C). Therefore, a eutectic of NaF/KF (mp 718 °C) was chosen for these crystal growth reactions in order to lower the melting point of the reaction below the melting point of the silver reaction vessels. An additional advantage, beyond its lower melting point, is the greater solubility with which the NaF/KF eutectic can be dissolved in water and thus removed to isolate the reaction products.

Several neodymium silicate compositions have been studied for their applications as laser hosts[3.2, 3.3] and for their ionic conductivity, which enables their applications in solid oxide fuel cells (SOFCs)[3.4, 3.5]. Many of the silicate materials that have been studied as electrolytes in SOFCs have been members of the apatite structural family. The simplest composition of the apatite structure is $A_5(BO_4)_3O$ where A represents an alkali,

alkaline-earth, lanthanide or mixture of those cations and *B* represents a silicon, phosphorous, boron, sulfur, vanadium or arsenic cation.[3.6] In this study, the flux crystal growth produced two phases with general compositions $Na_xNd_{5-x}(SiO_4)_3O_{1-y}F_y$, that form the apatite structure, where *A* has two cations (Na^+ and Nd^{3+}), Si takes on the *B* site, and one composition contains fluorine while the other does not. As with other apatites, the presence of fluorine creates mixing of the Na and Nd on both of the *A* sites, while the absence of fluorine allows mixing on only the *A*(1) site. It is well known that the apatite structure can crystallize in various space groups, including $P6_3/m$, in which two title compounds of this paper crystallize.

The third neodymium composition is an oxy-fluoride silicate, $Na_{4.74}Nd_{4.26}(O_{0.52}F_{0.48})[SiO_4]_4$, which is isostructural to other previously reported compounds, including $Na_5Nd_4(OH)[SiO_4]_4$, $Na_5Y_4F[SiO_4]_4$, and $K_5La_4F[SiO_4]_4$.[3.7-3.9] Unlike for the previously reported compounds, the new oxy-fluoride silicate compound has mixing of the lanthanide cation onto the alkali metal site and mixing of oxygen onto the OH / F site.

Herein we detail our approach to the single crystal growth of three Nd silicates from reactive hydroxide fluxes, $Na_{0.50}Nd_{4.50}(SiO_4)_3O$, $Na_{0.63}Nd_{4.37}(SiO_4)_3O_{0.74}F_{0.26}$, and $Na_{4.74}Nd_{4.26}(O_{0.52}F_{0.48})[SiO_4]_4$, and describe the crystal structures of the three new compounds.

Experimental

Crystal Growth

Crystals of $Na_{0.50}Nd_{4.50}(SiO_4)_3O$, $Na_{0.63}Nd_{4.37}(SiO_4)_3O_{0.74}F_{0.26}$, and $Na_{4.74}Nd_{4.26}(O_{0.52}F_{0.48})[SiO_4]_4$ were prepared by loading a 1mmol:0.75mmol ratio of

Nd_2O_3 (Alfa Aesar, 99.9 %) : SiO_2 (Aldrich, 99.99 %) into a silver crucible. 5.03g:4.63g of NaF (Alfa Aesar, 99 % min.) : KF (Alfa Aesar, 99 % min.) flux were placed on top of the reactants and a silver lid was loosely fitted onto the crucible. The crucible was placed into a programmable furnace that was heated to 850 °C in 1.5 h, allowed to dwell there for 24 h, and then slow cooled at a rate of 3 °C per hour to 600 °C, after which the furnace was shut off. The flux was washed away using water, aided by sonication, and then the crystals were isolated by filtration. Crystals of all three compositions formed during the same reaction.

Single Crystal X-ray Diffraction

X-ray intensity data from a light blue or purple $Na_{0.50}Nd_{4.50}(SiO_4)_3O$ hexagonal plate (100(2) K), a $Na_{0.63}Nd_{4.37}(SiO_4)_3(O_{0.74}F_{0.26})$ bar crystal (296(2) K), and a $Na_{4.74}Nd_{4.26}(O_{0.52}F_{0.48})[SiO_4]_4$ polyfaceted crystal (296(2) K) were collected using a Bruker SMART APEX diffractometer (Mo Kα radiation, λ = 0.71073 Å).[3.10, 3.11] The data collection covered 100% of reciprocal space to $2\theta_{max}$ = 70.2°, 71.0°, and 70.1° with an average reflection redundancy of 13.4, 15.3, and 9.8 and R_{int} = 0.064, 0.054, and 0.032, respectively, after absorption correction. The raw area detector data frames were reduced and corrected for absorption effects using the SAINT+ and SADABS programs.[3.11] Final unit cell parameters were determined by least-squares refinement of 1642, 2473, and 3918 respective reflections from the data set. Difference Fourier calculations and full-matrix least-squares refinement against F^2 of the structural model were performed with SHELXL-2014/1[2] using ShelXle.[3.12]

$Na_{0.50}Nd_{4.50}(SiO_4)_3O$ and $Na_{0.63}Nd_{4.37}(SiO_4)_3O_{0.74}F_{0.26}$ crystallize in the hexagonal space group $P6_3/m$ as determined by the pattern of systematic absences in the intensity

data and by structure solution. They both adopt the apatite, ($Ca_5(PO_4)_3F$), structure type. The asymmetric unit consists of two lanthanide sites, *Ln*(1) and *Ln*(2), where in $Na_{0.50}Nd_{4.50}(SiO_4)_3O$ the *Ln*(1) site is mixed with Nd(1) and Na(1) while *Ln*(2) is only Nd(2). In $Na_{0.63}Nd_{4.37}(SiO_4)_3O_{0.74}F_{0.26}$, the *Ln*(1) site is occupied by Nd(1) and Na(1) and the *Ln*(2) site is occupied by Nd(2) and Na(2). The asymmetric unit also consists of one silicon atom and four oxygen atom sites. In $Na_{0.50}Nd_{4.50}(SiO_4)_3O$, all four oxygen atom sites are oxygen while in $Na_{0.63}Nd_{4.37}(SiO_4)_3O_{0.74}F_{0.26}$ there are three pure oxygen sites and one mixed oxygen/fluorine site. *Ln*(1) atoms are located on a three-fold axis (Wyckoff symbol *4f*, site symmetry 3), *Ln*(2), Si(1), O(1), and O(2) atoms are located on mirror planes (site *6h*, site symmetry *m*). Oxygen O(3) is located on a general position (site 12*i*), and the O(4) or mixed oxygen/fluorine site O(4)/F(4) is located on site 2*a* with -6 site symmetry. Final atomic coordinates were standardized with Structure Tidy.[3.13-3.15] Further details of the crystal structure investigation on $Na_{0.50}Nd_{4.50}(SiO_4)_3O$ and $Na_{0.63}Nd_{4.37}(SiO_4)_3O_{0.74}F_{0.26}$ can be obtained from the Fachinformationszentrum Karlsruhe, 76344 Eggenstein-Leopoldshafen, Germany (email: crystdata@fiz-karlsruhe.de) using the depository numbers 428489 and 428490, respectively.

$Na_{4.74}Nd_{4.26}(O_{0.52}F_{0.48})[SiO_4]_4$ crystallizes with a body-centered tetragonal lattice. The pattern of systematic absences in the intensity data was consistent with the space groups *I*4, *I*-4 and *I*4/*m*. Space group *I*-4 (No. 82) was eventually shown to be correct. The finished structural model was checked with the ADDSYM program in PLATON, [3.16-3.19] which found no missed symmetry. The published data for the neodymium hydroxide analog[3.7] was taken as a starting model for refinement. The asymmetric unit of this structure type consists of one rare earth atom, one silicon atom, two sodium atoms and

five oxygen atoms. All atoms are located on positions of general crystallographic symmetry (Wyckoff site *8g*) except for sodium Na(2), located on the origin (site *2a*, -4 site symmetry) and a mixed oxide / fluoride site O(1)/F(1), located on site *2b* (-4 site symmetry). Further details of the crystal structure investigation on $Na_{4.74}Nd_{4.26}(O_{0.52}F_{0.48})[SiO_4]_4$ can be obtained from the Fachinformationszentrum Karlsruhe using the depository number 428491.

Magnetic Property Measurements

The magnetic properties of a sample containing all three phases were measured using a Quantum Design Magnetic Property Measurement System (QD-MPMS3 SQUID VSM). The multi-component sample followed Curie-Weiss behavior down to 2 K indicating the absence of any long range magnetic ordering in all three phases.

Results and Discussion

Crystal Structure

Single crystals of the three title compositions were grown out of a molten NaF:KF eutectic flux. The flux mixture of NaF (60 %) and KF (40 %) has a melting point of 718° C. The crystal growth reaction in this eutectic flux yielded three compositions, $Na_{0.50}Nd_{4.50}(SiO_4)_3O$, $Na_{0.63}Nd_{4.37}(SiO_4)_3O_{0.74}F_{0.26}$, and $Na_{4.74}Nd_{4.26}(O_{0.52}F_{0.48})[SiO_4]_4$, all of which incorporated sodium from the flux.

$Na_{0.50}Nd_{4.50}(SiO_4)_3O$ and $Na_{0.63}Nd_{4.37}(SiO_4)_3O_{0.74}F_{0.26}$ are both isostructural with known oxyapatites.[3.20, 3.21] Both of these compositions crystallize in the hexagonal space group $P6_3/m$. Relevant crystallographic data for the two structures are listed in **Table 3.1**. A previous paper reported the synthesis of a powder sample of $Na_{0.50}Nd_{4.50}(SiO_4)_3O$ via a

solid state reaction.[3.22] Based on powder X-ray diffraction data obtained on ground crystals, it appeared likely that the crystals we grew were the same compound. To confirm the identity of the material and to obtain a high-resolution structure refinement, we determined the single crystals structure. The advantage of a single crystal over a simple powder based X-ray structure solution is that one can typically locate the atomic positions with greater precision and, hence, generate more precise interatomic distances. For this reason, the single crystal structure data are included in this paper.

In the oxyapatite structure, there are two lanthanide sites (Nd(1) and Nd(2)), one silicon site, and four unique oxygen environments, one of which, (O(4)), can contain fluorine. Nd(1) is located in a six coordinated twisted trigonal prism coordination environment, while Nd(2) is located in a seven coordinated distorted pentagonal bipyramid. Si(1) is located in an isolated tetrahedron. The Nd(1) polyhedra form face-shared columns down the *c* axis (**Figure 3.1**) while the Nd(2) polyhedra form a column of corner-shared polyhedra down the *c* axis (**Figure 3.2**). Three $Nd(2)O_7$ polyhedra corner-share together through the O(4)/F(1) site forming a $Nd(2)_3O_{19}$ unit as seen in **Figure 3.3**. The $Nd(2)_3O_{19}$ units form columns down the *c* axis by corner-sharing with another $Nd(2)_3O_{19}$ unit. Each unit is rotated 60 ° clockwise from the unit before it as shown in **Figure 3.3**. The Nd(1) columns edge share with three of the Nd(2) columns and the isolated SiO_4 tetrahedra lie between a Nd(1) and a Nd(2) column, as shown in **Figure 3.4**. For the two compounds reported here the average Si-O bond distance is 1.627 Å, the average Nd(1)-O interatomic distance is 2.454 Å, and the average Nd(2) – O interatomic distance is 2.468 Å. The precision of these numbers represents a significant

improvement over the published values based on powder data.[3.22] Selected interatomic distances are given in **Table 3.1**.

$Na_{4.74}Nd_{4.26}(O_{0.52}F_{0.48})[SiO_4]_4$ is isostructural with $Na_5Nd_4(OH)[SiO_4]_4$, $Na_5Y_4F[SiO_4]_4$, and $K_5La_4F[SiO_4]_4$.[3.7-3.9] $Na_{4.74}Nd_{4.26}(O_{0.52}F_{0.48})[SiO_4]_4$ crystallizes in the tetragonal space group *I*-4. The crystallographic data are given in **Table 3.2**. This structure has one unique neodymium site, which is eight coordinate. The Nd polyhedra are face-shared with two other Nd polyhedra. Four Nd polyhedra bond to the O(1)/F(1) site creating a Nd_4O_{21} unit consisting of four polyhedra as shown in **Figure 3.5**. Each Nd_4O_{21} unit corner shares with four other Nd_4O_{21} units (**Figure 3.5**). Looking down the *b* axis, it is apparent that the Nd_4O_{21} units arrange in two unique sheets, where the first sheet contains isolated Nd_4O_{21} units and the second sheet contains Nd_4O_{21} units that occupy the openings left by sheet 1 (**Figure 3.6**). The sodium atoms Na(1) and Na(2) sit in the channels created by the Nd_4O_{21} units (**Figure 3.7**). Na(2) atoms are positioned directly under the O(1)/F(1) site and Na(1) atoms are arranged in a square shape, occupying the four corners of the channels between four of the Nd units, **Figure 3.5**. The SiO_4 tetrahedra are both edge and corner shared to Nd polyhedra. A view down the *c* axis is shown in **Figure 3.8.** In the case of $Na_{4.74}Nd_{4.26}(O_{0.52}F_{0.48})[SiO_4]_4$, both Na sites have mixed site occupancy and share the site with a small amount of Nd, 0.048(2) Nd on Na(1) and 0.069(4) Nd on Na(2). The mixing of Nd onto the sodium sites necessitates the mixing of oxygen on the F(1) (O: 0.52 / F: 0.48) site to charge balance the structure. The average Si – O bond distance is 1.629 Å, typical for SiO_4 tetrahedra. Other selected interatomic distances are given in **Table 3.3**. Bond valence sum calculations[3.23, 3.24] for

the three compositions resulted in values of 1.22 – 1.24, 4.11 – 4.12, and 2.76 – 2.81 for Na^{+}, Si^{4+}, and Nd^{3+}, respectively, consistent with the expected values.

Magnetic data was collected on a sample that contained all three phases. Since the multi-component sample showed no magnetic ordering down to 2 K, there was no attempt to get phase pure samples for magnetic measurements.

Conclusion

Using a eutectic mixture of KF/NaF, we have synthesized crystals of three new neodymium oxo-silicates and oxy-fluoride silicates. $Na_{0.50}Nd_{4.50}(SiO_4)_3O$ and $Na_{0.63}Nd_{4.37}(SiO_4)_3O_{0.74}F_{0.26}$ are members of the apatite structure and $Na_{4.74}Nd_{4.26}(O_{0.52}F_{0.48})[SiO_4]_4$ is the first reported member of a series of isostructural compounds that exhibits mixing of the lanthanide atom onto the sodium site.

References

3.1 Bugaris, D. E.; zur Loye, H.-C. *Angew. Chem. Int. Ed.* **2012**, *51*, 3780-3811.
3.2 Ross, M. *Proc. IEEE* **1968**, *56*, 196-197.
3.3 Hwang, M. S.; Hong, H. Y.-P.; Cheng, M. C.; Wang, Y. *Acta Crystallogr., Sect. C: Cryst. Struct. Commun.* **1987**, *43*, 1241-1243.
3.4 An, T.; Baikie, T.; Wei, F.; Pramana, S. S.; Schreyer, M. K.; Piltz, R. O.; Shin, J. F.; Wei, J.; Slater, P. R.; White, T. J. *Chem. Mater.* **2013**, *25*, 1109-1120.
3.5 Nakajima, T.; Nishio, K.; Ishigaki, T.; Tsuchiya, T. *J. Sol-Gel Sci. Technol.* **2005**, *33*, 107-111.
3.6 Leu, L.-C.; Thomas, S.; Sebastian, M. T.; Zdzieszynski, S.; Misture, S.; Ubic, R. *J. Am. Ceram. Soc.* **2011**, *94*, 2625-2632.
3.7 Malinovskii, Y. A. *Dokl. Akad. Nauk SSSR* **1984**, *274*, 75-78.
3.8 Merinov, B. V.; Maksinov, B. A.; Ilyukhin, V. V.; Belov, N. V. *Dokl. Akad. Nauk* **1980**, *255*, 348-351.
3.9 Schäfer, M. C.; Schleid, T. *Z. Anorg. Allg. Chem.* **2010**, *636*, 2069.
3.10 SMART Version 5.630, SAINT+ Version 6.45 and SADABS Version 2.10. Bruker Analytical X-ray Systems, Inc., Madison, Wisconsin, USA, 2003.
3.11 Sheldrick, G. M. *Acta. Cryst.* **2008**, *A64*, 112-122.
3.12 Hübschle, C. B.; Sheldrick, G. M.; Bittrich, B. *J. Appl. Cryst.* **2011**, *44*, 1281-1284.
3.13 Parthé, E.; Gelato, L. M. *Acta. Cryst.* **1984**, *A40*, 169-183.
3.14 Gelato, L. M.; Parthé, E. *J. Appl. Cryst.* **1987**, *20*, 139-143.
3.15 Hu, S.-Z.; Parthé, E. *Chinese J. Struct. Chem.* **2004**, *23*, 1150-1160.
3.16 LePage, Y. *J. Appl. Cryst.* **1987**, *20*, 264-269.
3.17 Spek, A. L. *J. Appl. Cryst.* **1988**, *21*, 578-579.
3.18 Spek, A. L. *Acta. Cryst., Sect. A* **1990**, *46*, C34.
3.19 PLATON, A Multipurpose Crystallographic Tool, Utrecht University, Utrecht, The Netherlands, Spek, A. L. 1998.
3.20 Toumi, M.; Smiri-Dogguy, L.; Bulou, A. *Ann. Chim. Sci. Mat.* **2002**, *27*, 17-26.
3.21 Maisonneuve, V.; Leduc, E.; Bohnke, O.; Leblanc, M. *Chem. Mater.* **2004**, *16*, 5220-5222.
3.22 Get'man, E. I.; Borisova, E. V.; Loboda, S. N.; Ignatov, A. V. *Russ. J. Inorg. Chem.* **2013**, *58*, 265-268.
3.23 Brese, N. E.; O'Keeffe, M. *Acta. Crystallogr.* **1991**, *B47*, 192.
3.24 Brown, I. D.; Altermatt, D. *Acta Crystallogr.* **1985**, *B41*, 244.

Table 3.1. Selected Interatomic Distances (in Å) for $Na_{0.50}Nd_{4.50}(SiO_4)_3O$, and $Na_{0.63}Nd_{4.37}(SiO_4)_3O_{0.74}F_{0.26}$.

	$Na_{0.50}Nd_{4.50}(SiO_4)_3O$	$Na_{0.63}Nd_{4.37}(SiO_4)_3O_{0.74}F_{0.26}$
Nd(1) – O(2) (x3)	2.423(3)	2.425(3)
Nd(1) – O(1) (x3)	2.487(3)	2.482(3)
Nd(1) – O(3) (x3)	2.828(4)	2.821(4)
Nd(2) – *X*	2.2585(3)	2.2638(3)
Nd(2) – O(3) (x2)	2.382(4)	2.396(3)
Nd(2) – O(1)	2.454(4)	2.451(4)
Nd(2) – O(3) (x2)	2.547(4)	2.545(3)
Nd(1) – O(2)	2.688(5)	2.703(5)

X = O(4) or F(1), respectively

Table 3.2. Crystallographic data for $Na_{0.50}Nd_{4.50}(SiO_4)_3O$, and $Na_{0.63}Nd_{4.37}(SiO_4)_3O_{0.74}0.26$, and $Na_{4.74}Nd_{4.26}(O_{0.52}F_{0.48})[SiO_4]_4$.

Formula	$Na_{0.50}Nd_{4.50}(SiO_4)_3O$	$Na_{0.63}Nd_{4.37}(SiO_4)_3O_{0.74}F_{0.26}$	$Na_{4.74}Nd_{4.26}(O_{0.52}F_{0.48})[SiO_4]_4$
Formula weight	952.85	938.04	1109.48
Temperature (K)	100(2)	296(2)	296(2)
Crystal system	Hexagonal	Hexagonal	Tetragonal
Space group	*P* $6_3/m$	*P* $6_3/m$	*I* -4
a (Å)	9.5400(3)	9.5533(3)	12.1255(3)
c (Å)	7.0331(5)	7.0510(4)	5.4656(2)
V (Å^3)	554.34(5)	557.30(5)	803.59(5)
Z	2	2	2
Density (mg/m^3)	5.709	5.590	4.585
Absorption coefficient (mm^{-1})	21.128	20.437	14.056
Crystal size (mm^3)	0.10 x 0.06 x 0.05	0.10 x 0.06 x 0.05	0.10 x 0.06 x 0.05
2 theta range (°)	4.93 to 70.19	4.92 to 70.06	4.75 to 70.18
reflections collected	11847	13540	9475
data/restraints/parameters	877 / 0 / 40	880 / 0 / 41	1774 / 0 / 71
R (int)	0.0643	0.0538	0.0318
GOF (F^2)	1.101	1.147	1.072
R indices (all data)	R_1 = 0.0381	R_1 = 0.0343	R_1 = 0.0270
	wR_2 = 0.0658	wR_2 = 0.0600	wR_2 = 0.0538

Table 3.3. Selected Interatomic Distances (in Å) for $Na_{4.74}Nd_{4.26}(O_{0.52}F_{0.48})[SiO_4]_4$.

	$Na_{4.74}Nd_{4.26}(O_{0.52}F_{0.48})[SiO_4]_4$
Nd(1) – O(2)	2.374(4)
Nd(1) – O(5)	2.419(4)
Nd(1) – O(5)	2.431(5)
Nd(1) – O(2)	2.465(5)
Nd(1) – O(4)	2.466(4)
Nd(1) – O(3)	2.470(4)
Nd(1) – O(4)	2.640(4)
Nd(1) – O(1)/F(1)	2.6523(3)

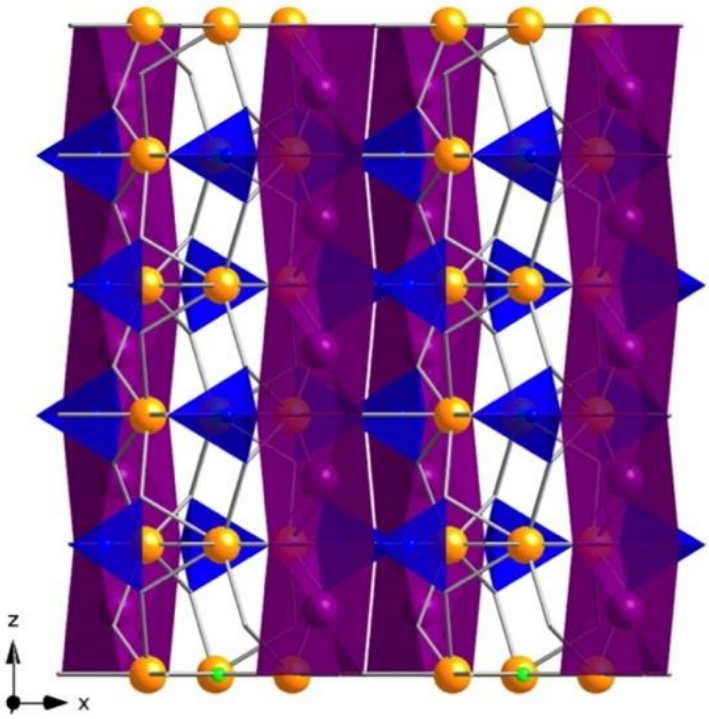

Figure 3.1. View down the *b*-axis of the crystal structure of $Na_{0.63}Nd_{4.37}(SiO_4)_3O_{0.74}F_{0.26}$, highlighting the Nd(1) columns. This representation also applies to the iso-structural $Na_{0.50}Nd_{4.50}(SiO_4)_3O$. Nd(1) columns are shown in purple, Nd(2) polyhedra are represented by the orange spheres and silver bonds, SiO_4 tetrahedra are shown in blue, and the O(4)/F(1) site is shown as green spheres.

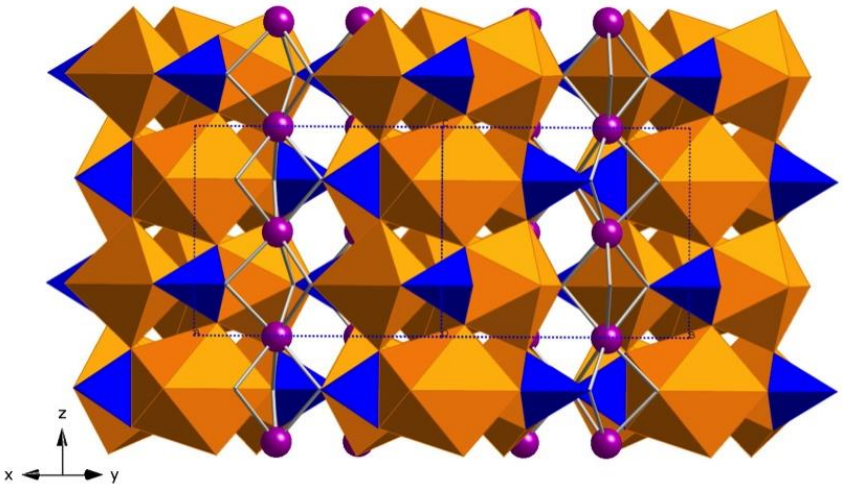

Figure 3.2. Crystal Structure of $Na_{0.63}Nd_{4.37}(SiO_4)_3O_{0.74}F_{0.26}$, illustrating the Nd(2) columns. This representation also applies to the iso-structural $Na_{0.50}Nd_{4.50}(SiO_4)_3O$. Nd(2) columns are shown in orange, Nd(1) polyhedra are represented by the purple spheres and silver bonds, and the SiO_4 tetrahedra are shown in blue.

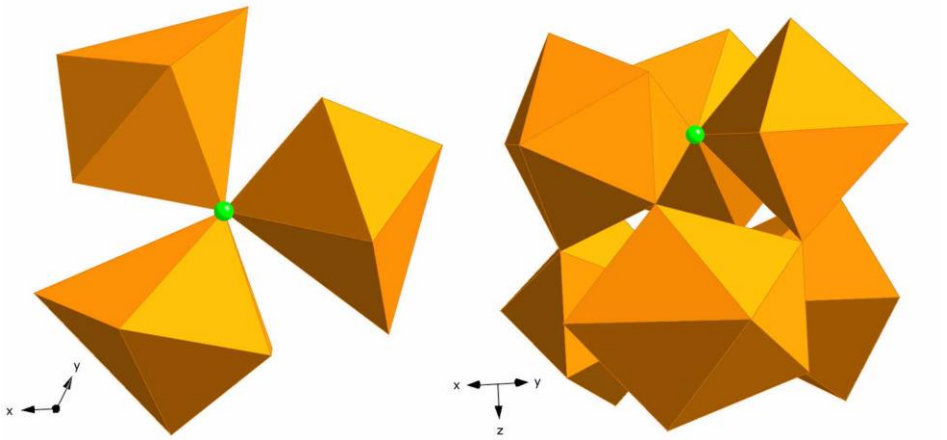

Figure 3.3. Crystal structure of $Na_{0.63}Nd_{4.37}(SiO_4)_3O_{0.74}F_{0.26}$. The $Nd(2)_3O_{19}$ unit is shown on the left looking down the *c*-axis. The same unit looking perpendicular to the *c*-axis is shown on the right. All Nd(2) atoms are shown in orange and the O(4)/F(1) site is shown in green.

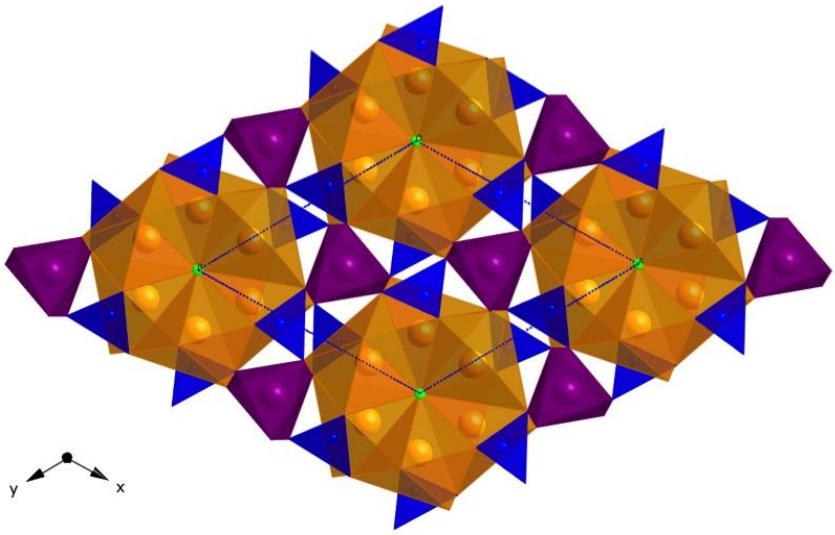

Figure 3.4. Crystal structure of $Na_{0.63}Nd_{4.37}(SiO_4)_3O_{0.74}F_{0.26}$ viewed down the *c*-axis. This representation also applies to the iso-structural $Na_{0.50}Nd_{4.50}(SiO_4)_3O$. Nd(1) polyhedra are shown in purple, Nd(2) polyhedra are shown in orange, SiO_4 tetrahedra are shown in blue, and the O(4)/F(1) site is shown as green spheres.

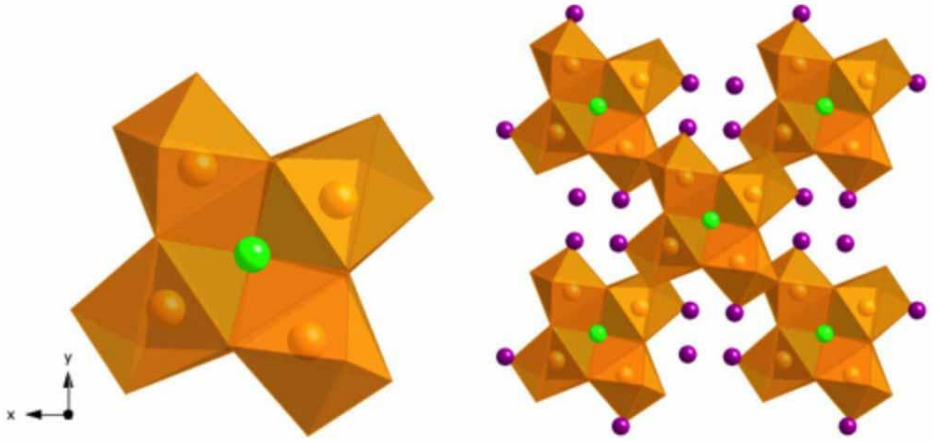

Figure 3.5. The Nd_4O_{21} building block of the crystal structure of $Na_{4.74}Nd_{4.26}(O_{0.52}F_{0.48})[SiO_4]_4$is shown on the left and a more expanded view illustrating the structural framework that includes the sodium cations is shown on the right. Nd polyhedra are shown in orange, O(1)/F(1) atoms are shown in green and Na(1) is shown as purple spheres.

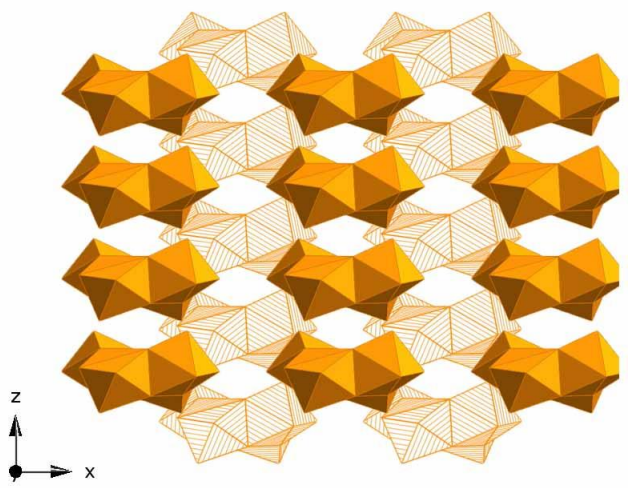

Figure 3.6. Crystal structure of $Na_{4.74}Nd_{4.26}(O_{0.52}F_{0.48})[SiO_4]_4$. The horizontal sheets of Nd_4O_{21} are shown, where sheet 1 is represented by the striped orange polyhedra and sheet 2 is represented by the solid orange polyhedra.

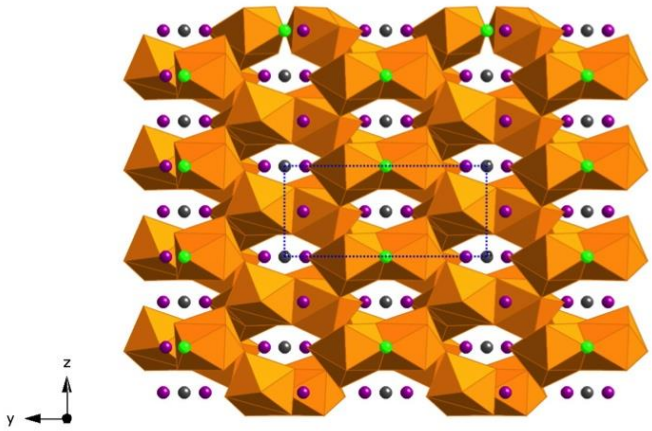

Figure 3.7. Crystal structure of $Na_{4.74}Nd_{4.26}(O_{0.52}F_{0.48})[SiO_4]_4$ viewed down the *a*-axis emphasizing the AB layering of the Nd units and the positions of Na. Nd is shown as orange polyhedra, Na(1) is shown as purple spheres, Na(2) is shown as gray spheres, and O(1)/F(1) is shown as green spheres.

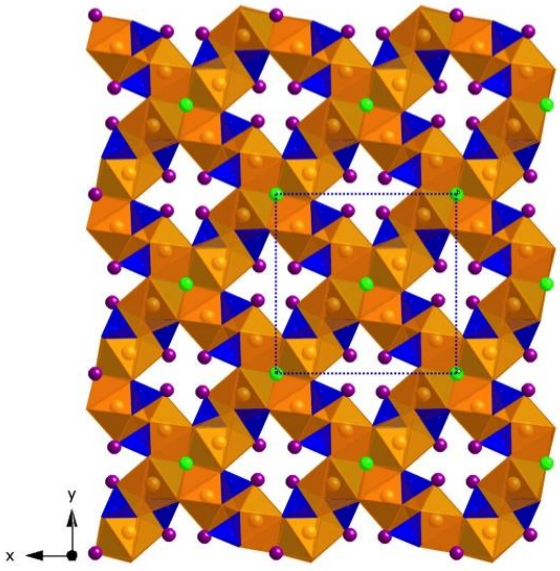

Figure 3.8. Crystal structure of $Na_{4.74}Nd_{4.26}(O_{0.52}F_{0.48})[SiO_4]_4$viewed down the *c*-axis. Nd is represented by orange polyhedra, Si is represented by blue tetrahedra, Na(1) shown as purple spheres, and O(1)/F(1) shown as green spheres.

Chapter 4

$A_5RE_4X[TO_4]_4$ Crystal Growth and Photoluminescence. Hydroflux Synthesis of Sodium Rare Earth Silicate Hydroxides*

*Latshaw, A. M.; Chance, W. M.; Trenor, N.; Morrison, G.; Smith, M. D.; Yeon, J.; Williams, D. E.; zur Loye, H.-C. *CrystEngComm*. **2015**, *17*, 4691-4698.

Introduction

The crystal growth of complex oxides and hydroxides is often carried out in high temperature solutions or fluxes.[4.1] One drawback of this approach can be the required high temperatures, as most high temperature solutions have a high (>400 °C) melting point, even when considering the existence of eutectic mixtures. To create lower temperature fluxes requires a modification of the high temperature solutions that goes beyond utilizing eutectic mixtures. One such approach is the hydroflux method,[4.2, 4.3] which utilizes a wet hydroxide flux, in which water has been purposefully added to control the acid-base chemistry of the molten flux as described by the Lux-Flood concept of oxo-acidity.[4.4, 4.5] These hydrofluxes occupy a low temperature regime where, importantly, they act as melts and not as aqueous solutions, and therefore do not generate high pressures during the crystal growth process. The low synthesis temperatures employed with hydrofluxes make them extremely advantageous for preparing hydroxides, such as for the title compounds discussed herein.

Rare earth containing tetragens, such as silicates and germanates, have been studied for their luminescent[4.6-4.9] and magnetic[4.10, 4.11] properties. The intense luminescent properties of many rare earth ions, especially when present in tetragen containing materials, have made them a popular synthetic target for solid state lighting applications. In fact, the majority of known rare earth containing tetragen compounds were investigated primarily for their photoluminescence properties, although a number of researchers have more recently investigated the ionic conductivity of some rare earth silicates and hydroxosilicates with the goal of expanding the number of ionically conducting solids for applications in fuel cells and battery materials.[4.12] In addition, rare

earth containing tetragens have been studied for their refractory nature and low thermal conductivity.[4.13, 4.14] Considering their potential for use in solid state lighting applications and for use as solid electrolytes, the rare earth silicates represent an exciting family of materials for continued exploration and materials discovery.

Among the many different classes of structures explored for use in solid state lighting, alkali metal containing silicate and germanate structures such as $Na_3RESi_2O_7$,[4.15-4.18] $K_3RESi_2O_7$ (RE=Eu-Lu, Sc),[4.8, 4.19, 4.20] $K_3HoSi_3O_9$,[4.21] $K_3NdSi_6O_{15}$,[4.22] $K_{1.32}Pr_{8.68}(SiO_4)_6O_{1.36}F_{0.64}$,[4.23] $Na_5RESi_4O_{12}$ (RE = Sm-Lu),[4.12] $Na_xRE_{10-x}(SiO_4)_6O_{2-y}F_y$ (RE = Sm, Eu, Gd),[4.23] and $NaREGeO_4$ (RE = Sm, Eu, Gd, Tb)[4.11] have been studied extensively. A similar structural family, $A_5RE_4X[TO_4]_4$, [A = alkali metal, RE = rare earth, T = tetragen] contains several known compounds in closely related structure types, and includes $Na_5Nd_4(OH)[SiO_4]_4$,[4.24] $Na_5Y_4F[SiO_4]_4$,[4.25] $K_5La_4F[SiO_4]_4$,[4.26] $Na_5Nd_4Ge_4O_{16}(OH)$,[4.27] and $(Na_{0.63(2)}Nd_{0.37(2)})(NaSiO_4)_4(O_{0.52}F_{0.48})$.[4.28] As most rare earths can be accommodated in this tetragen based structure type, it represents an attractive host material for new, rare earth based, luminescent materials.

Herein, we report the synthesis of alkali metal containing silicates $Na_5RE_4(OH)(SiO_4)_4$ (RE = Pr, Nd, Sm, Eu, Gd, Tb, Dy, Ho, Er, Tm, Yb, Y) using the hydroflux technique. The hydroflux synthetic technique has been demonstrated to reliably produce complex metal hydroxides, like those reported here, whose structures, magnetic, and luminescent properties are discussed.

Experimental Section

Reagents

The following reagents were used as received: KOH and NaOH (Fisher Scientific, ACS grade pellets), $Pr(NO_3)_3•5H_2O$ (Acros, 99.9 %), Nd_2O_3, Sm_2O_3, Eu_2O_3, Gd_2O_3, Tb_4O_7, Dy_2O_3, $H_{O2}O_3$, Er_2O_3, Tm_2O_3, Yb_2O_3, and Y_2O_3 (Alfa Aesar, 99.9 %), and $Na_2SiO_3•9H_2O$ (EM, 99+ %).

Crystal Growth

RE = Pr, Nd, Tb - Yb, Y

0.5 mmol of RE_2O_3 (RE = Nd, Dy - Yb, Y), or $Pr(NO_3)_3•5H_2O$ was added to a NaOH/KOH hydroflux (0.1 mol NaOH/0.1 mol KOH, 0.33 mol H_2O) with an excess of 10-40% of $Na_2SiO_3•9H_2O$. The excess of $Na_2SiO_3•9H_2O$ improved the product yield, which was essentially quantitative with respect to RE_2O_3. Reactions were heated at a rate of 5 ºC per minute to 230 ºC and held for 3 days with subsequent slow cooling at a rate of 0.2 ºC per minute to 80 ºC.

RE = Eu, Gd, Sm

0.5 mmol of RE_2O_3 was added to a NaOH hydroflux (0.25 mol NaOH/0.4 mol H_2O) with an excess of up to 10 % of $Na_2SiO_3•9H_2O$. The excess of $Na_2SiO_3•9H_2O$ improved the product yield, which was essentially quantitative with respect to RE_2O_3. Reactions were heated at a rate of 5 ºC per minute to 230 ºC and held for 2 days before cooling at a rate of 0.2 ºC per minute to 80 ºC. The gadolinium analogue was grown as a polycrystalline powder that matched the expected powder pattern based on the other analogues and data from a previous work that synthesized the gadolinium analogue.[4.29]

Powder X-ray Diffraction

Powder X-ray diffraction data were collected on the polycrystalline sample $Na_5Gd_4(OH)[SiO_4]_4$ using a Rigaku Dmax/2100 powder diffractometer using Cu Kα radiation. Data were collected using a step scan covering the 2θ range of 5 – 65 ° in steps of 0.04 °.

Magnetic Measurements

The DC magnetic susceptibilities were measured as a function of temperature using a Quantum Design MPMS 3 SQUID Magnetometer. Ground, polycrystalline samples were massed on a balance sensitive to 0.01 mg and loaded into VSM powder holder or into gelatin capsules for data collection. The temperature dependent susceptibilities of all samples were measured under zero-field-cooled conditions from 2-300 K in an applied field of 1000 Oe. The raw magnetic moments were corrected for sample shape and radial offset effects using the method outlined by Morrison and zur Loye.[4.30]

Luminescence

A Perkin Elmer LS 55 Fluorescence Spectrometer was used to measure emission and excitation spectra of members of the titled compounds that exhibited visible luminescence under short-wave UV excitation. The excitation wavelengths used for the emission spectra of $Na_5Tb_4(OH)[SiO_4]_4$, $Na_5Gd_4(OH)[SiO_4]_4$, and $Na_5Eu_4(OH)[SiO_4]_4$, were 237 nm, 250 nm, and 263 nm, respectively. The maximum emission wavelengths observed were 537 nm, 608 nm, and 384 nm, respectively, and were used for excitation spectra. All measurements were conducted at room temperature.

Fluorescence Quantum Yield Measurements

Emission spectra were acquired on an Edinburgh FS5 fluorescence spectrometer. A 150 W Continuous Wave Xenon Lamp was used for sample excitation, and the emission measured using a Hamamatsu R928P photomultiplier tube. For emission and excitation measurements, the polycrystalline powders were placed inside a 0.5 mm Teflon sample holder using the SC-10 front-facing module. The quantum yield measurements were acquired using the SC-30 integrating sphere module. The standard Floracle software was used to measure and plot each spectrum, as well as calculate the quantum yield.

Structure Determination

X-ray intensity data were collected for all samples at 296(2) K using a Bruker SMART APEX diffractometer (Mo Kα radiation, λ= 0.71073 Å).[4.31] The raw area detector data frames were reduced and corrected for absorption effects using the SAINT+ and SADABS programs.[4.31] The initial structural model was obtained by direct methods using SHELXS.[4.32, 4.33] Subsequent difference Fourier calculations and full-matrix least-squares refinement against F^2 were performed with SHELXL-2013/4[4.32] using the ShelXle interface.[4.33]

The compounds crystallize in the tetragonal system. The pattern of systematic absences in the intensity data indicated only body-centering lattice symmetry, leaving the space groups *I*4, *I*-4 and *I*4/*m*. The non-centrosymmetric group *I*-4 (No. 82) was established as correct by structure solution. This space group choice was checked with the ADDSYM program in PLATON, which found no missed symmetry.[4.34-4.37] The asymmetric unit consists of four metal atom positions (one rare earth, one silicon and two

sodium atoms) and five oxygen atom positions. All atoms occupy positions of general crystallographic symmetry (Wyckoff position 8*g*) except atoms Na(2) and O(5). Na(2) is located at position 4*f*, on a two-fold axis of rotation. O(5) is located at position 2*c* with -4 site symmetry. Sodium atom Na(2), located on a two-fold axis, is 0.4 Å from the nearby fourfold inversion axis at 0,½,¾, and is disordered over two sites by the -4 axis. The maximum chemical site occupancy of Na(2) is therefore 0.5. All atoms were refined with anisotropic displacement parameters. Trial refinements of the site occupancy factors of the rare earth site and Na(1) showed no significant deviations from full occupancy. The compound is assumed to be a hydroxide to preserve crystal electroneutrality. A reliable position for the hydroxy proton could not be located by difference synthesis and was not calculated. It is likely disordered about oxygen atom O(5). Refinement of the Na(2) site occupation factor resulted in small decrease from full occupancy (0.5), to 0.45(1), but with no change in the R_1/wR_2 values. No significant decrease in the site occupation factor for the associated hydroxide oxygen O(5) was observed. For this reason the Na(2) site was kept at full occupancy to maintain change balance. Further details of the crystal structure investigation can be obtained from the Fachinformationszentrum Karlsruhe (e-mail: crystdata@fiz-karlsruhe.de) on quoting the depository numbers CSD-429271 (Pr), 429269 (Nd), and 429267 (Sm), 429266 (Eu), 429273 (Tb), 429275 (Dy), 429274 (Ho), 429270 (Er), 429268 (Tm), 429265 (Yb), and 429272 (Y).

Results and Discussion

Synthesis

Single crystals of $Na_5RE_4(OH)[SiO_4]_4$ (RE = Pr, Nd, Sm, Eu, Tb - Yb, Y) were successfully grown in a hydroflux (**Figure 4.1**). In all cases, except the Gd analogue, it

was possible to obtain crystals of the desired product, however, the specific reaction conditions were refined based on experimental outcomes to maximize the yield of the product. In some cases this meant changing the cooling rate, while for others it meant using a different hydroflux composition. In fact, the conditions necessary to synthesize pure samples of these oxyhydroxides varied significantly with respect to the constituent rare earth, even though one would have expected them to behave chemically very similarly. All members of the series were synthesized as pure samples using fairly simple reaction profiles. For RE = Eu and Sm, it was necessary to utilize a pure sodium based hydroflux since the mixed sodium/potassium hydroflux, used for all other compositions, resulted in the formation of $RE(OH)_3$ as a secondary phase for these two rare earths. The specific rare earth precursor, oxide vs. chloride vs. nitrate also had an effect, although only the use of the oxide and one nitrate precursor are discussed in this paper. As with all crystal growth reactions, the conditions typically have to be optimized by varying slightly the reaction conditions for each individual composition.

Structures

The $Na_5RE_4(OH)[SiO_4]_4$ structures, like those previously reported in the literature, crystallize in the tetragonal space group *I*-4.[4.24, 4.28, 4.29] Even though the Nd analogue has already been published,[4.24] it is included in this work because our lattice parameters differ and because we investigated the magnetic properties of the composition. The crystallographic data for the $Na_5RE_4(OH)[SiO_4]_4$ crystals are given in **Table 4.1**. This structure consists of one unique silicon site, one unique rare earth site, and two unique sodium sites. SiO_4 tetrahedra which are isolated from one another edge- and corner-share oxygens with nearly square antiprismatic $REO_7(OH)$ polyhedra (**Figure**

4.2). Four of the $REO_7(OH)$ polyhedra share faces, creating the $RE_4O_{20}(OH)$ units depicted in **Figure 4.3**. The OH^- group, which is disordered, is located at the center of the unit. The $RE_4O_{20}(OH)$ units are corner-shared to eight other such units in the *ab* plane and separated from each other along the *c* axis by SiO_4 tetrahedra (**Figure 4.4**). Na(1) atoms are coordinated to seven oxygens in a distorted pentagonal bipyramidal environment as seen in **Figure 4.5**. These polyhedra share edges with four other NaO_7 polyhedra in what can be described as a tetrahedral ladder down the *c* axis (**Figure 4.5**). The Na(2) atoms are located in the channels between the $RE_4O_{20}(OH)$ units and sit directly in line with the OH site as seen in **Figure 4.6**. The overall structure is shown in **Figure 4.2**. Bond valence sums were calculated with ranges of 0.67 – 1.10 v.u. for Na, 2.70 – 3.12 v.u. for RE, and 3.90 – 4.24 v.u. for Si, which confirms the oxidation states of Na^+, RE^{3+}, and Si^{4+} for all reported analogues.[4.38, 4.39]

Magnetism

The magnetic data is summarized in **Table 4.2**. **Figure 4.7 a** and **b** show the inverse susceptibilities of $Na_5RE_4(OH)(SiO_4)_4$ (RE = Pr, Nd, Sm, Eu) and (RE = Gd, Tb, Dy, Ho, Er, Tm), respectively. **Figure 4.7c** shows the susceptibility data for the Eu member. All members of the series, with the exception of the Sm, and Eu containing members, follow Curie-Weiss behavior. Fitting the higher temperature (50 K – 300 K) inverse susceptibilities using the Curie-Weiss law yield effective moments in good agreement with the calculated moments for the RE^{3+} cations. The largest differences between the observed and calculated moments are for RE = Pr and Tb and are likely due to a higher uncertainty of the sample masses used in the magnetic measurements for these analogues.

The magnetic susceptibility data of $Na_5Tb_4(OH)(SiO_4)_4$, shown in the inset of **Figure 4.7b**, display a downturn at T = 2.8 K attributed to antiferromagnetic ordering. It is not clear why only this composition exhibits AF ordering, although it is quite possible that the other rare earth compositions do as well, however, at temperatures lower than we were able to measure on our instrument. For all samples measured, no differences were observed between the zero-field cooled and field cooled susceptibilities, as shown in the inset of **Figure 4.7b** for $Na_5Tb_4(OH)(SiO_4)_4$.

The Eu and Sm analogues do not exhibit Curie-Weiss behavior. The Eu analogue, shown in **Figure 4.7c**, exhibits Van Vleck paramagnetism, a form of temperature independent paramagnetism, below ~100 K. Below ~45 K, there is a positive deviation from the expected behavior. Previous studies have attributed similar increases in the low temperature susceptibility in Eu^{3+} compounds to small amounts of Eu^{2+}, which has strong Curie-like behavior at low temperatures.[4.40] This explanation is unlikely in this case, however, as the synthetic conditions used to prepare these samples are not conducive to reducing Eu^{3+} to Eu^{2+}. Due to the non-Curie Weiss behavior of these analogues, their effective moments are reported as their $\chi \bullet T$ values at 300 K of $2.827(\chi_m T)^{1/2}$. The two moments are consistent with those typically reported for Sm and Eu.[4.41]

Luminescence

The terbium, europium, and gadolinium analogues of the $Na_5RE_4(OH)[SiO_4]_4$ structure luminesce in the visible region under UV excitation. The terbium and europium analogues both exhibit sharp and intense emission lines intrinsic to their respective element and emit bright green and red light, respectively, under UV excitation (**Figure 4.8** and **4.9**). The gadolinium analogue, however, exhibits less intense luminescence, with

a violet emission (**Figure 4.10**). The color and relative intensity of the luminescence of each compound can be seen in **Figure 4.11** where the strong luminescence of $Na_5Tb_4(OH)[SiO_4]_4$ and $Na_5Eu_4(OH)[SiO_4]_4$ is clearly visible, while the weaker luminescence of $Na_5Gd_4(OH)[SiO_4]_4$ is only weakly visible.

In the emission spectrum for the Tb analogue, the peaks 482 nm, 537 nm, 578 nm, and 612 nm are likely caused by the $^5D_4 \rightarrow {}^7F_6$, $^5D_4 \rightarrow {}^7F_5$, $^5D_4 \rightarrow {}^7F_4$, and $^5D_4 \rightarrow {}^7D_3$ transitions, respectively. In the Eu analogue emission spectrum, the 584 nm peak is likely caused by the $^5D_0 \rightarrow {}^7F_1$ transition while the 608 nm peak is likely caused by the $^5D_0 \rightarrow {}^7F_2$ transition. The $^5D_0 \rightarrow {}^7F_2$ transition is larger than the $^5D_0 \rightarrow {}^7F_1$ transition which is expected due to the lack of an inversion center in the noncentrosymmetric $Na_5Eu_4(OH)[SiO_4]_4$. Laporte forbidden transitions such as the $J = 2$ of the $^5D_0 \rightarrow {}^7F_2$ transition can occur in noncentrosymmetric compounds.

Compared to other known luminescent silicates, the maximum Tb peak λ usually occurs within 22 nm, in the range 536 nm to 558 nm. Our Tb analogue has its maximum emission peak at 542 nm. In our Eu analogue, and those found in literature, the maximum Eu emission peak λ seems to be rather consistent at 608 nm and in Gd, the maximum visible peak λ can vary from a violet region 384 nm (this study) to a blue region, 491 nm, to a red emission such as 613 nm. [4.11, 4.19, 4.23]

Fluorescence quantum yields were measured on polycrystalline samples of $Na_5RE_4(OH)[SiO_4]_4$ (RE = Eu, Gd, Tb). To ensure accurate quantum yields, each analogue had three different samplings taken. The quantum yield for each sampling was determined using the Fluoracle software. The averaged quantum yields were determined to be 4.5(5) % for Eu, 1.9(7) % for Gd, and 20.8(1) % for Tb. Quantum yields of

commercially available phosphors such as $Y_3Al_5O_{12}:Ce^{3+}$ (YAG:Ce) $M_2SiO_4:Eu^{2+}$ (M = Ba^{2+}, Sr^{2+}, Ca^{2+}) and $M_2Si_5N_8$ (M = Ca^{2+}, Sr^{2+}, Ba^{2+}) range from 75-79 % for the green silicate ($Ba_2SiO_4:Eu^{2+}$) to 89 – 92 % for the red nitride ($M_2Si_5N_8$ (M = Ba^{2+}, Sr^{2+}, Ca^{2+}).[4.42] The quantum yield for the red (Eu) phosphor (4.6 %), while much lower than the yield of the commercial phosphor (89 – 92 %), is respectable. Our green (Tb) phosphor has a quantum yield in excess of 20 %, which is encouraging, even though it did not reached the commercial range of 75 – 79 %. Improvements via additional chemical substitutions into this system are likely and could enable this system to be competitive in the commercial phosphor market.

A previous report indicates that $Na_5Gd_4(OH)[SiO_4]_4$ exhibits second harmonic generation (SHG).[4.43] SHG measurements were performed on our samples and it was found that our samples either did not exhibit SHG, or the SHG was below the detection limit.

Conclusion

Crystals of twelve oxyhydroxide compositions were grown using the low temperature hydroflux method. Magnetic measurements on the terbium analogue reveal a downturn at T = 2.8 K indicating antiferromagnetic ordering at a T_N below 2.8 K. There is no indication of long range magnetic ordering for any of the other compounds within the temperature ranged investigated. $Na_5Eu_4(OH)[SiO_4]_4$, $Na_5Gd_4(OH)[SiO_4]_4$, and $Na_5Tb_4(OH)[SiO_4]_4$ are luminescent with the Eu and Tb analogues exhibiting intense visible luminescence. Fluorescence quantum yield studies indicate that the quantum yields are 4.5(5) % (Eu), 1.9(7) % (Gd), and 20.8(1) % (Tb). The fluorescence quantum yield result for the Tb analogue is very promising for future studies of this system.

References

4.1 Bugaris, D. E.; zur Loye, H.-C. *Angew. Chem. Int. Ed.* **2012**, *51*, 3780-3811.
4.2 Bugaris, D. E.; Smith, M. D.; zur Loye, H.-C. *Inorg. Chem.* **2013**, *52*, 3836-3844.
4.3 Chance, W. M.; Bugaris, D. E.; Sefat, A. S.; zur Loye, H.-C. *Inorg. Chem.* **2013**, *52*, 11723-11733.
4.4 Flood, H.; Fortland, T. *Acta Chem. Scand.* **1947**, *1*, 592.
4.5 Lux, H. Z.; *Z. Electrochemistry* **1939**, *45*, 303.
4.6 Ferdov, S.; Sa Ferreira, R.; Lin, Z. *Chem. Mater.* **2006**, *18*, 5958-5964.
4.7 Li, Y.-C.; Chang, Y.-H.; Lin, Y.-F.; Chang, Y.-S.; Lin, Y.-J. *J. Alloys Compd.* **2007**, *439*, 367-375.
4.8 Vidican, I.; Smith, M. D.; zur Loye, H.-C. *J. Solid State Chem.* **2003**, *170*, 203-210.
4.9 Zhao, F.; Guo, P.; Li, G.; Liao, F.; Tian, S.; Jing, X. *Mater. Res. Bull.* **2003**, *38*, 931-940.
4.10 Emirdag-Eanes, M.; Pennington, W. T.; Kolis, J. W. *J. Alloys Compd.* **2004**, *366*, 76-80.
4.11 Yeon, J.; Hardaway, J. B.; Sefat, A. S.; Latshaw, A. M.; zur Loye, H.-C. *Solid State Sci.* **2014**, *34*, 24-30.
4.12 Atovmyan, L. O.; Filipenko, O. S.; Ponomarev, V. I.; Leonova, L. S.; Ukshe, E. A. *Solid State Ionics* **1984**, *14*, 137-142.
4.13 Cao, X. Q.; Vassen, R.; Stoever, D. *J. Eur. Ceram. Soc.* **2004**, *24*, 1-10.
4.14 Wu, R.; Pan, W.; Ren, X.; Wan, C.; Qu, Z.; Du, A. *Acta Mater.* **2012**, *60*, 5536-5544.
4.15 Chicagov, A. V.; Litvin, B. N.; Belov, N. V. *Kristallografiya* **1969**, *14*, 119-122.
4.16 Maksimov, B. A.; Litvin, B. N.; Ilyukhin, V. V.; Belov, N. V. *Kristallografiya* **1969**, *14*, 498-501.
4.17 Sebais, M.; Pobedimskaya, E. A.; Dimitrova, O. V. *Kristallografiya* **1985**, *30*, 802-805.
4.18 Tamazyan, R. A.; Malinovskii, Y. A.; Sirota, M. I.; Simonov, V. I. *Kristallografiya* **1988**, *33*, 1128-1133.
4.19 Bondar, I. A.; Tenisheva, T. F.; Shepelev, Y. F.; Toropov, N. A. *Dokl. Akad. Nauk SSSR* **1965**, *160*, 1069-1071.
4.20 Napper, J. D.; Layland, R. C.; Smith, M. D.; zur Loye, H.-C. *J. Chem. Crystallogr.* **2004**, *34*, 347-351.
4.21 Ponomarev, V. I.; Filipenko, O. S.; Atoymyan, L. O. *Kristallografiya* **1988**, *33*, 98-104.
4.22 Haile, S. M.; Wuensch, B. J. *Acta Crystallogr. B* **2000**, *B56*, 773-779.
4.23 Latshaw, A. M.; Hughey, K. D.; Smith, M. D.; Yeon, J.; zur Loye, H.-C. *Inorg. Chem.* **2015**, *54*, 876-884.
4.24 Malinovskii, Y. A. *Dokl. Akad. Nauk SSSR* **1984**, *274*, 75-78.
4.25 Merinov, B. V.; Maksimov, B. A.; Ilyukhin, V. V.; Belov, N. V. *Dokl. Akad. Nauk SSSR* **1980**, *255*, 348-351.
4.26 Schafer, M. C.; Schleid, T. *Z. Anorg. Allg. Chem.* **2010**, *636*, 2069.
4.27 Hughey, K.; Yeon, J.; zur Loye, H.-C. *J. Chem. Crystallogr.* **2014**, *44*, 376-379.
4.28 Latshaw, A. M.; Smith, M. D.; zur Loye, H.-C. *Solid State Sci.* **2014**, *35*, 28-32.
4.29 Fallon, G. D.; Gatehouse, B. M. *Acta Crystallogr., Sect. B* **1982**, *B38*, 919-920.

4.30 Morrison, G.; zur Loye, H.-C. *J. Solid State Chem.* **2015**, *221*, 334-337.
4.31 SMART Version 5.631, SAINT+ Version 6.45 and SADABS Version 2.10, Bruker Analytical X-ray Systems, Inc., Madison, Wisconsin, USA, 2003.
4.32 Sheldrick, G. M. *Acta Crystallogr.* **2008**, *A64*, 112-122.
4.33 Hübschle, C. B.; Sheldrick, G. M.; Bittrich, B. *J. Appl. Cryst.* **2011**, *44*, 1281-1284.
4.34 LePage, Y. *J. Appl. Cryst.* **1987**, *20*, 264-269.
4.35 PLATON, A Multipurpose Crystallographic Tool, Utrecht University, Utrecht, The Netherlands, Spek, A. L. 1998.
4.36 Spek, A. L. *J. Appl. Cryst.* **1988**, *21*, 578-579.
4.37 Spek, A. L. *Acta Crystallogr., A* **1990**, *46*, C34.
4.38 Brese, N. E.; O'Keeffe. *Acta Crystallogr., Sect. B:* **1991**, *47*, 192-197.
4.39 Brown, I. D.; Altermatt, D. *Acta Crystallogr., Sect. B:* **1985**, *41*, 244-247.
4.40 Takikawa, Y.; Ebisu, S.; Nagata, S. *J. Phys. Chem. Solids* **2010**, *71*, 1592-1598.
4.41 Blundell, S. *Magnetism in Condensed Matter*; Oxford University Press: Oxford, 2010;
4.42 Gorrotxategi, P.; Consonni, M.; Gasse, A. *J. Solid State Light.* **2015**, *2*,
4.43 Avetisyan, E. I.; Chichagov, A. V.; Belov, N. V. *Kristallografiya* **1970**, *15*, 1066-1067.

Table 4.1. Crystallographic Data for $Na_5RE_4(OH)[SiO_4]_4$ (RE = Pr, Nd, Sm - Yb, and Y).

Formula	$Na_5Pr_4(OH)[SiO_4]_4$	$Na_5Nd_4(OH)[SiO_4]_4$	$Na_5Sm_4(OH)[SiO_4]_4$	$Na_5Eu_4(OH)[SiO_4]_4$
Formula weight	1063.96	1077.28	1101.72	1108.16
Crystal system	Tetragonal	Tetragonal	Tetragonal	Tetragonal
Space group	*I -4*	*I -4*	*I -4*	*I -4*
a (Å)	12.0588(3)	11.9726(3)	11.8467(14)	11.7872(2)
c (Å)	5.4668(2)	5.4824(2)	5.4846(13)	5.4813(2)
V (Å^3)	794.95(5)	785.86(5)	769.7(3)	761.56(4)
Z	2	2	2	2
Density (Mg/m^3)	4.445	4.553	4.753	4.833
Absorption coefficient (mm^{-1})	12.573	13.532	15.583	16.801
Crystal size (mm^3)	0.08 x 0.08 x 0.06	0.06 x 0.06 x 0.05	0.05 x 0.04 x 0.04	0.07 x 0.06 x 0.04
$2\theta_{max}$ (°)	36.276	36.293	36.255	36.322
reflections collected	9092	12490	8856	11811
independent reflections	1852	1888	1811	1849
GOF (F^2)	1.039	1.086	1.042	1.059
R indices (all data)	$R_1 = 0.0328$	$R_1 = 0.0200$	$R_1 = 0.0372$	$R_1 = 0.0245$
	$wR_2 = 0.0679$	$wR_2 = 0.0454$	$wR_2 = 0.0602$	$wR_2 = 0.0488$

Table 4.1 (Continued).

Formula	$Na_5Gd_4(OH)[SiO_4]_4$	$Na_5Tb_4(OH)[SiO_4]_4$	$Na_5Dy_4(OH)[SiO_4]_4$	$Na_5Ho_4(OH)[SiO_4]_4$
Formula weight	1129.52	1136.00	1150.32	1160.04
Crystal system	Tetragonal	Tetragonal	Tetragonal	Tetragonal
Space group	*I -4*	*I -4*	*I -4*	*I -4*
a (Å)	11.74272(3)	11.6845(7)	11.6435(3)	11.6002(3)
c (Å)	5.4668(22)	5.4574(6)	5.4322(3)	5.4231(3)
V (Å^3)	753.83	745.09(12)	736.45(5)	729.76(5)
Z	2	2	2	2
Density (Mg/m^3)		5.064	5.187	5.279
Absorption coefficient (mm^{-1})		19.319	20.632	22.027
Crystal size (mm^3)		0.06 x 0.06 x 0.04	0.018 × 0.012 × 0.06	0.012 × 0.010 × 0.04
$2\theta_{max}$ (°)	120	38.57	36.29	36.38
reflections collected		10635	8918	11389
independent reflections		2112	1693	1734
GOF (F^2)		1.031	1.091	1.104
R indices (all data)		$R_1 = 0.0334$	$R_1 = 0.0278$	$R_1 = 0.0254$
		$wR_2 = 0.0551$	$wR_2 = 0.0589$	$wR_2 = 0.0597$

Table 4.1 (Continued).

Formula	$Na_5Er_4(OH)[SiO_4]_4$	$Na_5Tm_4(OH)[SiO_4]_4$	$Na_5Yb_4(OH)[SiO_4]_4$	$Na_5Y_4(OH)[SiO_4]_4$
Formula weight	1169.36	1175.03	1192.48	855.96
Crystal system	Tetragonal	Tetragonal	Tetragonal	Tetragonal
Space group	*I -4*	*I -4*	*I -4*	*I -4*
a (Å)	11.5731(3)	11.5275(4)	11.5734(3)	11.6025(4)
c (Å)	5.4107(2)	5.3951(4)	5.4067(3)	5.4264(5)
V (Å^3)	724.69(5)	716.92(7)	724.19(5)	730.49(8)
Z	2	2	2	2
Density (Mg/m^3)	5.359	5.443	5.469	3.891
Absorption coefficient (mm^{-1})	23.506	25.100	26.173	16.310
Crystal size (mm^3)	0.06 x 0.05 x 0.05	0.04 x 0.04 x 0.02	0.06 x 0.05 x 0.05	0.05 x 0.04 x 0.02
$2\theta_{max}$ (°)	36.281	36.344	36.323	32.812
reflections collected	10726	10447	11352	8398
independent reflections	1652	1735	1750	1365
GOF (F^2)	1.066	1.062	1.061	1.024
R indices (all data)	$R_1 = 0.0292$	$R_1 = 0.0320$	$R_1 = 0.0327$	$R_1 = 0.0598$
	$wR_2 = 0.0660$	$wR_2 = 0.0603$	$wR_2 = 0.0710$	$wR_2 = 0.1049$

Table 4.2. Experimental magnetic moments (μ_{eff}) compared to calculated moments (μ_{calc}).

Compound	Fit Range (K)	T_N (K)	θ (K)	μ_{eff} (m_B/RE)	μ_{calc} (m_B/RE)
$Na_5Pr_4(OH)(SiO_4)_4$	50-300	-	-31.2	3.2[a]	3.58
$Na_5Nd_4(OH)(SiO_4)_4$	100-300	-	-52.4	3.74	3.62
$Na_5Sm_4(OH)(SiO_4)_4$	300	-	-	1.66[b]	1.74[c]
$Na_5Eu_4(OH)(SiO_4)_4$	300	-	-	3.79[b]	3.4[c]
$Na_5Gd_4(OH)(SiO_4)_4$	50-300	-	-1.8	7.91	7.94
$Na_5Tb_4(OH)(SiO_4)_4$	50-300	< 2	-15.5	10.0[a]	9.72
$Na_5Dy_4(OH)(SiO_4)_4$	50-300	-	-5.6	10.75	10.65
$Na_5Ho_4(OH)(SiO_4)_4$	50-300	-	-8.2	10.68	10.61
$Na_5Er_4(OH)(SiO_4)_4$	50-300	-	-7.9	9.63	9.58
$Na_5Tm_4(OH)(SiO_4)_4$	50-300	-	-1.1	7.7[a]	7.56

[a] Effective moments likely have a large error due to the small masses of these samples (uncertainty in sample mass ~10 %)
[b] Effective moments approximated as $2.827(\chi_m T)^{1/2}$ at 300 K due to non-Curie Weiss behavior
[c] μ_{obs} values reported due to the large difference between μ_{obs} and μ_{calc}. μ_{obs} values are from paramagnetic salts and are obtained from reference 4.39.

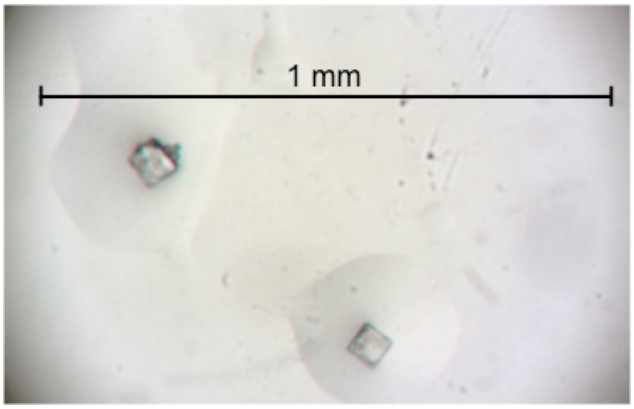

Figure 4.1. Crystals of $Na_5Tb_4(OH)[SiO_4]_4$, representative of all compositions.

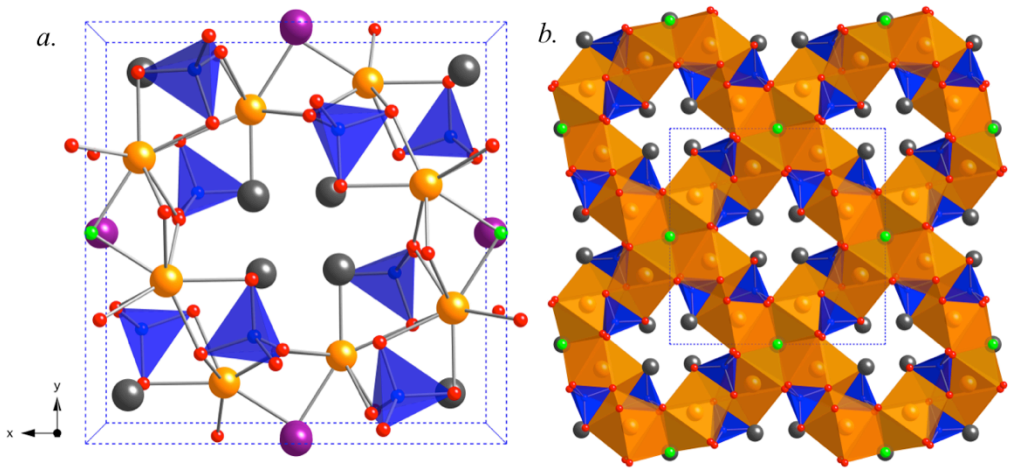

Figure 4.2. *a* is a polyhedral representation of the unit cell of $Na_5Tb_4(OH)[SiO_4]_4$ and *b* is an extended polyhedral representation displaying the interconnectivity of the rare earth and silicon environments. The rare earth atoms are shown in orange, silicon tetrahedra in blue, Na(1) atoms in grey, Na(2) atoms in purple, and oxygen atoms shown in red.

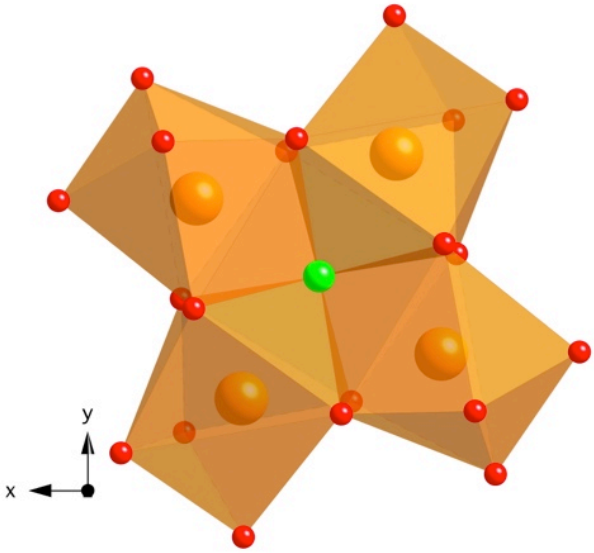

Figure 4.3. The $RE_4O_{20}OH$ unit in $Na_5Tb_4(OH)[SiO_4]_4$, which is representative of all of the title compounds, where the rare earth polyhedra are shown in orange, oxygen atoms shown in red, and the hydroxide molecule is shown in green

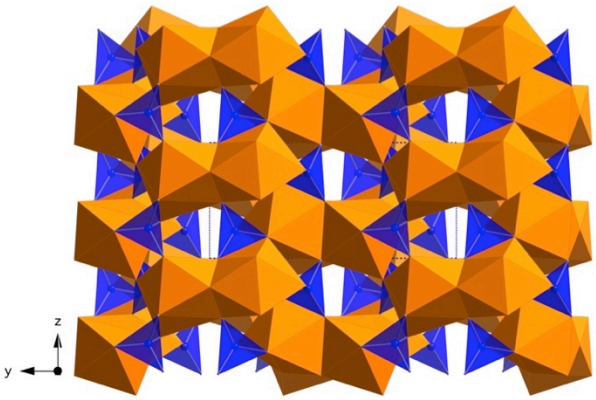

Figure 4.4. Crystal structure of $Na_5Tb_4(OH)[SiO_4]_4$, which is representative of all of the title compounds. The $RE_4O_{20}OH$ units are shown as orange polyhedra and the silicon tetrahedra are shown in blue. Oxygen, sodium, and hydroxide are omitted for clarity.

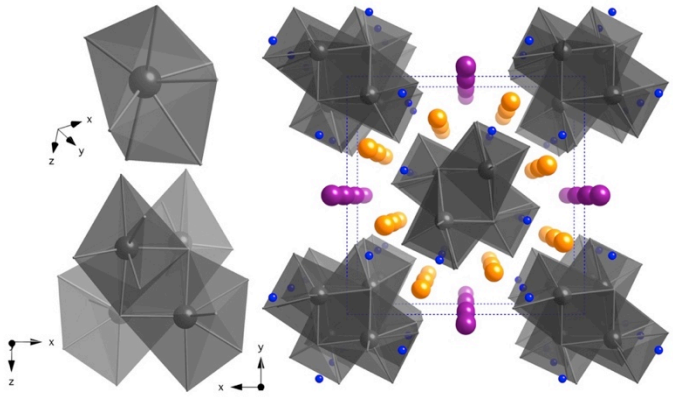

Figure 4.5. Crystal structure of $Na_5Tb_4(OH)[SiO_4]_4$, which is representative of all of the title compounds. The image on the top left indicates the Na(1) polyhedra, the image on the bottom left shows the Na(1) polyhedra stacking, and the image on the right shows the view of the Na(1) columns down the *c* axis. The gray polyhedra represent Na(1), the purple spheres are Na(2), the blue spheres are silicon, and the orange spheres are the rare atoms. Oxygen atoms are omitted for clarity.

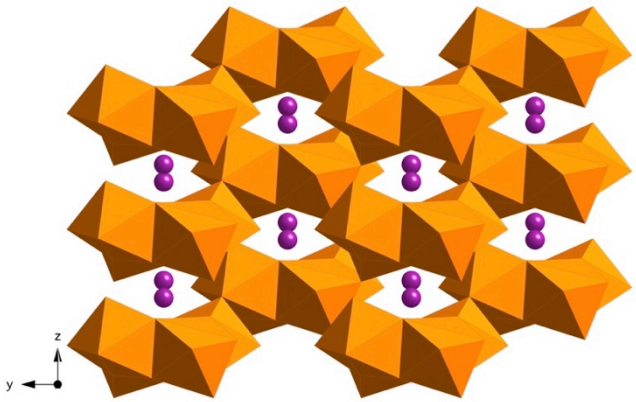

Figure 4.6. Crystal structure of $Na_5Tb_4(OH)[SiO_4]_4$, which is representative of all of the title compounds. The positions of the Na(2) atoms (shown in purple) are shown with respect to the rare earth polyhedral units (shown in orange). Oxygen, Na(1), and silicon are omitted for clarity.

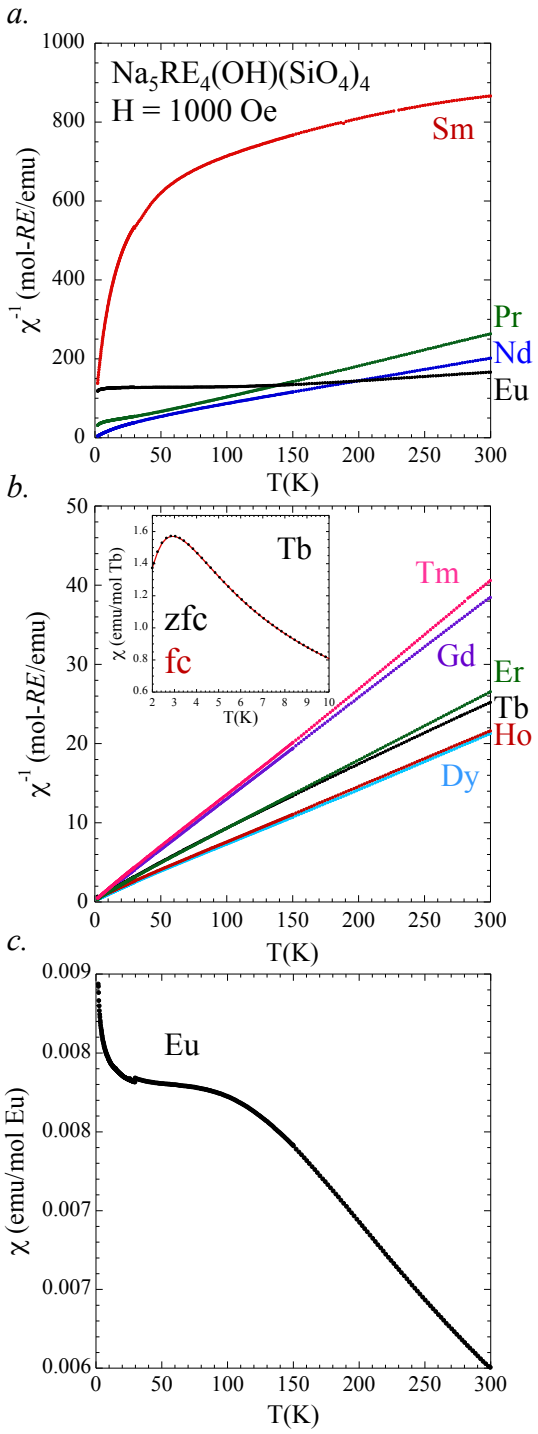

Figure 4.7. (a) and (b) show the inverse susceptibilities of $Na_5RE_4(OH)(SiO_4)_4$ (RE = Pr, Nd, Sm, Eu) and (RE = Gd, Tb, Dy, Ho, Er, Tm), respectively. Figure 6 (c) shows the susceptibility data for Eu member.

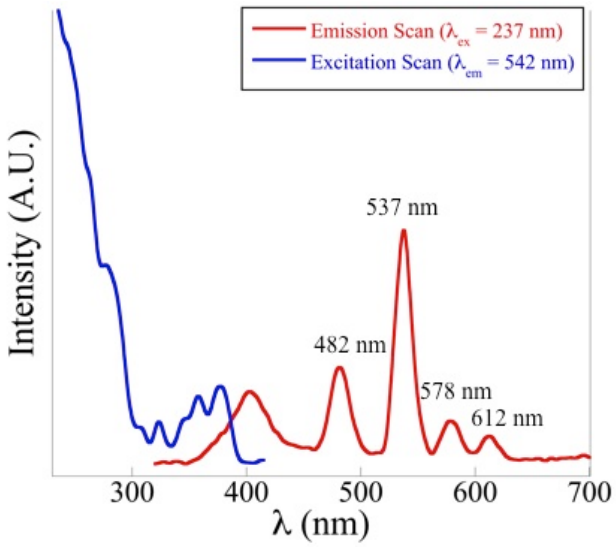

Figure 4.8. Room temperature luminescence spectra of $Na_5Tb_4(OH)[SiO_4]_4$.

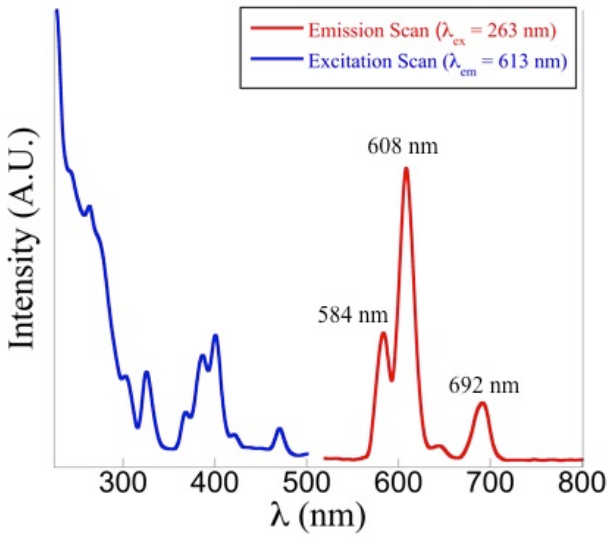

Figure 4.9. Room temperature luminescence spectra of $Na_5Eu_4(OH)[SiO_4]_4$.

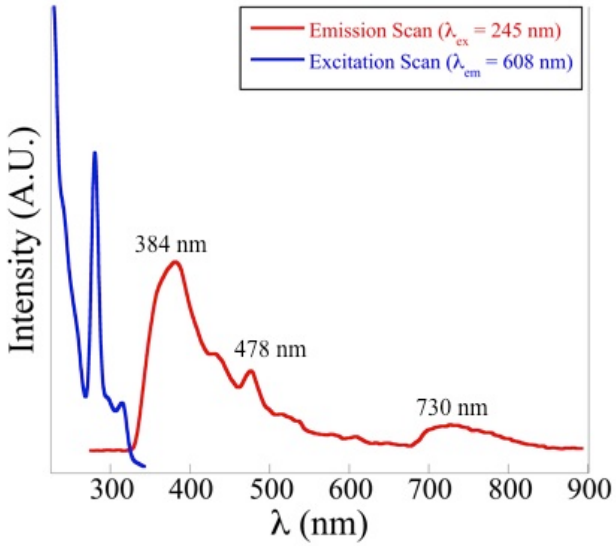

Figure 4.10. Room temperature luminescence spectra of $Na_5Gd_4(OH)[SiO_4]_4$.

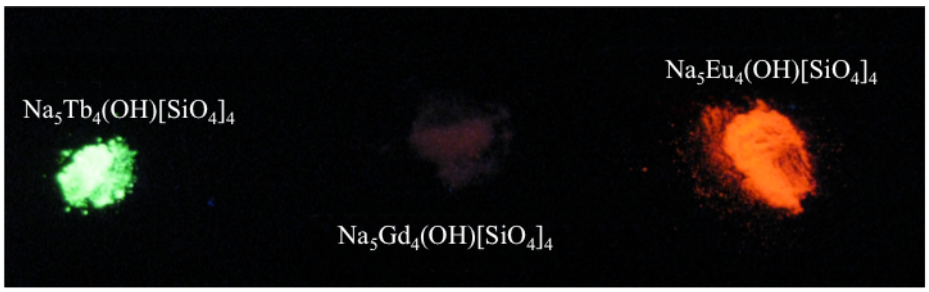

Figure 4.11. Side-by-side comparison of the room temperature luminescence of $Na_5Tb_4(OH)[SiO_4]_4$, $Na_5Gd_4(OH)[SiO_4]_4$, and $Na_5Eu_4(OH)[SiO_4]$.

Chapter 5

$A_5RE_4X[TO_4]_4$ Crystal Growth and Photoluminescence. Fluoride Flux Synthesis of Sodium and Potassium Rare Earth Silicate Oxyfluorides*

*Latshaw, A. M.; Wilkins, B. O.; Hughey, K. D.; Yeon, J.; Williams, D. E.; Tran, T. T.; Halasyamani, P. S.; zur Loye, H.-C. *CrystEngComm*. **2015**, *17*, 4654–4661.

Introduction

The field of solid-state lighting is constantly looking for better and cheaper materials that exhibit intense luminescence. To create such materials it is necessary to pursue different modes of materials discovery and combine it with judicious fine-tuning of the materials' composition and concomitant properties. We have pursued materials discovery via crystal growth from high temperature fluxes where we focus on expanding the number of compositions that can be prepared given a new structure as a starting point.

Flux crystal growth is a versatile synthetic method that has been used to grow crystals of many oxides, hydroxides, fluorides, and oxyfluorides.[5.1] In particular, the use of a eutectic flux continues to be a promising field of exploration as it enables different temperatures and ratios of fluxes than have been previously been used. Eutectics also lower the melting point for the overall reaction, which can be helpful for reaction vessel consideration. Alkali fluoride fluxes have been used to synthesize lanthanide containing silicate oxides[5.2, 5.3] and oxyfluorides[5.4-5.7] previously and the use of eutectic mixtures has allowed us to crystallize numerous new compositions, including rare earth containing compositions.

The latter represents a synthetic opportunity since once a new rare earth containing composition is isolated, many other compositions containing the remaining rare earths can typically be prepared. If the structure is fairly rigid and the rare earth crystallographic position size limited, then one often observes a size limitation as to which rare earth cations fit. If, on the other hand, the structure is fairly flexible and exhibits little restriction on the rare earth site, then it is often possible to incorporate all the rare earths (the one exception being radioactive promethium). In this paper we report

on a series of compounds, $Na_5RE_4F[SiO_4]_4$ (RE = Pr, Nd, Sm-Tm) and $K_5Pr_4F[SiO_4]_4$, that were prepared following the discovery of the first composition, $Na_5Eu_4F[SiO_4]_4$. In completing the series it became apparent that the gadolinium analogue is luminescent and that the terbium and europium analogues exhibit very intense luminescence. The ability of this structure to exhibit such intense luminescence could lead to potential solid-state lighting applications in the future, especially because the framework of the structure is made up of silicon, a relatively inexpensive framework. In addition, the presence of magnetic rare earth ions makes it of interest to study their magnetic properties.

Herein we present the synthesis, structural characterization and physical property measurements of the $Na_5RE_4F[SiO_4]_4$ (RE = Pr, Nd, Sm-Tm) and $K_5Pr_4F[SiO_4]_4$ series of new silicates.

Experimental Section

Reagents

Nd_2O_3 (99.9 %), Sm_2O_3 (99.9 %), Eu_2O_3 (99.9 %), Gd_2O_3 (99.9 %), Dy_2O_3 (99.9 %), Ho_2O_3 (99.9 %), Er_2O_3 (99.9 %), and Tm_2O_3 (99.9 %) were purchased from Alfa Aesar. Pr_2O_3 and Tb_2O_3 (Alfa Aesar) were reduced from Pr_6O_{11} (99.9 %) and Tb_4O_7 (99.9 %), respectively. SiO_2 (99.99 %) was purchased from Aldrich as fused pieces and ground to a powder in a ball mill. NaF (99 % min.) and KF (99 % min.) were purchased from Alfa Aesar, and NaCl (ACS grade, 99.9 %) was purchased from Fisher Scientific.

Synthesis

Single crystals of $Na_5RE_4F[SiO_4]_4$ (RE = Pr, Nd, Sm-Tm) complexes were grown using a NaF/NaCl eutectic flux. 2 mmol of RE_2O_3, 2 mmol Na_2CO_3, and 4 mmol SiO_2 were loaded into a silver crucible. 2.81g of NaF and 1.95g of NaCl were loaded on top of

the reactants as a eutectic flux and a silver lid was loosely fitted on the crucible. The crucible was then placed into a programmable furnace that was heated to 800 °C in 1.5 h, allowed to dwell there for 24 h and then slow cooled at a rate of 6 °C per hour to 600 °C, after which the furnace was shut off. The flux was washed away using water, aided by sonication, and then the products were isolated by filtration.

Single crystals of $K_5Pr_4F[SiO_4]_4$ were grown out of a molten potassium fluoride flux. 2 mmol of Pr_2O_3 and 4 mmol of SiO_2 were loaded into a copper tube that was welded shut on the bottom. 5g of KF flux was loaded on top of the reactants and the tube was crimped shut. The tube was loaded into a longer copper tube to contain any leaks and the long copper tube was placed into a quartz tube in a flow-through furnace under a stream of N_2 gas. The furnace was programmed to ramp to 1000 °C, dwell there for 24 h before slow cooling at a rate of 6 °C per hour to 800° C. Once the furnace reached 800 °C, it was shut off and allowed to cool to room temperature. Crystals were isolated by sonication and vacuum filtration.

Polycrystalline samples of $Na_5RE_4F[SiO_4]_4$ (RE = Pr, Nd, Sm-Ho) were synthesized via a solid state route in order to prepare the larger quantities needed for property measurements since the crystals were too small to pick large quantities. 1 mmol RE_2O_3 (prefired at 1000 °C for 12 h), 1 mmol Na_2SiO_3, 1 mmol SiO_2, and 0.5 mmol NaF (all ground and dried at 112 °C overnight before weighing) were ground for 30 min before being placed in a drying oven at 112 °C overnight. After drying, the sample was pressed into a pellet. The pellet was then loaded into a copper tube that was crimped at both ends to avoid the loss of fluoride. The crimped tube was loaded into a flow-through furnace that was purged with N_2 gas. The reactions were then heated to 900 °C for 25-

124 h, and reground up to 3 times, depending on the sample, until the desired product was the major phase with a minor phase of apatite (by powder X-ray diffraction). The solid state syntheses were adjusted to maximize the amount of the desired phase. Numerous trial syntheses showed that shorter heating times yielded starting material and $Na_5RE_4F[SiO_4]_4$, while longer heating times led to a smaller weight percent of $Na_5RE_4F[SiO_4]_4$ and a larger weight percent of the respective rare earth containing apatite ($Pr_{4.67}(SiO_4)_3O$,[5.8] $Na_{0.5}Sm_{4.5}(SiO_4)_3O$,[5.9] $Eu_{9.34}(SiO_4)_6O_2$,[5.6] $Na_{1.64}Gd_{8.36}(SiO_4)_6O_{0.72}F_{1.28}$,[5.6] $Tb_{4.67}(SiO_4)_3O$,[5.9] $Na_{0.5}Dy_{4.5}(SiO_4)_3O$,[5.9] and $Na_{1.135}Ho_{3.865}(SiO_4)_3O_{0.36}$,[5.10]). For that reason, reaction conditions were chosen to consume all starting materials while keeping the apatite impurity at a minimum. Ultimately, the flux and solid state methods and conditions we employed were unable to achieve phase pure polycrystalline samples.

Single-Crystal X-ray Diffraction

X-ray intensity data using single crystals of all of the title compounds were collected at 294(2) K using a Bruker SMART APEX CCD diffractometer (Mo Kα radiation, λ = 0.71073 Å).[5.11] The raw area detector data frames were reduced and corrected for absorption effects using the SAINT+ and SADABS programs.[5.11] The initial structural model was obtained by direct methods using SHELXS.[5.12, 5.13] Subsequent difference Fourier calculations and full-matrix least-squares refinement against F^2 were performed with SHELXL-2013/4[5.13] using the ShelXle interface.[5.12]

All compounds crystallize in the tetragonal system. The pattern of systematic absences in the intensity data indicated only body-centering lattice symmetry, leaving the space groups *I*4, *I*-4, and *I*4/*m*. The non-centrosymmetric space group *I*-4 (No. 82) was

found, by structure solution, to be correct. The space group choice was checked using the ADDSYM program in PLATON, where no missed symmetry was found.[5.14-5.17] The asymmetric unit cell contains four metal atom positions (one rare earth, one silicon, and two sodium or potassium atoms), four oxygen positions, and one fluorine position. All atoms occupy positions of general crystallographic symmetry (Wyckoff position 8*g*) except atoms Na(2)/K(2) and O(5). Na(2)/K(2) is located at position 4*f* on a two-fold axis of rotation and O(5) is located on position 2*c* with a -4 site symmetry. Na(2)/K(2) was found to have a maximum chemical site occupancy of 0.5. All atoms were refined with anisotropic displacement parameters. The site occupancies of the rare earth site and the Na(1)/K(1) site were found to be fully occupied. Further details of the crystal structure investigation can be obtained from the Fachinformationszentrum Karlsruhe (e-mail: crystdata@fiz-karlsruhe.de) on quoting the depository numbers CSD- 429315 (Tm), 429316 (Er), 429317 (Ho), 429318 (Dy), 429319 (Gd), 429320 (Eu), 429321 (Sm), 429322 (Nd), 429325 (Tb), 429323 ($Na_5Pr_4F[SiO_4]_4$), and 429324 ($K_5Pr_4F[SiO_4]_4$).

Powder X-ray Diffraction

Powder X-ray diffraction (PXRD) data were collected on the polycrystalline samples of $Na_5RE_4F[SiO_4]_4$ (RE = Pr, Nd, Sm-Ho) using a Rigaku Dmax/2100 powder diffractometer using Cu Kα radiation. Data for the compounds were collected using a step scan covering the 2θ range of 5 – 90 ° in steps of 0.04 °. After PXRD data were collected, the cif file of the $Na_5RE_4F[SiO_4]_4$ phase and the PDF or cif file of the apatite phase ($Pr_{4.67}(SiO_4)_3O$,[5.8] $Na_{0.5}Sm_{4.5}(SiO_4)_3O$,[5.9] $Eu_{9.34}(SiO_4)_6O_2$,[5.6] $Na_{1.64}Gd_{8.36}(SiO_4)_6O_{0.72}F_{1.28}$,[5.6] $Tb_{4.67}(SiO_4)_3O$,[5.9] $Na_{0.5}Dy_{4.5}(SiO_4)_3O$,[5.9] and

$Na_{1.135}Ho_{3.865}(SiO_4)_3O_{0.36}$,[5.10] respectively) were overlaid (**Figure 5.1**). Weight percent was then calculated using the JADE software package (**Table 5.1**).

Photoluminescence Measurements

Room temperature emission and excitation spectra were collected on powders of the title compounds using a Perkin Elmer LS 55 fluorescence spectrometer. Excitation and emission scans were performed in the 200 – 500 and 550 – 900 nm ranges, respectively.

Fluorescence Quantum Yield Measurements

Emission spectra were acquired on an Edinburgh FS5 fluorescence spectrometer. A 150 W Continuous Wave Xenon Lamp was used for sample excitation, and the emission measured using a Hamamatsu R928P photomultiplier tube. For emission and excitation measurements, the polycrystalline powders were placed inside a 0.5 mm quartz sample holder using the SC-10 front-facing module. The quantum yield measurements were acquired using the SC-30 integrating sphere module. The standard Fluoracle software was used to measure and plot each spectrum, as well as calculate the quantum yield.

Second-Harmonic Generation Measurements

Powder SHG measurements were performed on a modified Kurtz nonlinear-optical (NLO) system using a pulsed Nd:YAG laser with a wavelength of 1064 nm. Unsieved powder samples were placed separately in capillary tubes and no index matching fluid was used in any of the experiments. The SHG, i.e., the 532 nm light, was collected in reflection. Comparisons with known SHG materials were made using

ground crystalline α-SiO_2. A detailed description of the equipment and methodology has been published elsewhere.[5.18, 5.19]

Magnetic Property Measurements

The magnetic properties of the title compounds were measured using a Quantum Design Magnetic Property Measurement System (QD-MPMS3 SQUID VSM). The zero-field cooled magnetic susceptibility was measured as a function of temperature between 2-300 K in an applied field of 1000 Oe. The measured magnetic data were corrected for shape and radial offset effects using the method reported by Morrison et. al.[5.20]

Results and Discussion

Structures

Numerous silicates have been published in the literature, and in many cases there are common structural motifs. Similar to the apatite ($A_5(BO_4)_3X$) class of materials, where substitutions can be made on every site in the structure,[5.6, 5.21, 5.22] the class of $A_5RE_4X[TO_4]_4$ compositions, to which the title compounds belong, is very extensive and, although compositionally quite varied, the compounds can be considered isostructural. The presence of unique O^{2-}, F^- and OH^- anions or cations like Na^+, K^+, RE^{3+}, Si^{4+}, and Ge^{4+} on specific crystallographic sites is common and creates unique compositions. In this case, the title compounds are isostructural with $Na_{4.74}Nd_{4.26}(O_{0.52}F_{0.48})[SiO_4]_4$,[5.5] $Na_5Nd_4(OH)[SiO_4]_4$,[5.23] $Na_5Y_4F[SiO_4]_4$,[5.24] $K_5La_4F[SiO_4]_4$,[5.7] $Na_5Nd_4(OH)[GeO_4]_4$,[5.25] and $Na_5RE_4(OH)[SiO_4]_4$ (RE = Pr-Tm, Y),[5.26] where differences arise from the presence or absence of O^{2-}, F^- and OH^- on the F(1) **X** site, Na^+ or K^+ on the alkali **A** sites, and Si^{4+} or Ge^{4+} on the tetragen **T** site of this series. The title compounds crystallize in the tetragonal space group *I*-4 and the crystallographic data are given in **Table 5.2**. There are

two unique sodium or potassium sites, one unique rare earth site, and one unique silicon site.

The eight coordinate rare earth cations arrange into $RE_4O_{20}F$ units by sharing faces with the two adjacent polyhedra and by sharing a common apex (F(1) site) among the four rare earth polyhedra. These units form a layered arrangement consisting of two connected sheets. Viewed down the *b* axis, it is apparent that the $RE_4O_{20}F$ units are not connected to each other in the same sheet, but are connected to the adjacent sheet of $RE_4O_{20}F$ units. The arrangement is such that each $RE_4O_{20}F$ is corner shared to four $RE_4O_{20}F$ units in the sheet above and to four $RE_4O_{20}F$ units in the sheet below. The Na(1) and Na(2), or respective potassium atoms are located in the channels created by the $RE_4O_{20}F$ units where the Na(1) or K(1) atoms are located in a square arrangement to occupy the four corners of the channels between four of the RE units (**Figure 5.2a**); the Na(2) or K(2) atoms are located directly under the F(1) site (**Figure 5.2b**). The SiO_4 tetrahedra are corner and edge shared to the rare earth polyhedra and exhibit an average Si-O bond distance of 1.628 Å. Selected bond distances are given in **Table 5.3**. Bond valence sums were calculated for the RE, Si, and Na/K elements and were found to match the expected RE^{3+}, Si^{4+}, and Na^+/K^+ oxidation states with ranges of 2.81 – 3.17 v.u. for RE, 0.69 – 0.99 v.u. for the Na/K sites, and 4.10 – 4.16 v.u. for Si.[5.27, 5.28]

Powder X-ray Diffraction

The calculated and experimental PXRD patterns for the polycrystalline solid state reactions of $Na_5RE_4F[SiO_4]_4$ (RE = Pr, Nd, Sm-Ho) are in good agreement. The Nd sample contained a small quantity of an SiO_2 impurity while the other rare earths contained 17.6 – 28.7 wt% of a known apatite phase that could not be physically

separated from the $Na_5RE_4F[SiO_4]_4$ (RE = Pr, Nd, Sm-Ho) powders. Powder X-ray diffraction patterns can be found in (**Figure 5.1**) and a table of the weight percent fractions are given in (**Table 5.1**).

Photoluminescence

Fluorescence data were collected on polycrystalline powders of $Na_5RE_4F[SiO_4]_4$ (RE = Eu, Gd, Tb). The room temperature data indicate intense emission peaks in the visible range for the terbium and europium analogues and intense emission in the ultra-violet range for the gadolinium analogue. Since it is known that the apatite impurities are only very weakly luminescent,[5.6] the intense luminescence originates with the title compounds. The emission scans of the title compounds were collected using an excitation wavelength of 248 nm for Eu, 240 nm for Gd, and 234 nm for Tb and the excitation scans were collected at an emission wavelength of 608 nm for Eu, 604 nm for Gd, and 537 nm for Tb, **Figures 5.3-5.5**, respectively. The maximum emission peaks in the Eu, Gd, and Tb spectra are consistent with the colors seen when exciting the samples under 365nm light as shown in **Figure 5.6**. In the emission spectrum for the Eu analogue, the maxima doublet peaks at 584 nm and 609 nm are expected to be caused by $^5D_0 \rightarrow {}^7F_1$ transition in the Eu^{3+} ion while the peak at 690 nm is likely caused by the $^5D_0 \rightarrow {}^7F_2$ transition. The maxima peak (408 nm) in the Gd analogue is expected to be a result of the $^6P_{7/2} \rightarrow {}^8S_{7/2}$ transition in the Gd^{3+} ion. Finally, the emission peaks for the Tb analogue are expected to be caused by the $^5D_4 \rightarrow {}^7F_6$ (481 nm), $^5D_4 \rightarrow {}^7F_5$ (537 nm), $^5D_4 \rightarrow {}^7F_4$ (578 nm), and $^5D_4 \rightarrow {}^7D_3$ (613 nm) transitions, respectively.[5.29]

Fluorescence Quantum Yield

Fluorescence quantum yield was measured on polycrystalline samples of $Na_5RE_4F[SiO_4]_4$ (RE = Eu, Gd, Tb). To determine a reliable quantum yield, data collections on three different samplings of each analogue were taken. After collection, quantum yield on each data set was determined using Fluoracle, the vendor supplied software. The averaged quantum yields were 5.0(1) % for $Na_5Eu_4F[SiO_4]_4$, 7.3(4) % for $Na_5Gd_4F[SiO_4]_4$, and 17.7(1) % for $Na_5Tb_4F[SiO_4]_4$. These quantum yields are lower than what is found in commercially available phosphors such as $Y_3Al_5O_{12}:Ce^{3+}$ (YAG: Ce) $M_2SiO_4:Eu^{2+}$ (M = Ba^{2+}, Sr^{2+}, Ca^{2+}) and $M_2Si_5N_8$ (M = Ca^{2+}, Sr^{2+}, Ba^{2+}) where the green silicate ($Ba_2SiO_4:Eu^{2+}$) has a quantum yield of 75 – 79 % compared to the Tb analogue presented here with a quantum yield of 17.7 %, and the red nitride ($M_2Si_5N_8$ (M = Ba^{2+}, Sr^{2+}, Ca^{2+}) has a quantum yield of 89 – 92 % compared to the Eu analogue presented here with a quantum yield of 5 %.[5.30] These quantum yields, while lower than those in commercially available phosphors, are nonetheless very encouraging. They are the first observation in these compositions that have not been optimized, suggesting that future improvements are likely and will be pursued in the future.

Second-Harmonic Generation

$Na_5RE_4F[SiO_4]_4$ (RE = Pr, Nd, Sm-Tm) and $K_5Pr_4F[SiO_4]_4$ crystallize in the space group *I* -4 (Crystal Class = *I* 4/*m*; Point group = -4). The space group and crystal class indicate that the compound is non-centrosymmetric, and materials belonging to this crystal class can exhibit second-harmonic generation (SHG) and circular dichroism.[5.31] Interestingly, materials in this class are neither chiral nor polar. Measurements demonstrate that all but the Nd compound of the $Na_5RE_4F[SiO_4]_4$ series exhibit SHG

behavior. The Nd analogue may test negative for SHG behavior due to the dark color of the sample, which could cause it to absorb at either 1064 nm or 532 nm. The other analogues are weakly SHG active, with the most intense being the Ho analogue, which exhibits an efficiency twice that of α-SiO_2.

Magnetism

Rare earth containing silicates have not been studied extensively for their magnetic properties, and many of those investigated are paramagnetic down to 2 K.[5.6, 5.32, 5.33] Some examples, such as $Dy_2Si_2O_7$ and $Er_2Si_2O_7$,[5.34] Er_2SiO_7,[5.35] and $Na_5Tb_4(OH)[SiO_4]_4$[5.26] have exhibited antiferromagnetic behavior at low temperatures ~2 K. Interestingly, two of the compositions prepared by us, $Na_5Tb_4F[SiO_4]_4$ and $Na_5Dy_4F[SiO_4]_4$, order antiferromagnetically at low temperatures.

The magnetic data of the $Na_5RE_4F[SiO_4]_4$ series can be found in **Table 5.4** and **Figure 5.7**. At elevated temperatures, only the Sm and Eu analogues of the $Na_5RE_4F[SiO_4]_4$ compositions do not follow Curie-Weiss behavior. The inverse susceptibilities were corrected to reflect the amount of RE^{3+} ion present in both the $Na_5RE_4F[SiO_4]_4$ and apatite secondary phase ($Pr_{4.67}(SiO_4)_3O$,[5.8] $Na_{0.5}Sm_{4.5}(SiO_4)_3O$,[5.9] $Eu_{9.34}(SiO_4)_6O_2$,[5.6] $Na_{1.64}Gd_{8.36}(SiO_4)_6O_{0.72}F_{1.28}$,[5.6] $Tb_{4.67}(SiO_4)_3O$,[5.9] $Na_{0.5}Dy_{4.5}(SiO_4)_3O$,[5.9] and $Na_{1.135}Ho_{3.865}(SiO_4)_3O_{0.36}$,[5.10] respectively), the weight percent of which was determined by whole pattern fitting of the powder X-ray diffraction data.

Since changes in the apatite structure, such as presence or absence of fluorine on the *X* site, does not cause noticeable shifts in the PXRD data but does alter the amount of lanthanide ion present per mol of apatite (which affects the magnetic moments), two different calculations were done for each analogue to determine the ranges of the

magnetic moments. With the elements present in these reactions, three compositions of apatite were possible based on apatite literature:[6] $RE_{9.34}(SiO_4)_6$, $NaRE_9(SiO_4)_6O_2$, and $Na_{1.5}RE_{8.5}(SiO_4)_6OF$. To find the possible magnetic moment range of each sample, the lower ($Na_{1.5}RE_{8.5}(SiO_4)_6OF$) and upper ($RE_{9.34}(SiO_4)_6O_2$) limits of lanthanide concentration in apatites, with 8.5 and 9.34 mol RE per F.U., respectively, were used to calculate the ranges of the magnetic moments with a sample calculation shown in **Example 5.1**. The high temperature region (50-300 K) of the inverse susceptibility data were fit to the Curie-Weiss law to yield effective moments. In all cases, the range obtained from the two apatite compositions ($Na_{1.5}RE_{8.5}(SiO_4)_6OF$ and $RE_{9.34}(SiO_4)_6O_2$) created an uncertainty of less than 1 % in the measured effective moment, and, for this reason the average effective moment is reported. The effective moments are listed in **Table 5.4**, and are in good agreement with the calculated moments for RE^{3+} cations.

In the Tb and Dy analogues, **Figure 5.8**, a downturn in the susceptibilities is observed at T = 2.2 K and 2.4 K, respectively, which indicates the presence of antiferromagnetic ordering. In the isostructural $Na_5RE_4(OH)[SiO_4]_4$ RE = Pr, Nd, Sm – Yb, Y silicate family,[5.26] only Tb was found to exhibit AF ordering, while in this study, Dy also exhibits AF ordering. This could indicate that, as mentioned,[5.26] the AF ordering may occur in all compositions, albeit below our low temperature limit of 2 K.

The Eu analogue (**Figure 5.8**) does not exhibit Curie-Weiss behavior, but instead exhibits Van Vleck paramagnetism. Van Vleck paramagnetism is a form of paramagnetism that is independent of temperature and occurs in Eu(III) and Sm(III) samples below ~100 K. As seen in the temperature dependence of the susceptibility data, below about 40 K the slope of the susceptibility has a drastic positive increase, unlike the

magnetism of the other rare earth elements. Because of the Van Vleck paramagnetism, which is also observed in the Sm analogue, the effective moments of the Eu and Sm analogues are reported as the $2.827(\chi_m T)^{1/2}$ values at 300 K. The moments for both analogues agree with previously reported values.[5.36]

Conclusion

Flux crystal growth yielded new compositions of $Na_5RE_4F[SiO_4]_4$ (RE = Pr, Nd, Sm-Tm) and $K_5Pr_4F[SiO_4]_4$. Magnetic measurements on $Na_5RE_4F[SiO_4]_4$ (Tb, Dy) analogues show downturns at T = 2.2 K and 2.4 K, respectively, which indicates antiferromagnetic ordering at a T_N below 2 K. The $Na_5RE_4F[SiO_4]_4$ (RE = Nd, Pr, Sm-Ho) were tested for SHG due to their non-centrosymmetric space group *I*-4 and RE = Pr, Sm-Ho were found to be weakly SHG active. It is assumed that the Nd was not found to be SHG active due to its dark color. $Na_5RE_4F[SiO_4]_4$ (RE = Eu, Gd, Tb) exhibit strong luminescence. Fluorescence quantum yield measurements indicated yields of 5 – 17 % for the Eu, Gd, and Tb analogues. These quantum yields imply doping studies could improve the fluorescence quantum yield, possibly to current commercial standards.

References

5.1 Bugaris, D. E.; zur Loye, H.-C. *Angew. Chem. Int. Ed.* **2012**, *51*, 3780-3811.
5.2 Napper, J. D.; Layland, R. C.; Smith, M. D.; zur Loye, H.-C. *J. Chem. Crystallogr.* **2004**, *34*, 347-351.
5.3 Vidican, I.; Smith, M. D.; zur Loye, H.-C. *J. Solid State Chem.* **2003**, *170*, 203-210.
5.4 Chiang, P.-Y.; Lin, T.-W.; Dai, J.-H.; Chang, B. C.; Lii, K.-H. *Inorg. Chem.* **2007**, *46*, 3619-3622.
5.5 Latshaw, A. M.; Smith, M. D.; zur Loye, H.-C. *Solid State Sci.* **2014**, *35*, 28-32.
5.6 Latshaw, A. M.; Hughey, K. D.; Smith, M. D.; Yeon, J.; zur Loye, H.-C. *Inorg. Chem.* **2015**, *54*, 876-884.
5.7 Schäfer, M. C.; Schleid, T. *Z. Anorg. Allg. Chem.* **2010**, *636*, 2069.
5.8 Kolitsch, U.; Seifert, H. J.; Aldinger, F. *J. Solid State Chem.* **1995**, *120*, 38-42.
5.9 Felsche, J. *J. Solid State Chem.* **1972**, *5*, 266-275.
5.10 Rosales, I.; Orozco, E.; Bucio, L.; Fuentes, M. E.; Fuentes, L. *Acta Cryst.* **2009**, *E65*, 33.
5.11 SMART Version 5.631, SAINT+ Version 6.45 and SADABS Version 2.10, Bruker Analytical X-ray Systems, Inc., Madison, Wisconsin, USA, 2003.
5.12 Hübschle, C. B., Sheldrick, G. M., Bittrich, B. *J. Appl. Cryst.* **2011**, *44*, 1281-1284.
5.13 Sheldrick, G. M. *Acta Crystallogr.* **2008**, *A64*, 112-122.
5.14 LePage, Y. *J. Appl. Cryst.* **1987**, *20*, 264-269.
5.15 PLATON, A Multipurpose Crystallographic Tool, Utrecht University, Utrecht, The Netherlands, Spek, A. L. 1998.
5.16 Spek, A. L. *J. Appl. Cryst.* **1988**, *21*, 578-579.
5.17 Spek, A. L. *Acta Crystallogr., A* **1990**, *46*, C34.
5.18 Kurtz, S. K.; Perry, T. T. *J. Appl. Phys.* **1968**, *39*, 3798-3813.
5.19 Ok, K. M.; Chi, E. O.; Halasyamani, P. S. *Chem. Soc. Rev.* **2006**, *35*, 710-717.
5.20 Morrison, G.; zur Loye, H.-C. *J. Solid State Chem.* **2015**, *221*, 334-337.
5.21 White, T.; Ferraris, C.; Kim, J.; Madhavi, S. *Rev. Mineral Geochem.* **2005**, *57*, 307-401.
5.22 White, T. J.; ZhiLi, D. *Acta. Cryst.* **2003**, *B59*, 1-16.
5.23 Malinovskii, Y. A. *Dokl. Akad. Nauk SSSR* **1984**, *274*, 75-78.
5.24 Merinov, B. V.; Maksimov, B. A.; Ilyukhin, V. V.; Belov, N. V. *Dokl. Akad. Nauk SSSR* **1980**, *255*, 348-351.
5.25 Hughey, K.; Yeon, J.; zur Loye, H.-C. *J. Chem. Crystallogr.* **2014**, *44*, 376-379.
5.26 Latshaw, A. M.; Chance, W. M.; Morrison, G.; Smith, M. D.; Yeon, J.; zur Loye, H.-C. *CrystEngComm.* **2015**, *17*, 4691-4698.
5.27 Brese, N. E.; O'Keeffe. *Acta Crystallogr., Sect. B:* **1991**, *47*, 192-197.
5.28 Brown, I. D.; Altermatt, D. *Acta Crystallogr., Sect. B:* **1985**, *41*, 244-247.
5.29 Blasse, G.; Grabmaier, B. C. *Luminescent Materials*; Springer-Verlag: Berlin, 1994;
5.30 Gorrotxategi, P.; Consonni, M.; Gasse, A. *J. Solid State Light.* **2015**, *2*,
5.31 Halasyamani, P. S.; Poeppelmeier, K. R. *Chem. Mater.* **1998**, *10*, 2753-2769.
5.32 Chen, P. *J. Alloys Compd.* **2015**, *622*, 859-864.
5.33 Emirdag-Eanes, M.; Pennington, W. T.; Kolis, J. W. *J. Alloys Compd.* **2004**, *366*, 76-80.
5.34 Ueda, S.; Wakeshima, M.; Hinatsu, Y. *Kidorui* **2013**, *62*, 166-167.

5.35 Belov, K. P.; Toropov, N. A.; Bondar, I. A.; Mitina, L. P. *Izv. Akad. Nauk SSSR, Neorg. Mater.* **1969**, *5*, 565-568.
5.36 Blundell, S. *Magnetism in Condensed Matter*; Oxford University Press: Oxford, 2010.

Table 5.1. Weight percent of desired product to apatite or SiO_2 for $Na_5RE_4F[SiO_4]_4$ (RE = Pr, Nd, Sm-Ho) based on PXRD data.

	Weight Percent (%)		
Composition	$Na_5RE_4F[SiO_4]_4$	Apatite	SiO_2
$Na_5Pr_4F[SiO_4]_4$	71.2	28.7	-
$Na_5Nd_4F[SiO_4]_4$	96.6	-	3.4
$Na_5Sm_4F[SiO_4]_4$	82.2	17.8	-
$Na_5Eu_4F[SiO_4]_4$	79.0	21.0	-
$Na_5Gd_4F[SiO_4]_4$	79.4	20.6	-
$Na_5Tb_4F[SiO_4]_4$	80.3	19.7	-
$Na_5Dy_4F[SiO_4]_4$	79.5	20.5	-
$Na_5Ho_4F[SiO_4]_4$	82.4	17.6	-

Table 5.2. Crystallographic data for $Na_5RE_4F[SiO_4]_4$ (RE = Pr, Nd, Sm-Tm) and $K_5Pr_4F[SiO_4]_4$.

Formula	$Na_5Pr_4F[SiO_4]_4$	$Na_5Nd_4F[SiO_4]_4$	$Na_5Sm_4F[SiO_4]_4$	$Na_5Eu_4F[SiO_4]_4$
Formula weight	1065.95	1079.27	1103.71	1110.15
Crystal system	Tetragonal	Tetragonal	Tetragonal	Tetragonal
Space group	*I -4*	*I -4*	*I -4*	*I -4*
a (Å)	12.0109(2)	11.9435(2)	11.8246(2)	11.7718(3)
c (Å)	5.4620(2)	5.45910(10)	5.44190(10)	5.4349(3)
V (Å^3)	787.96(3)	778.73(2)	760.89(2)	753.14(5)
Z	2	2	2	2
Density (g/cm^3)	4.493	4.603	4.817	4.895
Absorption coefficient (mm^{-1})	12.689	13.661	15.769	16.993
Crystal size (mm^3)	0.12 × 0.06 × 0.06	0.16 × 0.12 × 0.08	0.12 × 0.12 × 0.12	0.05 × 0.05 × 0.03
2θ range (°)	4.80 to 56.52	4.82 to 56.52	4.88 to 56.54	4.90 to 56.48
reflections collected	5445	5339	5260	5226
data/restraints/parameters	982 / 0 / 70	973 / 0 / 70	953 / 0 / 70	941 / 0 / 69
R (int)	0.0197	0.0132	0.0164	0.0202
GOF (F^2)	1.106	1.125	1.085	1.100
R indices (all data)	R_1 = 0.0121 wR_2 = 0.0325	R_1 = 0.0097 wR_2 = 0.0260	R_1 = 0.0115 wR_2 = 0.0296	R_1 = 0.0177 wR_2 = 0.0430

Table 5.2. (Continued)

Formula	$Na_5Gd_4F[SiO_4]_4$	$Na_5Tb_4F[SiO_4]_4$	$Na_5Dy_4F[SiO_4]_4$	$Na_5Ho_4F[SiO_4]_4$
Formula weight	1131.31	1137.99	1152.31	1162.03
Crystal system	Tetragonal	Tetragonal	Tetragonal	Tetragonal
Space group	*I -4*	*I -4*	*I -4*	*I -4*
a (Å)	11.7244(2)	11.6746(2)	11.6243(2)	11.5844(2)
c (Å)	5.42960(10)	5.4113(2)	5.40420(10)	5.39570(10)
V (Å^3)	746.36(2)	737.54(3)	730.24(2)	724.09(2)
Z	2	2	2	2
Density (g/cm^3)	5.034	5.124	5.241	5.330
Absorption coefficient (mm^{-1})	18.112	19.522	20.813	22.205
Crystal size (mm^3)	0.08 x 0.08 x 0.04	0.14 × 0.04 × 0.04	0.19 × 0.04 × 0.04	0.16 x 0.06 x 0.04
2θ range (°)	4.92 to 56.52	4.94 to 56.52	4.96 to 56.50	4.98 to 56.60
reflections collected	5116	5117	5025	4974
data/restraints/parameters	925 / 0 / 69	923 / 0 / 70	909 / 0 / 70	908 / 0 / 70
R (int)	0.0162	0.0209	0.0202	0.0186
GOF (F^2)	1.166	1.065	1.078	1.144
R indices (all data)	R_1 = 0.0132 wR_2 = 0.0329	R_1 = 0.0169 wR_2 = 0.0422	R_1 = 0.0138 wR_2 = 0.0347	R_1 = 0.0133 wR_2 = 0.0348

Table 5.2. (Continued)

Formula	$Na_5Er_4F[SiO_4]_4$	$Na_5Tm_4F[SiO_4]_4$	$K_5Pr_4F[SiO_4]_4$
Formula weight	1171.35	1178.04	1146.50
Crystal system	Tetragonal	Tetragonal	Tetragonal
Space group	*I -4*	*I -4*	*I -4*
a (Å)	11.5410(2)	11.5094(2)	12.3745(2)
c (Å)	5.3850(2)	5.37000(10)	5.5011(2)
V (Å^3)	717.25(3)	711.34(2)	842.37(4)
Z	2	2	2
Density (g/cm^3)	5.424	5.500	4.520
Absorption coefficient (mm^{-1})	23.755	25.302	12.978
Crystal size (mm^3)	0.16 x 0.12 x 0.08	0.12 x 0.08 x 0.08	0.14 x 0.08 x 0.04
2θ range (°)	5.00 to 56.52	5.00 to 56.56	4.66 to 56.56
reflections collected	4916	4864	5796
data/restraints/parameters	892 / 0 / 70	885 / 0 / 70	1052 / 0 / 70
R (int)	0.0170	0.0187	0.0187
GOF (F^2)	1.133	1.159	1.128
R indices (all data)	R_1 = 0.0124	R_1 = 0.0128	R_1 = 0.0101
	wR_2 = 0.0323	wR_2 = 0.0337	wR_2 = 0.0253

Table 5.3. RE-O Bond Distances (in Å) for $Na_5RE_4F[SiO_4]_4$ (RE = Pr, Nd, Sm-Tm) and $K_5Pr_4F[SiO_4]_4$.

	$Na_5Pr_4F[SiO_4]_4$	$Na_5Nd_4F[SiO_4]_4$	$Na_5Sm_4F[SiO_4]_4$	$Na_5Eu_4F[SiO_4]_4$	$Na_5Gd_4F[SiO_4]_4$	$Na_5Tb_4F[SiO_4]_4$
RE(1) – O(3)	2.264(5)	2.346(2)	2.317(3)	2.299(4)	2.307(3)	2.288(4)
RE(1) – O(2)	2.318(5)	2.383(2)	2.362(3)	2.358(4)	2.339(3)	2.327(4)
RE(1) – O(4)	2.358(5)	2.4183(19)	2.394(2)	2.379(4)	2.375(3)	2.369(4)
RE(1) – O(2)	2.360(5)	2.432(2)	2.405(3)	2.397(4)	2.384(3)	2.372(4)
RE(1) – O(3)	2.360(5)	2.426(2)	2.400(3)	2.388(4)	2.373(3)	2.357(4)
RE(1) – O(1)	2.413(4)	2.4977(18)	2.470(2)	2.454(3)	2.442(3)	2.431(4)
RE(1) – F(1)	2.5176(3)	2.61239(13)	2.57628(16)	2.5615(2)	2.54718(18)	2.5325(2)
RE(1) – O(4)	2.538(5)	2.645(2)	2.599(3)	2.581(4)	2.562(3)	2.550(4)
	$Na_5Dy_4F[SiO_4]_4$	$Na_5Ho_4F[SiO_4]_4$	$Na_5Er_4F[SiO_4]_4$	$Na_5Tm_4F[SiO_4]_4$	$K_5Pr_4F[SiO_4]_4$	
RE(1) – O(3)	2.278(3)	2.264(3)	2.255(3)	2.237(4)	2.416(2)	
RE(1) – O(2)	2.319(3)	2.316(3)	2.303(3)	2.297(3)	2.461(2)	
RE(1) – O(4)	2.361(3)	2.352(3)	2.351(3)	2.335(3)	2.5521(18)	
RE(1) – O(2)	2.361(3)	2.350(3)	2.334(3)	2.324(4)	2.479(2)	
RE(1) – O(3)	2.347(3)	2.336(3)	2.333(3)	2.319(4)	2.510(2)	
RE(1) – O(1)	2.423(3)	2.407(3)	2.401(3)	2.392(3)	2.4620(17)	
RE(1) – F(1)	2.51774(18)	2.50744(17)	2.49443(17)	2.48452(19)	2.70734(13)	
RE(1) – O(4)	2.528(3)	2.521(3)	2.506(3)	2.506(4)	2.616(2)	

Table 5.4. Experimental magnetic moments (μ_{eff}) compared to calculated moments (μ_{calc}) for $Na_5RE_4F[SiO_4]_4$ (RE = Pr, Nd, Sm-Ho).

Compound	Fit Range (K)	T_N (K)	θ (K)	μ_{eff} (μ_B/RE)	μ_{calc} (μ_B/RE)
$Na_5Pr_4F[SiO_4]_4$	100 - 300	-	-35.4	3.5[a]	3.58
$Na_5Nd_4F[SiO_4]_4$	100 - 300	-	-43.4	3.71	3.62
$Na_5Sm_4F[SiO_4]_4$	300	-	-	1.7[a]	1.74[b]
$Na_5Eu_4F[SiO_4]_4$	300	-	-	3.3[a]	3.4[b]
$Na_5Gd_4F[SiO_4]_4$	50 – 300	-	-1.3	7.7[a]	7.94
$Na_5Tb_4F[SiO_4]_4$	100 – 300	< 2	-7.5	9.7[a]	9.72
$Na_5Dy_4F[SiO_4]_4$	100 – 300	< 2	-7.8	10.5[a]	10.65
$Na_5Ho_4F[SiO_4]_4$	50 – 300	-	-6.4	10.5[a]	10.61

[a] μ_{eff} values are approximated based on apatite calculations.
[b] μ_{calc} values reported due to the large difference between μ_{obs} and μ_{calc}. μ_{obs} values[36] are from paramagnetic salts.

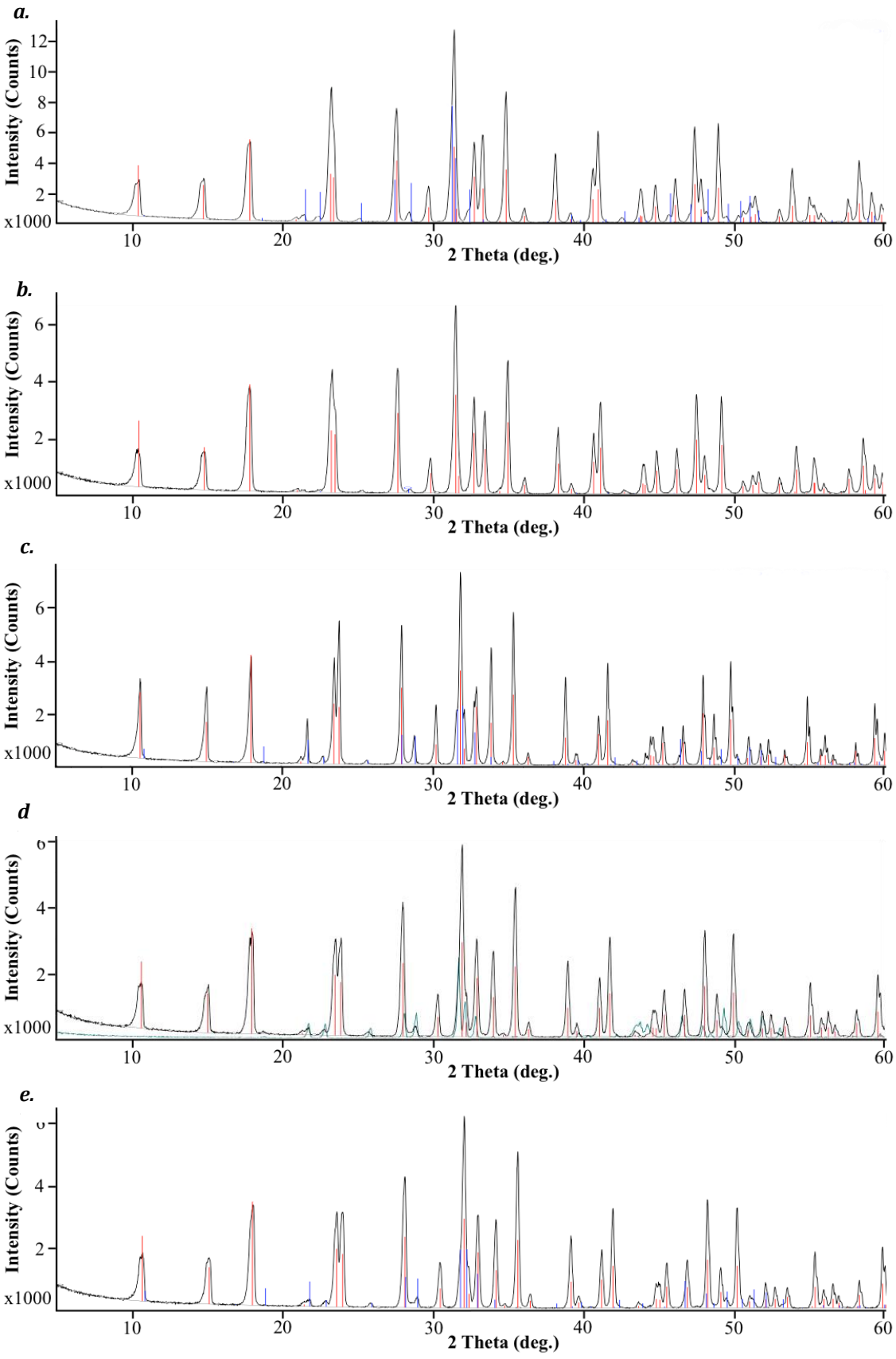

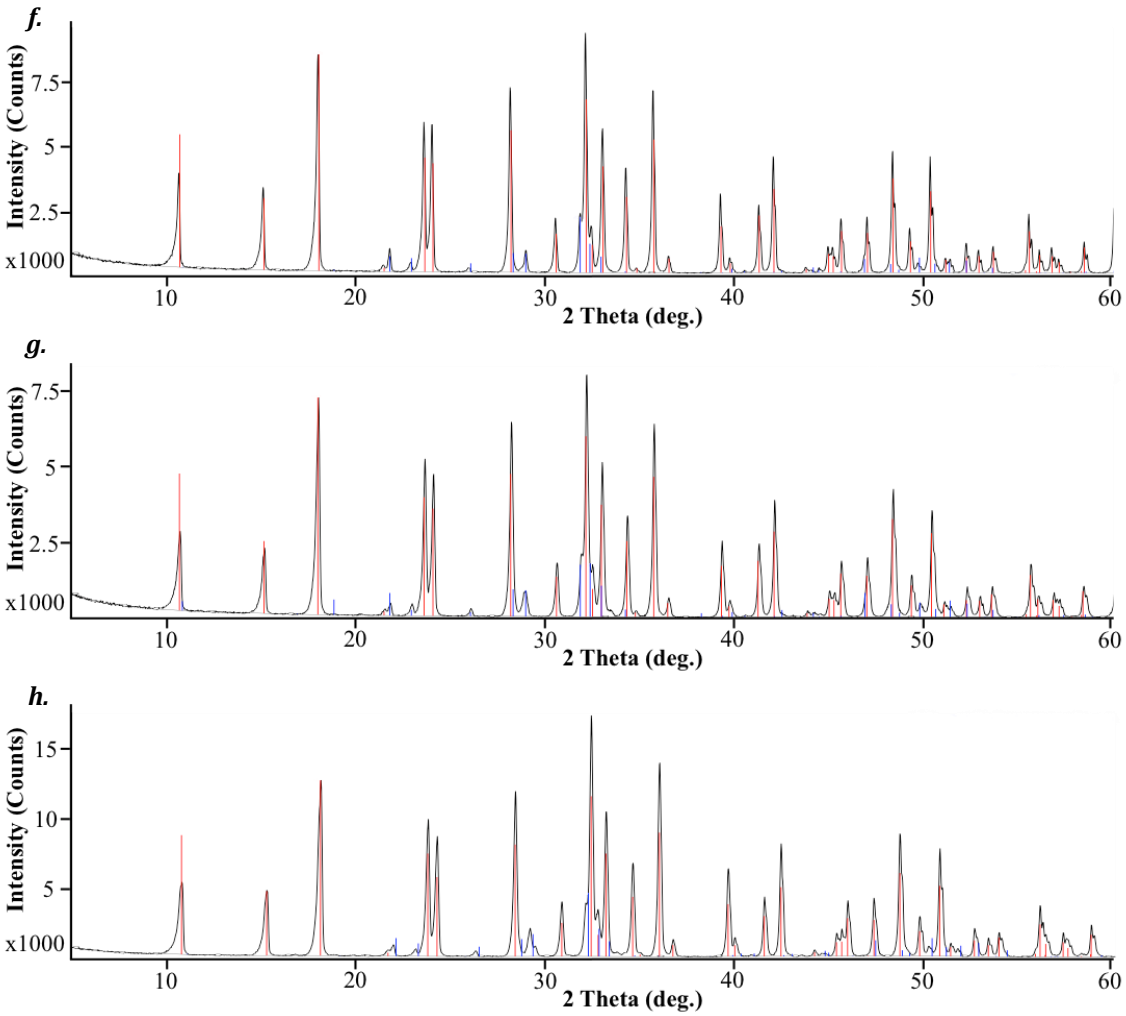

Figure 5.1. PXRD patterns of $Na_5RE_4F[SiO_4]_4$ where RE = Pr, Nd, Sm, Eu, Gd, Tb, Dy, and Ho, respectively. The cif file overlay of the $Na_5RE_4F[SiO_4]_4$ phases are shown in red and the impurity phases of $Pr_{4.67}(SiO_4)_3O$,[5.21] SiO_2, $Na_{0.5}Sm_{4.5}(SiO_4)_3O$,[5.22] $Eu_{9.34}(SiO_4)_6O_2$,[5.6] $Na_{1.64}Gd_{8.36}(SiO_4)_6O_{0.72}F_{1.28}$,[5.6] $Tb_{4.67}(SiO_4)_3O$,[5.22] $Na_{0.5}Dy_{4.5}(SiO_4)_3O$,[5.22] and $Na_{1.135}Ho_{3.865}(SiO_4)_3O$,[5.23] respectively, are shown in blue.

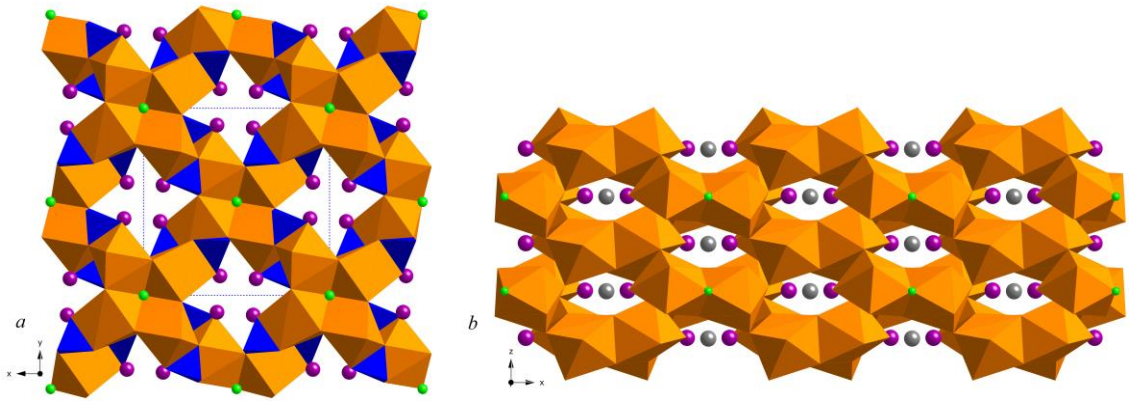

Figure 5.2. Structural representation of $Na_5Eu_4F[SiO_4]_4$ where *a* shows the overall view down the *c* axis and *b* indicates the structure down the *b* axis. Na(1) or K(1) atoms are shown as purple spheres Na(2) or K(2) as gray spheres, RE polyhedra are shown in orange, silicon tetrahedra shown in blue, F shown in green, and oxygens are omitted for clarity.

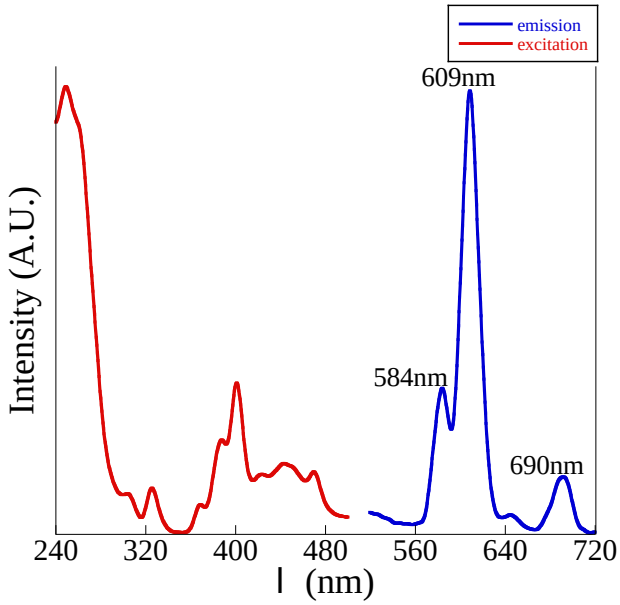

Figure 5.3. Fluorescence spectra for $Na_5Eu_4F[SiO_4]_4$ where the emission data was collected at an excitation wavelength of 248 nm and the excitation data was collected at an emission wavelength of 608 nm.

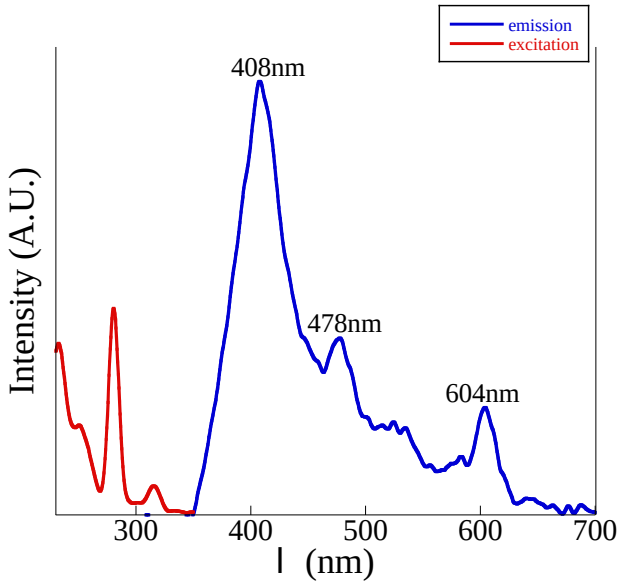

Figure 5.4. Fluorescence spectra of $Na_5Gd_4F[SiO_4]_4$ where the emission data were collected at an excitation λ of 240 nm and the excitation data were collected at an emission λ of 604 nm.

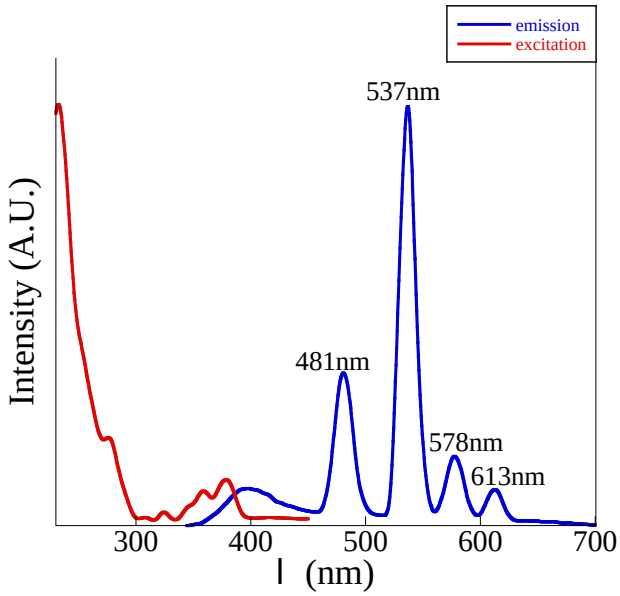

Figure 5.5. Fluorescence spectra of $Na_5Tb_4F[SiO_4]_4$ where the emission data were collected at an excitation wavelength of 234 nm and the excitation data were collected at an emission wavelength of 537 nm.

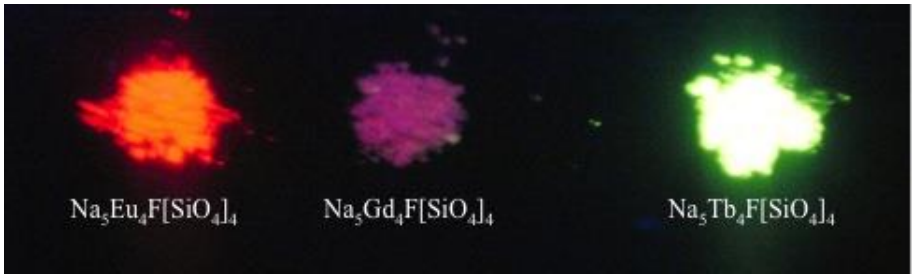

Figure 5.6. Image of room temperature emission under an excitation wavelength of 365 nm.

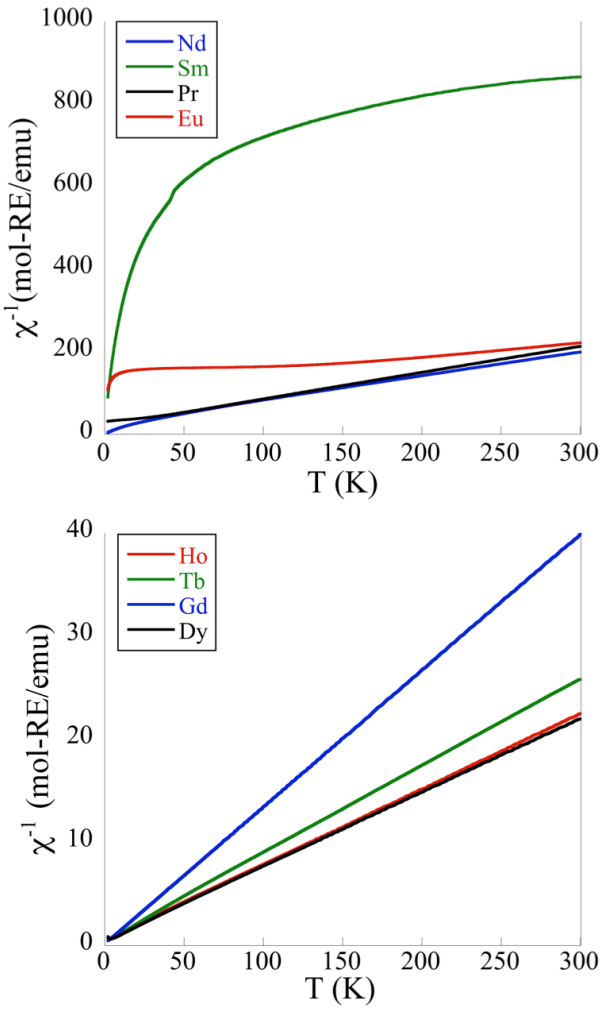

Figure 5.7. Inverse susceptibilities as a function of temperature of $Na_5RE_4F[SiO_4]_4$ (RE = Pr, Nd, Sm-Ho).

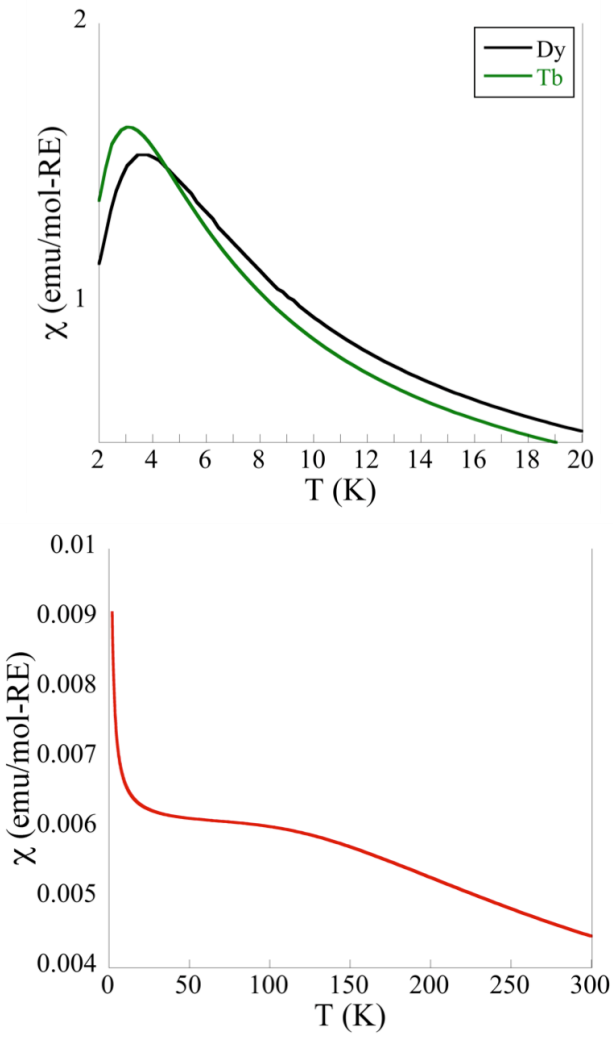

Figure 5.8. Temperature dependence of the magnetic susceptibilities of $Na_5Dy_4F[SiO_4]_4$ and $Na_5Tb_4F[SiO_4]_4$ analogues (top), indicating the antiferromagnetic ordering at 2.4 K and 2.2 K, respectively and $Na_5Eu_4F[SiO_4]_4$ (bottom) to show the Van Vleck paramagnetism.

Example 5.1. Example of how the magnetic moment was calculated.

Mass of Ho sample: 0.03093g

Weight % (from PXRD):
$Na_5Ho_4F[SiO_4]_4$ = 82.4%
Apatite = 17.6%

Mass of each component:
$Na_5Ho_4F[SiO_4]_4$ = 0.02549g
Apatite = 0.0054g

If apatite is $Na_{1.5}Ho_{8.5}(SiO_4)_6OF$ (low RE concentration):
mol calculations:

$$0.0255\ g\ Na_5Ho_4F[SiO_4]_4 * \frac{1\ mol}{1161.9\ g\ Na_5Ho_4F[SiO_4]_4} = 2.19E^{-5}\ mol\ Na_5Ho_4F[SiO_4]_4$$

$$0.0054\ g\ Na_{1.5}Ho_{8.5}(SiO_4)_6OF * \frac{1\ mol}{2023.7\ g\ Na_{1.5}Ho_{8.5}(SiO_4)_6OF} = 2.69E^{-6}\ mol\ Na_{1.5}Ho_{8.5}(SiO_4)_6OF$$

mol RE calculations:

$$2.19E^{-5}\ mol\ Na_5Ho_4F[SiO_4]_4 * \frac{4\ mol\ Ho}{1\ mol\ Na_5Ho_4F[SiO_4]_4} = 8.76E^{-5}\ mol\ Ho$$

$$2.69E^{-6}\ mol\ Na_{1.5}Ho_{8.5}(SiO_4)_6OF * \frac{8.5\ mol\ Ho}{1\ mol\ Na_{1.5}Ho_{8.5}(SiO_4)_6OF} = 2.29E^{-5}\ mol\ Ho$$

$Na_5Ho_4F[SiO_4]_4$ and $Na_{1.5}Ho_{8.5}(SiO_4)_6OF$ calculation:

$$8.76E^{-5}\ mol\ Ho + 2.29E^{-5}\ mol\ Ho = 1.11E^{-4}\ mol\ Ho$$

Magnetic susceptibility and inverse susceptibility plot:

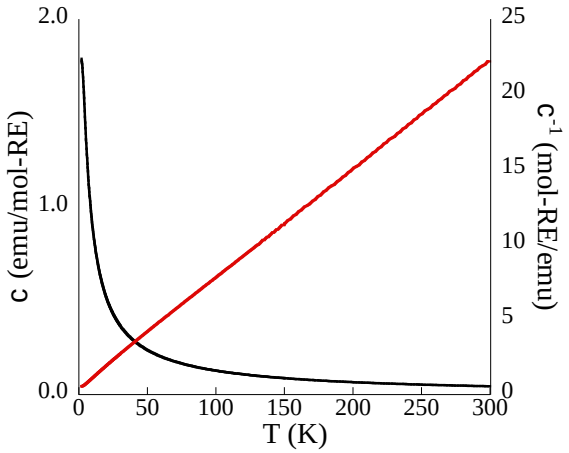

Magnetic susceptibility (black) and inverse susceptibility (red) of the holmium sample when apatite is $Na_{1.5}Ho_{8.5}(SiO_4)_6OF$.

Fitting the inverse susceptibility with the Curie Weiss law from 50-300 K gives an effective magnetic moment of 10.52 μ_B/Ho.

If apatite is $Ho_{9.34}(SiO_4)_6O_2$ (high RE concentration):

mol calculations:

$$0.0255\ g\ Na_5Ho_4F[SiO_4]_4 * \frac{1\ mol}{1161.9\ g\ Na_5Ho_4F[SiO_4]_4} = 2.19E^{-5}\ mol\ Na_5Ho_4F[SiO_4]_4$$

$$0.0054\ g\ Ho_{9.34}(SiO_4)_6O_2 * \frac{1\ mol}{2124.7\ g\ Ho_{9.34}(SiO_4)_6O_2} = 2.56E^{-6}\ mol\ Ho_{9.34}(SiO_4)_6O_2$$

mol RE calculations:

$$2.19E^{-5}\ mol\ Na_5Ho_4F[SiO_4]_4 * \frac{4\ mol\ Ho}{1\ mol\ Na_5Ho_4F[SiO_4]_4} = 8.76E^{-5}\ mol\ Ho$$

$$2.56E^{-6}\ mol\ Ho_{9.34}(SiO_4)_6O_2 * \frac{9.34\ mol\ Ho}{1\ mol\ Ho_{9.34}(SiO_4)_6O_2} = 2.39E^{-5}\ mol\ Ho$$

$Na_5Ho_4F[SiO_4]_4$ and $Ho_{9.34}(SiO_4)_6O_2$ calculation:

$$8.76E^{-5}\ mol\ Ho + 2.39E^{-5}\ mol\ Ho = 1.12E^{-4}\ mol\ Ho$$

Magnetic susceptibility and inverse susceptibility plot:

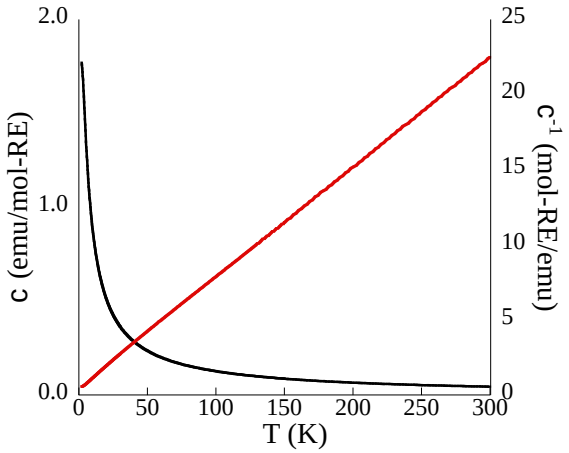

Magnetic susceptibility (black) and inverse susceptibility (red) of the holmium sample when apatite is $Ho_{9.34}(SiO_4)_6O_2$.

Fitting the inverse susceptibility with the Curie Weiss law from 50-300 K gives an effective magnetic moment of 10.48 μ_B/Ho.

Chapter 6

$A_5RE_4X[TO_4]_4$ Crystal Growth. Fluoride Flux Synthesis of $Na_5Ln_4F[GeO_4]_4$ (*Ln* = Pr, Nd), the First Quaternary Germanate Oxyfluorides*

*Latshaw, A. M.; Wilkins, B. O.; Morrison, G.; Smith, M. D.; zur Loye, H.-C. *J. Solid State Chem.*, **2016**, *239*, 200-203.

Introduction

Flux crystal growth is a versatile technique used for exploratory research,[6.1] where typically the flux is a crucial part of the reaction. Throughout the literature, the use of different fluxes or conditions has been observed to yield different products, highlighting the importance of choosing an appropriate flux.[6.2, 6.3] Fluoride fluxes have been demonstrated to readily dissolve starting material oxides, including rare earth oxides, silicon dioxide, and germanium oxide. Since it is known that rare earth silicate oxides and oxyfluorides have been grown out of alkali fluoride fluxes, these fluxes represent good choices when trying to grow new rare earth tetragen oxyfluorides.[6.2, 6.4-6.8]

The previously reported silicon analogues of the title compounds, $Na_5RE_4(OH)[SiO_4]_4$ (RE = Pr, Nd, Sm, Eu, Tb-Yb, Y) and $Na_5RE_4F[SiO_4]_4$ (RE = Pr, Nd, Sm-Tm), were studied for their magnetic, luminescent, and SHG properties.[6.4, 6.6] It was determined that in the oxyhydroxide analogues, the Tb analogue ordered antiferromagnetically, the Eu, Gd, and Tb members luminesce with fluorescence quantum yields from 2 – 21 %, and second harmonic generation (SHG) was not observed. In the oxyfluoride analogues, the Tb and Dy analogues were found to be antiferromagnetic, the Eu, Gd, and Tb members were found to be luminescent with fluorescence quantum yields from 5 – 17 %, and all but the Nd member were found to exhibit weak SHG. It is unknown if changing the tetragen changes the properties, however, with magnetic ordering occurring below 3 K, weak SHG, and fluorescence quantum yields below 25 % seen for the silicate analogues, synthesizing the germanate analogues is clearly of interest.

Various rare earth containing germanates have been found to exhibit magnetic properties, luminescence, and display ionic conductivity.[6.9-6.13] And yet, in spite of these properties, rare earth containing germanates have been studied far less extensively than the other tetragen family of rare earth containing silicates. In fact, $Na_5Pr_4F[GeO_4]_4$ and $Na_5Nd_4F[GeO_4]_4$ are the first quaternary germanium oxyfluorides that contain a rare earth element and either an alkali or alkaline earth element. This work reports only the second example of a germanium analogue from the $A_5RE_4X[TO_4]_4$ (A = Na, K; RE = rare earth, X = F, OH; T = Si, Ge) family. The $A_5RE_4X[TO_4]_4$ family crystallizes in the noncentrosymmetric tetragonal space group *I*-4.[6.4-6.6, 6.14-6.17]

Experimental Section

Synthesis

Crystals of $Na_5Ln_4F[GeO_4]_4$ (Ln = Pr, Nd) were grown via a sodium fluoride, sodium chloride eutectic flux growth. Ln_2O_3 (1 mmol), where Pr_2O_3 was reduced from Pr_6O_{11} (99.9 %; Alfa Aesar) and Nd_2O_3 (99.9 % Acros Organics) was used as received, Na_2CO_3 (1 mmol; ACS grade, Fisher Scientific), and GeO_2 (2 mmol; 99.98 %, Alfa Aesar) were loaded into a silver crucible and a eutectic flux mixture of NaF (2.81 g; 99 % min, Alfa Aesar) and NaCl (1.93 g; ACS grade, Fisher Scientific) were loaded on top of the reactants. The crucible was then loosely fitted with a silver lid and placed in a programmable furnace that was set to ramp to 800 °C where it dwelled for 24 h before being programmed to slow cool to 600 °C at a rate of 3 °C/h. After reaching 600 °C, the furnace was shut off. To isolate the crystals, the reactions were sonicated in water and the crystals were collected by vacuum filtration. $Na_5Ln_4F[GeO_4]_4$ (Ln = Pr, Nd) was determined to be the major product by powder X-ray diffraction analysis, with a small

amount GeO_2 (> 5 %) found in $Na_5Pr_4F[GeO_4]_4$ and Nd_2O_3 (approx. 6 % by JADE software analysis) found in $Na_5Nd_4F[GeO_4]_4$.

Polycrystalline samples of $Na_5Ln_4F[GeO_4]_4$ (Ln = Pr, Nd) were prepared using a solid state method to obtain phase pure samples for magnetic measurements. 1 mmol of Pr_2O_3 (reduced from Pr_6O_{11} and stored under a desiccator or Nd_2O_3 (prefired at 1000 °C for 12 h), 1 mmol Na_2CO_3 (ground and dried overnight at 100 °C), 0.5 mmol NaF (ground and dried overnight at 100 °C), and 2 mmol GeO_2 (ground and dried overnight at 100 °C) were weighed out and ground together for 30 minutes to promote intimate mixing. The sample was then pressed into a pellet and loaded into a copper tube that was crimped at both ends to avoid fluoride loss. The crimped copper tube was loaded into a flow-through furnace that was purged with N_2 gas. The reactions were then calcined at 600 °C for 10 h before ramping to 900 °C and dwelling there for 24 h. After 24 h at 900 °C the furnace was shut off and allowed to reach room temperature. The reactions were ground and characterized by powder X-ray diffraction and found to be phase pure.

Single Crystal X-ray Diffraction

X-ray intensity data were collected on a colorless prismatic crystal of $Na_5Pr_4F[GeO_4]_4$ and a blue-purple plate crystal of $Na_5Nd_4F[GeO_4]_4$ at 300(2) and 293(2) K, respectively, using a Bruker D8 QUEST diffractometer equipped with a PHOTON 100 CMOS area detector and an Incoatec microfocus source (Mo Kα radiation, λ = 0.71073 Å),[6.18] and a Bruker SMART APEX CCD diffractometer (Mo Kα radiation, λ = 0.71073 Å), respectively.[6.19] The data collections covered 100 % of reciprocal space to $2\theta_{max}$ = 75.66 ° and 56.6 °, with R_{int} = 0.034 and 0.0425 after absorption corrections. The raw area detector frames were reduced and corrected for absorption effects using the

SAINT+ and SADABS programs.[6.19] Final unit cell parameters were determined by least-squares refinement of 9889 and 3488 reflections from each data set. Difference Fourier calculations and full-matrix least squares refinement against F^2 of the structural model were performed with SHELXL-2014/1[6.20] using OLEX2.[6.21] Further details of the crystal structure investigation can be obtained from the Fachinformationszentrum Karlsruhe, 76344 Eggenstein-Leopoldshafen, Germany (fax:+497247808666; e-mail: crystdata@fiz-karlsruhe.de) on quoting the depository numbers 431182 (Pr) and 430347 (Nd).

Magnetic Property Measurements

The magnetic properties of $Na_5Ln_4F[GeO_4]_4$ (Ln = Pr, Nd) were measured using a Quantum Design Magnetic Property Measurement System (QD-MPMS3 SQUID VSM). The zero-field cooled magnetic susceptibility was measured as a function of temperature between 2 and 300 K in an applied field of 1000 Oe. Radial offset and shape corrections were performed using the method outlined by Morrison and zur Loye.[6.22]

Results and Discussion

Synthesis

An alkali fluoride/alkali chloride eutectic flux was used to grow crystals of $Na_5Ln_4F[GeO_4]_4$ (*Ln* = Pr, Nd). The eutectic mixture of NaF and NaCl was chosen to lower the melting point of the NaF flux in order to perform the reaction in a silver instead of a platinum vessel. By choosing the eutectic ratio of 33 % NaCl to 67 % NaF, which lowered the melting point of the flux from 996 °C (NaF) to 679 °C, the use of a reaction dwell temperature more than 100 °C above the melting point of the flux becomes feasible without coming close to the melting point of silver (962 °C).

Overall, germanate compounds are more difficult to synthesize due to the relative lower reactivity of germanium when compared to silicon. In this system, the identical conditions were used to grow $Na_5Ln_4F[GeO_4]_4$ (*Ln* = Pr, Nd) as were used to grow the $Na_5RE_4F[SiO_4]_4$ (RE = Pr, Nd, Sm – Tm) compounds.[6.4] However, only in the case of Pr and Nd, was the desired phase obtained and even adaptations to the reaction did not result in the crystallization of any of the other rare earth analogues, while routinely yielding the known $NaREGeO_4$ germanate analogues.[6.12, 6.23]

Structure

$Na_5Ln_4F[GeO_4]_4$ (*Ln* = Pr, Nd) crystallizes in the tetragonal space group *I*-4, with the same structure as the other reported $A_5RE_4X[TO_4]_4$ (A = Na, K; RE = rare earth, X = F, OH; T = Si, Ge).[6.4-6.6, 6.14-6.17] The $Na_5Ln_4F[GeO_4]_4$ structure contains one unique lanthanide site, one unique germanium site, two unique sodium sites, one unique fluorine site, and four unique oxygen sites. The lanthanide site is eight coordinate with seven bonds to oxygen and one bond to fluorine. Each lanthanide polyhedron is face shared to two other lanthanide polyhedra. In total, four lanthanide polyhedra share the fluorine site, thereby creating the $Ln_4O_{20}F$ unit shown in **Figure 6.1**. These lanthanide units stack down the *c* axis where down the column each *Ln* unit is connected through corner and edge sharing to GeO_4 tetrahedra as shown in **Figure 6.2**. Adjacent columns of *Ln* units are connected through edge sharing of *Ln* polyhedra and edge and corner sharing of *Ln* units with GeO_4 tetrahedra (**Figure 6.2**). The Na(1) atoms sit in line with the fluorine atoms down the *c* axis and fill the channels between the *Ln* units as shown in **Figure 6.3**. Four Na(2) atoms sit in the channels between the *Ln* columns down the *c* axis (**Figure 6.3**). The overall structure down the *c* axis is shown in **Figure 6.3** with crystallographic

data presented in **Table 6.1** and *Ln* – O and Ge – O interatomic distances presented in **Table 6.2**.

Magnetism

In the $A_5RE_4X[TO_4]_4$ family, where A = Na, K; RE = Pr, Nd, Sm-Yb, Y; X = F, OH; and T = Si or Ge, reports of magnetism are solely focused on the A = Na and T = Si compounds. Here, we report the first magnetic property measurements of the family when T = Ge and the first magnetic property measurements ever reported on quaternary germanate oxyfluorides. In the previous magnetic studies when T = Si, it has been seen that unless the rare earth is small, like terbium or dysprosium, the resulting magnetism is paramagnetic. In the germanates this appears to be the case as well. Down to 2 K, $Na_5Ln_4F[GeO_4]_4$ (*Ln* = Pr, Nd) are both strictly paramagnetic with the magnetic data summarized in **Table 6.3** and the magnetic susceptibilities and inverse susceptibilities are shown in **Figure 6.4**. For both analogues, the inverse susceptibility was fit over the range of 100 – 300 K. The effective moments are 3.6 μ_B (Pr) and 3.67 μ_B (Nd) which compare well with the expected moments of 3.56 μ_B (Pr) and 3.3 – 3.7 μ_B (Nd).

Conclusion

$Na_5Ln_4F[GeO_4]_4$ (*Ln* = Pr, Nd) crystals were grown using a sodium fluoride, sodium chloride eutectic flux. Both compositions crystallize in the tetragonal space group *I*-4 like previously reported analogues. The compounds represent the second germanium analogues of this family reported and are the first germanium oxyfluoride analogues. Germanate oxides and oxyfluorides are not found often in literature due to the difficulty encountered when trying to synthesize gemanates. These new compounds may indicate new pathways to synthesize future germanate compounds. Other members of

this germanate oxyfluoride family could have the potential to exhibit SHG or interesting magnetic properties.

References

6.1 Bugaris, D. E.; zur Loye, H.-C. *Angew. Chem. Int. Ed.* **2012**, *51*, 3780-3811.
6.2 Latshaw, A. M.; Yeon, J.; Smith, M. D.; zur Loye, H.-C. *J. Solid State Chem.* **2016**, *235*, 100-106.
6.3 Morrison, G.; zur Loye, H.-C. *Cryst. Growth Des.* **2016**, *16*, 1294-1299.
6.4 Latshaw, A. M.; Wilkins, B. O.; Hughey, K.; Yeon, J.; Williams, D. E.; Tran, T. T.; Halasyamani, P. S.; zur Loye, H.-C. *CrystEngComm* **2015**, *17*, 4654-4661.
6.5 Latshaw, A. M.; Smith, M. D.; zur Loye, H.-C. *Solid State Sci.* **2014**, *35*, 28-32.
6.6 Latshaw, A. M.; Chance, W. M.; Morrison, G.; Smith, M. D.; Yeon, J.; zur Loye, H.-C. *CrystEngComm* **2015**, *17*, 4691-4698.
6.7 Latshaw, A. M.; Hughey, K. D.; Smith, M. D.; Yeon, J.; zur Loye, H.-C. *Inorg. Chem.* **2015**, *54*, 876-884.
6.8 Vidican, I.; Smith, M. D.; zur Loye, H.-C. *J. Solid State Chem.* **2003**, *170*, 203-210.
6.9 Aung, Y. L.; Nakayama, S.; Sakamoto, M. *J. Mater. Sci.* **2005**, *40*, 129-133.
6.10 Emirdag-Eanes, M.; Pennington, W. T.; Kolis, J. W. *J. Alloys Compd.* **2004**, *366*, 76-80.
6.11 Wang, X.; Wang, Y.; Liu, Q.; Li, Y.; Yu, J.; Xu, R. *Inorg. Chem.* **2012**, *51*, 4779-4783.
6.12 Yeon, J.; Hardaway, J. B.; Sefat, A. S.; Latshaw, A. M.; zur Loye, H.-C. *Solid State Sci.* **2014**, *34*, 24-30.
6.13 Zhao, X.; Yan, T.; Wang, K.; Yan, Y.; Zou, B.; Yu, J.; Xu, R. *Eur. J. Inorg. Chem.* **2012**, *2012*, 2527-2532.
6.14 Hughey, K.; Yeon, J.; zur Loye, H.-C. *J. Chem. Crystallogr.* **2014**, *44*, 376-379.
6.15 Malinovskii, Y. A. *Dokl. Akad. Nauk SSSR* **1984**, *274*, 75-78.
6.16 Merinov, B. V.; Maksimov, B. A.; Ilyukhin, V. V.; Belov, N. V. *Dokl. Akad. Nauk SSSR* **1980**, *255*, 348-351.
6.17 Schäfer, M. C.; Schleid, T. *Z. Anorg. Allg. Chem.* **2010**, *636*, 2069.
6.18 APEX2 Version 2014.9-0, SAINT+ Version 8.34A and SADABS Version 2014/4. Bruker Analytical X-ray Systems, Inc., Madison, Wisconsin, USA, 2014.
6.19 SMART Version 5.631, SAINT+ Version 6.45 and SADABS Version 2.10, Bruker Analytical X-ray Systems, Inc., Madison, Wisconsin, USA, 2003.
6.20 Sheldrick, G. M. *Acta Crystallogr.* **2008**, *A64*, 112-122.
6.21 Dolomanov, O. V.; Bourhis, L. J.; Gildea, R. J.; Howard, J. A. K.; Puschmann, H. *J. Appl. Cryst.* **2009**, *42*, 339-341.
6.22 Morrison, G.; zur Loye, H.-C. *J. Solid State Chem.* **2015**, *221*, 334-337.
6.23 Emirdag-Eanes, M.; Krawiec, M.; Kolis, J. W. *J. Chem. Crystallogr.* **2001**, *31*, 281-285.

Table 6.1. Crystallographic table for single crystal X-ray data for $Na_5Ln_4F[GeO_4]_4$ (*Ln* = Pr, Nd).

Formula	$Na_5Pr_4F[GeO_4]_4$	$Na_5Nd_4F[GeO_4]_4$
Formula weight (g/mol)	1243.95	1257.27
Temperature (K)	300(2)	293(2)
Crystal system	Tetragonal	Tetragonal
Space group	*I*-4	*I*-4
a (Å)	12.1173(4)	12.0642(17)
c (Å)	5.6795(2)	5.6674(11)
V (Å^3)	833.92(6)	824.9(3)
Z	2	2
Density (Mg/m^3)	4.954	5.062
Absorption coefficient (mm^{-1})	18.772	19.754
Crystal size (mm)	0.10 x 0.04 x 0.03	0.14 x 0.04 x 0.04
2 theta range (°)	4.75 to 75.66	4.78 to 56.60
reflections collected	24672	3488
data/restraints/parameters	2244 / 0 / 32	1005 / 0 / 70
R (int)	0.0339	0.0425
GOF (F^2)	1.064	1.105
R indices (all data)	R_1 = 0.0128 wR_2 = 0.0209	R_1 = 0.0212 wR_2 = 0.0561

Table 6.2. *Ln* – O and Ge – O bond distances (in Å).

	$Na_5Pr_4F[GeO_4]_4$	$Na_5Nd_4F[GeO_4]_4$
Ln(1) – O(4)	2.4700(17)	2.320(9)
Ln(1) – O(1)	2.3403(19)	2.416(8)
Ln(1) – O(4)	2.4086(17)	2.431(9)
Ln(1) – O(1)	2.4415(19)	2.441(9)
Ln(1) – O(3)	2.6210(17)	2.451(8)
Ln(1) – O(2)	2.5566(16)	2.533(7)
Ln(1) – O(3)	2.4528(17)	2.604(8)
Ln(1) – F(1)	2.61981(14)	2.6037(6)
Ge(1) – O(1)	1.7479(18)	1.726(9)
Ge(1) – O(2)	1.7470(16)	1.740(7)
Ge(1) – O(4)	1.7391(17)	1.754(9)
Ge(1) – O(3)	1.7695(16)	1.773(8)

Table 6.3. Experimental magnetic moments (μ_{eff}) compared to calculated moments (μ_{calc}) for $Na_5Ln_4F[GeO_4]_4$ (*Ln* = Pr, Nd).

Compound	Fit Range (K)	θ (K)	μ_{eff} (μ_B/RE)	μ_{calc} (μ_B/RE)
$Na_5Pr_4F[GeO_4]_4$	100 – 300	-32.81	3.61	3.56
$Na_5Nd_4F[GeO_4]_4$	100 – 300	-36.59	3.67	3.3-3.7

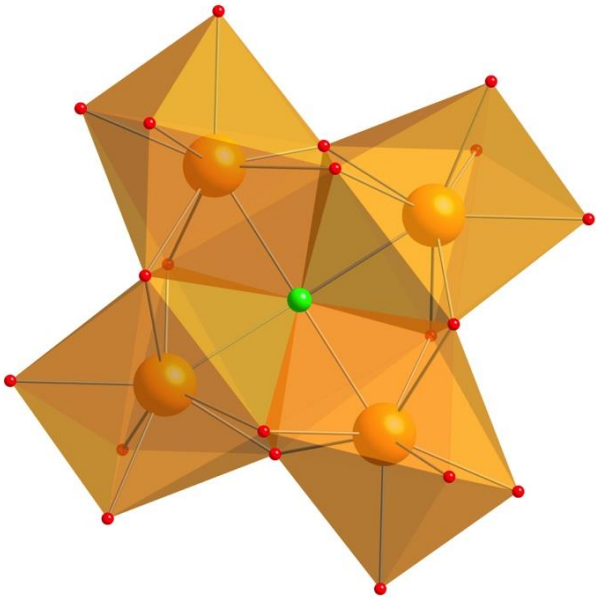

Figure 6.1. $Na_5Nd_4F[GeO_4]_4$, representative of both compositions, showing the $Ln_4O_{20}F$ units formed through the face sharing of the *Ln* polyhedra where *Ln* is shown in orange, oxygen in red, and fluorine in green.

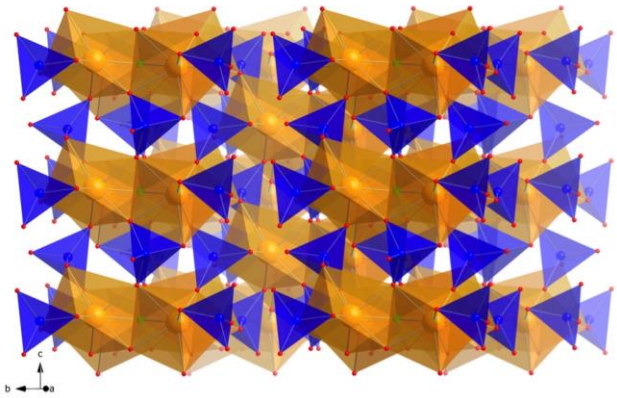

Figure 6.2. Representation of how the *Ln* unit columns are connected by corner and edge sharing Ge and how the adjacent columns are connected by Ge and *Ln* edge and corner sharing. *Ln* is shown in orange, Ge is shown in blue, oxygen is shown in red, and fluorine is shown in green.

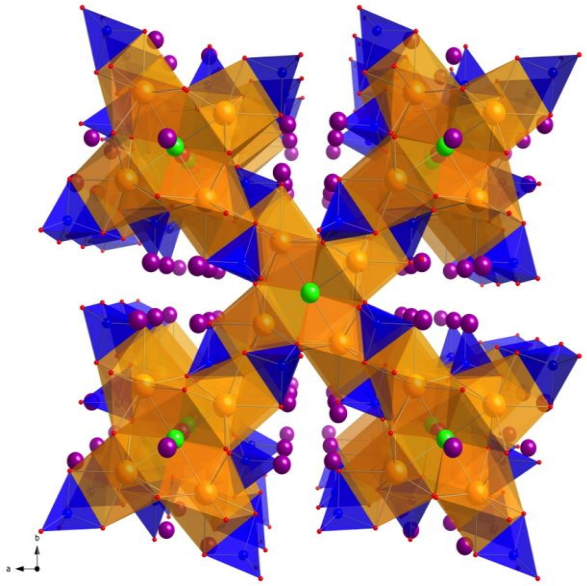

Figure 6.3. Overall representation of $Na_5Ln_4F[GeO_4]_4$ down the *c* axis where the sodium atoms can be seen in purple while the other colors follow the scheme described in Figure 6.2.

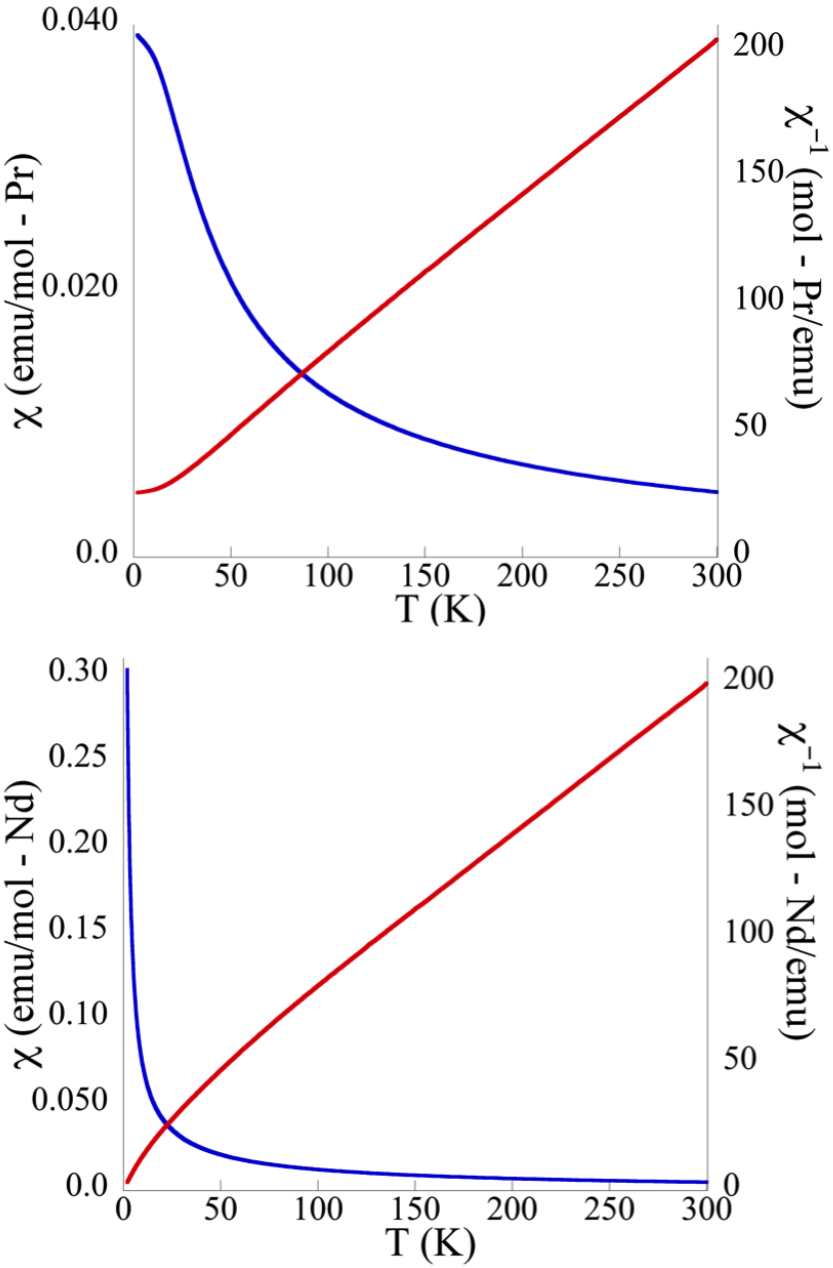

Figure 6.4. Magnetic susceptibility and inverse magnetic susceptibility data of $Na_5Pr_4F[GeO_4]_4$ (top) and $Na_5Nd_4F[GeO_4]_4$ (bottom).

Chapter 7

Influence of Rare Earth Cation size on the Crystal Structure in Rare Earth Silicates, $Na_2RESiO_4(OH)$ (RE = Sc, Yb) and $NaRESiO_4$ (RE = La, Yb)*

*Latshaw, A. M., Wilkins, B. O., Chance, W. M., Smith, M. D., zur Loye, H.-C. *Solid State Sci.*, **2016**, *51*, 59-65.

Introduction

Silicates are an expansive class of extended structures that are based on linked SiO_4 tetrahedral building blocks and that encompass many diverse compositions[7.1-7.6] including numerous examples of complex rare earth containing silicate structures. The presence of rare earth elements in the silicate structure can lead to interesting optical[7.5, 7.7-7.10] and magnetic[7.4, 7.11-7.14] properties. Furthermore, a unique feature of the rare earth silicates is the existence of a series of structural analogs and, at times, new structure types when a rare earth cation size limit is reached above or below the point at which a given structure ceases to form. Identifying such structural limits and exploring all the diverse structures that form for the rare earth group can lead to improved understanding of the overall crystal chemistry of silicates. While each case is unique, one can state that, in general, the rigidity of the crystal structure controls the size range of lanthanides that can be incorporated. Some structures, such as $Na_5RE_4X[SiO_4]_4$ (RE = Pr, Nd, Sm-Yb, Y; X = F, OH), are not very rigid and their rare earth coordination environment site is capable of accommodating a wide range of rare earths extending in size from 0.985 Å (Yb) to 1.126 Å (Pr).[7.13, 7.15, 7.16] Other silicate structures that have a more rigid framework structure are often limited to only a small sub-set of rare earths and the structure tends to change when the next sized rare earth falls outside the size range that can be accommodated. Often, this results in a new composition at the same time.

The synthesis of new silicates can be accomplished by a number of methods, including solid-state reactions to obtain polycrystalline samples and solution based routes to obtain single crystals. For the latter case fluoride containing fluxes have been shown to be very effective means of dissolving SiO_2 as well as rare earth oxides to produce rare

earth containing compositions.[7.12, 7.17, 7.18] When using fluoride-containing fluxes with rare earths and silica, products are usually rare earth silicate oxides or oxyfluorides. For the particular system discussed in this paper, the large and small rare earths tend to form oxides, while the middle-sized rare earths tend to form oxyfluorides.

The hydroflux method is another approach to create single crystals, albeit one that operates in a much lower temperature regime. This new technique encompasses the best of many crystal growth techniques. By operating at a low temperature (180 °C – 240 °C)[7.13, 7.15, 7.19-7.24] and a low pressure, this technique allows for the preparation of materials that are stable only at low temperatures and that could not be obtained via the more traditional high temperature flux growth.[7.17] In addition, this method does not have the high pressure concerns found in traditional hydrothermal growth methods. The hydroflux occupies a place in the compositional regime that is between a wet flux and an aqueous solution, where its acid base properties are controlled by the Lux-Flood concept of oxo-acidity[7.25, 7.26] and where unique compositions can be isolated as single crystals.

Herein we present the use of both the hydroflux method and the fluoride flux crystal growth approach for the synthesis of new complex rare earth silicates, $NaLaSiO_4$, $NaYbSiO_4$, $Na_2YbSiO_4(OH)$, and $Na_2ScSiO_4(OH)$, and discuss the effect of both the crystal growth temperature/method and the rare earth cation size on the structures that are obtained.

Experimental Section

Sample preparation

Materials preparation

Sc_2O_3 (>99 %) was purchased from Aran Isles Chemical Inc., Yb_2O_3 and La_2O_3 (99.9 %) were purchased from Alfa Aesar, NaOH (ACS grade) was purchased from Fisher Scientific, $Na_2SiO_3 \cdot 9H_2O$ (99+ %) was purchased from EM Science, NaF (99 % min.) was purchased from Alfa Aesar, and NaCl (99.9 %) was purchased from Fisher Scientific. SiO_2 (99.99 %) was purchased from Aldrich as fused pieces and ground to a powder in a ball mill.

Single crystals

$Na_2RESiO_4(OH)$ (RE = Sc, Yb)

Crystals of $Na_2ScSiO_4(OH)$ and $Na_2YbSiO_4(OH)$ were grown in 23 mL polytetrafluoroethylene (PTFE)-lined stainless steel autoclaves by utilizing an NaOH hydroflux. For $Na_2ScSiO_4(OH)$, $Na_2SiO_3 \cdot 9H_2O$ (1.91 mmol), Sc_2O_3 (1.03 mmol), NaOH (9.68 g), and deionized water (8.5 g) were loaded into a PTFE liner that was placed into a steel autoclave before being placed into a programmable oven that was ramped at 5 °C/min to 230 °C and held for 48 h before slow cooling to 80 °C at a rate of 0.1 °C/min. After reaching 80 °C, the oven was shut off. For $Na_2YbSiO_4(OH)$, $Na_2SiO_3 \cdot 9H_2O$ (1.86 mmol), Yb_2O_3 (0.975 mmol), NaOH (9.24 g), deionized water (8.17 g), and WO_3 (1.1 mmol), which acted as a mineralizer, were added to a PTFE liner that was loaded into a steel autoclave that was placed into a programmable oven that was ramped at a rate of 5 °C/min. to 230 °C, where it dwelled for 48 h. After the dwelling period, the reaction was quenched by removing it from the oven between 200 – 230 °C. If the reaction was pulled

out after the flux had cooled below 200 °C, an impurity of YbO(OH) was consistently observed. Reactions quenched between 200 – 230 °C yielded phase pure crystals, albeit twinned, with no difference observed between different quenching temperatures above 200 °C. The crystals from these reactions were gently scraped from the inside of the PTFE liners and sonicated in methanol to remove the flux before being collected via vacuum filtration and then dried.

$NaRESiO_4$ (RE = La, Yb)

Crystals of $NaLaSiO_4$ were synthesized by loading La_2O_3 (1 mmol), Na_2CO_3 (1 mmol), and SiO_2 (2 mmol) into a silver crucible. The eutectic flux of NaF (1.41 g) and NaCl (0.96 g) was placed on top of the reactants. The crucible was then loosely fitted with a silver lid and placed into a programmable furnace that was programmed to ramp in 1.5 h to 900 °C where it dwelled for 48 h before slow cooling to 650 °C at a rate of 3 °C/h before the furnace was shut off. The flux was washed away by sonication in water to yield crystals of $NaLaSiO_4$.

Crystals of $NaYbSiO_4$ were synthesized by loading Yb_2O_3 (2 mmol), Na_2CO_3 (2 mmol), and SiO_2 (4 mmol) into a silver crucible. The eutectic flux of NaF (2.80 g) and NaCl (1.93 g) was added on top of the reactants. The crucible was loosely fitted with a silver lid and placed into a programmable furnace that was programmed to ramp in 1.5 h to 800 °C where it dwelled for 24 h before slow cooling to 600 °C at a rate of 6 °C/h. After reaching 600 °C, the furnace was shut off. Crystals were isolated by sonication in water to wash away the flux. The $NaYbSiO_4$ phase was the major product, with a minor amount of a second new ytterbium containing composition, $Na_3YbSi_2O_7$.

Characterization

Single Crystal X-ray Diffraction

Structure determinations were performed using single crystal X-ray intensity data from a colorless needle crystal [$Na_2YbSiO_4(OH)$], a colorless octahedral crystal [$Na_2ScSiO_4(OH)$], a colorless needle crystal [$NaLaSiO_4$], and a colorless rectangular block crystal [$NaYbSiO_4$]. The X-ray data of $Na_2YbSiO_4(OH)$, $Na_2ScSiO_4(OH)$, and $NaYbSiO_4$ were collected using a Bruker SMART APEX diffractometer (Mo Kα radiation, λ = 0.71073 Å)[7.27] and the X-ray data from $NaLaSiO_4$ were collected using a Bruker D8 QUEST diffractometer equipped with a PHOTON 100 CMOS area detector and an Incoatec microfocus source (Mo Kα radiation, λ = 0.71073 Å).[7.28] The raw area detector data frames were reduced and corrected for absorption effects using the SAINT+ and SADABS programs.[7.27] Final unit cell parameters were determined by least-squares refinement of large sets of reflections from the data sets. The initial structural models were obtained by direct methods using SHELXS.[7.29] Subsequent difference Fourier calculations and full-matrix least-squares refinement against F^2 were performed with SHELXL-2013/4[7.29] using the ShelXle interface. The final structural models were checked for missed symmetry elements using the ADDSYM program in PLATON,[7.30-7.33] which found no missed symmetry in any case.

$NaLaSiO_4$ crystallizes in the orthorhombic system. The space groups *Pna*2_1 and *Pnma* were consistent with the pattern of systematic absences in the intensity data. The acentric group *Pna*2_1 was eventually determined to be correct by structure solution. $NaYbSiO_4$ also crystallizes in the orthorhombic system. The space groups *Pnma* and *Pna*2_1 were consistent with the pattern of systematic absences in the intensity data. The

centrosymmetric group *Pnma* was confirmed by structure solution. For $Na_2RESiO_4(OH)$, the compounds crystallize in the polar space group $Pca2_1$ as determined by the pattern of systematic absences in the intensity data and by structure solution.

For $Na_2RESiO_4(OH)$ the two unique hydrogen (hydroxyl) atoms necessary for crystal electroneutrality could not be reliably located or refined. They are presumably bonded to the two unique non-silicate oxygen atoms O9 and O10. Small residual electron density peaks were observed near the two oxygens, but did not give acceptable positional or displacement parameters, even with restraints applied. A soft restraint (SHELX ISOR instruction) was applied to the displacement parameters of one oxygen atom (O3) to prevent an oblate ellipsoid shape. The reason for this is not clear, but may be due to minor positional disorder of the silicate group [Si1/O1-O4] around the Si1-O4 bond, as the displacement ellipsoids for O1 and O2 are also slightly oblate. The absolute structure (Flack) parameter near convergence for the $Na_2YbSiO_4(OH)$, $Na_2ScSiO_4(OH)$, and $NaLaSiO_4$ compounds refined to 0.41(2), 0.49(10), and 0.50(2) respectively, indicating the data crystals are two-component inversion twins. An inversion twin law was included in the final refinement cycles. Further details of the crystal structure investigation can be obtained from the Fachinformationszentrum Karlsruhe, 76344 Eggenstein-Leopoldshafen, Germany (fax:+497247808666; e-mail: crystdata@fiz-karlsruhe.de) on quoting the depository numbers 430196 ($NaLaSiO_4$), 430197 ($NaYbSiO_4$), 430198 ($Na_2ScSiO_4(OH)$), and 430199 ($Na_2YbSiO_4(OH)$).

Magnetic Property Measurements

The DC magnetic susceptibilities of $Na_2YbSiO_4(OH)$ and $NaYbSiO_4$ were measured as a function of temperature using a Quantum Design MPMS 3 SQUID

Magnetometer. 82.39 mg of a ground polycrystalline powder of $Na_2YbSiO_4(OH)$ and 52.70 mg of a mixed ground polycrystalline powder of $NaYbSiO_4$ and $Na_3YbSi_2O_7$, the second new ytterbium containing composition mentioned earlier, were massed on a balance sensitive to 0.01 mg and loaded into a gelatin capsule for data collection. Zero-field-cooled conditions from 2 – 300 K in an applied field of 1000 Oe were used to measure the temperature dependent susceptibilities of the samples. The raw magnetic moments were corrected for sample shape and radial offset effects using the method outlined by Morrison and zur Loye.[7.34]

Results and Discussion

Structure Description

$Na_2RESiO_4(OH)$ (RE = Sc, Yb)

$Na_2ScSiO_4(OH)$ and $Na_2YbSiO_4(OH)$ crystallize in a new structure type in the orthorhombic space group $Pca2_1$. Within the structure are two unique silicon environments, two unique rare earth environments, four sodium environments, and ten oxygen environments. Both silicon environments result in isolated SiO_4 units that are corner shared to two RE(1) and to two RE(2) octahedra. Both rare earth environments consist of REO_6 octahedra that corner share to two Si(1) tetrahedra, two Si(2) tetrahedra, and to two of the other rare earth octahedra (**Figure 7.1**). The oxygen sites O(9) and O(10), which make up the corner-shared sites of the RE octahedra, are presumed to be the location of the hydroxyl groups. Na(1), Na(2), Na(3), and Na(4) sit in the channels between O(1), O(7), O(3), and O(6), respectively, where O(1) corner shares Si(1) and RE(2) polyhedra, O(7) corner shares Si(2) and RE(1) polyhedra, O(3) corner shares Si(1) and RE(2), and O(6) corner shares Si(2) and RE(1). The overall structural representation

is shown in **Figure 7.2**, relevant crystallographic information is listed in **Table 7.1**, and rare earth – oxygen interatomic distances are collected in **Table 7.2**.

$NaYbSiO_4$

$NaYbSiO_4$ crystallizes in the orthorhombic space group *Pnma* in a structure type that is similar to one observed for the many other compositional analogs of this structure type, such as germanates. Known $NaRETO_4$ (RE = rare earth, T = tetragen) examples include $NaREGeO_4$ (RE = Sm-Tb, Ho-Lu)[7.35-7.37] and $NaRESiO_4$ (RE = La[7.38], Nd[7.39], Sm[7.40], Gd[7.41, 7.42], Ho[7.39], Er[7.39], Lu[7.39, 7.43], Y[7.44, 7.45]), where the germanate examples crystallize in the orthorhombic space group *Pnma,* while the silicon examples are reported to crystallize in the orthorhombic space groups *Pmcn* (La), *Pna*2_1 (Nd), *Pmnb* (Gd[7.42]), *Pbn*2_1 (Er, Lu[7.39], Y[7.44]), *Pc*2_1*n* (Y[7.45]), and *Pnma* (Lu[7.43]), and in the tetragonal space group *I*4/*m* (Sm, Gd[7.41], Ho) . Since *Pmcn* and *Pmnb* are non-standard settings of *Pnma*, $NaLaSiO_4$, $NaGdSiO_4$, and a polymorph of $NaLuSiO_4$ crystallize in the same space group as the reported $NaYbSiO_4$.

$NaYbSiO_4$ crystallizes in the space group *Pnma* in the olivine structure type. As expected, it is isostructural with the known germanates. The structure contains one unique sodium, one unique silicon, one unique ytterbium, and three unique oxygen environments. The Yb atoms are located in a distorted YbO_6 octahedra that corner shares with other YbO_6 octahedra and corner and edge share to SiO_4 tetrahedra (**Figure 7.3**). The SiO_4 tetrahedra are isolated from each other and contribute to the overall structure only via corner and edge sharing with YbO_6 octahedra, which transforms the two-dimensional sheets of the Yb polyhedra along the *a* axis to a three-dimensional structure (**Figure 7.4**) while the sodium atoms fill the channels between the ytterbium and silicon

polyhedra as shown in **Figure 7.5**. **Figure 7.4** shows the overall structure down the *c* axis. The relevant crystallographic information is listed in **Table 7.1**, and ytterbium – oxygen interatomic distances are collected in **Table 7.3**.

$NaLaSiO_4$

$NaLaSiO_4$ crystallizes in the space group $Pna2_1$, which is similar to the previously reported $NaNdSiO_4$, $NaErSiO_4$, and a polymorph of $NaLuSiO_4$ where the Er and Lu analogues are reported in the space group $Pbn2_1$, which is a non-standard setting of the space group $Pna2_1$.[7.39] In this structure there are three unique lanthanum sites, three unique silicon sites, three unique sodium sites, and twelve unique oxygen sites. All three La sites are 8 CN where all are edge and corner shared to isolated SiO_4 units, and all are corner and face shared with other La polyhedra. The La polyhedra form face shared columns down the *a* axis where the columns corner share with each other, making it look as though the columns are overlapped when looking down the *c* axis (**Figure 7.6**). The Si form isolated SiO_4 units and the sodium atoms fill the channels in the structure where the Na(1) atoms sit in line with the Si(3) atoms down the *a* axis, the Na(2) atoms sit in line with the Si(2) atoms down the *a* axis, and the Na(3) atoms sit in line with the Si(1) atoms down the *a* axis. The relevant crystallographic information is listed in **Table 7.1**, and lanthanum – oxygen interatomic distances are collected in **Table 7.4**. Overall structural views down the *a* and *c* axis are shown in **Figures 7.7** and 7.**8**, respectively.

Figure 7.9 depicts the range of synthetic conditions under which the different complex rare earth silicates can be synthesized. From the figure it is clear that both temperature and rare earth cation size play important roles in determining the structure that forms. It is interesting to note that for the middle range of rare earth cation radii, the

$Na_5RE_4X[SiO_4]_4$ structure type forms, as the oxyfluoride when crystallized out of high temperature fluoride fluxes and as the oxyhydroxide when crystallized out of a low temperature hydroflux. Furthermore, the $Na_5RE_4X[SiO_4]_4$ structures are bracketed by four other structure types for larger and for smaller rare earth cations: $Na_2RESiO_4(OH)$ and $NaLaSiO_4$ for larger cations at low and high synthesis temperatures, respectively, and $Na_2RESiO_4(OH)$ and $NaRESiO_4$ for smaller cations at low and high synthesis temperatures, respectively.

In this study we found that the fluoride/chloride eutectic flux growth conditions that yield the $Na_5RE_4F[SiO_4]_4$ structure for RE = Pr, Nd, Sm-Tm, surprisingly resulted in the formation of the $NaRESiO_4$ structure for RE = La, Yb, Lu,[7.43] for the larger and smaller rare earths, while the hydroflux and hydrothermal growth reaction conditions that form the $Na_5RE_4(OH)[SiO_4]_4$ structure for RE = Pr, Nd, Sm-Yb, Y, unexpectedly resulted in the formation of the $Na_2RESiO_4(OH)$ structure for RE = La,[7.46] Yb, Sc, for the larger and smaller rare earths, respectively. It should be noted that for the reported conditions and compositions, as a function of rare earth size, different structure types occur for larger and smaller rare earths with the $NaRESiO_4$ structure adopting the $Pna2_1$ space group for larger rare earths and adopting the *Pnma* space group for smaller rare earths and the $Na_2RESiO_4(OH)$ structure adopting the *Pnma* space group for the larger rare earths and adopting the $Pca2_1$ space group for the smaller rare earths.

Magnetic Properties

The magnetic data of $Na_2YbSiO_4(OH)$ and $NaYbSiO_4$ are summarized in **Table 7.5**. The $NaYbSiO_4$ sample used for the collection of the magnetic susceptibility data contained roughly a quarter of a second ytterbium silicate phase, $Na_3YbSi_2O_7$, to be

reported on in detail in the near future. The magnetic data were corrected for the presence of the 2nd phase by determining the exact phase fraction, 75.2 % $NaYbSiO_4$ and 24.8 % of $Na_3YbSi_2O_7$, by analyzing powder X-ray diffraction data using the JADE software package. The magnetic susceptibilities and the inverse susceptibilities for both compounds are shown in **Figure 7.10**. The samples are paramagnetic and the inverse susceptibilities were fit over the range of 100 – 300 K using the modified Curie-Weiss law $\chi = \chi_0 + C/(T-\theta)$, where χ is susceptibility, χ_0 is the temperature independent susceptibility, C is the Curie constant, and θ is the Weiss temperature. The χ_0 values from the fit (**Table 7.5**) were positive, as has previously been reported for ytterbium containing compounds, where the positive values were thought to arise from crystal field effects in the ytterbium.[7.47, 7.48] The fit to the inverse magnetic susceptibility yielded effective moments of 4.20 μ_B for $Na_2YbSiO_4(OH)$ and 4.18 μ_B for the $NaYbSiO_4$ mixed sample.

Conclusion

The new compositions $Na_2YbSiO_4(OH)$ and $Na_2ScSiO_4(OH)$ were synthesized using the hydroflux crystal growth method, while $NaLaSiO_4$ and $NaYbSiO_4$ were prepared using a traditional high temperature fluoride/chloride eutectic flux. Interestingly, these compositions all grow under the same conditions used to synthesize $Na_5RE_4X[SiO_4]_4$ (RE = Pr, Nd, Sm-Yb, Y; X = OH, F) indicating the substantial influence of rare earths size effects in silicate systems. Paramagnetic behavior was observed for both Yb analogues.

References

7.1 Chicagov, A. V.; Litvin, B. N.; Belov, N. V. *Kristallografiya* **1969**, *14*, 119-122.
7.2 Felsche, J. *J. Solid State Chem.* **1972**, *5*, 266-275.
7.3 Latshaw, A. M.; Smith, M. D.; zur Loye, H.-C. *Solid State Sci.* **2014**, *35*, 28-32.
7.4 Latshaw, A. M.; Hughey, K. D.; Smith, M. D.; Yeon, J.; zur Loye, H.-C. *Inorg. Chem.* **2015**, *54*, 876-884.
7.5 Vidican, I.; Smith, M. D.; zur Loye, H.-C. *J. Solid State Chem.* **2003**, *170*, 203-210.
7.6 Wierzbicka-Wieczorek, M.; Goeckeritz, M.; Kolitsch, U.; Lenz, C.; Giester, G. *Eur. J. Inorg. Chem.* **2015**, *2015*, 948-963.
7.7 Ananias, D.; Paz, F. A. A.; Yufit, D. S.; Carlos, L. D.; Rocha, J. *J. Am. Chem. Soc.* **2015**, *137*, 3051-3058.
7.8 Chiang, P.-Y.; Lin, T.-W.; Dai, J.-H.; Chang, B. C.; Lii, K.-H. *Inorg. Chem.* **2007**, *46*, 3619-3622.
7.9 Ferdov, S.; Sa Ferreira, R.; Lin, Z. *Chem. Mater.* **2006**, *18*, 5958-5964.
7.10 Fernández-Carrión, A. J.; Ocaña, M.; García-Sevillano, J.; Cantelar, E.; Becerro, A. I. *J. Phys. Chem. C* **2014**, *118*, 18035-18043.
7.11 Belov, K. P.; Toropov, N. A.; Bondar, I. A.; Mitina, L. P. *Izv. Akad. Nauk SSSR, Neorg. Mater.* **1969**, *5*, 565-568.
7.12 Latshaw, A. M.; Wilkins, B. O.; Hughey, K. D.; Yeon, J.; Williams, D. E.; Tran, T. T.; Halasyamani, P. S.; zur Loye, H.-C. *CrystEngComm.* **2015**, *17*, 4654-4661.
7.13 Latshaw, A. M.; Chance, W. M.; Morrison, G.; Smith, M. D.; Yeon, J.; zur Loye, H.-C. *CrystEngComm.* **2015**, *17*, 4691-4698.
7.14 Ueda, S.; Wakeshima, M.; Hinatsu, Y. *Kidorui* **2013**, *62*, 166-167.
7.15 Latshaw, A. M.; Smith, M. D.; Chance, W. M.; zur Loye, H.-C. *Solid State Sci.* **2015**, *42*, 14-19.
7.16 Shannon, R. D. *Acta Crystallogr., Sect. A: Cryst. Phys. Diffr., Theor. Gen. Crystallogr.* **1976**, *32*, 751.
7.17 Bugaris, D. E.; zur Loye, H.-C. *Angew. Chem. Int. Ed.* **2012**, *51*, 3780-3811.
7.18 Napper, J. D.; Layland, R. C.; Smith, M. D.; zur Loye, H.-C. *J. Chem. Crystallogr.* **2004**, *34*, 347-351.
7.19 Bugaris, D. E.; Smith, M. D.; zur Loye, H.-C. *Inorg. Chem.* **2013**, *52*, 3836-3844.
7.20 Chance, W. M.; Bugaris, D. E.; Sefat, A. S.; zur Loye, H.-C. *Inorg. Chem.* **2013**, *52*, 11723-11733.
7.21 Chance, W. M.; Smith, M. D.; zur Loye, H.-C. *J. Chem. Crystallogr.* **2014**, *44*, 20-24.
7.22 Chance, W. M.; zur Loye, H.-C. *Solid State Sci.* **2014**, *28*, 90-94.
7.23 zur Loye, K. D.; Latshaw, A. M.; Smith, M. D.; Chance, W. M.; zur Loye, H.-C. *J. Chem. Crystallogr.* **2014**, *45*, 20-25.
7.24 zur Loye, K. D.; Chance, W. M.; Yeon, J.; zur Loye, H.-C. *Solid State Sci.* **2014**, *37*, 86-90.
7.25 Flood, H.; Fortland, T. *Acta Chem. Scand.* **1947**, *1*, 592.
7.26 Lux, H. Z.; *Z. Electrochemistry* **1939**, *45*, 303.
7.27 SMART Version 5.630, SAINT+ Version 6.45a and SADABS Version 2.10, Bruker Analytical X-ray Systems, Inc., Madison, Wisconsin, USA, 2003.
7.28 APEX2 Version 2014.9-0, SAINT+ Version 8.34A and SADABS Version 2014/4.

Bruker Analytical X-ray Systems, Inc., Madison, Wisconsin, USA, 2014.
7.29 Sheldrick, G. M. *Acta Crystallogr.* **2008**, *A64*, 112-122.
7.30 LePage, Y. *J. Appl. Crystallogr.* **1987**, *20*, 264-269.
7.31 PLATON, A Multipurpose Crystallographic Tool, Utrecht University, Utrecht, The Netherlands, Spek, A. L. 1998.
7.32 Spek, A. L. *J. Appl. Crystallogr.* **1988**, *21*, 578-579.
7.33 Spek, A. L. *Acta Crystallogr. Sect A* **1990**, *46*, C34.
7.34 Morrison, G.; zur Loye, H.-C. *J. Solid State Chem.* **2015**, *221*, 334-337.
7.35 Emirdag-Eanes, M.; Krawiec, M.; Kolis, J. W. *J. Chem. Crystallogr.* **2001**, *31*, 281-285.
7.36 Yeon, J.; Hardaway, J. B.; Sefat, A. S.; Latshaw, A. M.; zur Loye, H.-C. *Solid State Sci.* **2014**, *34*, 24-30.
7.37 Zhao, X.; Wang, K.; Yan, T.; Yan, Y.; Zou, B.; Jihong, Y.; Xu, R. *Chin. J. Chem.* **2012**, *30*, 2066-2072.
7.38 Blasse, G. *Phillips Res. Labs, Eindhoven Netherlands Private Communication* **1967**,
7.39 Chichagov, A. V.; Belov, N. V. *Geochem. Int.* **1968**, *5*, 858.
7.40 Chichagov, A. V.; Ilyukhin, V. V.; Belov, N. V. *Dokl. Akad. Nauk SSSR* **1967**, *177*, 574.
7.41 Avetisyan, E. I.; Chichagov, A. V.; Belov, N. V. *Kristallografiya* **1970**, *15*, 1066.
7.42 Shannon, R. D.; Gier, T. E.; Foris, C. M.; Nelen, J. A.; Appleman, D. E. *Phys. Chem. Miner.* **1980**, *5*, 245-253.
7.43 Blasse, G.; Bril, A. *J. Inorg. Nucl. Chem.* **1967**, *29*, 2231-2241.
7.44 Maksimov, B. A.; Ilyukhin, V. V.; Belov, N. V. *Kristallografiya* **1966**, *11*, 681.
7.45 Merinov, B. V.; Maksimov, B. A.; Ilyukhin, V. V.; Belov, N. V. *Dokl. Akad. Nauk SSSR* **1979**, *248*, 1108.
7.46 Chiragov, M. I.; Mamedov, K. S. *Uch. zap. Azerb. un-t. Ser. geol.-geogr. n.* **1974**, *4*, 3-6.
7.47 Diviš, M.; Hölsä, J.; Lastusaari, M.; Litvinchuk, A. P.; Nekvasil, V. *J. Alloys Compd.* **2008**, *451*, 662-665.
7.48 Jin, G. B.; Choi, E. S.; Guertin, R. P.; Brooks, J. S.; Booth, C. H.; Albrecht-Schmitt, T. E. *J. Solid State Chem.* **2007**, *180*, 2581-2586.

Table 7.1. Crystallographic data for $Na_2RESiO_4(OH)$ (RE = Sc, Yb) and $NaRESiO_4$ (RE = La, Yb).

Formula	$Na_2ScSiO_4(OH)$	$Na_2YbSiO_4(OH)$	$NaLaSiO_4$	$NaYbSiO_4$
Formula weight	200.04	328.12	253.99	288.12
Temperature (K)	296(2)	296(2)	301(2)	296(2)
Crystal System	Orthorhombic	Orthorhombic	Orthorhombic	Orthorhombic
Space group	*Pca*2$_1$	*Pca*2$_1$	*Pna*2$_1$	*Pnma*
a (Å)	13.6153(7)	13.9074(5)	21.4726(10)	11.0329(3)
b (Å)	5.4215(3)	5.5366(2)	9.4441(4)	6.3536(2)
c (Å)	12.1083(7)	12.4876(5)	5.5008(3)	5.1054(2)
V (Å^3)	893.78(9)	961.54(6)	1115.50(9)	357.88(2)
Z	8	8	12	4
Density (Mg/m^3)	2.973	4.533	4.537	5.347
Absorption coefficient (mm^{-1})	2.027	19.806	11.786	26.440
Crystal size (mm^3)	0.06 x 0.06 x 0.05	0.08 x 0.03 x 0.02	0.05 x 0.04 x 0.01	0.08 x 0.040 x 0.03
2 theta range (°)	5.98 to 65.19	5.86 to 65.29	4.71 to 80.68	7.388 to 70.466
reflections collected	26026	27619	88663	9114
data/restraints/parameters	3246 / 1 / 164	3503 / 7 / 164	7027 / 1 / 192	860 / 0 / 41
R (int)	0.0796	0.0544	0.0404	0.0349
GOF (F^2)	1.081	1.048	1.203	1.133
R indices (all data)	R_1 = 0.0626	R_1 = 0.0307	R_1 = 0.0226	R_1 = 0.0280
	wR_2 = 0.1107	wR_2 = 0.0527	wR_2 = 0.0441	wR_2 = 0.0444

Table 7.2. RE bond distances (in Å) for $Na_2RESiO_4(OH)$ (RE = Sc, Yb).

	$Na_2ScSiO_4(OH)$	$Na_2YbSiO_4(OH)$
RE(1) – O(4)	2.057(5)	2.207(6)
RE(1) – O(2)	2.078(5)	2.204(7)
RE(1) – O(6)	2.120(12)	2.275(13)
RE(1) – O(7)	2.121(10)	2.200(9)
RE(1) – O(9)	2.128(5)	2.240(6)
RE(1) – O(10)	2.171(5)	2.262(6)
RE(2) – O(8)	2.069(5)	2.193(6)
RE(2) – O(5)	2.086(5)	2.190(6)
RE(2) – O(10)	2.119(5)	2.262(6)
RE(2) – O(1)	2.127(9)	2.261(8)
RE(2) – O(3)	2.129(10)	2.187(13)
RE(2) – O(9)	2.161(6)	2.287(6)

Table 7.3. Yb bond distances (in Å) for $NaYbSiO_4$.

	$NaYbSiO_4$
Yb(1) – O(2)	2.170(3)
Yb(1) – O(3)	2.221(3)
Yb(1) – O(1)	2.235(2)
Yb(1) – O(1)	2.235(2)
Yb(1) – O(1)	2.235(2)
Yb(1) – O(1)	2.235(2)

Table 7.4. La bond distances (in Å) for $NaLaSiO_4$.

La(1)		La(2)		La(3)	
La(1) – O(3)	2.422(3)	La(2) – O(5)	2.442(2)	La(3) – O(9)	2.404(3)
La(1) – O(12)	2.452(3)	La(2) – O(4)	2.459(3)	La(3) – O(7)	2.488(3)
La(1) – O(4)	2.501(3)	La(2) – O(7)	2.490(3)	La(3) – O(6)	2.517(3)
La(1) – O(1)	2.521(3)	La(2) – O(10)	2.519(3)	La(3) – O(3)	2.525(3)
La(1) – O(2)	2.527(2)	La(2) – O(8)	2.545(2)	La(3) – O(12)	2.533(3)
La(1) – O(1)	2.555(3)	La(2) – O(2)	2.600(2)	La(3) – O(11)	2.547(2)
La(1) – O(11)	2.581(2)	La(2) – O(9)	2.658(3)	La(3) – O(8)	2.573(2)
La(1) – O(5)	2.619(3)	La(2) – O(6)	2.683(3)	La(3) – O(10)	2.763(3)

Table 7.5. Experimental magnetic moments (μ_{eff}) compared to calculated moments (μ_{calc}) for $Na_2YbSiO_4(OH)$ and $NaYbSiO_4$.

	$Na_2YbSiO_4(OH)$	$NaYbSiO_4$
Fit Range (K)	100 – 300	100-300
χ_0	0.00085	0.0029
θ (K)	-95.92	-75.81
μ_{eff} (μ_B/RE)	4.20	4.18
μ_{calc} (μ_B/RE)	4.54	4.54

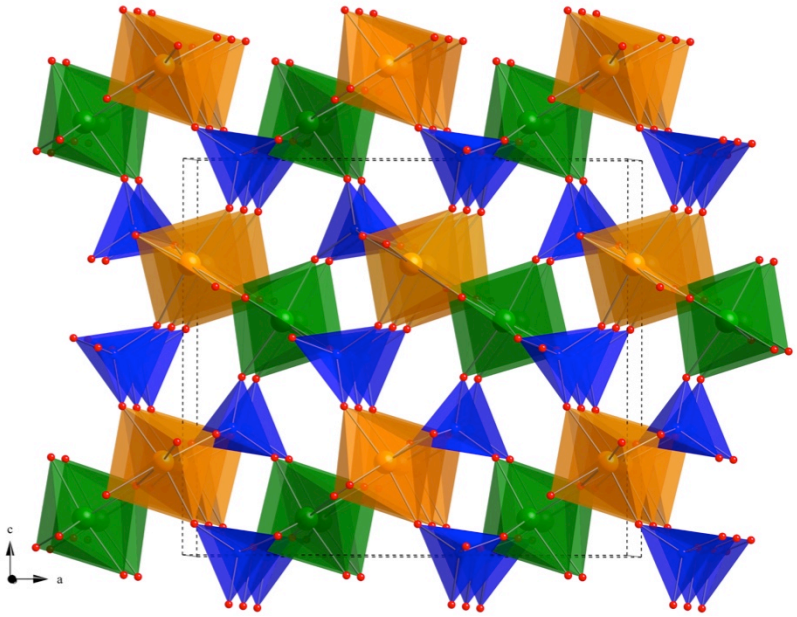

Figure 7.1. Visual representation of the two REO_6 octahedra and mode of octahedra corner sharing in $Na_2ScSiO_4(OH)$, where RE(1) is represented in green, RE(2) is in orange, silicon is in blue, and oxygens are in red.

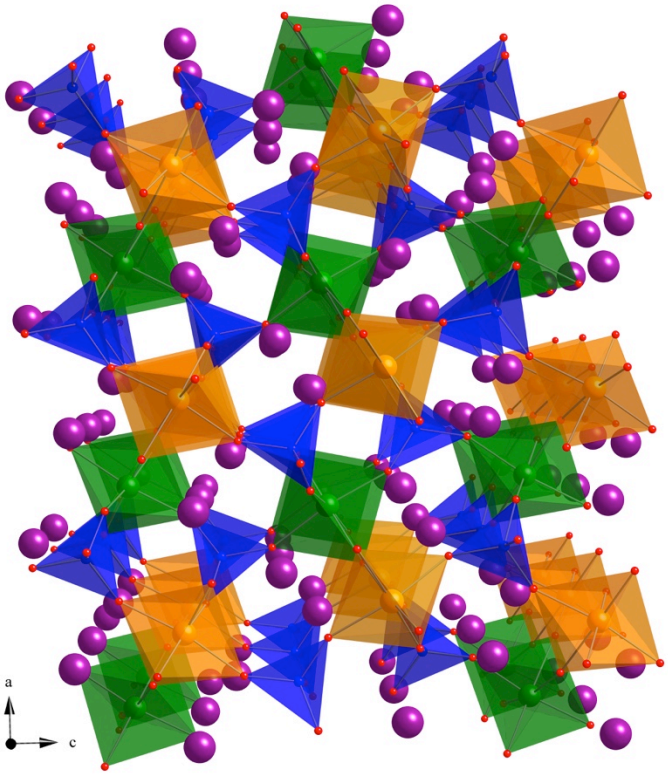

Figure 7.2. Overall representation of the structure of $Na_2ScSiO_4(OH)$ where RE(1) are green, RE(2) are orange, Na are purple, silicon are blue, and oxygens are red.

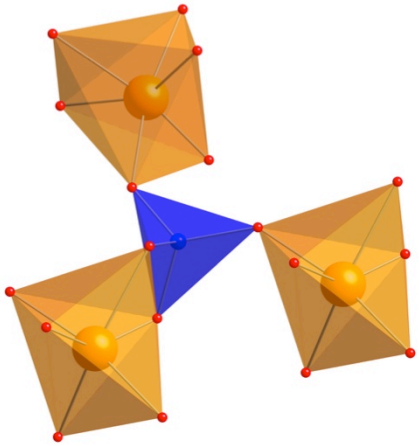

Figure 7.3. Illustration of $NaYbSiO_4$ highlighting the edge- and corner-sharing of the SiO_4 tetrahedra to the REO_6 octahedra.

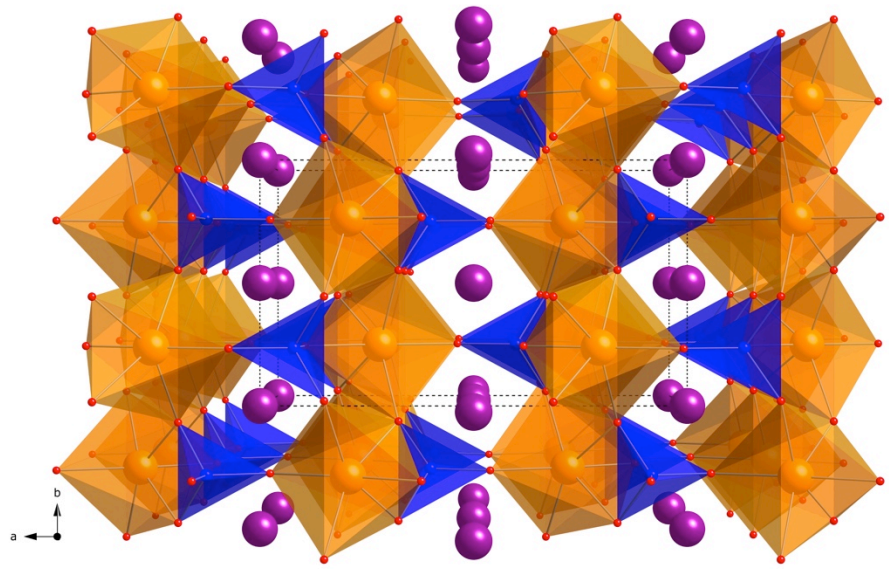

Figure 7.4. Structural image of $NaYbSiO_4$, which highlights the overall olivine structure down the *c* axis. Ytterbium is shown in orange, silicon is shown in blue, and sodium is shown in purple.

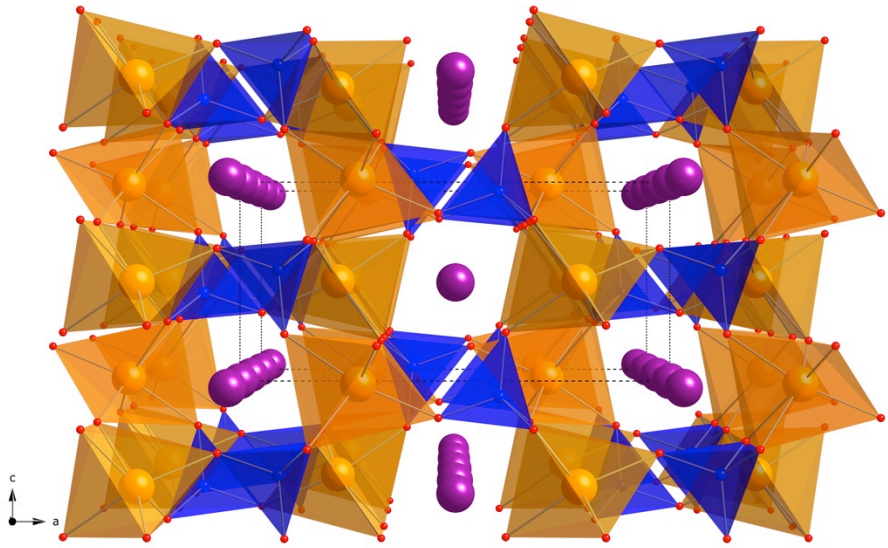

Figure 7.5. Visual representation of $NaYbSiO_4$ illustrating how the sodium atoms (purple) fill the channels created by the REO_6 octahedra (orange) and SiO_4 tetrahedra (blue).

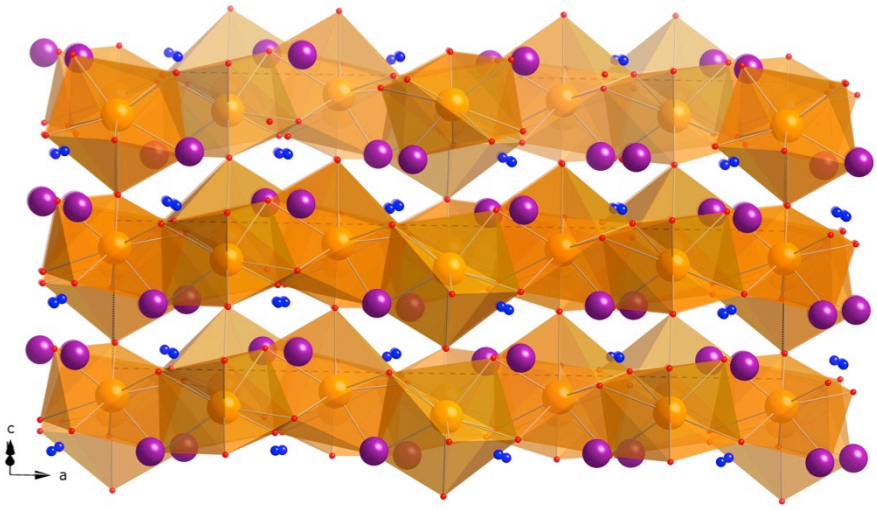

Figure 7.6. Structural image of $NaLaSiO_4$ where the La columns along the *c* axis are shown. La polyhedra are shown in orange, Si is shown in blue, Na is shown in purple, and O is shown in red.

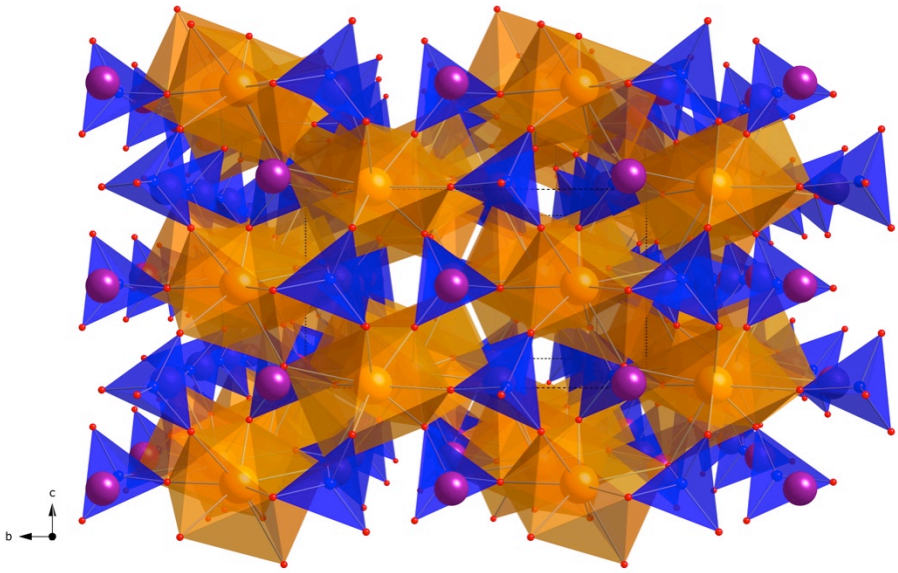

Figure 7.7. Structural representation of $NaLaSiO_4$ down the *a* axis where the color scheme is the same as Figure 7.6.

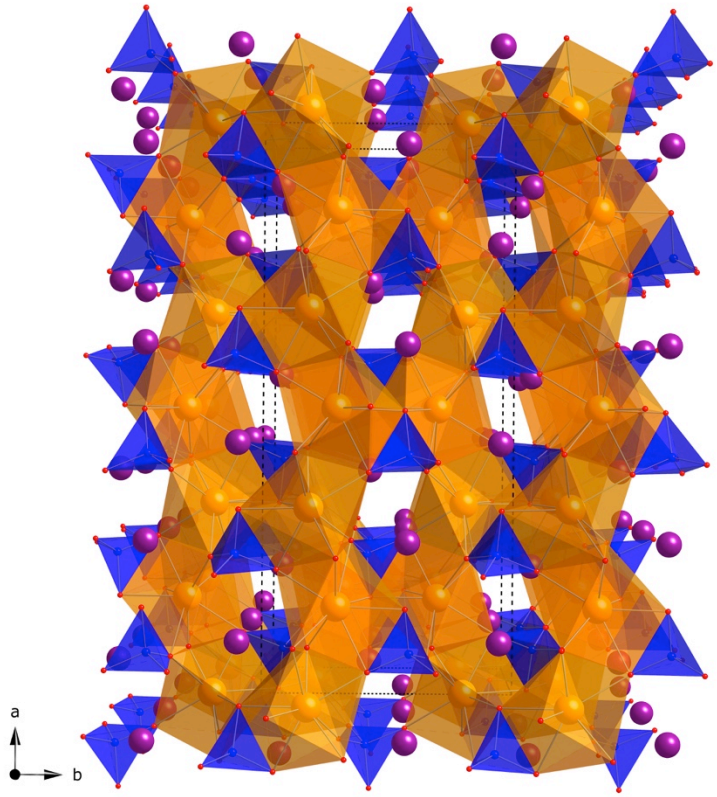

Figure 7.8. Structural representation of $NaLaSiO_4$ showing the structure down the *c* axis where the color scheme follows the one detailed in Figure 7.6.

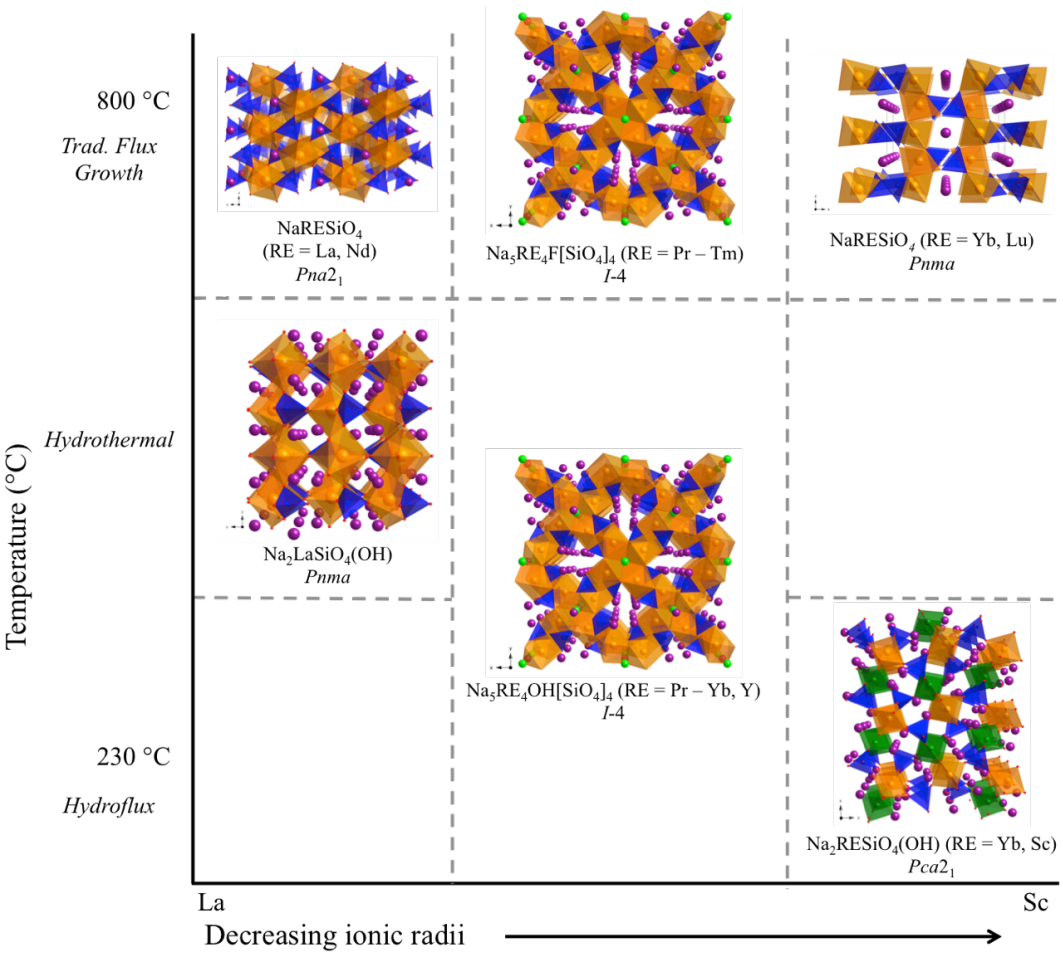

Figure 7.9. Scheme to organize the reported phases based on their synthesis conditions and as a function of rare earth cation size.

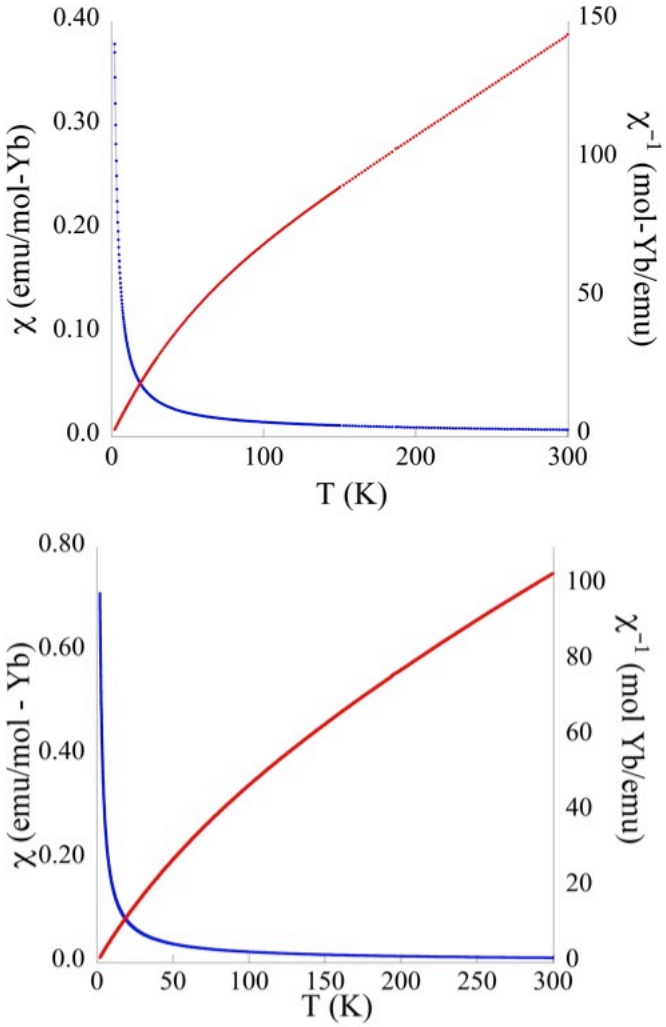

Figure 7.10. Magnetic susceptibility and inverse magnetic susceptibility data of $Na_2YbSiO_4(OH)$ (top) and $NaYbSiO_4$ (bottom).

Chapter 8

Synthesis, Structure, and Polymorphism of $A_3LnSi_2O_7$ (A = Na, K; *Ln* = Sm, Ho, Yb)*

*Latshaw, A. M.; Yeon, J.; Smith, M. D.; zur Loye, H.-C. *J. Solid State Chem.*, **2016**, *235*, 100-106.

Introduction

Lanthanide containing silicates are an intensively researched area. With a highly adaptive framework that can incorporate many lanthanide elements, it has been possible to synthesize numerous compositions and structural series of rare earth silicates. The extensive research in lanthanide silicates is often driven by the wide range of optical and magnetic properties observed in these silicates.[8.1-8.6] Herein we report the crystal growth of $K_3SmSi_2O_7$ and $Na_3LnSi_2O_7$ (*Ln* = Ho, Yb) and magnetic property measurements of the $Na_3LnSi_2O_7$ (*Ln* = Ho, Yb) compositions.

The $A_3LnSi_2O_7$ type silicates have been structurally characterized and many examples are known. When A = K, reported compositions include $K_3NdSi_2O_7$,[8.7] $K_3EuSi_2O_7$,[8.8] $K_3GdSi_2O_7$ – $K_3LuSi_2O_7$,[8.6] and even $K_3ScSi_2O_7$.[8.9] $K_3SmSi_2O_7$ fills the gap in the $K_3LnSi_2O_7$ (*Ln* = Nd – Lu) series so that now all except radioactive promethium have been reported. When A = Na, the known compositions are not as extensive and the only published sodium analogues are $Na_3LnSi_2O_7$ (*Ln* = Tm, Y, Sc)[8.10] and $Na_3LuSi_2O_7$.[8.11] We report two new $Na_3LnSi_2O_7$ compositions; holmium and ytterbium where two polymorphs of the ytterbium phase were found.

All compositions were synthesized using fluoride fluxes, with $K_3SmSi_2O_7$ being grown out of a KF flux and all $Na_3LnSi_2O_7$ compositions grown out of a NaF/NaCl eutectic flux. Fluoride fluxes have, in general, been found to be very good at dissolving silicon dioxide and lanthanide oxides.[8.12] Alkali fluoride fluxes are also useful because they can be either reactive or non-reactive. Examples in the literature include systems like $K_5Y_2FSi_4O_{13}$[8.13] and $A_5RE_4F[SiO_4]_4$ (A = Na, K; RE = Pr, Nd, Sm – Tm)[8.3] where the fluoride source was either the KF or NaF/NaCl eutectic flux, respectively. In the

ubiquitous apatite family, $A_xLn_{10-x}(SiO_4)_6O_{2-y}F_y$ (A = Na, K; *Ln* = Pr, Sm – Gd)[8.14], $0 \leq y \leq 1.28$ the fluoride from the alkali fluoride fluxes may or may not incorporate itself into the structure. In the system discussed herein, $A_3LnSi_2O_7$ (A = Na, K; *Ln* = Sm, Ho, Yb, Y) fluoride incorporation does not occur, which is analogous to what has been found for $K_3LnSi_2O_7$ (*Ln* = Gd – Lu).[8.6] With this in mind, one can begin to understand how small changes in fluoride flux conditions can often impact the compositions crystallized, making fluoride flux growth both versatile and, however, at times unpredictable.

Many times, small changes in reaction conditions lead to different compositions or, in reactions that yield mixed products, may favor one composition over the other. In the current system, it was observed that changes in reaction conditions, while maintaining the same eutectic flux ratio, caused the $Na_3YbSi_2O_7$ composition to crystallize in both the hexagonal $P6_3/m$ and trigonal $P31c$ space groups. Interestingly, the conditions that led to the $P31c$ space group for $Na_3YbSi_2O_7$ led to the different space group of $P6_3/m$ for $Na_3HoSi_2O_7$, which one might have expected from the use of the identical synthetic conditions.

Experimental Section

Reagents

Sm_2O_3 (99.9 %), Ho_2O_3 (99.9 %), Yb_2O_3 (99.9 %), KF (99 % min.), and NaF (99 % min.) were purchased from Alfa Aesar. Na_2CO_3 (ACS grade), and NaCl (ACS grade) were purchased from Fisher Scientific. SiO_2 (99.99 %) was purchased from Aldrich as fused pieces and ground to a powder in a ball mill.

Synthesis

Crystals of $K_3SmSi_2O_7$ were grown using a KF flux. Sm_2O_3 (0.5 mmol) and SiO_2 (1 mmol) were loaded into a silver crucible. KF (5 g) was loaded on top of the reactants and a silver lid was loosely fitted on the crucible. The crucible was placed into a programmable furnace that was set to ramp to 900 °C and dwell there for 12 h before slow cooling to 700 °C at a rate of 6 °C/h. Upon cooling to 700 °C the furnace was shut off. Crystals were isolated by dissolving the KF flux in water, aided by sonication, followed by vacuum filtration. $K_3SmSi_2O_7$ was the major phase with a small amount of unreacted Sm_2O_3 remaining.

Crystals of $Na_3HoSi_2O_7$ and $Na_3YbSi_2O_7$ (*P*31*c*) were grown through a NaF/NaCl eutectic flux. Ln_2O_3 (2 mmol), Na_2CO_3 (2 mmol), and SiO_2 (4 mmol) were added to a silver crucible. NaF (2.81 g) and NaCl (1.98 g) were then added to the crucible. A silver lid was loosely fitted to the crucible and the crucible was loaded into a programmable box furnace. The furnace was programmed to ramp to 800 °C, dwell there for 24 h, then slow cool to 600 °C at a rate of 6 °C/h before being shut off. Crystals were isolated by dissolving the NaF/NaCl flux in water, aided by sonication, followed by vacuum filtration. For Ho, the synthesis yielded a mixture of crystals of $Na_3HoSi_2O_7$ and $Na_5Ho_4F[SiO_4]_4$[8.3] and for Yb, the synthesis yielded a mixture of $Na_3YbSi_2O_7$ and $NaYbSiO_4$.[8.15]

Crystals of $Na_3YbSi_2O_7$ (*P*6$_3$/*m*) were grown through a NaF/NaCl eutectic flux. Yb_2O_3 (1 mmol), Na_2CO_3 (1 mmol), and SiO_2 (2 mmol) were loaded into a silver crucible. NaF (2.81 g) and NaCl (1.93 g) were then added to the crucible. A silver lid was loosely fitted on the crucible and the crucible was loaded into a programmable box

furnace. The furnace was programmed to go to 900 °C, dwell there for 60 h, then slow cool to 650 °C at a rate of 3 °C/h before being shut off. Crystals were isolated by dissolving the NaF/NaCl flux in water, aided by sonication, followed by vacuum filtration. The reaction product was a mixture of $Na_3YbSi_2O_7$, $NaYbSiO_4$,[8.15] and Yb_2O_3 as determined by powder X-ray diffraction.

A polycrystalline powder of $Na_3HoSi_2O_7$ was synthesized using traditional solid state methods. Ho_2O_3 (0.5 mmol), SiO_2 (2 mmol), and Na_2CO_3 (1.5 mmol) were ground for 30 minutes, placed into an open alumina crucible, and then put in a programmable furnace. The furnace was programmed to reach 600 °C and dwell there for 6 h to calcine the reaction before being set to its final dwelling temperature of 800 °C. With 30 min regrindings occurring every 24 – 48 h, the reaction was dwelled at 800 °C for a total of 456 h. At this point, the reaction had stopped changing, as evidenced by an invariant powder X-ray diffraction pattern, and consisted of the desired phase and a small amount of unreacted Ho_2O_3 and SiO_2. 10 % of the original amount of Na_2CO_3 was then added to the reaction, which was ground for another 30 min. The reaction was then put in a programmable furnace which was programmed to dwell at 600 °C to calcine the reaction before dwelling at 800 °C for 48 h. After 48 h, the reaction was phase pure. A traditional solid state reaction was also attempted for the Yb analogues, however, both polymorphs formed at the same temperatures.

Single-Crystal X-ray Diffraction

$P6_3/mcm$: $K_3SmSi_2O_7$

X-ray intensity data from a colorless multifaceted prismatic crystal were collected at 296(2) K using a Bruker SMART APEX diffractometer (Mo Kα radiation, λ = 0.71073

Å).[8.16] The data collection covered 100% of reciprocal space to $2\theta_{max}$ = 70.5º, with an average reflection redundancy of 26.6 and R_{int} = 0.036 after absorption correction. The raw area detector data frames were reduced and corrected for absorption effects with the SAINT+ and SADABS programs.[8.16] Final unit cell parameters were determined by least-squares refinement of 7870 reflections from the data set. The initial structural model was taken from the literature.[8.6] Subsequent difference Fourier calculations and full-matrix least-squares refinement against F^2 were performed with SHELXL-2013/4[8.17] using the ShelXle interface.[8.18] All atoms were refined with anisotropic displacement parameters. There was no deviation from full occupancy observed for any of the metal atoms, based on trial refinement of the site occupation factors. The largest residual electron density peak and hole in the final difference map are +1.04 and -0.78 e-/Å3, located 0.68 and 0.15 Å from Sm(2) and K(1), respectively.

$P6_3/m$: $Na_3HoSi_2O_7$ and $Na_3YbSi_2O_7$

X-ray intensity data from a pale yellow hexagonal prism crystal ($Na_3YbSi_2O_7$), and a pale pink block crystal ($Na_3HoSi_2O_7$) were collected at 294(2) K using a Bruker SMART APEX diffractometer (Mo Kα radiation, λ = 0.71073 Å).[8.16] The data collection covered 100 % of reciprocal space to $2\theta_{max}$ = 56.6° with an R_{int} = 0.0335, and 0.0312, respectively, after absorption correction. The raw area detector data frames were reduced and corrected for absorption effects with the SAINT+ and SADABS programs.[8.16] Final unit cell parameters were determined by least-squares refinement the data set. An initial structural model was obtained with direct methods.[8.17] Subsequent difference Fourier calculations and full-matrix least-squares refinement against F^2 were performed with SHELXL-2013/4[8.17] using ShelXle.[8.18] All atoms were refined with anisotropic

displacement parameters. All atoms were fully occupied based on trial refinement of the site occupation factors.

P31c: $Na_3YbSi_2O_7$

X-ray intensity data from a colorless hexagonal plate crystal of $Na_3YbSi_2O_7$ were collected at 296(2) K using a Bruker SMART APEX diffractometer (Mo Kα radiation, λ = 0.71073 Å).[8.16] The data collection covered 100% of reciprocal space to $2\theta_{max}$ = 70.5º, with an average reflection redundancy of 17.6 and R_{int} = 0.048 after absorption correction. The raw area detector data frames were reduced and corrected for absorption effects with the SAINT+ and SADABS programs.[8.16] Final unit cell parameters were determined by least-squares refinement of 8934 reflections from the data set. An initial structural model was obtained with direct methods.[8.17] Subsequent difference Fourier calculations and full-matrix least-squares refinement against F^2 were performed with SHELXL-2013/4[8.17] using ShelXle.[8.18]

The compound crystallizes in the trigonal system. The pattern of systematic absences in the intensity data suggested the space groups *P*31*c*, *P*-31*c* *P*6$_3$*mc*, *P*-62*c* and *P*6$_3$/*mmc*. Some difficulty was encountered in identifying the proper space group, most likely because of the twinning discussed below. The non-centrosymmetric group *P*31*c* (No. 159) was eventually confirmed by structure solution. The completed model in *P*31*c* was checked for missed symmetry elements with ADDSYM, which found none.[8.19-8.22] The crystal was refined as a four-component, combined merohedral and inversion twin. Two domains related by a two-fold axis of rotation along the trigonal [110] direction were generated by the twin law [010 / 100 / 00-1]. The major domain volume fraction refined to 0.753(8). Each of these two domains was further twinned by inversion, with

refined volume fractions of 0.791(8) (for the major domain) and 0.890(8) (minor domain). The crystal therefore was modeled as being composed of four domains making up 59.6, 15.7, 22.0, and 2.7 % of the crystal. The twin laws were determined by trial-and-error after a reasonable model in *P*31*c* appeared to reach a refinement minimum of *R*1 ~ 8%. Including the merohedral twin law lowered the *R*1-value to 2.6 %, and produced a Flack parameter of 0.149(5). The non-zero Flack parameter suggested the presence of inversion twinning, though with only a small contribution to the diffraction data. Accounting for inversion twinning of both domains lowered the *R*1-factors to the reported 2.4 %. All atoms were refined with anisotropic displacement parameters. No deviation from full occupancy was observed for any of the ytterbium atoms. The largest residual electron density peak and hole in the final difference map are +1.54 and -2.16 e-/Å3, located 1.01 and 0.55 Å from Yb(2) and Yb(4), respectively.

Further details of the crystal structure investigation can be obtained from the Fachinformationszentrum Karlsruhe, 76344 Eggenstein-Leopoldshafen, Germany (fax:+497247808666; e-mail: crystdata@fiz-karlsruhe.de) on quoting the depository numbers 430192 ($Na_3YbSi_2O_7$ – hexagonal), 430193 ($K_3SmSi_2O_7$), 430194 ($Na_3HoSi_2O_7$), 430195 ($Na_3YbSi_2O_7$ – trigonal).

Powder X-ray Diffraction

Powder X-ray diffraction (PXRD) data were collected on powders, either ground crystals or polycrystalline, of $Na_3YbSi_2O_7$ (both phases) and $Na_3HoSi_2O_7$ using a Rigaku Dmax/2100 powder diffractometer using Cu Kα radiation for the $Na_3YbSi_2O_7$ samples and a Rigaku Ultima IV diffractometer with a Cu Kα source (λ 1.54056 Å) and a D/teX detector for $Na_3HoSi_2O_7$. Data for the compounds were collected using a step scan

covering the 2θ range of 5 – 65 ° in steps of 0.02 °. After PXRD data were collected, the cif file of the respected phases were overlaid and it was determined that $Na_3YbSi_2O_7$ ($P6_3/m$) was a mixture of $Na_3YbSi_2O_7$, $NaYbSiO_4$, and a small amount of Yb_2O_3; $Na_3YbSi_2O_7$ ($P31c$) was a mixture of $Na_3YbSi_2O_7$ and $NaYbSiO_4$; and $Na_3HoSi_2O_7$ was phase pure (**Figure 8.1**).

Magnetic Measurements

The DC magnetic susceptibilities of $Na_3YbSi_2O_7$ and $Na_3HoSi_2O_7$ were measured as a function of temperature using a Quantum Design MPMS 3 SQUID Magnetometer. 52.70 mg of a mixed ground polycrystalline powder of $Na_3YbSi_2O_7$ ($P31c$) and $NaYbSiO_4$, 75.91 mg of a mixed ground polycrystalline powder of $Na_3YbSi_2O_7$ ($P6_3/m$) $NaYbSiO_4$, and Yb_2O_3, and 45.91 mg of a pure polycrystalline sample of $Na_3HoSi_2O_7$ were massed on a balance sensitive to 0.01 mg and loaded into a gelatin capsule for data collection. The zero-field cooled magnetic susceptibility was measured as a function of temperature between 2-300 K in an applied field of 1000 Oe. The measured magnetic data were corrected for shape and radial offset effects using the method reported by Morrison et. al.[8.23]

Results and Discussion

Synthesis

Two different fluxes, KF and a 67 % NaF/ 33% NaCl eutectic mixture were used to synthesize four new silicate materials. Using the eutectic sodium halide flux, two different crystals, $Na_3HoSi_2O_7$, which crystallizes in the space group $P6_3/m$, and $Na_3YbSi_2O_7$, which crystallizes in the space group $P31c$, were crystallized under the identical reaction conditions, however, when the reaction temperature was increased, the

*P*6$_3$/*m* polymorph of $Na_3YbSi_2O_7$ was obtained. Crystals of the Yb *P*6$_3$/*m* phase were obtained when the reaction was dwelled 100 °C higher, dwelled for 36 hours longer, and cooled at half the cooling rate. Since all conditions were changed (except the eutectic flux ratio), it is impossible to be certain exactly what caused the space group change, however, it is clear that a longer reaction at a higher temperature was needed to crystallize the ytterbium containing *P*6$_3$/*m* phase. The space group change could therefore be the result of a size effect, a kinetic effect, or a thermodynamic effect. A size effect would make sense since in the $K_3LnSi_2O_7$ system reported by Vidican[8.6] it was found that under identical reaction conditions the lanthanides Gd – Lu, all crystallized in the *P*6$_3$/*mcm* space group, except for the Lu member, which crystallized in *P*6$_3$/*mmc*. It is possible that when using identical conditions for the lanthanide series that there is a size effect where the composition still crystallizes but crystallizes in a different space group. If the space group of the crystal is under kinetic control, then the longer dwelling and cooling times could have favored the hexagonal space group. Finally, if it was a thermodynamic effect, the higher reaction temperatures might have caused a change in the structure. After attempting a solid state reaction with Yb and finding that at 800 °C both phases formed, thermodynamic effects can most likely be ruled out leaving size and kinetic effects, or perhaps some combination of both.

Structures

P6$_3$/mcm: $K_3SmSi_2O_7$

$K_3SmSi_2O_7$ is isostructural with $K_3LnSi_2O_7$ (*Ln* = Nd, Eu – Tm).[8.6, 8.7] In this *P*6$_3$/*mcm* space group, there are two unique samarium sites, one unique silicon site, three unique potassium sites, and three unique oxygen sites. Crystallographic data is listed in

Table 8.1 with selected interatomic distances contained in **Table 8.2**. In this structure, both samarium sites are 6 coordinated, with $Sm(1)O_6$ forming a trigonal prism and $Sm(2)O_6$ forming an octahedra. Silicon is found in bent Si_2O_7 units where the bend occurs towards the Sm(1) trigonal prisms. The bridging Si – O – Si angles for the Si_2O_7 units are shown in **Table 8.3**. Three Si_2O_7 units corner share with the Sm(1) trigonal prism through O(2) (**Figure 8.2**). The other four oxygen sites (O(1)) on the Si_2O_7 that are not making the Si – O(3) – Si bond or corner share to the Sm(1) trigonal prism are corner sharing to the Sm(2) octahedra. When viewed down the *c* axis, it can be seen that the Sm(1) trigonal prisms are each rotated 60 ° with respect to the one above it and that the Sm(2) octahedra perfectly stack on top of one another (**Figure 8.3**). K(1) atoms are located in line with the Si atoms and K(2) atoms are located in line with the Sm(2) atoms down the *c* axis; finally the K(3) atoms are located in line with Sm(1) atoms down the *c* axis. The overall structure viewed down the *b* axis is shown in **Figure 8.4**.

$P6_3/m$: $Na_3HoSi_2O_7$ and $Na_3YbSi_2O_7$

$Na_3HoSi_2O_7$ and one polymorph of $Na_3YbSi_2O_7$ crystallize in the hexagonal space group $P6_3/m$ and are isostructural with $Na_3YSi_2O_7$ and $Na_3LuSi_2O_7$.[8.10, 8.11] Crystallographic tables for both reported compositions are included in **Table 8.1** with selected interatomic distances shown in **Table 8.2**. In this structure there are two unique lanthanide sites, one unique silicon site, four unique sodium sites, and four unique oxygen sites. As in $K_3SmSi_2O_7$, both *Ln* sites are 6 coordinated with *Ln*(1) adopting a trigonal prism and *Ln*(2) an octahedral coordination environment. Also, as found in $K_3SmSi_2O_7$, the silicon is located in bent Si_2O_7 units that are once again corner shared to the Sm(1) trigonal prisms, however, unlike in $K_3SmSi_2O_7$, the bend of the Si_2O_7 unit does

not point towards the trigonal prism (**Figure 8.5**). Bridging Si – O – Si angles for the Si_2O_7 units are summarized in **Table 8.3**. The remaining oxygens on the Si_2O_7 unit, O(1) and O(3) corner share to the *Ln*(2) octahedra. When looking down the *c* axis, the structure appears similar to that of $K_3SmSi_2O_7$ because the *Ln*(1) trigonal prisms are again rotated 60 ° with respect to the one above it and the *Ln*(2) octahedra are again stacked perfectly on top of each other. The Si_2O_7 units are responsible for the major difference between this structure and the $K_3SmSi_2O_7$ structure down the *c* axis. Because the Si_2O_7 units do not bend towards *Ln*(1), they do not form a perfectly symmetrical pinwheel shape when viewing the structure down the *c* axis (**Figure 8.6**). The structure has four sodium sites compared to the three in the $K_3SmSi_2O_7$ structure. The Na(1) atoms are in line with the *Ln*(1) atoms down the *c* axis, the Na(2) and Na(3) atoms alternate and are in line with the *Ln*(2) atoms down the *c* axis, and the Na(4) atoms fill in the channels of the Si_2O_7 units down the *c* axis. The overall structural image viewed down the *b* axis is shown in **Figure 8.7**.

P31c: $Na_3YbSi_2O_7$

$Na_3YbSi_2O_7$ crystallizes in the trigonal space group *P*31*c*. Crystallographic tables for the composition are shown in **Table 8.1** with selected interatomic distances shown in **Table 8.2**. In this structure, there are 43 unique atomic positions in the asymmetric unit: 5 ytterbium atoms, 6 silicon atoms, 11 sodium atoms and 21 oxygen atoms. All atoms are located on general positions (site 6*c*) except for Yb(3), Yb(4), Na(9), and Na(10), which are located on the threefold axis at (1/3,2/3,*z*) (site 3*b*), and Yb(5) and Na(11), which are located on the threefold axis at (0,0,*z*) (site 3a). Like the previous structures, all ytterbium sites are 6 coordinated with octahedral, trigonal prismatic, and distorted CN

= 6 coordination environments. In this structure, Yb(1) and Yb(2) are all octahedral while Yb(4) is trigonal prismatic. Yb(3) and Yb(5) are distorted. The silicon, as in the previous structures, occupies bent Si_2O_7 units that are corner shared to ytterbium polyhedra. The bridging Si – O – Si angles of the Si_2O_7 units are listed in **Table 8.3**. The Si_2O_7 units are formed by Si(1) and Si(2), Si(3) and Si(4), and Si(5) and Si(6), respectively. Each Si_2O_7 unit corner shares with two Yb(1) and two Yb(2) polyhedra with Si(1) and Si(2) also corner sharing to two Yb(5), Si(3) and Si(4) with two Yb(3), and Si(5) and Si(6) with two Yb(4). The sodium atoms fill channels between the ytterbium and silicon polyhedra. The overall structural images viewed down the *a* and *c* axes are shown in **Figures 8.8** and **8.9**, respectively. The view down the *c* axis emphasizes how the additional ytterbium, silicon, and sodium sites change the structure between the three different structures.

Magnetic Measurements

Herein we present the first reported magnetism on the $A_3LnSi_2O_7$ compositions. The magnetic data for $Na_3HoSi_2O_7$ is summarized in **Table 8.4**. The $Na_3HoSi_2O_7$ sample was a phase pure polycrystalline sample while the magnetism samples of both $Na_3YbSi_2O_7$ contained a mixture of $Na_3YbSi_2O_7$ and $NaYbSiO_4$, with the hexagonal phase also containing some Yb_2O_3. The magnetic susceptibilities and inverse susceptibilities are shown in **Figure 8.10**. All three samples are paramagnetic. We did not calculate the moments for the Yb samples due to the presence of impurities. For Ho, the inverse susceptibility was fit over the range of 150 – 300 K. The effective moment is 10.16 μ_B for $Na_3HoSi_2O_7$, which is close to the expected moment for Ho, 10.4 μ_B.

Conclusion

$K_3SmSi_2O_7$, $Na_3HoSi_2O_7$, and two polymorphs of $Na_3YbSi_2O_7$ are reported, where the compositions reported herein crystallize in three different space groups. $P6_3/mcm$ and $P6_3/m$ are space groups that have been previously reported for members of the $A_3LnSi_2O_7$ family, however, $P31c$ represents a new structure type for $A_3LnSi_2O_7$ compositions. We report the first magnetic studies on this structural family, in which it was determined that these compositions are paramagnetic.

References

8.1 Belov, K. P.; Toropov, N. A.; Bondar, I. A.; Mitina, L. P. *Izv. Akad. Nauk SSSR, Neorg. Mater.* **1969**, *5*, 565-568.
8.2 Emirdag-Eanes, M.; Pennington, W. T.; Kolis, J. W. *J. Alloys Compd.* **2004**, *366*, 76-80.
8.3 Latshaw, A. M.; Wilkins, B. O.; Hughey, K. D.; Yeon, J.; Williams, D. E.; Tran, T. T.; Halasyamani, P. S.; zur Loye, H.-C. *CrystEngComm.* **2015**, *17*, 4654-4661.
8.4 Latshaw, A. M.; Chance, W. M.; Morrison, G.; Smith, M. D.; Yeon, J.; zur Loye, H.-C. *CrystEngComm* **2015**, *17*, 4691-4698.
8.5 Ueda, S.; Wakeshima, M.; Hinatsu, Y. *Kidorui* **2013**, *62*, 166-167.
8.6 Vidican, I.; Smith, M. D.; zur Loye, H.-C. *J. Solid State Chem.* **2003**, *170*, 203-210.
8.7 Hwang, M. S.; Hong, H. Y.-P. *Acta Crystallogr., Sect. C: Cryst. Struct. Commun.* **1987**, *43*, 1241-1243.
8.8 Bondar, I. A.; Tenisheva, T. F.; Toropov, N. A.; Shepelev, Y. F. *Dokl. Akad. Nauk SSSR* **1965**, *160*, 1069-1071.
8.9 Napper, J. D.; Layland, R. C.; Smith, M. D.; zur Loye, H.-C. *J. Chem. Crystallogr.* **2004**, *34*, 347-351.
8.10 Sebais, M.; Pobedimskaya, E. A.; Dimitrova, O. V. *Kristallografiya* **1985**, *30*, 802-805.
8.11 Tamazyan, R. A.; Malinovskii, Y. A.; Sirota, M. I.; Simonov, V. I. *Kristallografiya* **1988**, *33*, 1128-1133.
8.12 Bugaris, D. E.; zur Loye, H.-C. *Angew. Chem. Int. Ed.* **2012**, *51*, 3780-3811.
8.13 Latshaw, A. M.; Myers, A. R.; Smith, M. D.; zur Loye, H.-C. *J. Chem. Crystallogr.* **2015**, *45*, 207-211.
8.14 Latshaw, A. M.; Hughey, K. D.; Smith, M. D.; Yeon, J.; zur Loye, H.-C. *Inorg. Chem.* **2015**, *54*, 876-884.
8.15 Latshaw, A. M.; Wilkins, B. O.; Chance, W. M.; Morrison, G.; Smith, M. D.; zur Loye, H.-C. *Solid State Sciences* **2016**, *51*, 59-65.
8.16 SMART Version 5.631, SAINT+ Version 6.45a and SADABS Version 2.10, Bruker Analytical X-ray Systems, Inc., Madison, Wisconsin, USA, 2003.
8.17 Sheldrick, G. M. *Acta. Cryst.* **2008**, *A64*, 112-122.
8.18 ShelXle: a Qt graphical user interface for SHELXL. Hübschle, C. B., Sheldrick, G. M., Bittrich, B. J. Appl. Cryst. 2011, 44, 1281-1284.
8.19 LePage, Y. *J. Appl. Crystallogr.* **1987**, *20*, 264-269.
8.20 Spek, A. L. *Acta. Cryst.* **1990**, *A 46*, C34.
8.21 Spek, A. L. *J. Appl. Crystallogr.* **1988**, *21*, 578-579.
8.22 PLATON, A Multipurpose Crystallographic Tool, Utrect University, Utrecht, The Netherlands, Spek, A. L. 1998.
8.23 Morrison, G.; zur Loye, H.-C. *J. Solid State Chem.* **2015**, *221*, 334-337.

Table 8.1. Crystallographic data for $K_3SmSi_2O_7$, $Na_3HoSi_2O_7$, and two crystals of $Na_3YbSi_2O_7$.

Formula	$K_3SmSi_2O_7$	$Na_3HoSi_2O_7$	$Na_3YbSi_2O_7$	$Na_3YbSi_2O_7$
Formula weight	435.83	402.88	410.19	410.19
Temperature (K)	296(2)	294(2)	294(2)	294(2)
Crystal system	Hexagonal	Hexagonal	Hexagonal	Trigonal
Space group	*P* $6_3/mcm$	*P* $6_3/m$	*P* $6_3/m$	*P* 31*c*
a (Å)	9.97640(10)	9.42330(10)	9.3770(2)	16.2081(2)
c (Å)	14.4844(3)	13.7882(3)	13.7187(4)	13.7077(4)
V ($Å^3$)	1248.47(4)	1060.34(3)	1044.65(4)	3118.60(12)
Z	6	6	6	18
Density (mg/m^3)	3.478	3.778	3.912	3.931
Absorption coefficient (mm^{-1})	8.842	11.711	13.954	14.023
Crystal size (mm^3)	0.14 × 0.10 × 0.08	0.08 × 0.08 × 0.04	0.16 × 0.08 × 0.08	0.20 × 0.16 × 0.05
2 theta range (°)	4.71 to 70.53	5.00 to 56.56	5.02 to 56.70	2.90 to 70.54
reflections collected	28791	14230	14399	86609
data/restraints/parameters	1047 / 0 / 41	926 / 0 / 64	926 / 0 / 64	9324 / 1 / 356
R (int)	0.0363	0.0312	0.0335	0.0476
GOF (F^2)	1.184	1.231	1.273	1.069
R indices (all data)	R_1 = 0.0354 wR_2 = 0.0766	R_1 = 0.0190 wR_2 = 0.0443	R_1 = 0.0143 wR_2 = 0.0350	R_1 = 0.0256 wR_2 = 0.0536

Table 8.2. Lanthanide interatomic distances for the reported compositions.

	Ln **– O distances (Å)**
$K_3SmSi_2O_7$	
Sm(1) – O(2) (x6)	2.338(2)
Sm(2) – O(1) (x6)	2.300(2)
$Na_3HoSi_2O_7$	
Ho(1) – O(2) (x6)	2.285(3)
Ho(2) – O(1) (x3)	2.235(3)
Ho(2) – O(3) (x3)	2.260(3)
$Na_3YbSi_2O_7$ – *P*6_3/*m*	
Yb(1) – O(3) (x6)	2.252(3)
Yb(2) – O(3) (x3)	2.203(3)
Yb(2) – O(4) (x3)	2.225(3)
$Na_3YbSi_2O_7$ – *P*31*c*	
Yb(1) – O(4)	2.179(6)
Yb(1) – O(9)	2.180(5)
Yb(1) – O(12)	2.206(5)
Yb(1) – O(7)	2.234(8)
Yb(1) – O(16)	2.239(6)
Yb(1) – O(19)	2.256(6)
Yb(2) – O(6)	2.178(6)
Yb(2) – O(18)	2.193(8)
Yb(2) – O(21)	2.206(8)
Yb(2) – O(11)	2.222(6)
Yb(2) – O(3)	2.233(5)
Yb(2) – O(14)	2.275(5)
Yb(3) – O(13) (x3)	2.209(6)
Yb(3) – O(10) (x3)	2.238(6)
Yb(4) – O(20) (x3)	2.252(5)
Yb(4) – O(17) (x3)	2.254(5)
Yb(5) – O(5) (x3)	2.217(6)
Yb(5) – O(2) (x3)	2.239(6)

Table 8.3. Si-Si bend angles for the reported compositions.

	Si-Si bend angles (°)
$K_3SmSi_2O_7$	
O(2) – O(3) – O(2)	68.27
$Na_3HoSi_2O_7$	
O(2) – O(4) – (O2)	69.86
$Na_3YbSi_2O_7$ – *P*6_3/*m*	
O(1) – O(2) – O(1)	68.72
$Na_3YbSi_2O_7$ – *P*31*c*	
Si(1) – Si(2)	
O(5) – O(1) – O(2)	69.61
Si(3) – Si(4)	
O(10) – O(8) – O(13)	67.58
Si(5) – Si(6)	
O(17) – O(15) – O(20)	68.13

Table 8.4. Experimental magnetic moments (μ_{eff}) compared to calculated moments (μ_{calc}) for $Na_3HoSi_2O_7$.

	$Na_3HoSi_2O_7$
Fit Range (K)	150 – 300
χ_0	--
θ (K)	-5.64
μ_{eff} (μ_B/RE)	10.16
μ_{calc} (μ_B/RE)	10.4

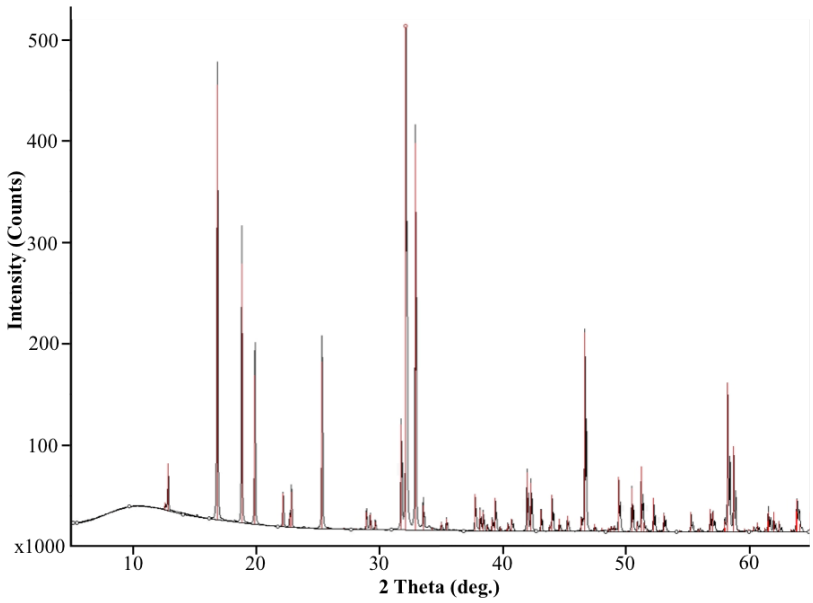

Figure 8.1. PXRD pattern of $Na_3HoSi_2O_7$ sample used for magnetic measurements where the observed pattern is shown in black with the cif file of $Na_3HoSi_2O_7$ overlaid in red.

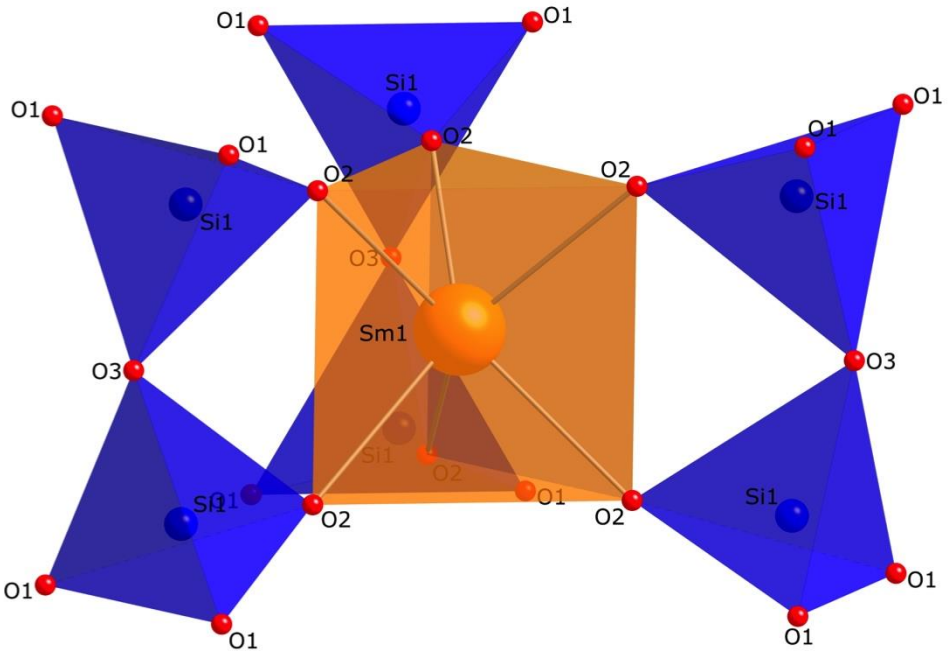

Figure 8.2. Illustration of how the Si_2O_7 units bend towards the Sm(1) trigonal prism.

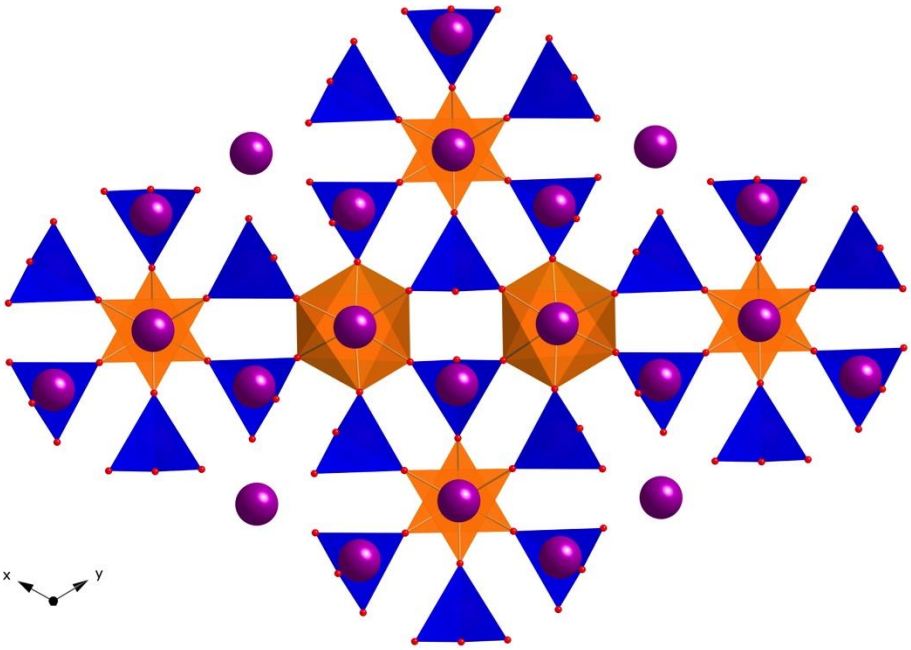

Figure 8.3. View down the *c* axis of $K_3SmSi_2O_7$ where Sm is shown in orange, Si is shown in blue, K is shown in purple, and O is shown in red.

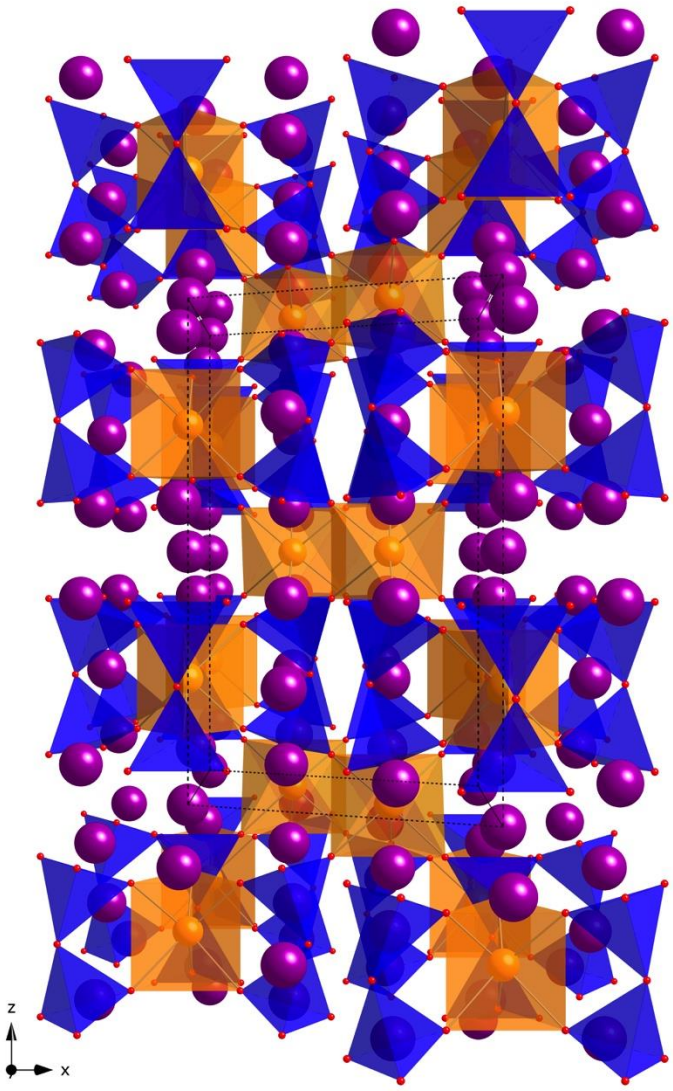

Figure 8.4. $K_3SmSi_2O_7$ shown down the *b* axis using the color scheme found in Figure 8.3.

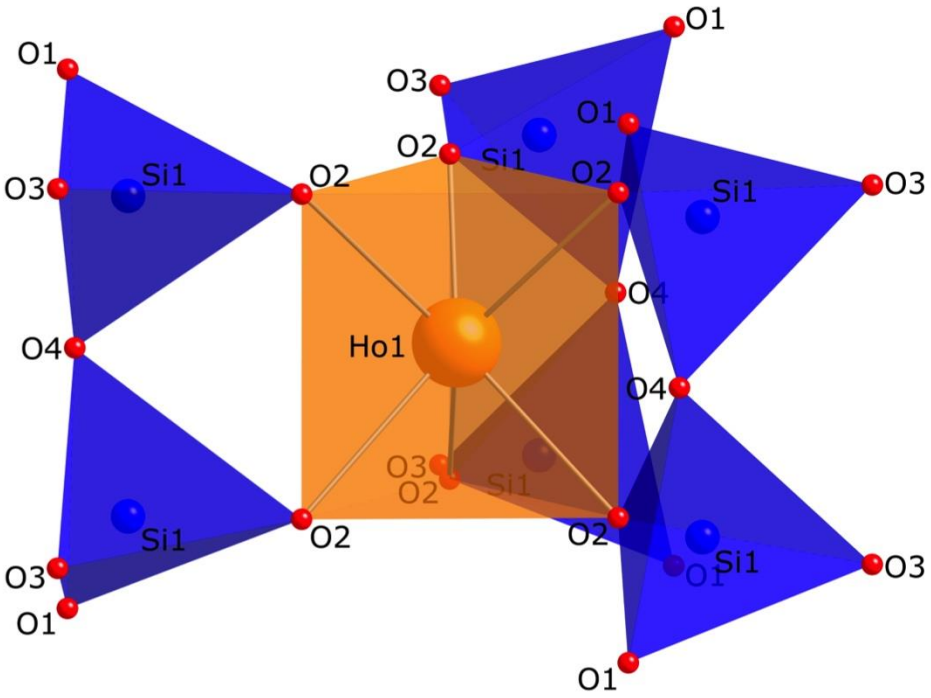

Figure 8.5. Illustration of bridging Si – O – Si angles and how the Si_2O_7 units do not point at the Ho(1) atom.

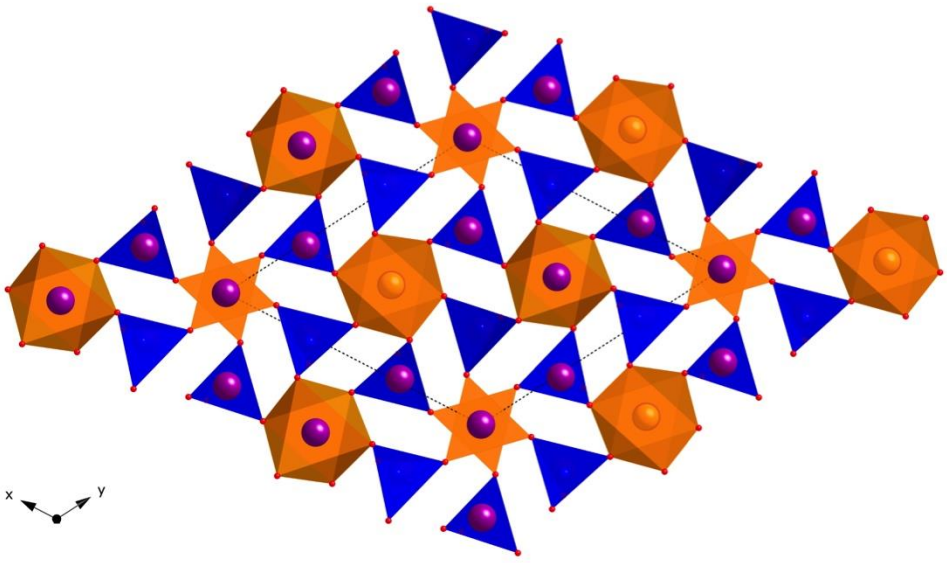

Figure 8.6. Illustration of $Na_3HoSi_2O_7$, representative of $Na_3YbSi_2O_7$ ($P6_3/m$), where the stacking of the lanthanide polyhedra and the tilt of the silicon polyhedra can be seen. Ho is shown in orange, Si is shown in blue, Na is shown in purple, and O is shown in red.

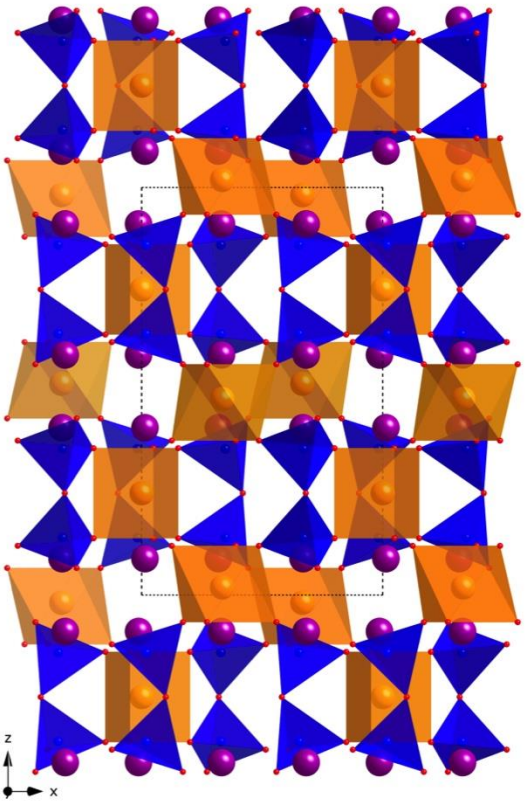

Figure 8.7. Overall structural image of $Na_3HoSi_2O_7$ down the *b* axis. Color scheme is described in Figure 8.6.

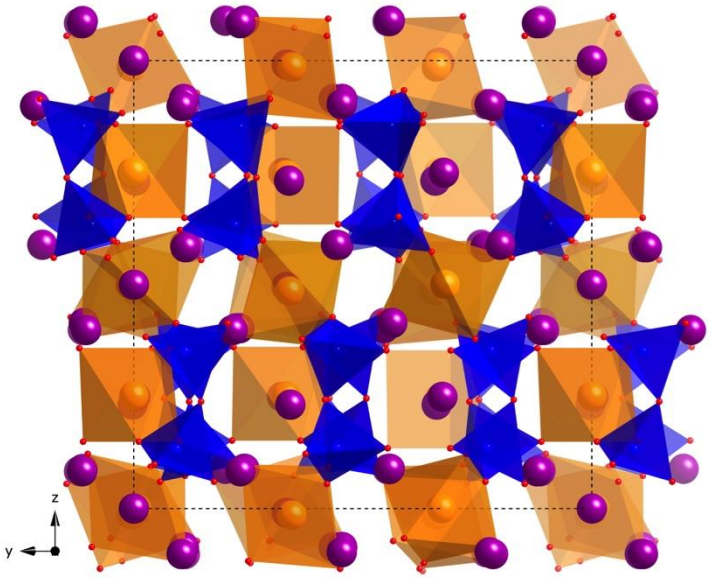

Figure 8.8. Visual representation of $Na_3YbSi_2O_7$ (*P*31*c*) down the *a* axis where Yb is shown in orange, Si is shown in blue, Na is shown in purple, and O is shown in red.

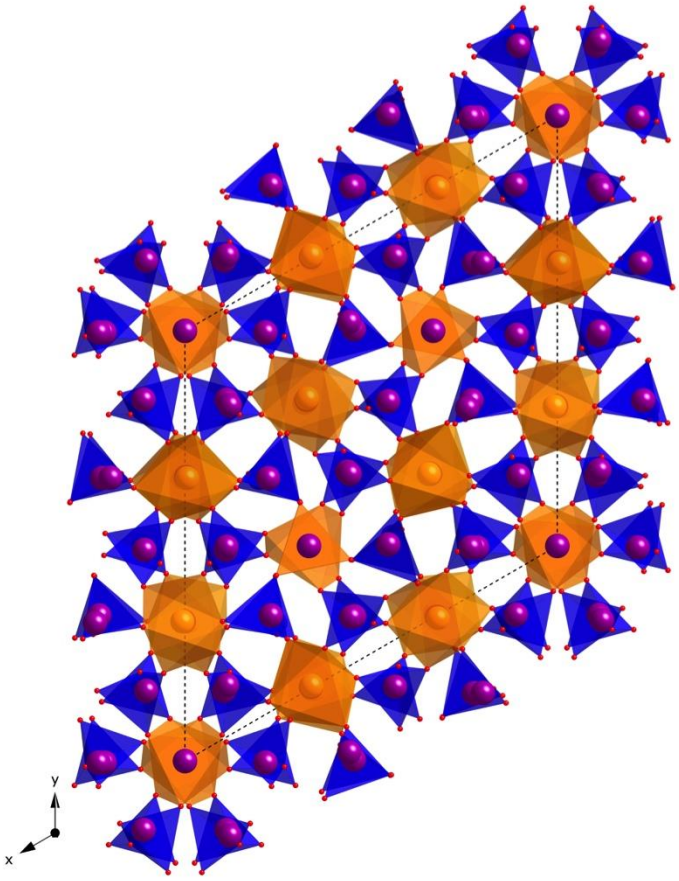

Figure 8.9. Visual representation of $Na_3YbSi_2O_7$ (*P*31*c*) down the *c* axis where the color scheme is the same as Figure 8.8.

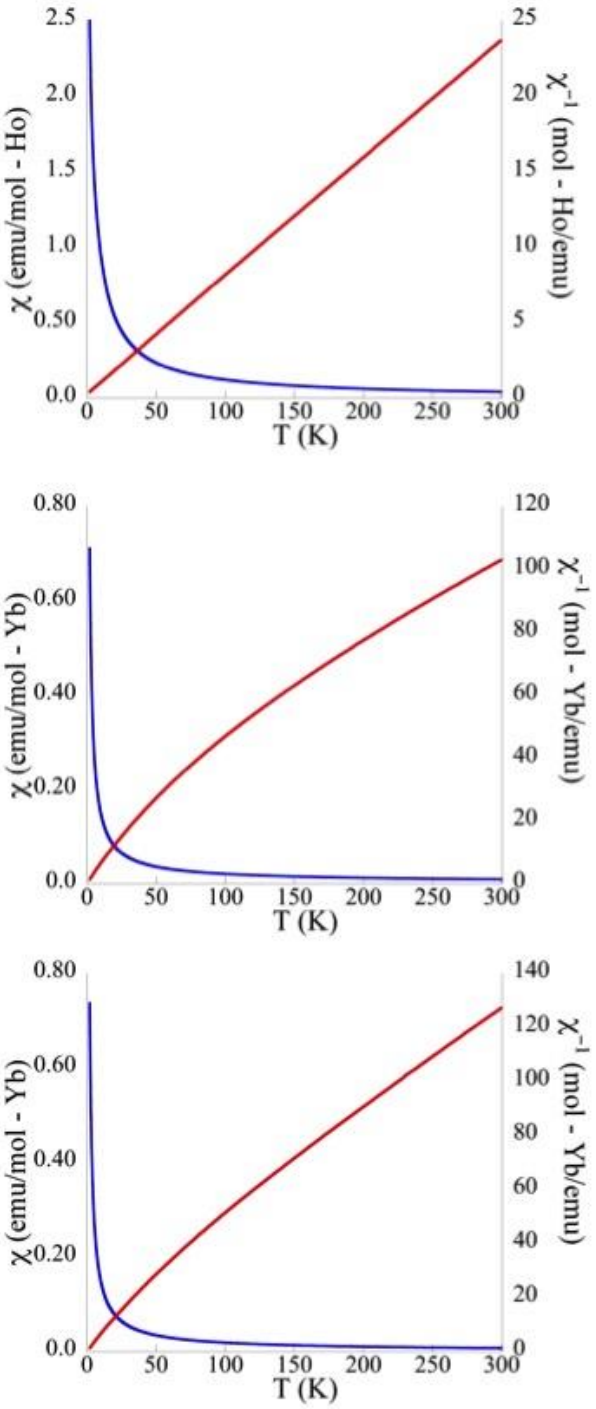

Figure 8.10. Magnetic susceptibility and inverse magnetic susceptibility data of $Na_3HoSi_2O_7$ (top), $Na_3YbSi_2O_7$ *P*6$_3$/*m* (middle), and $Na_3YbSi_2O_7$ *P*31*c* (bottom).

Chapter 9

Intrinsic Blue-White Luminescence, Luminescence Color Tunability, Synthesis, Structure, and Polymorphism of $K_3YSi_2O_7$*

*Latshaw, A. M.; Morrison, G.; zur Loye, K. D.; Myers, A. R.; Smith, M. D.; zur Loye, H.-C. *CrystEngComm*, **2016**, *18(13)*, 2294-2302

Introduction

The development of new luminescent host materials is motivated by the need for improved materials in numerous important applications, including new optical materials for use in solid state lighting,[9.1-9.4] in biomedical imaging (upconversion in particular),[9.5-9.7] and in optoelectronic devices.[9.8-9.10] These needs continue to advance research in the field of rare earth doped luminescent materials, where the development of new materials that emit in the visible portion of the electromagnetic spectrum when excited by higher energy visible light is of particular interest.[9.11] Many of the trivalent rare earths display luminescence due to the ease with which excited states can be populated, coupled with the prevalence of radiative rather than non-radiative decays to the ground state.[9.12] Trivalent europium specifically has attracted attention due to its intense red luminescence around 610 nm. The local environment plays a crucial role in the intensity of this luminescence and, hence, many inorganic materials, including oxides,[9.13-9.15] nitrides,[9.16] and other matrices[9.17] have been evaluated as hosts for luminescent rare earths. In addition, Eu^{3+} luminescence is enhanced and more tunable if it is the activator ion in a system that has a sensitizer ion.[9.18] Past research and LED technology has heavily relied on Ce^{3+} as the sensitizer ion in systems. Unfortunately, Ce^{3+} compositions must be synthesized in reducing conditions so it has become important to find other ions that can be sensitizers. Recently, a large amount of research has focused on Dy^{3+} as the sensitizer ion in compositions for LED technology.[9.18-9.23] Dy^{3+} has two strong emissions, a blue emission caused by the $^4F_{9/2}$ to $^6H_{15/2}$ transition and a yellow emission due to the $^4F_{9/2}$ to $^6H_{13/2}$ transition. Despite the positive change away from the need for reduced reaction conditions, the global shortage of select rare earth elements, specifically europium, has

driven up price and greatly restricted availability, driving a renewed interest in exploring self-activated luminescent materials.

Luminescent oxides can broadly be subdivided into self-activated or intrinsic, and rare earth activated phosphors, that encompass several classes of luminescent materials of current interest. Self-activated luminescent hosts often contain d^0 early transition metals, including tungstates and niobates, but do not contain late transition metals with d-electrons. As previously mentioned, there is a global shortage of select rare earth elements, which, along with the renewed interest in self-activated luminescent materials, is fueling the search for new intrinsic phosphors whose emissions can be tuned with very small quantities of rare earth elements to achieve white light emission.

Solid state lighting research is continuously focused on achieving the next advance in light emitting diode (LED) technology, where advanced phosphor coatings have to be more economical and exhibit better efficiencies than those currently on the market. In order to be more economical, it is important to only require small amounts of costly rare earth elements like europium. For that reason, over the past decade, researchers have explored the luminescence properties of yttrium and lutetium containing silicates that exhibit intrinsic luminescence.[9.24-9.27] Although intrinsically luminescent silicates are rare, sufficient numbers have been analyzed to conclude that the intrinsic luminescence arises from self-trapped excitons in the silicate structure.

In addition to intrinsically luminescent silicates, rare earth containing silicates have been studied as rare earth activated phosphors because the rigid silicate frameworks have few interactions with the rare earth ions, thereby not dampening the rare earth luminescence.[9.28-9.32] Despite their rigid frameworks, silicate compositions are often able

to incorporate many, if not all of the rare earth elements such as is seen in some structural families such as $A_5RE_4X[SiO_4]_4$ (A = Na, K; RE = Pr, Nd, Sm – Yb; X = F, OH),[9.30, 9.32] $K_3RESi_2O_7$ (RE = Nd, Sm-Lu, Sc),[9.33-9.36] and $Na_3LnSi_2O_7$ (*Ln* = Ho, Tm – Lu, Y, Sc).[9.37, 9.38] The ability to combine intrinsic luminescence in silicates with their ability to be color tuned via the introduction of small amounts of rare earths, such as europium, makes this a very promising class of luminescent materials.

We chose to use flux crystal growth to explore the preparation of new intrinsically luminescent silicates and, furthermore, to use flux crystal growth to dope small quantities of rare earth dopants, such as europium, into the silicate framework to fine tune the color emission. Fluoride fluxes are known to be good choices for synthesizing rare earth silicates, as they easily dissolve the silicon and rare earth starting materials, allowing new compositions to be synthesized in short reaction times.[9.39] Using optimized reaction conditions, phase pure products can be obtained and the amount of rare earth doped into such silicates can be confirmed by single crystal X-ray diffraction.

During our exploration of the alkali-metal:rare-earth:silicate system we synthesized two new polymorphs of a member of the $A_3RESi_2O_7$ compositional family, one of which is intrinsically luminescent. Herein we discuss the synthesis of the two polymorphs of $K_3YSi_2O_7$ and our doping studies that lead to white light emitting phosphors containing only 0.1 % of europium.

Experimental Section

Reagents

Y_2O_3 (99.99 % and 99.999 %) were purchased from Aldrich and Alfa Aesar, respectively. Dy_2O_3 (99.9 %), Eu_2O_3 (99.9 %), and KF (99 % min.) were purchased from

Alfa Aesar. SiO_2 (99.99 %) was purchased from Aldrich as fused pieces and ground to a powder in a ball mill.

Synthesis

Crystals of the $K_3YSi_2O_7$ composition that crystallizes in the space group $P6_3/mmc$ (**1**) were grown out of molten potassium fluoride flux. Y_2O_3 (99.99 %, 0.5 mmol), SiO_2 (1 mmol), and KF (1 g) were added to a silver tube that had been welded shut on the bottom. The tube containing the reactants was dried in a vacuum oven for 30 min before the other end of the tube was welded shut. The tube was placed in a programmable oven that was set to heat to 900 °C, dwell for 12 h, then slow cool to 700 °C at a rate of 6 °C/h at which point the furnace was shut off. The tube was then cut open and the flux was washed away by sonication in water before the crystals were isolated by vacuum filtration. This reaction led to a mix of both phases of $K_3YSi_2O_7$ and $K_5Y_2FSi_4O_{13}$, where there were very few crystals of the $K_3YSi_2O_7$ phase that crystallizes in the space group $P6_3/mmc$ (**1**). An SEM image is shown in **Figure 9.1**.

Crystals of $K_3YSi_2O_7$ that crystallize in the space group $P6_3/mcm$ (**2**) were grown out of a molten potassium fluoride flux. Y_2O_3 (99.999 %; 1 mmol), SiO_2 (2 mmol), and KF (1 g) were loaded into a silver tube that had been welded shut on the bottom. The loaded tube was dried in a drying oven at 110 °C for one h before it was crimped and folded three times. The crimped tube was loaded into a programmable furnace that was set to an identical program as that used to grow polymorph **1**, with the exception of a cooling rate of 3 °C/h instead of 6 °C/h. The tube was opened and the flux was removed by sonication in water before isolation by vacuum filtration. Other reaction conditions explored include the use of welded silver tubes, open silver crucibles, extended dwell

times, and faster cooling rates. The conditions reported were found to be the best conditions to favor the product and maximize crystal growth. An SEM image is shown in **Figure 1**.

Crystals of $K_3Y_{0.9}Dy_{0.1}Si_2O_7$ (**2-Dy**), where an SEM image is shown in **Figure 9.1**, and crystalline samples of doping levels of 0.1 % Eu, 15 % Dy and 0.12 % Eu, 15 % Dy and 0.1 % Eu, 10 % Dy and 0.1 % Eu (**2-Dy,Eu**), and 9 % Dy and 0.1 % Eu were grown out of the idealized conditions for the parent $K_3YSi_2O_7$ (**2**) composition using the appropriate doping levels of the respective rare earths. Accurate amounts of Eu doping were obtained by creating a 1 % Eu : 99 % Y stock of Eu_2O_3 and Y_2O_3 that was ground together for 30 min to mix. This stock was then weighed out along with appropriate Y_2O_3 amounts to obtain the desired ratios.

Single-Crystal X-ray Diffraction

X-ray intensity data from a colorless needle crystal of $K_3YSi_2O_7$ (**2**) and a colorless rod of $K_3Y_{0.9}Dy_{0.1}Si_2O_7$ (**2-Dy**) were collected at 298(2) and 303(2) K, respectively, using a Bruker D8 QUEST diffractometer equipped with a PHOTON100 CMOS area detector and an Incoatec microfocus source (Mo Kα radiation, λ = 0.71073 Å).[9.40] The data collection covered 100 % of reciprocal space to $2\theta_{max}$ = 72.7 º and 75.5 °, with R_{int} = 0.042 and 0.058, respectively, after absorption correction. The raw area detector data frames were reduced and corrected for absorption effects using the SAINT+ and SADABS programs.[9.40] Final unit cell parameters were determined by least-squares refinement of large sets (> 8800) reflections taken from the data set. An initial structural model was taken from the literature.[9.36] Subsequent difference Fourier calculations and

full-matrix least-squares refinement against F^2 were performed with SHELXL-2014[9.41] using the ShelXle and OLEX2 interfaces, respectively.[9.42, 9.43]

Both compounds (**2** and **2-Dy**) crystallize in the hexagonal system. The space group $P6_3/mcm$ (No. 193) was determined by successful structure solution. The compounds are isostructural with the Gd, Tb, Dy, Ho, Er, Tm, and Yb rare earth analogues reported previously.[9.36] All atoms were refined with anisotropic displacement parameters. Trial refinements of the site occupation factors showed no significant deviations from full occupancy for any atoms. The largest residual electron density peaks of 0.59 e-/Å^3 (**2**) and 0.61 e-/Å^3 (**2-Dy**) in the final difference maps are located < 0.6 Å from K1 (**2**) and K2 (**2-Dy**), and the deepest holes are -0.55 e$^-$/Å^3 (**2**) and -0.65 e$^-$/Å^3 (**2-Dy**), located <0.6 Å from K1 (**2**) and K2 (**2-Dy**).

X-ray intensity data from a colorless hexagonal prism of $K_3YSi_2O_7$ (**1**) were collected at 296(2) K using a Bruker SMART APEX diffractometer (Mo Kα radiation, λ = 0.71073 Å).[9.44] The data collection covered 100 % of reciprocal space to $2\theta_{max}$ = 70.2 º, with an average reflection redundancy of 19.5 (Laue group 6/mmm) and R_{int} = 0.0404 after absorption correction. The raw area detector data frames were reduced and corrected for absorption effects with the SAINT+ and SADABS programs.[9.44] Final unit cell parameters were determined by least-squares refinement of 2261 strong reflections taken from the data set. Atomic coordinates for the initial structural model were taken from the literature data for $K_3LuSi_2O_7$.[9.36] Full-matrix least-squares refinement against F^2 of this model and difference Fourier calculations and were performed with SHELXL[9.41] using the ShelXle interface.[9.42]

The compound crystallizes in the hexagonal system. Systematic absences in the intensity data were consistent with expected space group $P6_3/mmc$, which was confirmed by structure solution. The compound is isostructural with $K_3LuSi_2O_7$, and refinement of that model converged rapidly with yttrium on the rare earth site. All atoms were refined with anisotropic displacement parameters. The largest residual electron density peak of 0.39 e-/Å3 in the final difference map is located 0.46 Å from O1, and the deepest hole is -0.74 $e^-/Å^3$, located 1.10 Å from Si1. Further details of the crystal structure investigation can be obtained from the Fachinformationszentrum Karlsruhe, 76344 Eggenstein-Leopoldshafen, Germany (fax:+497247808666; e-mail: crystdata@fiz-karlsruhe.de) on quoting the depository numbers CSD- 430536 ($K_3Y_{0.9}Dy_{0.1}Si_2O_7$ – **2-Dy**), 430537 ($K_3YSi_2O_7$ – **1**), and 430538 ($K_3YSi_2O_7$ – **2**).

Powder X-ray Diffraction

Powder X-ray diffraction (PXRD) data were collected on ground samples of $K_3YSi_2O_7$ (**2**) and the doped compositions of 0.1 % Eu, 10 % Dy, 15 % Dy and 0.12 % Eu, 15 % Dy and 0.1 % Eu, 10 % Dy and 0.1 % Eu, 9 % Dy and 0.1 % Eu using a Rigaku Dmax/2100 powder diffractometer with a Cu Kα source (λ = 1.54056 Å). Data for the compounds were collected using a step scan covering the 2θ range of 5 – 80 ° in steps of 0.02 ° at a scan speed of 0.1 °/min. After PXRD data were collected, a diffraction pattern calculated using the cif file of the parent phase was overlaid to determine the purity of the samples. It was found that the samples also contained some SiO_2,[9.45] which does not affect the luminescence. X-ray diffraction patterns of the $K_3YSi_2O_7$ (**2**) and the white light emitting sample of 10 % Dy, 0.1 % Eu (**2-Dy,Eu**) are shown in **Figures 9.2** and **9.3**.

Fluorescence Spectroscopy

Room temperature emission spectra were collected on powders of the parent $K_3YSi_2O_7$ (**2**) and doped compounds at an excitation λ of 254 nm using an Edinburgh FS5 fluorescence spectrometer. A 150 W Continuous Wave Xenon Lamp was used for sample excitation, and the emission measured using a Hamamatsu R928P photomultiplier tube. For emission measurements, the ground powders were placed inside a 0.5 mm quartz sample holder using the SC-10 front-facing module. Emission scans were performed in the 410 – 800 nm range. Room temperature excitation and emission spectra of the parent $K_3YSi_2O_7$ (**2**) and doped compounds were collected using a Perkin Elmer LS 55 fluorescence spectrometer. Excitation spectra of **2-Dy,Eu** were collected in the 200 – 450 nm range at an emission λ of 401 nm and emission spectra were collected in the 200 – 750 nm range at an excitation λ of 280 nm.

Results and Discussion

Flux Growth

The use of high temperature solutions for crystal growth is well established [9.39] and, while crystals of most materials can be grown out of more than one solvent system, it is known empirically that some fluxes work especially well for some classes of materials. This is the case for alkali fluoride melts, which are believed to be one of the best solvent systems for oxides, corroborated by the fact that they have been used with great success for the crystal growth of a wide variety of complex oxides, including silicates. [9.31, 9.32, 9.35, 9.36, 9.46-9.48] There are of course many reasons why fluoride melts work so well for growing oxide crystals, including their relatively low melt temperatures and extensive capacity for dissolving oxides. In rare earth silicate chemistry, there has

been a recent surge in the use of molten fluoride flux growth[9.49-9.51] as it has been observed that fluorides enable quick dissolution of the rare earth oxides and silicon dioxide[9.30, 9.31, 9.35, 9.36, 9.46-9.48, 9.52-9.55] so complex oxides can be formed in relatively short reaction times.

The two polymorphs differ in structure as discussed below and their luminescent properties are quite different. For this reason the conditions under which phase pure products of (**2**) could be obtained were investigated. Depending on the rate used to cool from 900 °C to 700 °C, either a mixture of $K_3YSi_2O_7$ (**1**) and $K_5Y_2FSi_4O_{13}$,[9.48] (6 °C/h) or phase pure $K_3YSi_2O_7$ (**2**) (3 °C/h), were obtained. Europium and dysprosium substituted $K_3Y_{1-x-y}Dy_xEu_ySi_2O_7$ compositions were obtained as phase pure samples in the space group $P6_3/mcm$ when the 3 °C/h. cooling rate was employed.

Structure

$K_3YSi_2O_7$ (**1**) is isostructural to the previously reported compositions $K_3LuSi_2O_7$[9.36] and $K_3ScSi_2O_7$.[9.35] Interestingly, studies by Vidican et al.[9.36] observed a size dependence for the lanthanides in the $K_3LnSi_2O_7$ family, where for *Ln* = Gd – Tm all crystallize in the space group $P6_3/mcm$, while *Ln* = Lu crystallizes in the space group $P6_3/mmc$. Since the ionic radius of Y (0.9 Å), falls between the radii of Er (0.89 Å) and Ho (0.901 Å), it was predicted by Vidican that the yttrium containing composition would crystallize in the space group $P6_3/mcm$. [9.36, 9.56]

For $K_3YSi_2O_7$ (**1**) crystallizing in the space group $P6_3/mmc$, there is one unique yttrium site, one unique silicon site, two unique potassium sites, and two unique oxygen sites. The yttrium is located in an undistorted octahedral coordination environment. The yttrium sites are isolated from each other with every oxygen in the YO_6 octahedron being

corner shared with a silicon SiO_4 tetrahedra. The silicon tetrahedra form bent Si_2O_7 pyrosilicate units with bridging Si – O – Si linkages of 109 °. The potassium atoms are located in channels where K(1) is aligned with the silicon atoms down the *c*-axis and K(2) is aligned with the yttrium atoms down the *c*-axis. Images of the crystal structure viewed down the *a*- and *c*-axes are shown in **Figures 9.4** and **9.5**, respectively. Crystallographic tables and Y – O bond distances are given in **Tables 9.1** and **9.2**, respectively.

For $K_3YSi_2O_7$ (**2**) crystallizing in the space group $P6_3/mcm$, there are two unique yttrium sites, one unique silicon site, three unique potassium sites, and three unique oxygen sites. The two yttrium sites are both isolated and both are in six-fold coordination environments with Y(1) adopting a regular octahedral environment and Y(2) adopting a regular trigonal prismatic environment. The yttrium polyhedra stack in line down the *c*-axis with the trigonal prisms each rotated 60 ° from the trigonal prism above and below it. The yttrium YO_6 polyhedra are again corner shared to silicon SiO_4 tetrahedra via all six oxygen sites. The silicon tetrahedra form bent Si_2O_7 pyrosilicate units with bridging Si – O – Si linkages of 66 °. The potassium fills channels throughout the structure with K(1) aligned with the Si atom down the *c*-axis, K(2) aligned with the Y(1) atoms down the *c*-axis, and K(3) aligned with the Y(2) atoms down the *c*-axis. The overall structure, viewed down the *a*- and *c*-axes is illustrated in **Figures 9.6** and **9.7**, respectively. Crystallographic data and Y – O bond distances are included in **Tables 9.1** and **9.2**, respectively.

The structures of dysprosium substituted crystals, $K_3Y_{0.9}Dy_{0.1}Si_2O_7$ (**2-Dy**), were also determined by single crystal X-ray diffraction. Crystal data were collected on two

crystals and, in both cases, the single crystal diffraction data was consistent with a combined 10% dysprosium content on the yttrium sites of the crystal. One of these data sets is included in the crystallographic tables and Y/Dy – O bond distances reported in **Tables 9.1** and **9.2**, respectively. Since the two crystals selected from the reaction both yielded a 10 % doping level of Dy, it was presumed that the other reactions acted accordingly with respect to both Dy and Eu doping. Since the ideal doping level of Eu, based on the reactant stoichiometry, was found to be 0.1 %, single crystal analysis, in any case, would be unable to determine the presence or amount of such a small quantity of europium on the yttrium site.

While both polymorphs of $K_3YSi_2O_7$ are presented, it should be noted that polymorph **2**, which crystallizes in the space group $P6_3/mcm$ and adopts the structure type predicted by Vidican, appears to be the favored phase. Even in the reaction that crystallizes polymorph **1** in the space group $P6_3/mmc$, polymorph **2** was always found to be present along with another previously reported phase, $K_5Y_2Si_4O_{13}F$.[9.48] Any attempts to modify the reaction to favor polymorph **1**, always favored one of the other phases present in the original reaction as well. Since the only difference in the reaction conditions is the cooling rate, it appears that there is a size effect brought about by the kinetics in the slow cooling step of the reaction which favors the formation of polymorph **2**; it is however possible to crystallize a small amount of polymorph **1** when using a faster cooling rate.

Fluorescence Spectroscopy

Fluorescence data were collected on powders consisting of ground crystals of polymorph **2** of $K_3YSi_2O_7$, as well as on the compositions containing dysprosium and europium on the yttrium site (0.1 % Eu; 10 % Dy; 15 % Dy and 0.12 % Eu; 15 % Dy and

0.1 % Eu; 10 % Dy and 0.1 % Eu; 9 % Dy and 0.1 % Eu). The emission scan for the parent compound $K_3YSi_2O_7$ (**2**), collected using an excitation λ of 254 nm, is shown in **Figure 9.8**. It can be seen that the parent compound exhibits fluorescence peaks around the 370 – 480 nm and 700 – 750 nm ranges. The strong fluorescence in the UV to blue region is likely the cause of the bluish tint to this compound. The broad fluorescence in both ranges causes the white light emission. Since this compound contains potassium, yttrium, silicon, and oxygen, fluorescence is not expected and we can classify polymorph **2** of $K_3YSi_2O_7$ as an intrinsic luminescent material.

Previous examples of intrinsic luminescence in compounds containing yttrium have hypothesized that the intrinsic luminescence is caused by the existence of self-trapped excitons (STEs).[9.25-9.27] Throughout the literature, these STEs can be caused by distortions in Al or Si tetrahedra[9.24, 9.57] or in systems containing rare earth cations where an oxygen or anion from a rare earth polyhedron is not also shared with a silicon polyhedra.[9.25]

As can be seen in **Figure 9.6**, the luminescent polymorph **2** of $K_3YSi_2O_7$ has only one Si site, which forms a non-distorted tetrahedron and the two unique yttrium sites are located in polyhedra that are oxygen bridged to a silicon tetrahedra at every oxygen site. Based on the structure, therefore, it is unexpected for polymorph **2** of $K_3YSi_2O_7$ to exhibit intrinsic luminescence and we are unable to make a structural argument that the intrinsic luminescence observed arises from STEs. We have to hypothesize, therefore, that STEs can occur in the absence of certain structural components as well, which would be consistent with the observation of intrinsic luminescence in the other reported yttrium and lutetium compounds.[9.24-9.27]

Since the parent $K_3YSi_2O_7$ (**2**) composition generated an intrinsic luminescence that was too blue to be an improvement in single phase WLED technology, a systematic adjustment to the composition, consisting of the addition of Dy and Eu into the structure to add yellow and red color components, respectively, was undertaken to achieve white light emission. In the literature, compositions like $KLa(MoO_4)_2$,[9.21] Y_6WO_{12},[9.19] $NaGdTiO_4$,[9.18] $KSr_4(BO_3)_3$,[9.20] Y_2SiO_5,[9.22] and $ZnWO_4$[9.23] were all doped with small amounts of Dy^{3+} and Eu^{3+} like polymorph **2** to achieve tunable white light emission. The light emissions of several of our Dy and Eu containing compositions are plotted on the CIE diagram shown in **Figure 9.9**, where the emission data used to plot the CIE diagram for **2** and **2-Dy,Eu** are shown in **Figures 9.10** and **9.11**, with visual images of the luminescence shown in **Figure 9.12**. The CIE coordinates were calculated using the CIE Coordinate Calculator Matlab code created by Patil.[9.58] The composition that resulted in the best white light emission by visual and calculated means, $K_3Y_{0.899}Dy_{0.1}Eu_{0.001}Si_2O_7$ (**2-Dy,Eu**), contains 10 % Dy and 0.1 % Eu.

The emission spectrum at an excitation λ of 254 nm is shown in **Figure 9.13**. In this figure, fluorescence is still observed in the violet to blue region like in the parent compound; however, there are three new intense peaks at 487 nm, 580 nm, and 625 nm. The 487 and 580 nm peaks are attributed to the Dy^{3+} ion where the 487 nm peak is the $^4F_{9/2}$ to $^6H_{15/2}$ transition and the yellow emission of 580 nm should correspond to the $^4F_{9/2}$ to $^6H_{13/2}$ transition. The 625 nm peak is in the orange region and should be due to the $^5D_0$ to $^7F_2$ transition seen in Eu^{3+} complexes where the europium sits on an inversion center.[9.59] This implies that in this centrosymmetric structure the europium substitutes exclusively onto the octahedral yttrium site, while the single crystal X-ray analysis

confirms that the dysprosium substitutes onto both yttrium sites. The excitation λ of 254 nm was chosen for the fluorescence data so that the coloring seen in **Figure 9.12** matched the coloring reported on the CIE diagram. Additional fluorescence indicated that the optimum excitation λ for this system is 280 nm and the optimum emission λ is 401 nm. Figures of this data are shown in **9.14** and **9.15**.

From the images and CIE diagrams it is readily apparent that chemical composition changes to introduce additional emissions, such as yellow and red, can be used to systematically adjust the emission color of this system. The white light emission achieved in this investigation suggests that further research targeted to create new yttrium silicates is one promising research direction for solid state lighting. In particular, the synthesis of more intense intrinsic luminescent materials and their fine tuning towards white light emission may result in less expensive and more earth abundant phosphors that are based on underutilized rare earths. These yttrium silicates could then be utilized as phosphor coatings in current LED technology.

Conclusion

Crystals of two polymorphs of $K_3YSi_2O_7$ were obtained for different cooling rates during the flux based crystal growth process. Polymorph **2**, which crystallizes in the space group $P6_3/mcm$, exhibits bluish-white intrinsic luminescence. A systematic adjustment to the composition, consisting of the addition of Dy and Eu into the structure to add yellow and red color components, respectively, was performed to achieve white light emission. A substitution level of 10 % dysprosium and 0.1 % europium resulted in the white light emitter $K_3Y_{0.899}Dy_{0.1}Eu_{0.001}Si_2O_7$.

References

9.1 George, N. C.; Denault, K. A.; Seshadri, R. *Annu. Rev. Mater. Res.* **2013**, *43*, 481-501.
9.2 Li, G.; Tian, Y.; Zhao, Y.; Lin, J. *Chem. Soc. Rev.* **2015**, *44*, 8688-8713.
9.3 Xu, C.; Poduska, K. M. *J. Mater. Sci: Mater. Electon* **2015**, *26*, 4565-4570.
9.4 Koparkar, K. A.; Bajaj, N. S.; Omanwar, S. K. *Defect and Diffusion Forum* **2015**, *361*, 95-119.
9.5 Liu, Z.; Peng, R. *Eur. J. Nucl. Med. Mol. Imaging* **2010**, *37*, S147-S163.
9.6 Min, Y.; Li, J.; Liu, F.; Padmanabhan, P.; Yeow, E. K. L.; Xing, B. *Nanomaterials* **2014**, *4*, 129-154.
9.7 Wu, X.; Chen, G.; Shen, J.; Li, Z.; Zhang, Y.; Han, G. *Bioconjugate Chem.* **2015**, *26*, 166-175.
9.8 Pan, C.; Chen, M.; Yu, R.; Yang, Q.; Hu, Y.; Zhang, Y.; Wang, Z. L. *Adv. Mater.* **2016**, *28*, 1535-1552.
9.9 Song, Y.; Fang, W.; Brenes, R.; Kong, J. *Nano Today* **2015**, *10*, 681-700.
9.10 Wang, W.; Yang, H.; Li, G. *J. Mater. Chem. C* **2013**, *1*, 4070-4077.
9.11 Hu, Y.; Zhuang, W.; Ye, H.; Zhang, S.; Fang, Y.; Huang, X. *J. Lumin.* **2005**, *111*, 139-145.
9.12 Bünzli, J.-C. G.; Piguet, C. *Chem. Soc. Rev.* **2005**, *34*, 1048-1077.
9.13 Nyman, M.; Rodriguez, M. A.; Alam, T. M.; Anderson, T. M.; Ambrosini, A. *Chem. Mater.* **2009**, *21*, 2201-2208.
9.14 Nyman, M.; Rodriguez, M. A.; Rohwer, L. E. S.; Martin, J. E.; Waller, M.; Osterloh, F. E. *Chem. Mater.* **2009**, *21*, 4731-4737.
9.15 Palasyuk, O.; Palasyuk, A.; Maggard, P. A. *J. Solid State Chem.* **2010**, *183*, 814-822.
9.16 Shi, J.; Chandrashekhar, M. V. S.; Reiherzer, J.; Schaff, W. J.; Lu, J.; Disalvo, F. J.; Spencer, M. G. *J. Cryst. Growth* **2008**, *310*, 452-456.
9.17 Hui, Y. Y.; Lin, C.-F. *Mater. Lett.* **2007**, *61*, 3802-3804.
9.18 Bharat, L. K.; Du, P.; Yu, J. S. *J. Alloys Compd.* **2016**, *666*, 270-278.
9.19 Bharat, L. K.; Jeon, Y. I.; Yu, J. S. *Ceram. Int.* **2016**, *42*, 5677-5685.
9.20 Leng, Z.; Li, L.; Liu, Y.; Zhang, N.; Gan, S. *J. Lumin.* **2016**, *173*, 171-176.
9.21 Liu, Y.; Zuo, H.; Li, J.; Shi, X.; Ma, S.; Zhao, M.; Zhang, K.; Wang, C. *Ceram. Int.* **2016**,
9.22 Ramakrishna, G.; Naik, R.; Nagabhushana, H.; Basavaraj, R. B.; Prashantha, S. C.; Sharma, S. C.; Anantharaju, K. S. *Optik* **2016**, *127*, 2939-2945.
9.23 Zhai, Y.; Wang, M.; Zhao, Q.; Yu, J.; Li, X. *J. Lumin.* **2016**, *172*, 161-167.
9.24 Cooke, D. W.; Bennett, B. L.; Muenchausen, R. E.; Lee, J.-K.; Nastasi, M. A. *J. Lumin.* **2004**, *106*, 125-132.
9.25 Ivanov, V. Y.; Shlygin, E. S.; Pustovarov, V. A.; Mazurenko, V. V.; Shul'gin, B. V. *Phys. Solid State* **2008**, *50*, 1692-1698.
9.26 Pankratov, V.; Kirm, M.; von Seggern, H. *J. Lumin.* **2005**, *113*, 143-150.
9.27 Zorenko, Y.; Zorenko, T.; Voznyak, T.; Sidletskiy, O. *J. Lumin.* **2013**, *137*, 204-207.
9.28 Brgoch, J.; Borg, C. K. H.; Denault, K. A.; Mikhailovsky, A.; DenBaars, S. P.; Seshadri, R. *Inorg. Chem.* **2013**, *52*, 8010-8016.

9.29 Fernández-Carrioń, A. J.; Allix, M.; Ocaña, M.; Garcıá -Sevillano, J.; Cusso, F.; Fitch, A. N.; Suard, E.; Becerro, A. I. *Inorg. Chem.* **2013**, *52*, 13469-13479.
9.30 Latshaw, A. M.; Wilkins, B. O.; Hughey, K. D.; Yeon, J.; Williams, D. E.; Tran, T. T.; Halasyamani, P. S.; zur Loye, H.-C. *CrystEngComm* **2015**, *17*, 4654-4661.
9.31 Latshaw, A. M.; Hughey, K. D.; Smith, M. D.; Yeon, J.; zur Loye, H.-C. *Inorg. Chem.* **2014**, *54*, 876-884.
9.32 Latshaw, A. M.; Chance, W. M.; Trenor, N.; Morrison, G.; Smith, M. D.; Yeon, J.; Williams, D. E.; zur Loye, H.-C. *CrystEngComm* **2015**, *17*, 4691-4698.
9.33 Bondar, I. A.; Tenisheva, T. F.; Toropov, N. A.; Shepelev, Y. F. *Dokl. Akad. Nauk SSSR* **1965**, *160*, 1069-1071.
9.34 Hwang, M. S.; Hong, H. Y.-P. *Acta Cryst.* **1987**, *C43*, 1241-1243.
9.35 Napper, J. D.; Layland, R. C.; Smith, M. D.; zur Loye, H.-C. *J. Chem. Crystallogr.* **2004**, *34*, 347-351.
9.36 Vidican, I.; Smith, M. D.; zur Loye, H.-C. *J. Solid State Chem.* **2003**, *170*, 203-210.
9.37 Sebais, M.; Pobedimskaya, E. A.; Dimitrova, O. V. *Kristallografiya* **1985**, *30*, 802-805.
9.38 Tamazyan, R. A.; Malinovskii, Y. A.; Sirota, M. I.; Simonov, V. I. *Kristallografiya* **1988**, *33*, 1128-1133.
9.39 Bugaris, D. E.; zur Loye, H.-C. *Angew. Chem. Int. Ed.* **2012**, *51*, 3780-3811.
9.40 APEX2 Version 2014.9-0, SAINT+ Version 8.34A and SADABS Version 2014/4. Bruker Analytical X-ray Systems, Inc., Madison, Wisconsin, USA, 2014.
9.41 Sheldrick, G. M. *Acta Cryst.* **2008**, *A64*, 112-122.
9.42 ShelXle: a Qt graphical user interface for SHELXL. Hübschle, C. B., Sheldrick, G. M., Bittrich, B. J. Appl. Cryst. **2011**, 44, 1281-1284.
9.43 Dolomanov, O. V.; Bourhis, L. J.; Gildea, R. J.; Howard, J. A. K.; Puschmann, H. *J. Appl. Cryst.* **2009**, *42*, 339-341.
9.44 SMART Version 5.630, SAINT+ Version 6.45 and SADABS Version 2.10. Bruker Analytical X-ray Systems, Inc., Madison, Wisconsin, USA, 2003.
9.45 Di-Pompinio, A.; Continenza, A. *Phys. Rev. B* **1993**, *48*, 12558.
9.46 Latshaw, A. M.; Morrison, G.; zur Loye, H.-C. *J. Chem. Crystallogr.* **2015**, *45*, 350-354.
9.47 Latshaw, A. M.; Yeon, J.; Smith, M. D.; zur Loye, H.-C. *J. Solid State Chem.* **2016**, *235*, 100-106.
9.48 Latshaw, A. M.; Myers, A. R.; Smith, M. D.; zur Loye, H.-C. *J. Chem. Crystallogr.* **2015**, *45*, 207-211.
9.49 Lee, C.-S.; Wang, S.-L.; Chen, Y.-H.; Lii, K.-H. *Inorg. Chem.* **2009**, *48*, 8357-8361.
9.50 Morrison, G.; Smith, M. D.; Tran, T. T.; Halasyamani, P. S.; zur Loye, H.-C. *CrystEngComm* **2015**, *17*, 4218-4224.
9.51 Morrison, G.; Ramanantoanina, H.; Urland, W.; Smith, M. D.; zur Loye, H.-C. *Inorg. Chem.* **2015**, *54*, 5504-5511.
9.52 Latshaw, A. M.; Smith, M. D.; zur Loye, H.-C. *Solid State Sci.* **2014**, *35*, 28-32.
9.53 Kahlenberg, V.; Manninger, T. *Acta Cryst.* **2014**, *E70*, i11.
9.54 Liao, C.-H.; Chang, P.-C.; Kao, H.-M.; Lii, K.-H. *Inorg. Chem.* **2005**, *44*, 9335-9339.

9.55 Tang, M.-F.; Chiang, P.-Y.; Su, Y.-H.; Jung, Y.-C.; Hou, G.-Y.; Chang, B.-C.; Lii, K.-H. *Inorg. Chem.* **2008**, *47*, 8985-8989.
9.56 Shannon, R. D. *Acta Crystallogr., Sect. A: Cryst. Phys. Diffr., Theor. Gen. Crystallogr.* **1976**, *32*, 751.
9.57 Lecoq, P.; Mikhail, K. *IEEE Trans. Nucl. Sci.* **2002**, *49*, 1651-1654.
9.58 Patil, P. *MATLAB Central File Exchange* **2010**,
9.59 Blasse, G.; Grabmaier, B. C. *Luminescent Materials*; Springer-Verlag: Berlin, 1994;

Table 9.1. Crystallographic table for single crystal X-ray data for $K_3YSi_2O_7$ and $K_3Y_{0.9}Dy_{0.1}Si_2O_7$.

Formula	$K_3YSi_2O_7$ (**1**)	$K_3YSi_2O_7$ (**2**)	$K_3Y_{0.9}Dy_{0.1}Si_2O_7$ (**2-Dy**)
Formula weight	374.39	374.39	382.12
Temperature (K)	296(2)	298(2)	303(2)
Crystal system	Hexagonal	Hexagonal	Hexagonal
Space group	*P* $6_3/mmc$	*P* $6_3/mcm$	*P* $6_3/mcm$
a (Å)	5.76270(10)	9.8450(2)	9.8496(2)
c (Å)	14.0205(6)	14.3236(3)	14.3292(4)
V (Å^3)	403.22(2)	1202.30(5)	1203.90(6)
Z	2	6	6
Density (Mg/m^3)	3.084	3.102	3.162
Absorption coefficient (mm^{-1})	9.076	9.131	9.334
Crystal size (mm^3)	0.07 × 0.05 × 0.04	0.12 × 0.08 × 0.06	0.10 x 0.06 x 0.02
2 theta range (°)	5.81 to 70.16	4.78 to 72.69	5.68 to 75.54
reflections collected	8333	62868	39224
data/restraints/ parameters	390 / 0 / 19	1092 / 0 / 41	1195 / 0 / 43
R (int)	0.0404	0.0415	0.0584
GOF (F^2)	1.171	1.102	1.019
R indices (all data)	R_1 = 0.0291 wR_2 = 0.0655	R_1 = 0.0272 wR_2 = 0.0514	R_1 = 0.0324 wR_2 = 0.0509

Table 9.2. Y – O bond distances (in Å).

	$K_3YSi_2O_7$ (**1**)	$K_3YSi_2O_7$ (**2**)	$K_3Y_{0.9}Dy_{0.1}Si_2O_7$ (**2-Dy**)
Y(1) – O(1) (x6)	2.2499(15)	2.2394(9)	2.2424(11)
Y(2) – O(2) (x6)	-	2.2841(12)	2.2866(13)

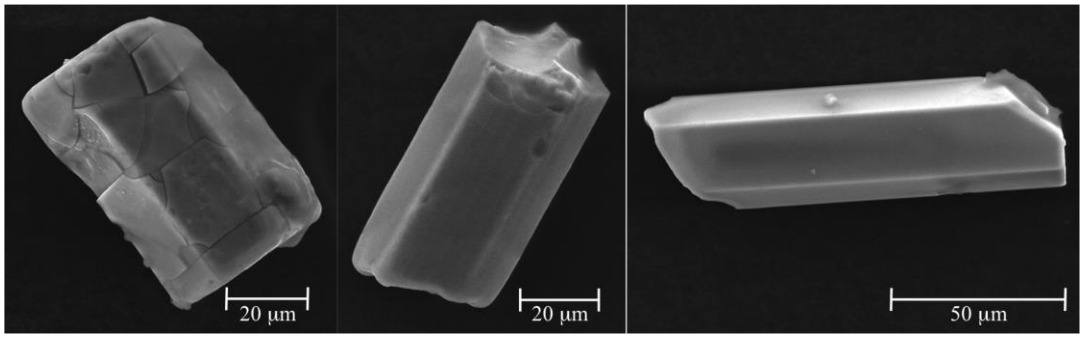

Figure 9.1. SEM images (from left to right) of $K_3YSi_2O_7$ (**1**), $K_3YSi_2O_7$ (**2**), and $K_3Y_{0.899}Dy_{0.1}Eu_{0.001}Si_2O_7$ (**2-Dy,Eu**).

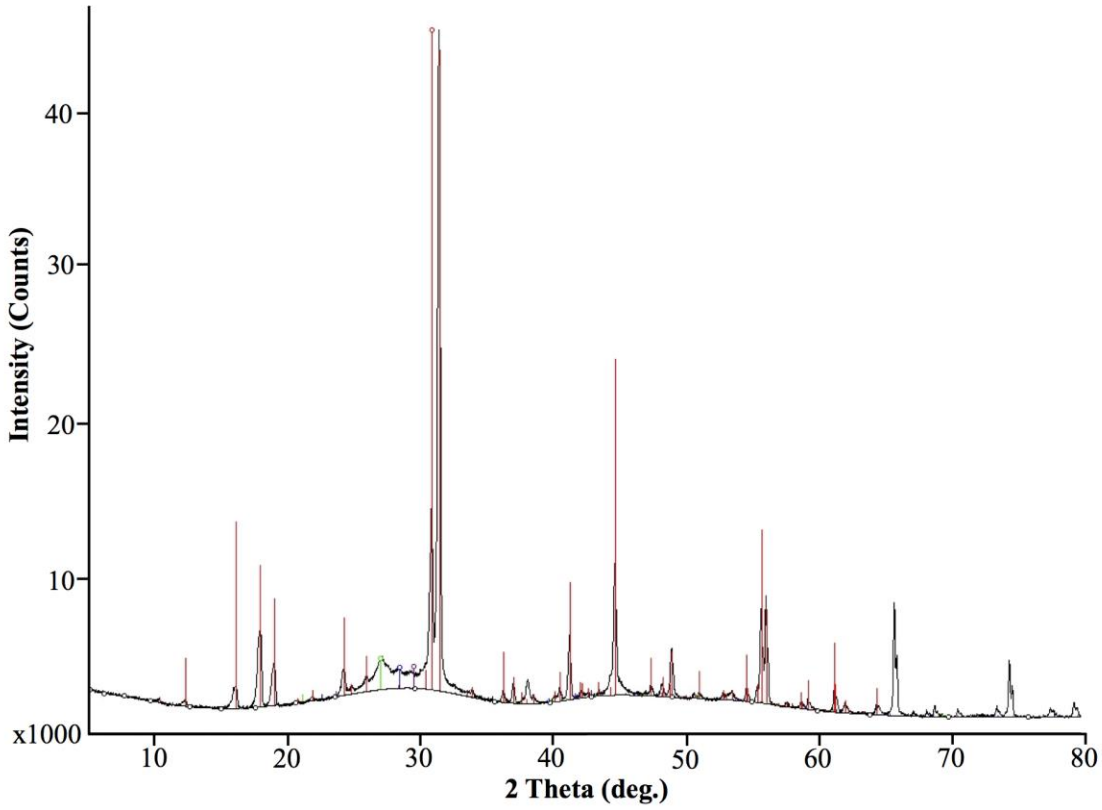

Figure 9.2. PXRD pattern of $K_3YSi_2O_7$ (**2**). The observed pattern is in good agreement with the calculated pattern with a small amount of three types of SiO_2. The calculated pattern is the red overlay, and the green, blue, and purple overlays are SiO_2.

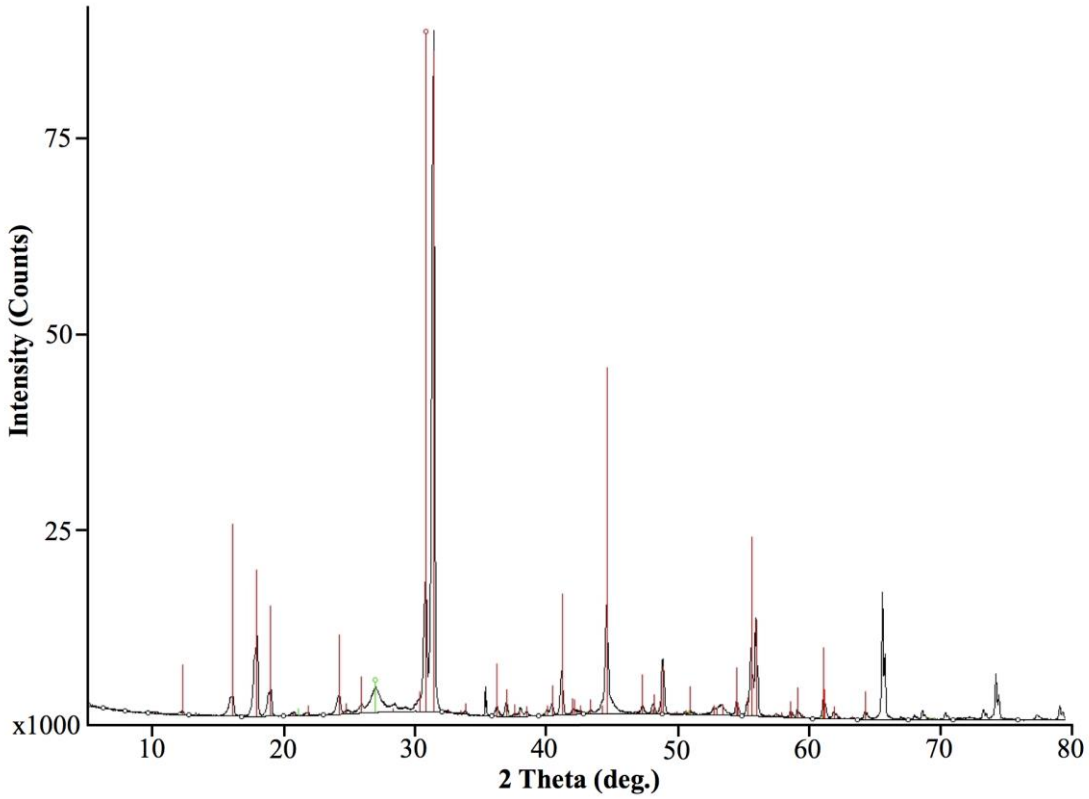

Figure 9.3. PXRD pattern of $K_3YSi_2O_7$ doped with 10 % Dy and 0.1 % Eu (**2-Dy,Eu**). The observed pattern is in good agreement with the calculated pattern with a small amount of SiO_2. The calculated pattern is shown in red and the SiO_2 is shown in green.

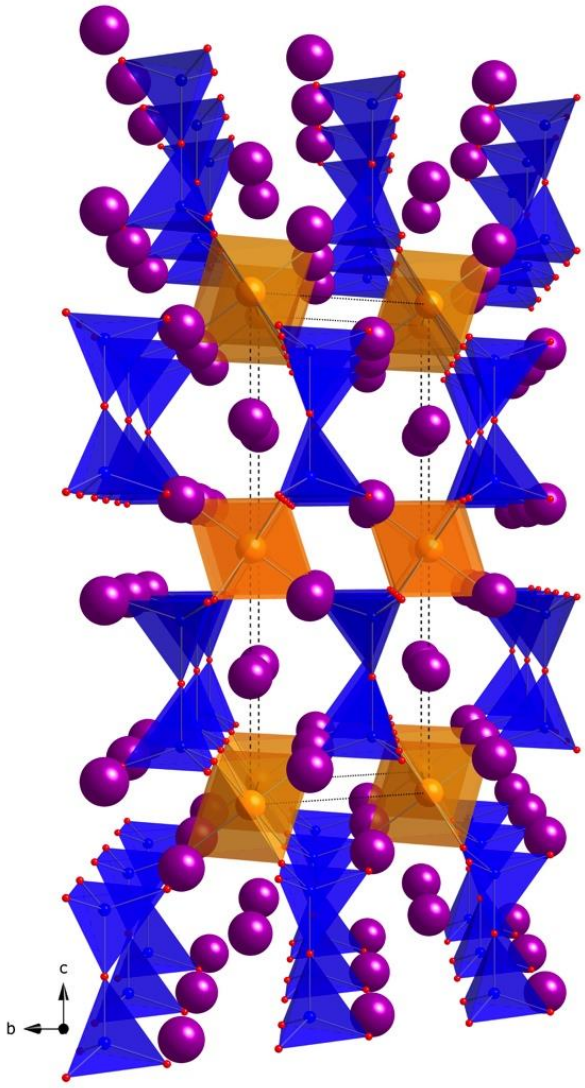

Figure 9.4. View down the *a*-axis of the $K_3YSi_2O_7$ polymorph **1** where Y is orange, Si is blue, K is purple, and O is red.

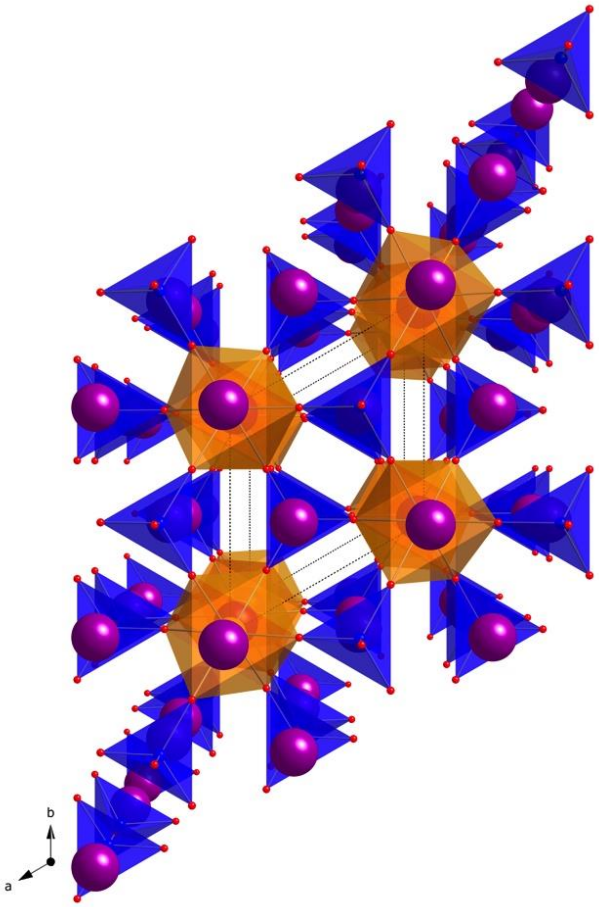

Figure 9.5. View down the *c*-axis of polymorph **1** of $K_3YSi_2O_7$. Color scheme follows Figure 9.4.

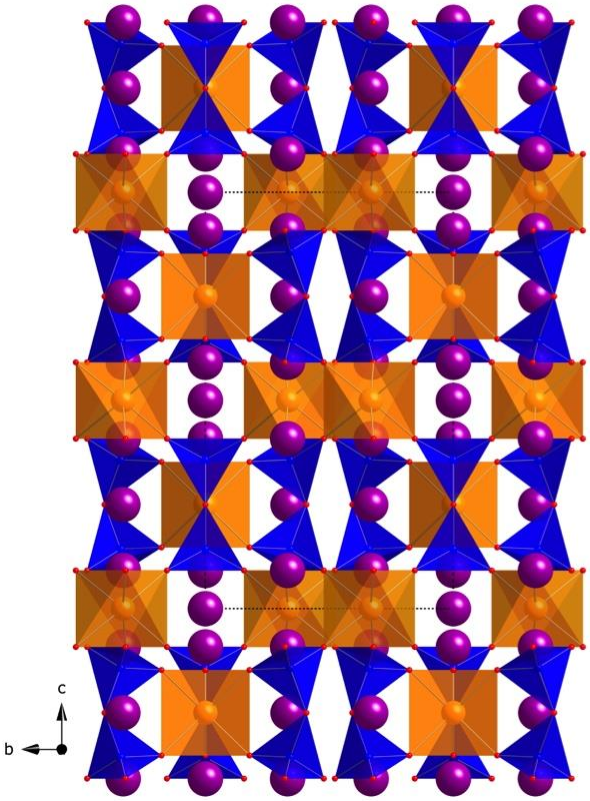

Figure 9.6. View down the *a*-axis of the $K_3YSi_2O_7$ polymorph **2**. Color scheme is the same as in Figure 9.4.

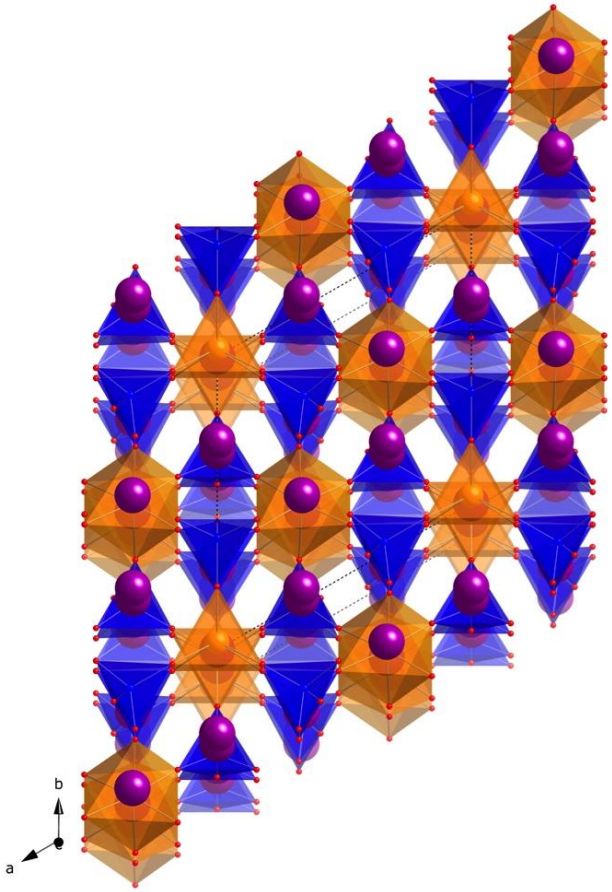

Figure 9.7. The view down the *c*-axis of polymorph **2** of $K_3YSi_2O_7$. Color scheme is the same as in Figure 9.4.

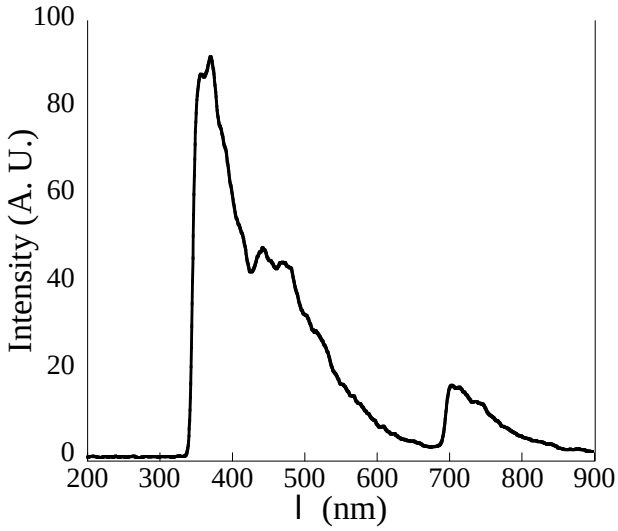

Figure 9.8. Emission spectrum at an excitation λ of 254 nm for polymorph **2**. The cut off at 350 nm is due to the use of a filter to prevent the excitation wavelength to enter the detector.

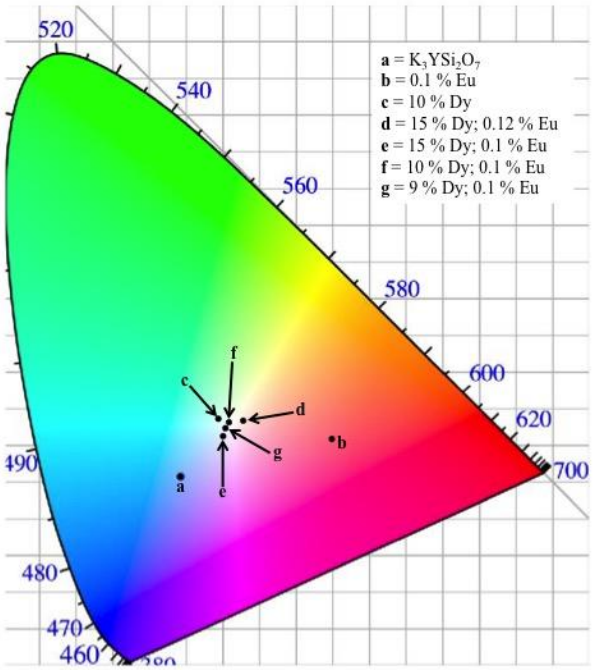

Figure 9.9. Overall CIE diagram indicating the color rendering of polymorph **2** and the various doping studies.

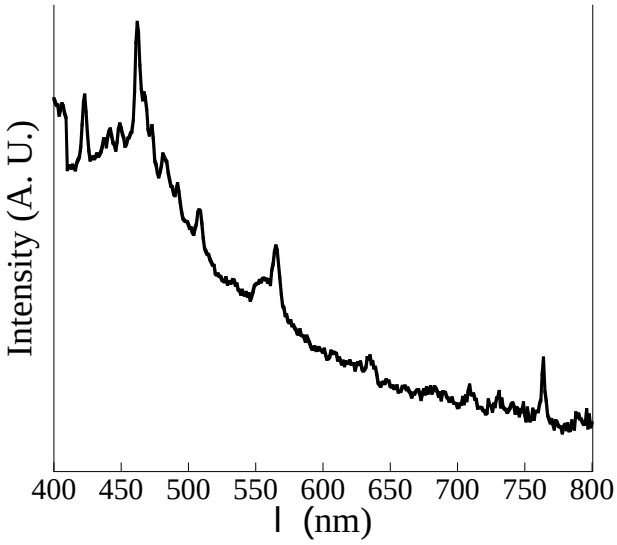

Figure 9.10. Emission spectrum used for the CIE analysis at an excitation λ of 254 nm for polymorph **2**.

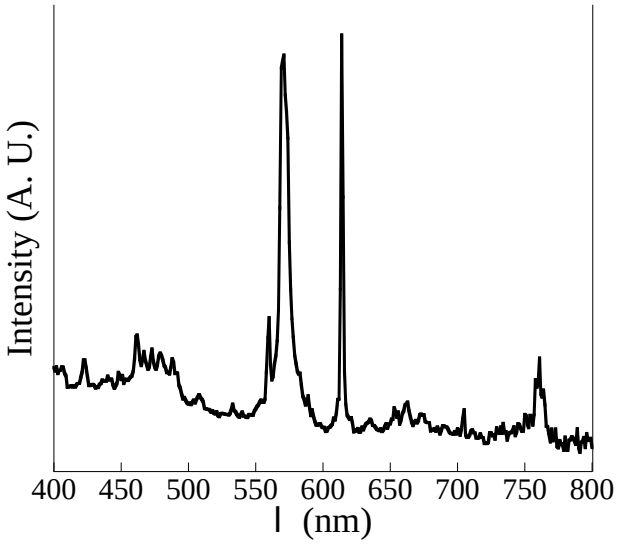

Figure 9.11. Emission spectrum used for the CIE analysis at an excitation λ of 254 nm of $K_3YSi_2O_7$:10%Dy,0.1%Eu (**2-Dy,Eu**).

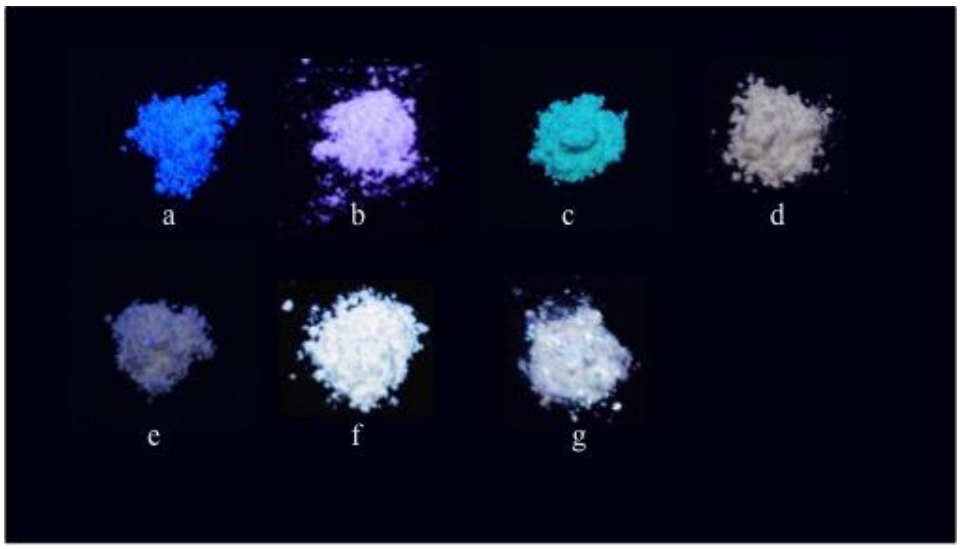

Figure 9.12. Visual images when the samples are excited at 254 nm in a black box where a = $K_3YSi_2O_7$, b = 0.1 % doped Eu, c = 10 % Dy, d = 15 % Dy; 0.12 % Eu, e = 15 % Dy; 0.1 % Eu, f = 10 % Dy; 0.1 % Eu, and g = 9 % Dy; 0.1 % Eu.

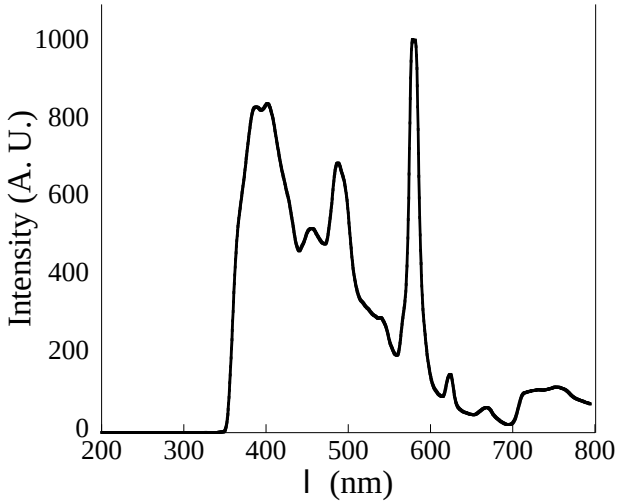

Figure 9.13. Emission spectrum at an excitation λ of 254 nm of $K_3YSi_2O_7$:10%Dy,0.1%Eu (**2-Dy,Eu**). The cut off at ~350 nm is due to the use of a filter to prevent the excitation wavelength to enter the detector.

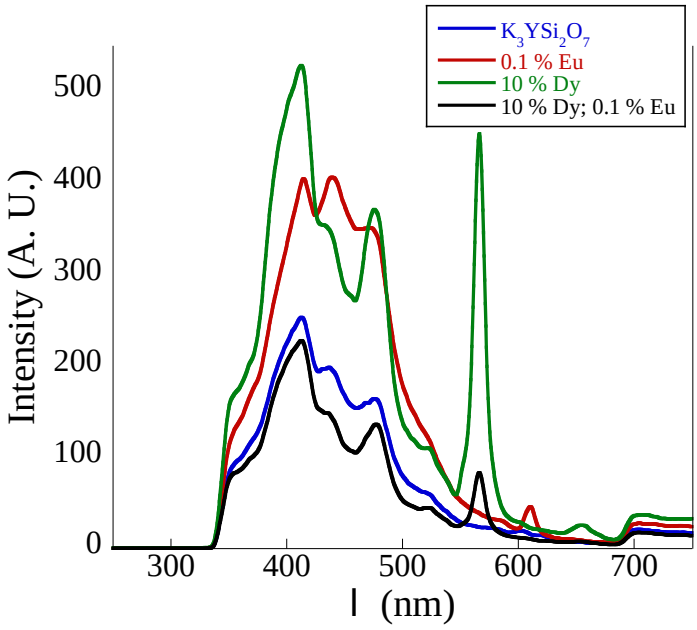

Figure 9.14. Emission spectra of polymorph **2**, **2-Dy**, **2-Eu**, and **2-Dy,Eu** at an excitation λ of 280 nm. The cut off at ~350 nm is due to the use of a filter to prevent the excitation wavelength to enter the detector.

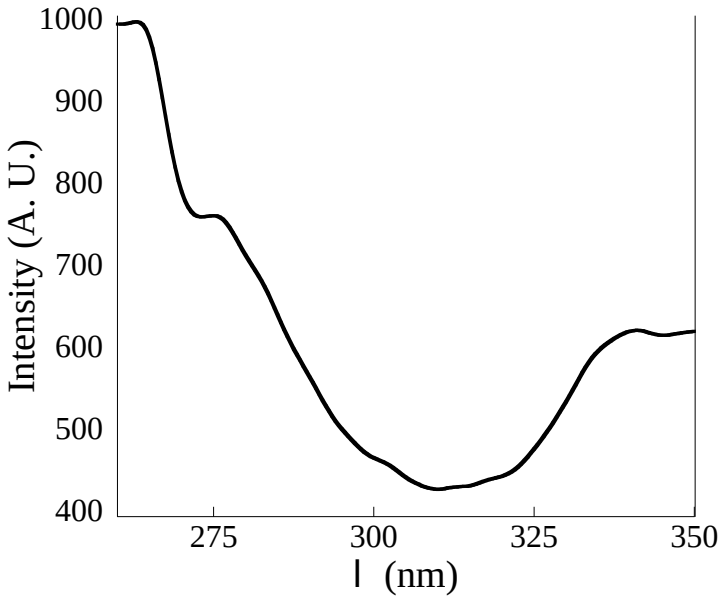

Figure 9.15. Excitation spectra of **2-Dy,Eu** at an emission λ of 401 nm.

Chapter 10

Fluoride Flux Crystal Growth and Structure Determination of $K_5RE_2FSi_4O_{13}$ (RE = Y, Sc)*

*Latshaw, A. M., Myers, A. R., Smith, M. D., zur Loye, H.-C. *J. Chem. Cryst.*, **2015**, *45(4)*, 207-211.
Latshaw, A. M., Morrison, G., zur Loye, H.-C. *J. Chem. Cryst.*, **2015**, *45(7)*, 350-354.

Introduction

Flux crystal growth has proven to be an excellent synthetic technique for exploratory materials discovery.[10.1] The ability to routinely obtain single crystals of new compositions, and potentially new structures, makes flux growth an extremely useful synthetic method. Flux crystal growth works with many different fluxes, including alkali or alkaline earth halides, hydroxides, or carbonates, that can be used for different crystal growth temperature ranges. Furthermore, some of these fluxes can act as "reactive fluxes" where one or more of the flux components are incorporated into the crystal products. For example, one method to obtain oxyfluoride single crystals, as described herein, is to use molten fluoride fluxes, which are known to act as reactive fluxes in many situations.[10.1-10.3]

Rare earth containing silicates, such as $K_5RE_2FSi_4O_{13}$ (RE = Y, Sc) are of interest as potential inorganic hosts into which transition metal and rare earth oxide dopants can be incorporated, as well as hosts that can accommodate extensive elemental substitutions to create new phosphors for solid state lighting applications. The ionic radii of yttrium and scandium[10.4] in $K_5RE_2FSi_4O_{13}$ (RE = Y, Sc) coupled with the ionic radius of europium in $K_5Eu_2FSi_4O_{13}$[10.5] an isostructural composition that has been published previously, enable us to define the range of trivalent cations that are accommodated by this structure and, thus, to establish the ionic radii size limits of 0.745Å – 0.947Å for the lanthanide sites in this composition. This extensive size range suggests that this host structure has the ability accommodate other rare earth ions to yield compositions that exhibit luminescence and can be fine tuned to a desired coloring.

Experimental Section

Sample Preparation

Y_2O_3 (99.99%) was purchased from Aldrich, Sc_2O_3 (>99%) was purchased from Aran Isles Chemical Inc., KF (99% min.) was purchased from Alfa Aesar, and SiO_2 (99.99%) was purchased from Aldrich as fused pieces and ground to a powder in a ball mill.

Crystals of $K_5Y_2FSi_4O_{13}$ were prepared by loading Y_2O_3 (0.5 mmol) and SiO_2 (1 mmol) into a four inch long, ½ inch diameter, silver tube that was welded shut on the bottom. KF (1 g, ~17 mmol) was loaded on top of the reactants as a flux. The tube was then placed in a drying oven under vacuum for one hour before the top of the tube was welded shut. The tube was loaded into a programmable box furnace that was heated to 900°C where it was held for 12 hrs. before slow cooling to 700°C at a rate of 6°C/hr. After it reached 700°C, the furnace was shut off. The tube was then cut open and the products were sonicated in H_2O to break up the flux. The crystals were isolated using vacuum filtration.

Single crystals of $K_5Sc_2FSi_4O_{13}$ were prepared by loading Sc_2O_3 (1 mmol) and SiO_2 (2 mmol) into a silver crucible. KF (1g) was then added to the silver crucible as the flux. A silver lid was loosely fitted on the silver crucible before it was placed into a programmable furnace that was set to ramp to 900 °C, where it dwelled for 12 hours before slow cooling at a rate of 6 °C/h to 700 °C. After the furnace reached 700 °C it was shut off. Crystals were separated from the flux by sonication in water and then isolated by vacuum filtration.

Characterization

Single Crystal X-ray Diffraction

X-ray intensity data from a colorless plate crystal of $K_5Y_2FSi_4O_{13}$ and a rod crystal of $K_5Sc_2FSi_4O_{13}$ were collected at 296(2) and 293(2) K, respectively, using a Bruker SMART APEX CCD diffractometer (Mo Kα radiation, λ = 0.71073 Å).[10.6] The raw area detector data frames were reduced and corrected for absorption effects with SAINT+ and SADABS programs.[10.6] Final unit cell parameters were determined by least-squares refinement of 1842 and 3813 reflections from the data set, respectively. The reported atomic coordinates of $K_5Eu_2FSi_4O_{13}$[10.5] were used as an initial structural model. Difference Fourier calculations and full-matrix least-squares refinement against *F*2 were performed with WinGX.

$K_5RE_2FSi_4O_{13}$ (RE = Y, Sc) crystallizes in the monoclinic system. The space group was found to be $P2_1/m$. The asymmetric unit consists of five potassium atoms, two rare earth atoms, four silicon atoms, nine oxygen atoms, and two fluorine atoms. All atoms occupy positions on the mirror plane at *x*, ¼, *z* (Wyckoff site 2*e*) except O(1), O(4), O(6), and O(8), which are on general positions (site 4*f*). Because of the prolate nature of the F site when the $K_5Sc_2FSi_4O_{13}$ structure was solved using one fluorine site, asymmetric unit cell shown in **Figure 10.1**, the site was split, unlike in the $K_5Y_2FSi_4O_{13}$, which only has one fluorine site. Freely refining the two site occupancies with a total occupancy of one resulted in F(1) and F(2) having occupancy of 0.34 and 0.66, respectively. In the $K_5Sc_2FSi_4O_{13}$ structure, attempts to fix the occupancies as 50/50 lead to an increased R value and a large ADP for F(1). Since the two F sites are only 0.51 Å apart, the two sites were refined isotropically.

Further details of the crystal structure investigation on $K_5RE_2FSi_4O_{13}$ can be obtained from the Fachinformationszentrum Karlsruhe using the depository numbers 429093 for $K_5Y_2FSi_4O_{13}$ and 429225 for $K_5Sc_2FSi_4O_{13}$.

Results and Discussion

Structure Determination

$K_5RE_2FSi_4O_{13}$ (RE = Y, Sc) crystallizes in the monoclinic space group $P2_1/m$ and is isostructural with $K_5Eu_2FSi_4O_{13}$.[10.5] Crystallographic data for $K_5RE_2FSi_4O_{13}$ (RE = Y, Sc) can be found in **Table 10.1**. The structure contains two unique rare earth sites that are six coordinate distorted octahedra. In $K_5Y_2FSi_4O_{13}$, the yttrium environments form distorted YO_5F octahedra where the Y(1) octahedra is corner-shared to the Y(2) octahedra through the F(1) site. The yttrium connected octahedra form AB slabs along the *c* axis where the A slab is the $Y(1)O_5F$ octahedra on top of the connected $Y(2)O_5F$ while the B slab has the $Y(2)O_5F$ octahedra on top of the connected $Y(1)O_5F$ as depicted in **Figure 10.2**. In the $K_5Sc_2FSi_4O_{13}$ compound, the Sc(1) and Sc(2) octahedra corner share through the disordered fluorine sites (**Figure 10.3**). The scandium octahedra have an ScO_5F coordination environment where the fluorine site is fractionally occupied, such that F(1) is occupied 34(3) % of the time and F(2) 66(3) % percent of the time. The disordered F sites are the major structural difference between the scandium and the yttrium and europium analogues. The disordered fluorine sites result in Sc – F interaction lengths of 2.240Å - 2.873Å. These interaction lengths are longer than other known Sc-F bonds, which include 2.01Å (ScF_3),[10.7] 1.95Å – 2.04Å ($KScF_4$),[10.8] 2.00Å – 2.08Å ($K_2ScF(Si_4O_{10})$),[10.9] and 2.13Å – 2.28Å (ScOF).[10.10] Not unexpectedly, the closest Sc-F lengths to those observed in our structure is the oxyfluoride ScOF. Selected

interatomic distances for $K_5RE_2FSi_4O_{13}$ (RE = Y, Sc), along with those of the previously published $K_5Eu_2FSi_4O_{13}$,[10.5] are provided in **Table 10.2**. The bond lengths of Sc(1) – F(1) and Sc(2) – F(2) are shorter than those observed for the other RE-F analogues (**Table 10.2**), as is expected given the smaller ionic radii of Sc^{3+}.[10.4] This suggests that the small size of the Sc^{3+} compared to Y^{3+} and Eu^{3+} leads to the disordered fluorine, which can no longer adequately bond to both scandium atoms at the same time.

The silicon atoms are found in SiO_4 tetrahedra that corner share to form Si_2O_7 units that in turn corner share to form isolated Si_4O_{13} units (**Figure 10.4**). Si_4O_{13} truncated sorosilicate units are not exceptionally common with only two minerals (hubeite[10.11] and ruizite[10.12]) exhibiting Si_4O_{13} units. In literature there are also some cases of these truncated silicate units with some examples including $Ag_{18}(SiO_4)_2(Si_4O_{13})$,[10.13] $K_5(UO_2)_2[Si_4O_{12}(OH)]$,[10.14] and $Ba_2Gd_2(Si_4O_{13})$.[10.15] The Si_2O_7 units are bent, as observed in many other silicates. For the Y and Sc analogues, respectively, the Si(1) – O(3) – Si(2) bond angles are 138.6 ° and 139.3 °, the Si(2) – O(7) – Si(3) bond angles are 133.1 ° and 135.5 °, and the Si(3) – O(5) – Si(4) bond angles are 135.5 ° and 140.0 °, with the bond angles for the Eu analogue given in **Table 10.3**. The larger bond angles seen in the Sc analogue coincide with longer Sc(1) – Sc(2) bond distances, 5.11 Å, for the Eu(1) – Eu(2) distances, 5.04 Å, and Y(1) – Y(2) distances, 4.96 Å. The larger RE – RE distances in the Sc analogue are interesting, given its smaller lattice parameters. It is likely that the direct RE – F – RE bonding in the Eu and Y analogues applies chemical pressure to the Si_4O_{13} units. The breaking of the one RE – F bond in the Sc analogue, leading to Sc – F – Sc relieves this chemical pressure, allowing for the Si_4O_{13} unit to become more linear (**Figure 10.5**). The K(1) ion

occupies a site in the channel between the fluorine sites that runs down the *b* axis, the K(2) occupies a site in the channel between the Si(3) tetrahedra down the *b* axis, K(3) occupies a site in the channel between Si(1) and Si(2), almost in line with O(3) down the *b* axis, K(4) occupies a site in the channel between O(2), which is the oxygen that corner shares the RE(1) octahedra and the Si(1) tetrahedra, and K(5) occupies a site in the channel between O(9), which is the oxygen that corner shares the RE(2) octahedra and the Si(4) tetrahedra. The overall structural image is shown in **Figure 10.6**.

Conclusion

Crystals of $K_5RE_2FSi_4O_{13}$ (RE = Y, Sc) have been synthesized using a molten potassium fluoride flux. The small size of Sc^{3+} has led to fluorine site disorder in this composition that is not observed in the Y analogue and the previously reported $K_5Eu_2FSi_4O_{13}$ analogue.

References

10.1 Bugaris, D. E.; zur Loye, H.-C. *Angew. Chem. Int. Ed.* **2012**, *51*, 3780-3811.
10.2 Latshaw, A. M.; Smith, M. D.; zur, L., H.-C. *Solid State Sci.* **2014**, *35*, 28-32.
10.3 Latshaw, A. M.; Hughey, K. D.; Smith, M. D.; Yeon, J.; zur Loye, H.-C. *Inorg. Chem.* **2015**, *54*, 876-884.
10.4 Shannon, R. D. *Acta Crystallogr., Sect. A: Cryst. Phys. Diffr., Theor. Gen. Crystallogr.* **1976**, *32*, 751.
10.5 Chiang, P.-Y.; Lin, T.-W.; Dai, J.-H.; Chang, B. C.; Lii, K.-H. *Inorg. Chem.* **2007**, *46*, 3619-3622.
10.6 SMART Version 5.630, SAINT+ Version 6.45 and SADABS Version 2.10. Bruker Analytical X-ray Systems, Inc., Madison, Wisconsin, USA, 2003.
10.7 Fedorov, P. P.; Trncova, V.; Kocherba, G. I.; Sobolev, B. P. *Z. Kristallogr.* **1995**, *40*, 716-720.
10.8 Champarnaud-Mesjard, J. C.; Frit, B. *Eur. J. Solid State Inorg. Chem.* **1992**, *29*, 161-170.
10.9 Kolitsch, U.; Tillmanns, E. *Eur. J. Mineral.* **2004**, *16*, 143-149.
10.10 Vlasse, M.; Saux, M.; Echegut, P.; Villeneuve, G. *Mater. Res. Bull.* **1979**, *14*, 807-812.
10.11 Cooper, M. A.; Hawthorne, F. C. *Can. Mineral.* **2004**, *42*, 825-834.
10.12 Hawthorne, F. C. *Mineral. Petrol* **1984**, *33*, 135-146.
10.13 Heiderbrecht, K.; Jansen, M. *Z. Anorg. Allg. Chem.* **1991**, *597*, 79-86.
10.14 Chen, C.-S.; Kao, H.-M.; Lii, K.-H. *Inorg. Chem.* **2005**, *44*, 935-940.
10.15 Wierzbicka-Wieczorek, M.; Kolitsch, U.; Tillmanns, E. *Acta Cryst.* **2010**, *C66*, i29-i32.

Table 10.1. Crystallographic data for $K_5RE_2FSi_4O_{13}$ (RE = Y, Sc).

Formula	$K_5Y_2FSi_4O_{13}$	$K_5Sc_2FSi_4O_{13}$
Formula weight	712.68	624.78
Temperature (K)	296(2)	293(2)
Crystal system	Monoclinic	Monoclinic
Space group	*P* $2_1/m$	*P*$2_1/m$
a (Å)	7.1567(12)	6.9681(14)
b (Å)	5.7627(9)	5.5830(11)
c (Å)	18.005(3)	17.829(4)
β (°)	92.396(4)	91.52(3)
V ($Å^3$)	741.9(2)	693.3(2)
Z	2	2
Density (Mg/m^3)	3.190	2.993
Absorption coefficient (mm^{-1})	9.587	2.909
Crystal size (mm^3)	0.08 x 0.06 x 0.02	0.2 x 0.07 x 0.07
2 theta range (°)	4.53 to 61.32	2.28 to 56.62
reflections collected	17921	9525
data/restraints/parameters	2498 / 0 / 139	1893 / 0 / 140
R (int)	0.0681	0.0272
GOF (F^2)	1.018	1.322
R indices (all data)	R_1 = 0.0497	R_1 = 0.0377
	wR_2 = 0.0814	*w*R_2 = 0.0818

Table 10.2. Selected interatomic distances in $K_5Sc_2FSi_4O_{13}$, $K_5Y_2FSi_4O_{13}$, and $K_5Eu_2FSi_4O_{13}$.

	$K_5Sc_2FSi_4O_{13}$	$K_5Y_2FSi_4O_{13}$	$K_5Eu_2FSi_4O_{13}$
Sc(1) – F(1)	2.36(3) Å		
Sc(1) – F(2)	2.87(3) Å		
Sc(2) – F(1)	2.75(3) Å		
Sc(2) – F(2)	2.24(3) Å		
RE(1) – F		2.511(4) Å	2.550(4) Å
RE(2) - F		2.453(4) Å	2.490(4) Å
RE(1) – RE(2)	5.11(6) Å	4.964(8) Å	5.040(8) Å

Table 10.3. Selected bond angles for $K_5Sc_2FSi_4O_{13}$, $K_5Y_2FSi_4O_{13}$, and $K_5Eu_2FSi_4O_{13}$.

	$K_5Sc_2FSi_4O_{13}$	$K_5Y_2FSi_4O_{13}$	$K_5Eu_2FSi_4O_{13}$
Si(1) – O – Si(2)	139.3°	138.6°	135.9°
Si(2) – O – Si(3)	135.5°	133.1°	132.4°
Si(3) – O – Si(4)	140.0°	135.5°	135.9°

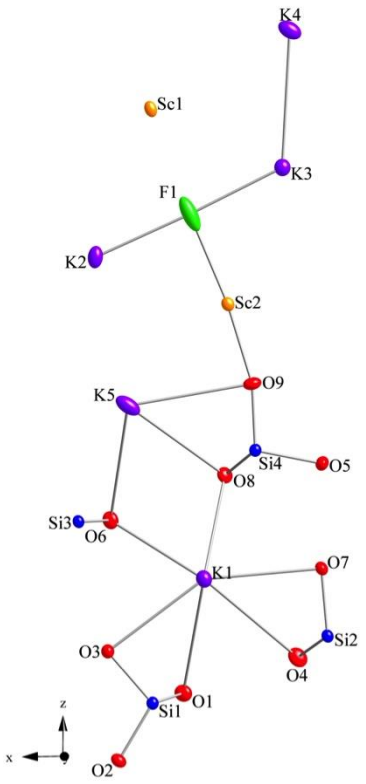

Figure 10.1. Asymmetric unit of $K_5Sc_2FSi_4O_{13}$ when solved with only one F site, showing the prolate nature of the F site if it is not split.

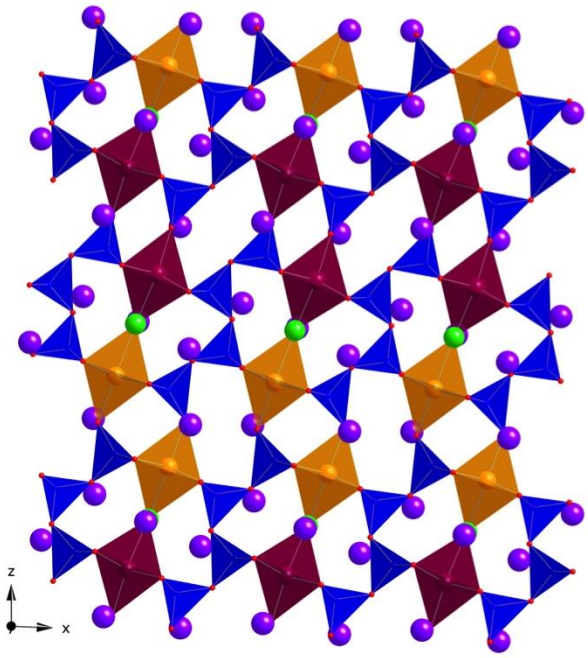

Figure 10.2. Crystal structure of $K_5Y_2FSi_4O_{13}$ highlighting the slabs created by the Y(1) and Y(2) atoms. Y(1) is shown in orange, Y(2) shown in red-violet, silicon is shown in blue, potassium is represented by purple spheres, fluorine is green, and the oxygens are shown in red.

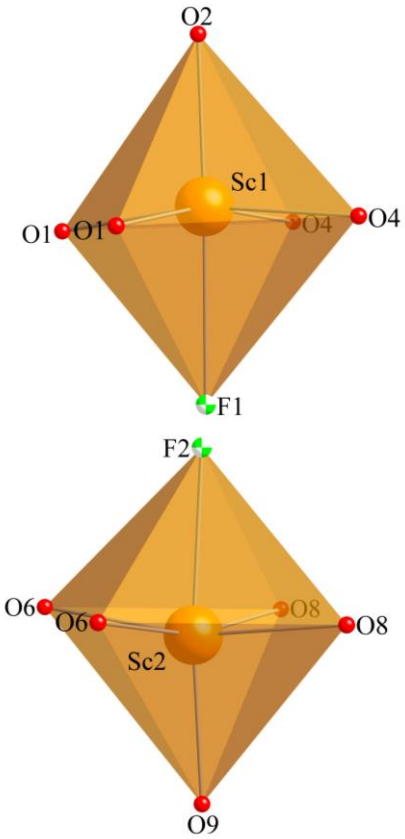

Figure 10.3. Structural image of $K_5Sc_2FSi_4O_{13}$ illustrating how the Sc(1) and Sc(2) polyhedra are corner shared through a fluorine. Both of the disordered fluorine atoms are shown where F1 is occupied 34(3) % of the time and F2 is occupied 66(3) % of the time.

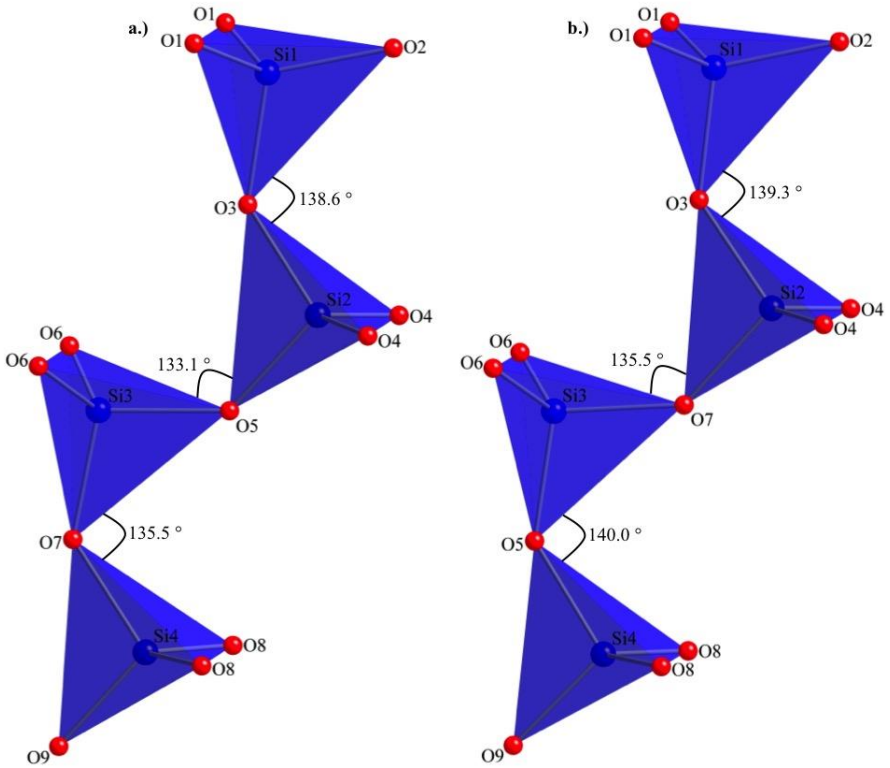

Figure 10.4. Structural representation of a.) $K_5Y_2FSi_4O_{13}$ and b.) $K_5Sc_2FSi_4O_{13}$ where the tilt angles of Si – O – Si are shown. Silicon is represented in blue and oxygen in red.

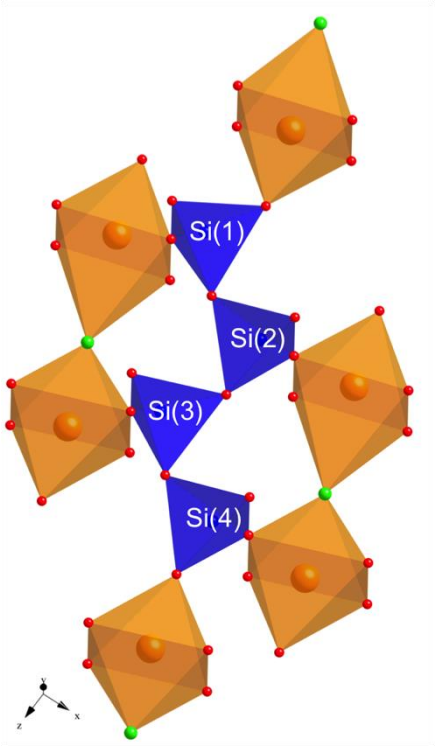

Figure 10.5. Visual representation of $K_5Sc_2FSi_4O_{13}$, indicating how the bond lengths of the Sc octahedra affect the Si – O – Si bond angles. Sc is shown in orange, Si is shown in blue, F is shown in green, and O is shown in red and the other disordered fluorine atom (F1) is omitted for clarity.

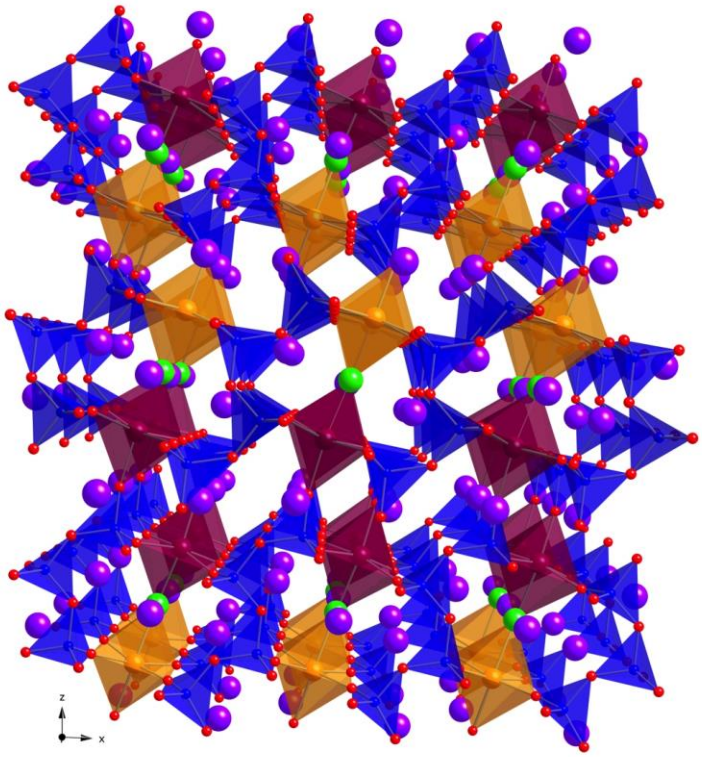

Figure 10.6. Overall structure of $K_5Y_2FSi_4O_{13}$, representative of $K_5Sc_2FSi_4O_{13}$. Potassium is shown in purple, RE(1) and RE(2) are shown in orange and red-violet, respectively, silicon is shown in blue, fluorine is shown in green, and oxygen is shown in red.

Chapter 11

Scintillation, Luminescence, and Magnetic Properties of a New Structure Type, $Cs_3LnSi_4O_{10}F_2$ (*Ln* = Gd, Tb, Dy)

Introduction

Lanthanide containing silicates are an extensively explored area. With a rigid framework due to the silicate structure and the presence of luminescent and magnetic centers from the lanthanide elements, lanthanide silicates have many potential uses in optical and magnetic applications. Despite the fact that lanthanide silicates are extensively explored, there are very few reports on cesium containing lanthanide silicates. In fact, $Cs_3EuSi_6O_{15}$,[11.1] $CsDy_{0.33}Si_2O_5$,[11.2] $Cs_6Nd_2Si_{21}O_{18}$, $Cs_{3.1}NdSi_8O_{19}$,[11.3] $Cs_3LnSi_8O_{19}$ (*Ln* = Sc, Y),[11.4, 11.5] $Cs_2Ln[Si_4O_{10}]F$ (*Ln* = Y, Er),[11.6] and $Cs_2Er[Si_6O_{14}]F$ [11.7] are the only known single-crystal cesium lanthanide silicates and, furthermore, of those only three compositions involve the presence of fluorine.

In addition to the dearth of cesium lanthanide silicates known, the structure reported here is also interesting due to its new silicate framework. There are many silicate units known, including isolated SiO_4 tetrahedra, Si_2O_7 dimers, chains of silicates, and silicate rings. This structure is the first reported case of a tetramer consisting of three rings of Si_3O_9 connected through another silicon tetrahedra.

Not only is the field of cesium lanthanide silicates an underexplored area but, it appears that it is an important area when considering scintillator materials. Scintillator materials are phosphors that convert the absorbed energy of a single photon of ionizing radiation from hard-UV, X-ray, or gamma-ray sources into numerous emitted photons with energies in the visible or near visible range.[11.8-11.10] As such, scintillator materials have applications in medical imaging techniques,[11.8] high energy physics,[11.11] oil well logging,[11.12] environmental monitoring, and security and defense.[11.13, 11.14]

Since scintillators are usually solids where there is a host lattice and an emission center (activator), lanthanide-activator-containing silicates are potential scintillator materials. While Ce^{3+} has been the most heavily studied lanthanide element as the emission center for a scintillator material, many other lanthanide elements, including Nd^{3+}, Eu^{2+}, Ho^{3+}, Er^{3+}, and Tm^{3+} have been proposed as strong candidates.[11.10] Currently, there are many Ce^{3+} doped silicates on the market due to their high chemical stability, fast decay times, and high light yield. We report new lanthanide silicates where both the terbium and europium analogues are scintillators.

Experimental Section

Reagents

$DyCl_3 \bullet 6\ H_2O$ (Alfa Aesar, 99.99 %), $GdCl_3 \bullet 6\ H_2O$ (Alfa Aesar, 99.9 %) CsCl (Alfa Aesar, 99 %), $TbCl_3 \bullet 6\ H_2O$ (Alfa Aesar, 99.9 %), $EuCl_3 \bullet x\ H_2O$ (Alfa Aesar, 99.9 %), SiO_2 (Alfa Aesar, 1.0 micron, 99.9 %), CsCl (Alfa Aesar, 99 %), and CsF (Strem Chemicals, 99+ %) were used as received.

Synthesis

X-ray diffraction quality single crystals of $Cs_3LnSi_4O_{10}F_2$ (*Ln* = Gd, Dy) were grown by placing $LnCl_3 \bullet x\ H_2O$ (1 mmol) and SiO_2 (1 mmol) into a silver tube crucible with a length of 6 – 7 cm. CsCl (11 mmol) and CsF (9 mmol) were mixed together and then loaded onto the reactants. A silver lid was loosely fitted on the crucible and the crucible was loaded into the furnace. The furnace was set to ramp to 900 ° C in 1.5 h, dwell at 900 ° C for 12 h, and then cool to 400 ° C at 6 ° C/h before the furnace was shut off. The crystals were then isolated from the flux by sonication in water and filtering by vacuum filtration.

Larger single crystals to be collected for property measurements were grown by using a stoichiometric ratio of $LnCl_3 \bullet x\ H_2O$ (1 mmol) and SiO_2 (4 mmol) with everything else held constant from the previous growth method.

Single-Crystal X-ray Diffraction

X-ray intensity data from hexagonal plate crystals of the gadolinium and dysprosium analogues were collected at 303(2) K using a Bruker D8 QUEST diffractometer equipped with a PHOTON100 CMOS area detector and an Incoatec microfocus source (Mo Kα radiation, λ = 0.71073 Å).[11.15] The data covered 100 % of reciprocal space to $2\theta_{max}$ = 72.7 ° (Gd) and 75.8 ° (Dy). The raw area detector data frames were reduced and corrected for absorption effects using the SAINT+ and SADABS programs.[11.16] Final unit cell parameters were determined by least-squares refinements of large sets of reflections taken from the data set. Subsequent difference Fourier calculations and full-matrix least-squares refinement against F^2 were performed with SHELXL-2014 using the ShelXle and OLEX2 interfaces.[11.17, 11.18]

Powder X-ray Diffraction

Crystals of each lanthanide were picked and ground. Powder X-ray diffraction (PXRD) data were collected on the ground samples using a Rigaku Ultima IV diffractometer with a Cu Kα source (λ = 1.54056 Å) and a D/teX detector. Data for the compounds were collected using a step scan covering the 2θ range of 5 – 65 ° in steps of 0.02 °. After PXRD data were collected, a cif file of either $Cs_3DySi_4O_{10}F_2$ or $Cs_3GdSi_4O_{10}F_2$ was overlaid to determine purity. The PXRD patterns of the Gd, Tb, and Dy analogues are provided in **Figure 11.1**.

Fluorescence Spectroscopy

Room temperature excitation and emission spectra of the Tb analogue were collected using a Perkin Elmer LS 55 fluorescence spectrometer. For the compounds, the emission spectra were collected over a range of 455 – 800 nm with an excitation λ of 268 nm and the excitation spectra were collected over a range of 240 - 448 nm with an emission λ of 544 nm.

Magnetic Measurements

The DC magnetic susceptibilities of $Cs_3LnSi_4O_{10}F_2$ (*Ln* = Gd, Tb, Dy) were measured as a function of temperature using a Quantum Design MPMS 3 SQUID Magnetometer. 5.72 mg (Gd), 6.05 mg (Tb), and 6.60 mg (Dy) of a ground sample of picked crystals were massed on a balance sensitive to 0.01 mg and loaded into a VSM powder holder for data collection. The zero-field cooled magnetic susceptibility was measured as a function of temperature between 2 – 300 K in an applied field of 1000 Oe. The measured magnetic data were corrected for shape and radial offset effects using the method reported by Morrison and zur Loye.[11.19]

Results and Discussion

Synthesis

Alkali halide fluxes have been used extensively to synthesize new silicate compositions.[11.20-11.31] When considering lanthanide containing silicate compositions, alkali halide fluxes are a good choice as they readily dissolve both the lanthanide starting material and the silicon dioxide. Furthermore, frequently when using an alkali halide flux the alkali or halide elements become incorporated into the product. Since our previous research has illustrated that fluorine appears to play a crucial role in the intensity

of fluorescence, CsF was chosen for this reaction. To lower the melting point of the flux, a CsF/CsCl eutectic was ultimately chosen. When the reaction was performed using off stoichiometry ratios of the elements (1 mmol *Ln* : 1 mmol Si), high quality single crystals were obtained. When, however, the reaction was performed using stoichiometric ratios of the elements (1 mmol *Ln* : 4 mmol Si), larger, easy to pick crystals that were easy to pick were obtained. Crystal pictures of the Eu, Gd, and Tb analogues are shown in **Figure 11.2**.

Structure

$Cs_3LnSi_4O_{10}F_2$ crystallizes in a new structure type in the triclinic space group *P*-1, where the crystallographic data are presented in **Table 11.1** and selected bond distances are provided in **Table 11.2**. In this structure there are two unique lanthanide sites, four unique silicon sites, three unique cesium sites, two unique fluorine sites, and ten unique oxygen sites. The silicon tetrahedra in this structure form a new silicate framework. Three SiO_4 tetrahedra form a Si_3O_9 ring where three Si_3O_9 rings are connected through a fourth silicon tetrahedra as shown in **Figure 11.3**. This silicate framework forms slabs where the slabs are separated by the lanthanide octahedra. The silicate slabs separated by the $Ln(2)O_6$ units are closer together than the silicate slabs separated by the $Ln(1)O_2F_4$ octahedra. This is due to the fact that all lanthanide oxygens are part of the silicate slabs causing the $Ln(2)O_6$ octahedra to be tilted more than the $Ln(1)O_2F_4$ octahedra. The cesium atoms fill in the spaces in the structure. A view down the *a* axis of the structure is shown in **Figure 11.4** and a view down the *c* axis is shown in **Figure 11.5**.

Fluorescence Spectroscopy

A phase pure sample of the terbium analogue was picked as single crystals from the flux reaction. The crystals were ground and a powder X-ray diffraction pattern was obtained to verify purity. Room temperature emission and excitation scans were collected on the terbium analogue as shown in **Figure 11.6**. The emission spectrum has peaks ranging from the blue region to the red region. The peaks from 535 – 550 nm are indicative of terbium containing compounds, however, there are usually five strong peaks in this region. Future studies with more sample are currently underway to verify these preliminary results.

Scintillation (Preliminary Results)

Due to the presence of heavy elements, specifically cesium and terbium, and the luminescent nature of the material, preliminary scintillation tests were done on the terbium analogue. **Figure 11.7** shows the how the terbium analogue scintillates when exposed to copper source X-ray radiation. Future studies in collaboration with Oak Ridge National Laboratory are ongoing to determine how the material scintillates quantitatively under numerous radiation sources, including neutrons.

Magnetic Properties

The magnetic data for the $Cs_3LnSi_4O_{10}F_2$ (*Ln* = Gd, Tb, Dy) family is presented in **Table 11.3**. The magnetic samples were obtained by picking hexagonal plate crystals of each analogue and grinding them into powders. The powders were verified to be phase pure by powder X-ray diffraction. The magnetic susceptibilities and inverse susceptibilities are shown in **Figure 11.8**. All samples are paramagnetic, however, the gadolinium analogue does not follow Curie Weiss behavior. For terbium and

dysprosium, the inverse susceptibility was fit over the range of 100 – 300 K. The effective moments of 9.63 μ_B (Tb) and 10.42 μ_B (Dy), are consistent with the theoretical moments of 9.72 μ_B (Tb) and 10.65 μ_B (Dy).

Conclusion

We have synthesized a new family of cesium-lanthanide-silicates. The compositions $Cs_3LnSi_4O_{10}F_2$ (*Ln* = Gd, Tb, Dy) represent a rare example of a cesium-lanthanide-silicate and, furthermore, are the first example of a new silicate framework. Physical property measurements indicate strong luminescence and strong scintillation abilities. Future studies, including expanding the $Cs_3LnSi_4O_{10}F_2$ family to include all lanthanides, doping multiple lanthanides into the structure to tune scintillation and luminescent properties, and expansion by replacing the tetragen from silicon to germanium are ongoing and show promise.

References

11.1 Meowhu, H.; Chen, Y.-H.; Borchen, C.; Lii, K.-H. *Chem. Mater.* **2005**, *17*, 5743-5747.
11.2 Xinguang, Z.; Jiyang, L.; Peng, C.; Yi, L.; Qigxin, C.; Xiaoyang, L.; Jihong, Y.; Ruren, X. *Inorg. Chem.*
11.3 Schaefer, M. C.; Schleid, T. *Z. Naturforsch., B: Chem. Sci.* **2009**, *64*, 1329-1338.
11.4 Kolitsch, U.; Tillmanns, E. *Mineral. Mag.* **2004**, *68*, 677-686.
11.5 Kolitsch, U.; Wierzbicka Wieczorek, M.; Tillmanns, E. *Can. Mineral.* **2009**, *47*, 421-431.
11.6 Schaefer, M. C.; Schleid, T. *Z. Anorg. Allg. Chem.* **2007**, *633*, 1018-1023.
11.7 Dabić, P.; Kahlenberg, V.; Schmidmair, D.; Kremenović, A.; Vulić, P. *Z. Kristallogr.* **2016**, *231*, 195-207.
11.8 Horiai, T.; Kurosawa, S.; Murakami, R.; Pejchal, J.; Yamaji, A.; Shoji, Y.; Chani, V. I.; Ohashi, Y.; Kamada, K.; Yokota, Y.; Yoshikawa, A. *Opt. Mater.* **2016**, *58*, 14-17.
11.9 Lecoq, P.; Annenkov, A.; Gektin, A.; Korzhik, M.; Pedrini, C. *Inorganic Scintillators for Detector Systems*; Springer: Netherlands, 2006; pp 1-27.
11.10 Yanagida, T. *Opt. Mater.* **2013**, *35*, 1987-1992.
11.11 Bartosiewicz, K.; Babin, V.; Kamada, K.; Yoshikawa, A.; Mares, J. A.; Beitlerova, A.; Nikl, M. *Opt. Mater.* **2016**, *In Press*,
11.12 Yamaguchi, H.; Kamada, K.; Kurosawa, S.; Pejchal, J.; Shoji, Y.; Yokota, Y.; Ohashi, Y.; Yoshikawa, A. *Opt. Mater.* **2016**, *In Press*,
11.13 Yanagida, T.; Koshimizu, M.; Okada, G.; Kojima, T.; Osada, J.; Kawaguchi, N. *Opt. Mater.* **2016**, *In Press*,
11.14 Totsuka, D.; Yanagida, T.; Fukuda, K.; Kawaguchi, N.; Fujimoto, Y.; Pejchal, J.; Yokota, Y.; Yoshikawa, A. *Nucl. Instrum. Methods Phys. Res., Sect. A* **2011**, *659*, 399-402.
11.15 APEX2 Version 2014.9-0, SAINT+ Version 8.34A and SADABS Version 2014/4. Bruker Analytical X-ray Systems, Inc., Madison, Wisconsin, USA, 2014.
11.16 SMART Version 5.630, SAINT+ Version 6.45 and SADABS Version 2.10. Bruker Analytical X-ray Systems, Inc., Madison, Wisconsin, USA, 2003.
11.17 ShelXle: a Qt graphical user interface for SHELXL. Hübschle, C. B., Sheldrick, G. M., Bittrich, B. J. Appl. Cryst. **2011**, *44*, 1281-1284.
11.18 Dolomanov, O. V.; Bourhis, L. J.; Gildea, R. J.; Howard, J. A. K.; Puschmann, H. *J. Appl. Cryst.* **2009**, *42*, 339-341.
11.19 Morrison, G.; zur Loye, H.-C. *J. Solid State Chem.* **2015**, *221*, 334-337.
11.20 Bugaris, D. E.; zur Loye, H.-C. *Angew. Chem. Int. Ed.* **2012**, *51*, 3780-3811.
11.21 Latshaw, A. M.; Wilkins, B. O.; Hughey, K. D.; Yeon, J.; Williams, D. E.; Tran, T. T.; Halasyamani, P. S.; zur Loye, H.-C. *CrystEngComm.* **2015**, *17*, 4654-4661.
11.22 Latshaw, A. M.; Morrison, G.; zur Loye, H.-C. *J. Chem. Crystallogr.* **2015**, *45*, 350-354.
11.23 Latshaw, A. M.; Myers, A. R.; Smith, M. D.; zur Loye, H.-C. *J. Chem. Crystallogr.* **2015**, *45*, 207-211.
11.24 Latshaw, A. M.; Hughey, K. D.; Smith, M. D.; Yeon, J.; zur Loye, H.-C. *Inorg. Chem.* **2015**, *54*, 876-884.

11.25 Latshaw, A. M.; Yeon, J.; Smith, M. D.; zur Loye, H.-C. *J. Solid State Chem.* **2016**, *235*, 100-106.
11.26 Latshaw, A. M.; Smith, M. D.; zur Loye, H.-C. *Solid State Sci.* **2014**, *35*, 28-32.
11.27 Morrison, G.; Smith, M. D.; Tran, T. T.; Halasyamani, P. S.; zur Loye, H.-C. *CrystEngComm* **2015**, *17*, 4218-4224.
11.28 Morrison, G.; zur Loye, H.-C.
11.29 Morrison, G.; Ramanantoanina, H.; Urland, W.; Smith, M. D.; zur Loye, H.-C. *Inorg. Chem.* **2015**, *54*, 5504-5511.
11.30 Morrison, G.; Tran, T. T.; Halasyamani, P. S.; zur Loye, H.-C. *Inorg. Chem.* **2016**, *55*, 3215-3217.
11.31 Morrison, G.; Smith, M. D.; zur Loye, H.-C. *J. Am. Chem. Soc.* **2016**, *138*, 7121-7129.

Table 11.1. Crystallographic table for single crystal X-ray data for $Cs_3LnSi_4O_{10}F_2$ (*Ln* = Gd, Dy).

Formula	$Cs_3GdSi_4O_{10}F_2$	$Cs_3DySi_4O_{10}F_2$
Formula weight	866.34	871.59
Temperature (K)	300.1	303.9
Crystal system	Triclinic	Triclinic
Space group	*P*-1	*P*-1
a (Å)	7.0994(3)	7.0856(2)
b (Å)	7.1499(3)	7.1360(3)
c (Å)	16.2572(7)	16.1856(5)
V (Å^3)	711.67(5)	705.72(4)
Z	2	2
Density (Mg/m^3)	4.043	4.102
Absorption coefficient (mm^{-1})	12.621	13.322
Crystal size (mm^3)	0.04 × 0.08 × 0.1	0.03 × 0.07 × 0.08
2 theta range (°)	5.05 to 72.70	5.07 to 75.75
reflections collected	41718	63900
data/restraints/ parameters	6895 / 0 / 186	7633 / 0 / 186
R (int)	0.0319	0.0315
GOF (F^2)	1.139	1.235
R indices (all data)	R_1 = 0.0366 wR_2 = 0.0492	R_1 = 0.0281 wR_2 = 0.0658

Table 11.2. *Ln* – O and *Ln* – F bond lengths.

	$Cs_3GdSi_4O_{10}F_2$	$Cs_3DySi_4O_{10}F_2$
Ln(1) – F(1) (x2)	2.238(2) Å	2.217(3) Å
Ln(1) – F(2) (x2)	2.240(2) Å	2.215(3) Å
Ln(1) – O(2) (x2)	2.258(2) Å	2.218(3) Å
Ln(2) – O(5) (x2)	2.296(2) Å	2.273(3) Å
Ln(2) – O(7) (x2)	2.291(2) Å	2.261(3) Å
Ln(2) – O(10) (x2)	2.288(2) Å	2.256(3) Å

Table 11.3. Experimental magnetic moments (μ_{eff}) compared to calculated moments (μ_{calc}) for $Cs_3LnSi_4O_{10}F_2$ (*Ln* = Tb, Dy).

Compound	Fit Range (K)	θ (K)	μ_{eff} (μ_B/*Ln*)	μ_{calc} (μ_B/*Ln*)
$Cs_3TbSi_4O_{10}F_2$	100 – 300 K	0.3	9.63	9.72
$Cs_3DySi_4O_{10}F_2$	100 – 300 K	3.9	10.42	10.65

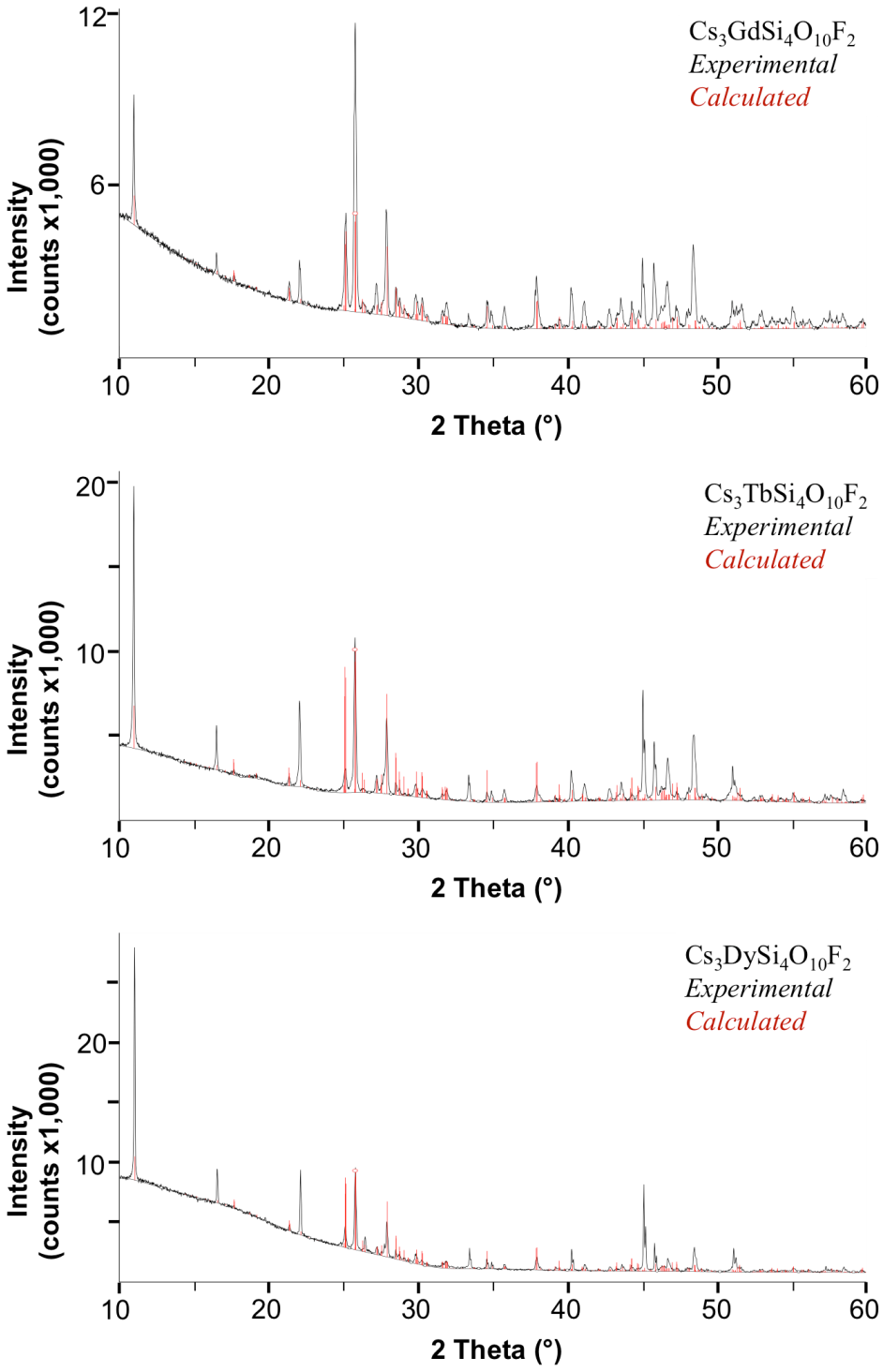

Figure 11.1. Powder X-ray diffraction patterns of $Cs_3LnSi_4O_{10}F_2$ (*Ln* = Gd, Tb, Dy) where the experimental powder is provided in black and the calculated pattern of $Cs_3DySi_4O_{10}F_2$ or $Cs_3GdSi_4O_{10}F_2$ is overlaid in red.

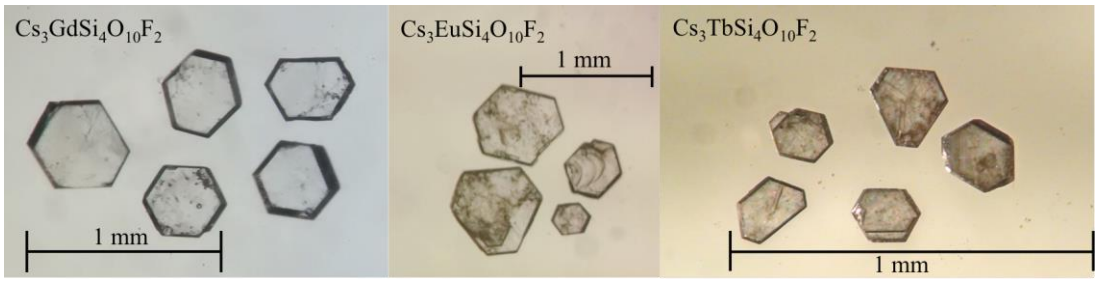

Figure 11.2. Crystal images of $Cs_3LnSi_4O_{10}F_2$ (*Ln* = Eu, Gd, Tb).

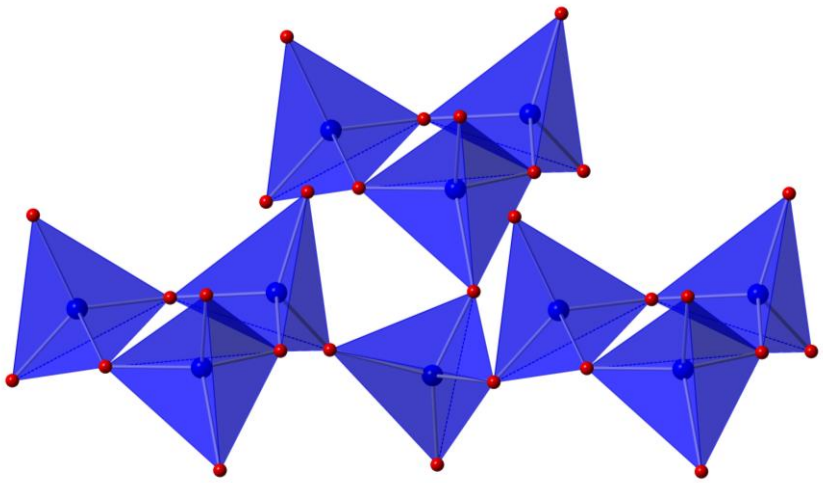

Figure 11.3. Representation of the new silicate framework where Si is shown in blue and oxygen is shown in red.

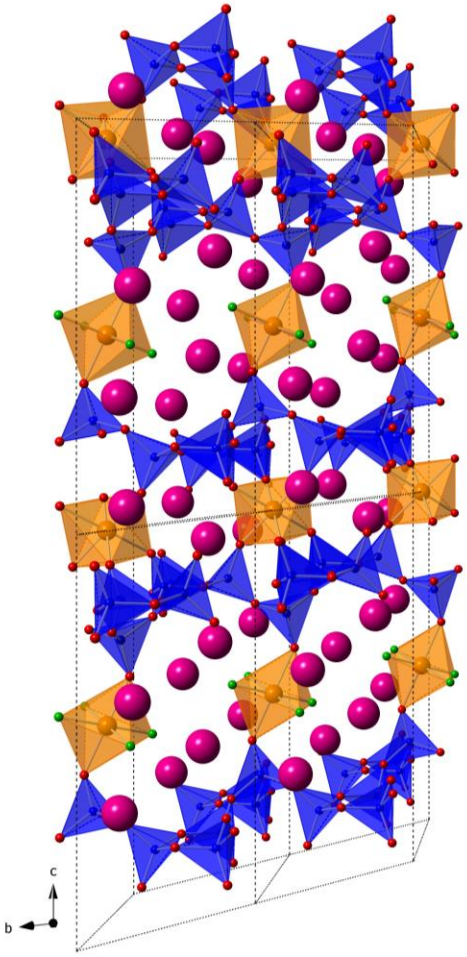

Figure 11.4. View of $Cs_3LnSi_4O_{10}F_2$ down the *a* axis where the lanthanide is shown in orange, the silicon in blue, cesium in pink, and oxygen in red.

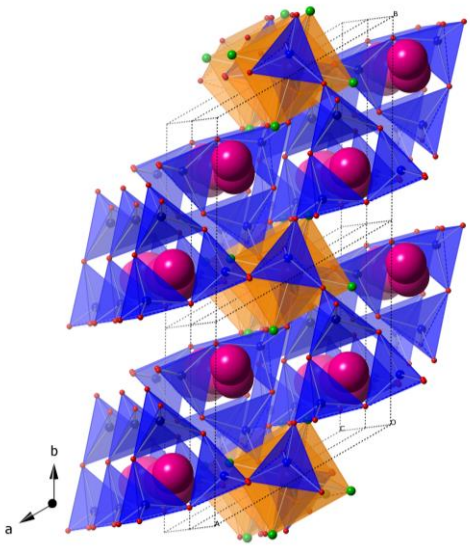

Figure 11.5. View down the *c* axis of $Cs_3LnSi_4O_{10}F_2$ where the color scheme follows **Figure 11.4**.

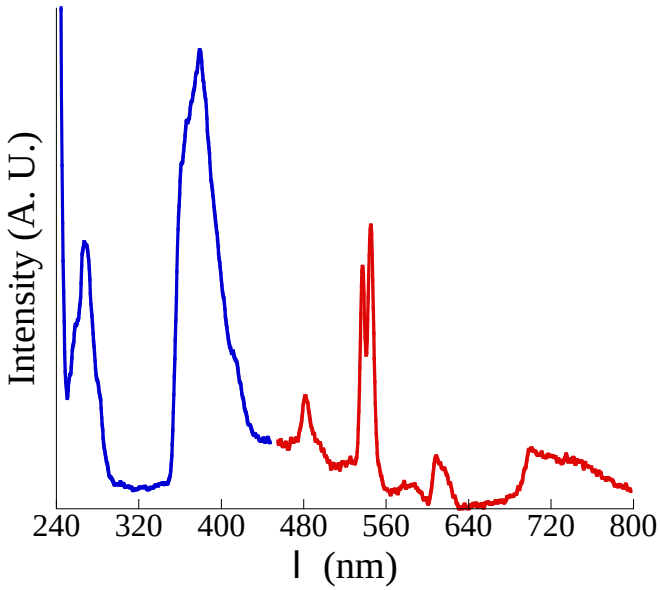

Figure 11.6. Fluorescence plots of $Cs_3TbSi_4O_{10}F_2$ where the excitation plot at an emission λ of 544 nm is shown in blue and the emission plot at an excitation λ of 268 nm is shown in red.

Figure 11.7. Preliminary scintillation tests showing how the $Cs_3TbSi_4O_{10}F_2$ scintillates under a Cu X-ray source.

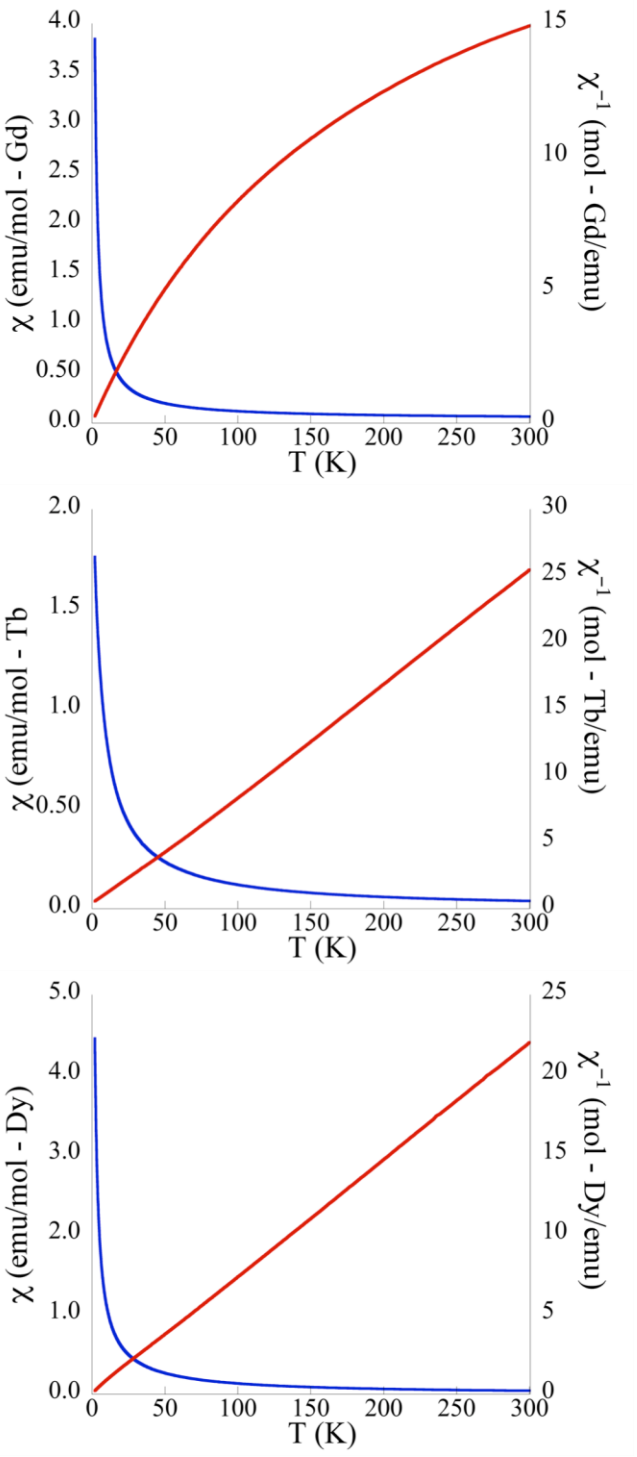

Figure 11.8. Magnetic susceptibilities and inverse susceptibilities of $Cs_3GdSi_4O_{10}F_2$ (top), $Cs_3TbSi_4O_{10}F_2$ (middle), and $Cs_3DySi_4O_{10}F_2$ (bottom).

Appendix A

Hydroflux Synthesis and Crystal Structure of New Lanthanide Tungstate Oxyhydroxides*

*Latshaw, A. M., Smith, M. D., Chance, W. M., zur Loye, H.-C. *Solid State Sci*., **2015**, *42*, 14-19.

Introduction

A recent surge in the use of the hydroflux method to synthesize crystals has proven that this method is adaptable and can be used for the creation of crystals of complex structures that contain diverse elements, including alkali and alkaline earth elements, lanthanides, arsenic, manganese, cobalt, nickel, copper, silicon, and tungsten. The hydroflux method is quite general and can be used to grow single crystals of oxides, hydroxides, oxyhydroxides, and hydrated oxides;[A.1-A.7] where it exemplifies one important approach for the preparation of single crystals of thermally unstable phases.

The hydroflux method uses a very high water content hydroxide flux as the "high" temperature solution in which crystals are grown. By using a wet hydroxide flux, the dwelling temperature needed for the reactions is lowered from a range of 320-1300°C in hydroxide flux reactions[A.8] to 180-230°C in hydroflux reactions.[A.1-A.6] The amount of water added is important as it controls the acid-base chemistry of the flux when it is molten, following the Lux-Flood concept of oxo-acidity.A.9-A.11 Because the hydroflux is a melt and not simply an aqueous solution, there is no significant pressure buildup in the reaction vessel.

While a significant number of complex oxides containing tungsten are known, there are very few reports of tungsten containing oxyhydroxides, especially of those also containing an alkali and a lanthanide cation.[A.12, A.13] Looking at early transition metal examples, there are many instances of single crystals grown as oxides and a few examples of oxyhydroxides. These oxides and oxyhydroxides include but are not limited to Na*Ln*TiO_4 (*Ln* = La, Pr, Nd),[A.14] $K_2Hf_2O_5$ and $K_4Hf_5O_{12}$,[A.15] $A_5(VO_4)_3(OH)$ (A = Sr, Ba),[A.16] *Ln*KNaMO_5 (*Ln* = La, Pr, Nd, Sm, Eu, Gd, Tb; M = Nb, Ta),[A.17-A.19]

$Ln_4Na_2K_2M_2O_{13}$ (*Ln* = Nd, Sm, Eu, Gd; M = Nb, Ta),[A.20] $Rb_4Al_2Nb_{35}O_{70}$,[A.21] $Li_3Al(MoO_4)_3$,[A.22] $Cs_{0.33}MoO_3$ and $CsFe(MoO_4)_2$,[A.23] $KBaMnO_4$,[A.6] $K_2Ba(MO_4)_2$ (M = Cr, Mo, W),[A.3] Ba_2MgWO_6 and Ba_2ZnWO_6,[A.24] $Sr_2Mn(OH)_6$ and $Ba_2Mn(OH)_6$.[A.1] Herein we present the hydroflux crystal growth of a series of new tungsten containing oxyhydroxides and report their crystal structures.

Experimental Section

Sample Preparation

Reactants.

Er_2O_3, Tm_2O_3, and Yb_2O_3 (99.9%) were purchased from Alfa Aesar. WO_3 (99.8%) was purchased from Alfa Aesar, $Na_2SiO_3 \cdot 9H_2O$ (99.9%) was purchased from EM Science, and NaOH (ACS grade) was purchased from Macron.

Synthesis.

Crystals of $Na_5Ln(OH)_6WO_4$ where *Ln* = Er, Tm, and Yb were grown in a hydroflux. Na_2SiO_3 (2.93 mmol), Ln_2O_3 (0.3 mmol), and WO_3 (0.7 mmol) were put into a hydroflux of NaOH (9.5g) and H_2O (7g) and were placed into a 23 mL PTFE-lined stainless steel autoclave. The autoclaves were loaded into a programmable oven at a temperature of 230° C. The oven was programmed to hold at 230° C for 12 hr before cooling to 80° C at a rate of 0.1° C/min. The flux was then washed away from the crystals by sonication in methanol. Crystals were kept in methanol to prevent the degradation of the crystals that occurs in moisture over a period of weeks.

Characterization

Single Crystal X-ray Diffraction

Crystals of all compounds formed as colorless (Tm, Yb) and pink (Er) rod crystals that decompose in methanol over a period of weeks, presumably due to moisture sensitivity. Intensity data for each were collected at 100(2) K using a Bruker SMART APEX diffractometer (Mo Ka radiation, λ = 0.71073 Å).[A.25] The data collections covered > 98.7% of reciprocal space to $2\theta_{max}$ = 70º, with an average reflection redundancies of at least 4.7. The raw area detector data frames were reduced and corrected for absorption effects with the SAINT+ and SADABS programs.[A.25] Final unit cell parameters were determined by least-squares refinement of large sets of reflections taken from the data sets. An initial structural model was obtained with direct methods.[A.26] Subsequent difference Fourier calculations and full-matrix least-squares refinement against F^2 were performed with SHELXL-2014[A.26] using the ShelXle interface.[A.27]

The compounds are isostructural and crystallize in the monoclinic system. The space group *I*2/*a* (No. 15) was consistent with the pattern of systematic absences in the intensity data and was confirmed by structure solution. The asymmetric unit consists of one tungsten atom, two unique lanthanide atoms, six sodium atoms, 10 oxygen atoms and six hydrogen atoms. Tungsten W(1), sodium atoms Na(1)-Na(4) and all oxygen and hydrogen atoms are located on general positions (Wyckoff site 8*f*). Both lanthanide atoms *Ln*(1) and *Ln*(2) and sodium atoms Na(5) and Na(6) are located on two-fold axes (site 4*e*). In the Tm and Yb crystals, sodium atom Na(6) is disordered over two 4*e* sites with occupancies Na(6A)/Na(6B) = 0.839(5) / 0.161(5) and 0.843(5) / 0.157(5), respectively (constrained to sum to one). For *Ln* = Er, no two-fold disorder was observed

for Na(6). Only electron density peak is observed in this region, corresponding to the major Na(6A) site in the *Ln* = Tm and Yb crystals. From trial refinement models site Na(6A) refined to an occupancy factor of 0.98(1), and was fixed at full occupancy for the final cycles. All non-hydrogen atoms were refined with anisotropic displacement parameters. No deviation from full occupancy was observed for any of the metal atoms except Na(6). Positions for six hydroxyl hydrogen atoms were located in Fourier difference maps, at reasonable distances from the six independent oxygen atoms of the two $Ln(OH)_6$ octahedra (O(1)-O(6)). The hydrogen atoms were refined isotropically subject to *d*(O-H) = 0.84(2) Å distance restraints. The largest residual electron density peak and hole in the final difference maps are: Er, +1.46 and -2.16 e-/Å3, located 0.66 and 0.74 Å from W(1) and Er(2), respectively; Tm, +1.59 and -1.47 e-/Å3, both located 0.69 and 0.76 Å from W(1); Yb, +1.82 and -1.91 e-/Å3, located 0.72 Å and 0.62 Å from W(1) and Yb(2), respectively. Further details of the crystal structure investigation can be obtained from the Fachinformationszentrum Karlsruhe, 76344 Eggenstein-Leopoldshafen, Germany (fax:+497247808666; e-mail: crystdata@fiz-karlsruhe.de) on quoting the depository numbers CSD-429090, 429091, and 429092 for the Er, Tm, and Yb analogues, respectively.

Powder X-ray Diffraction

Powder X-ray diffraction (PXRD) data of a collection of hand-picked crystals were collected. Although hand-picked, the data analysis indicated the presence of $Na_5Ln(OH)_6WO_4$, $Na_2(WO_4)(H_2O)_2$,[A.28] and SiO_2. Even in the Er sample, where only pink colored crystals were picked, this mixture was identified in the PXRD data,

suggesting that the two other phases are either bound to the crystal surface or form as inclusions within the crystals of $Na_5Ln(OH)_6WO_4$.

Results and Discussion

Hydroflux Approach

High temperature solutions have been used extensively for materials discovery via the crystal growth of complex oxides where, typically, very high quality crystals are obtained in the 300 to over 1200 °C temperature range. While the high temperatures aid in the formation of high quality crystals, they limit the discovery process to phases that are stable at high temperatures. To obtain new, low temperature stable phases, requires a different approach. The hydroflux approach is one that enables the preparation of compositions that are not thermally stable, such as hydroxides, oxyhydroxides, and hydrated oxides. For example, we have previously used the hydroflux method to prepare a series of complex platinum metal containing hydroxide, $Sr_6NaPd_2(OH)_{17}$, $Li_2Pt(OH)_6$, $Na_2Pt(OH)_6$, $Sr_2Pt(OH)_8$, and $Ba_2Pt(OH)_8$, that have limited thermal stability.[A.7] Similarly, the synthesis of complex transition metal based hydroxides and of hydrated transition metal oxides was achieved via the hydroflux approach.[A.2] The oxyhydroxides prepared in this study are another example of materials with limited stability that can be obtained as single crystals by operating the crystal growth process at 230 °C.

Structural Discussion

Single crystals of $Na_5Ln(OH)_6WO_4$ where *Ln* = Er, Tm, Yb all crystallize in the *I*2/*a* space group. The crystallographic data are given in **Table A.1** and crystal pictures are shown in **Figure A.1**. During the structure refinement, the initial indexations of the diffraction patterns of each compound repeatedly produced a *C*-centered monoclinic unit

cell with a = 11.23 Å, b = 16.22 Å, c = 6.01 Å, β = 102.0º and V = 1070.1 Å^3, *i.e.*, a subcell with half the volume of the reported cell (unit cell data for RE = Tm). Solution in *C*2/*m* gave good refinement statistics ($R1$ = 2.4%), but imposed disorder of oxygen atoms of the WO_4 tetrahedron. The metal atom positions (except Na(6), see below) and most other oxygen atoms are consistent with the smaller cell. In *C*2/*m*, the WO_4 group is located on the mirror plane with one oxygen disordered across the mirror, showing a highly prolate displacement parameter (U_3/U_1 = 11.7) along with two large residual electron density peaks (*ca*. 2 e^-/Å^3 each) indicating further splitting of this oxygen position. In *C*2/*m* adjacent WO_4 groups appear superimposed (related by a unit cell translation) along the *c* axis direction. Closer inspection of the area detector data frames showed many weak reflections unindexable to the *C*2/*m* cell, but which could be fit to a body centered monoclinic cell with a doubled *c* axis. For ease of comparison with the *C*-centered subcell, (and because the *I*-centered cell is actually the conventional cell), an *I*-centered monoclinic cell with a = 11.23 Å, b = 16.22 Å, c = 12.01 Å, β = 102.0º, V = 2139.9 Å^3 was selected. The weaker reflections consistent with the doubled cell arise because the WO_4 tetrahedra show a small modulation, which generate alternating tetrahedra along the *c* axis, with a repeating unit of two tetrahedra. The WO_4 tetrahedra refine with spherical displacement parameters, accompanied by no unusual residual electron density. The WO_4 groups are now located on a general position with no imposed symmetry and do not superimpose when viewed along the *c* axis direction, with adjacent tetrahedra related by a glide plane. Another consequence of the enlarged cell is the observation of partial or complete occupational ordering of the disordered Na(6) position. In the *C*2/*m* subcell, this atom is disordered across a mirror plane with equal populations

by symmetry. In the correct *I*2/*a* cell this mirror plane is absent, and the major disorder fraction now refines to *ca*. 84% for *Ln* = Tm and Yb, showing partial ordering. For *Ln* = Er, no Na(6) disorder was observed as the Na(6A) site refined to 100% occupancy within experimental error. The heavy metal atom substructure, which dominates the X-ray scattering, along with five of the six independent sodium atoms and 8 of the 10 independent oxygen atoms are described by the smaller *C*2/*m* cell. The enlarged *I*2/*a* cell is caused primarily by modulation of only two oxygen atoms of the WO_4 tetrahedron by site occupancy ordering of a sodium atom, which is the reason the reflections generating this correct cell are weak.

In the structure solved in the *I*2/*a* space group, there are six sodium, two lanthanide, one tungsten, ten oxygen, and six hydrogen sites. Both lanthanide sites form isolated octahedra that alternate down the *b* axis, as shown in **Figure A.2**. The tungsten site forms isolated tetrahedra that are slightly offset so that they do not perfectly align down the *c* axis (**Figure A.3**). The tungsten tetrahedra are boxed in by sodium atoms with lanthanide atoms occupying the corners of the boxes, as shown in **Figures A.3** and **A.4**. **Figure A.4** also illustrates the split sodium site Na(6A) and Na(6B) seen in the Tm and Yb analogues but absent in the Er analogue. The hydroxides are bound to the lanthanide octahedra (**Figure A.5**). The overall structure is shown down the *c* axis in **Figure A.6**. The average W-O bond distance is 1.78 Å and other select bond distances are given in **Table A.2**. The charges of the tungsten and lanthanide ions have been identified by bond valence sum to be W^{6+} and Ln^{3+} for both unique *Ln* sites with the bond valence sums given in **Table A.3**.

Conclusion

Three new lanthanide tungsten oxyhydroxides were synthesized by the hydroflux method and characterized by single crystal X-ray diffraction. The ability to stabilize this series of oxidehydroxides further demonstrates the usefulness of the hydroflux method for the preparation of single crystals of low temperature phases.

References

A.1 Chance, W. M.; Bugaris, D. E.; Sefat, A. S.; zur Loye, H.-C. *Inorg. Chem.* **2013**, *52*, 11723-11733.
A.2 Chance, W. M.; Smith, M. D.; zur Loye, H.-C. *J. Chem. Crystallogr.* **2014**, *44*, 20-24.
A.3 Chance, W. M.; zur Loye, H.-C. *Solid State Sci.* **2014**, *28*, 90-94.
A.4 Latshaw, A. M.; Chance, W. M.; Morrison, G.; Smith, M. D.; Yeon, J.; zur Loye, H.-C. *CrystEngComm* **2015**, *17*, 14-19.
A.5 zur Loye, K. D.; Latshaw, A. M.; Smith, M. D.; Chance, W. M.; zur Loye, H.-C. *J. Chem. Crystallogr.* **2014**, *45*, 20-25.
A.6 zur Loye, K. D.; Chance, W. M.; Yeon, J.; zur Loye, H.-C. *Solid State Sci.* **2014**, *37*, 86-90.
A.7 Bugaris, D. E.; Smith, M. D.; zur Loye, H.-C. *Inorg. Chem.* **2013**, *52*, 3836-3844.
A.8 Bugaris, D. E.; zur Loye, H.-C. *Angew. Chem. Int. Ed.* **2012**, *51*, 2-34.
A.9 Flood, H.; Fortland, T. *Acta Chem. Scand.* **1947**, *1*, 592.
A.10 Lux, H. Z.; *Z. Electrochemistry* **1939**, *45*, 303.
A.11 Mugavero III, S. J.; Gemmill, W. R.; Roof, I. P.; zur Loye, H.-C. *J. Solid State Chem.* **2009**, *182*, 1950-1963.
A.12 Ismail, A. H.; Dickman, M. H.; Kortz, U. *Inorg. Chem.* **2009**, *48*, 1559-1565.
A.13 Ismail, A. H.; Bassil, B. S.; Suchopar, A.; Kortz, U. *Eur. J. Inorg. Chem.* **2009**, *34*, 5247-5252.
A.14 Stackhouse, C. A.; Bugaris, D. E.; Khalsa, H. S.; Zhao, Q.; Bharathy, M.; zur Loye, H.-C. *J. Chem. Crystallogr.* **2012**, *42*, 529-532.
A.15 Zhao, Q.; Bugaris, D. E.; Stackhouse, C. A.; Smith, M. D.; zur Loye, H.-C. *Mater. Res. Bull.* **2011**, *46*, 166-169.
A.16 Mugavero, S. J., III; Bharathy, M.; McAlum, J.; zur Loye, H.-C. *Solid State Sci.* **2008**, *10*, 370-376.
A.17 Roof, I. P.; Jagau, T.-C.; Zeier, W. G.; Smith, M. D.; zur Loye, H.-C. *Chem. Mater.* **2009**, *21*, 1955-1961.
A.18 Roof, I. P.; Smith, M. D.; Park, S.; zur Loye, H.-C. *J. Am. Chem. Soc.* **2009**, *131*, 4202-4203.
A.19 Roof, I. P.; Smith, M. D.; zur Loye, H.-C. *Solid State Sci.* **2010**, *12*, 759-764.
A.20 Jagau, T.-C.; Roof, I. P.; Smith, M. D.; zur Loye, H.-C. *Inorg. Chem.* **2009**, *48*, 8220-8226.
A.21 Geselbracht, M. J.; Stacy, A. M. *J. Solid State Chem.* **1994**, *110*, 1-5.
A.22 Bugaris, D. E.; zur Loye, H.-C. *Acta Crystallogr., Sect. C: Cryst. Struct. Commun.* **2012**, *68*, i34-i36.
A.23 Mahjoor, P.; Latturner, S. E. *Philos. Mag.* **2012**, *92*, 2582-2595.
A.24 Bugaris, D. E.; Hodges, J. P.; Huq, A.; zur Loye, H.-C. *J. Solid State Chem.* **2011**, *184*, 2293-2298.
A.25 SMART Version 5.631, SAINT+ Version 6.45 and SADABS Version 2.10. Bruker Analytical X-ray Systems, Inc., Madison, Wisconsin, USA, 2003.
A.26 Sheldrick, G. M. *Acta Cryst.* **2008**, *A64*, 112-122.
A.27 ShelXle: a Qt graphical user interface for SHELXL. Hübschle, C. B., Sheldrick, G. M., Bittrich, B. J. Appl. Cryst. **2011**, 44, 1281-1284.

A.28 Okada, K.; Morikawa, H.; Marumo, F.; Iwai, S. I. *Bull. Tokyo Inst. Technol.* **1974**, *120*, 7-11.

Table A.1. Crystallographic data for $Na_5Er(OH)_6WO_4$, $Na_5Tm(OH)_6WO_4$, and $Na_5Yb(OH)_6WO_4$.

Formula	$Na_5Er(OH)_6WO_4$	$Na_5Tm(OH)_6WO_4$	$Na_5Yb(OH)_6WO_4$
Formula weight	632.11	633.78	637.89
Temperature (K)	100(2)	100(2)	100(2)
Crystal system	Monoclinic	Monoclinic	Monoclinic
Space group	*I* 2/*a*	*I* 2/*a*	*I* 2/*a*
a (Å)	11.2412(6)	11.2257(7)	11.2024(7)
b (Å)	16.2074(9)	16.2220(10)	16.1850(10)
c (Å)	12.0323(7)	12.0133(8)	11.9913(7)
β (°)	102.025(2)	101.999(2)	102.021(2)
V (Å^3)	2144.1(2)	2139.9(2)	2126.5(2)
Z	8	8	8
Density (mg/m^3)	3.916	3.935	3.985
Absorption coefficient (mm^{-1})	18.734	19.219	19.792
Crystal size (mm^3)	0.12 x 0.10 x 0.05	0.12 x 0.10 x 0.05	0.12 x 0.10 x 0.05
2 theta range (°)	4.28 to 70.24	4.28 to 70.20	4.29 to 70.38
GOF (F^2)	1.063	1.036	1.022
R indices (all data)	R_1 = 0.0374	R_1 = 0.0415	R_1 = 0.0400
	wR_2 = 0.0636	wR_2 = 0.0525	wR_2 = 0.0616

Table A.2. Selected Bond Distances (in Å) for $Na_5Er(OH)_6WO_4$, $Na_5Tm(OH)_6WO_4$, and $Na_5Yb(OH)_6WO_4$.

	$Na_5Er(OH)_6WO_4$	$Na_5Tm(OH)_6WO_4$	$Na_5Yb(OH)_6WO_4$
W(1) – O(10)	1.769(3)	1.771(3)	1.769(3)
W(1) – O(9)	1.778(3)	1.767(3)	1.772(3)
W(1) – O(8)	1.788(3)	1.781(3)	1.782(3)
W(1) – O(7)	1.792(3)	1.785(3)	1.788(3)
Ln(1) – O(2) (x2)	2.220(3)	2.212(3)	2.195(3)
Ln(1) – O(3) (x2)	2.241(3)	2.228(3)	2.216(3)
Ln(1) – O(1) (x2)	2.275(3)	2.268(3)	2.261(3)
Ln(2) – O(6) (x2)	2.207(3)	2.196(3)	2.182(3)
Ln(2) – O(5) (x2)	2.229(3)	2.222(3)	2.206(3)
Ln(2) – O(4) (x2)	2.266(3)	2.257(3)	2.242(3)

Table A.3. Bond valence sum calculation results for $Na_5Ln(OH)_6WO_4$ (*Ln* = Er, Tm, Yb).

	$Na_5Er(OH)_6WO_4$	$Na_5Tm(OH)_6WO_4$	$Na_5Yb(OH)_6WO_4$
W(1)	5.767	5.857	5.829
Ln(1)	2.999	3.177	2.988
Ln(2)	3.09	3.27	3.10

Figure A.1. Crystal images of the average size of $Na_5Er(OH)_6WO_4$ (left), $Na_5Yb(OH)_6WO_4$ (center), and $Na_5Tm(OH)_6WO_4$ (right) crystals where the scale bar below the crystals denotes mm increments.

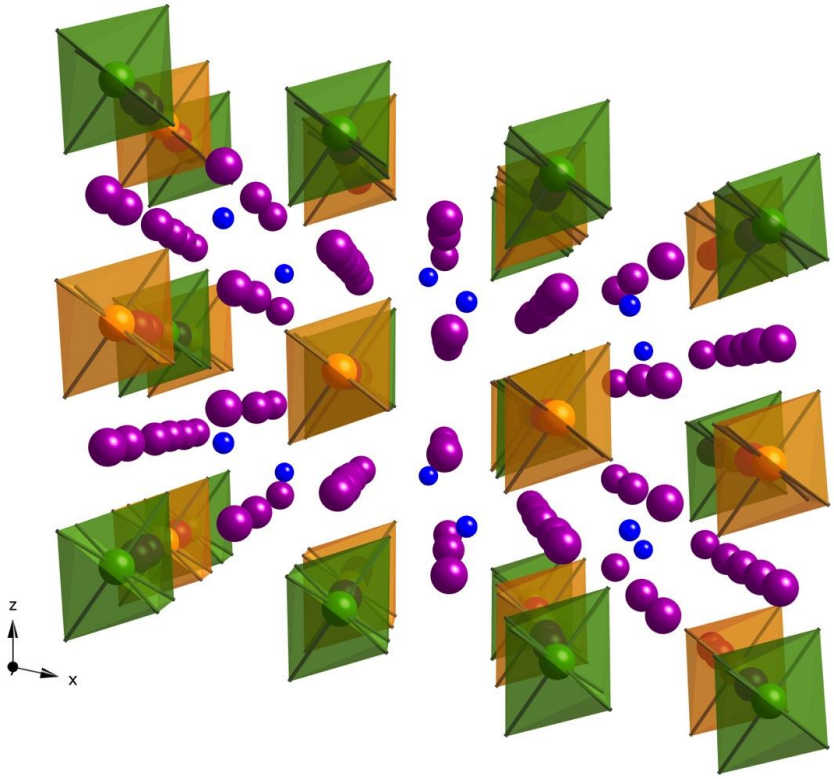

Figure A.2. Crystal structure of $Na_5Yb(OH)_6WO_4$, which is representative of the three title compounds where the alternating isolated lanthanide polyhedra are shown. *Ln*(1) is shown in orange, *Ln*(2) is shown in green, tungsten is shown in blue, sodium is shown in purple, and oxygen and hydrogen are omitted for clarity.

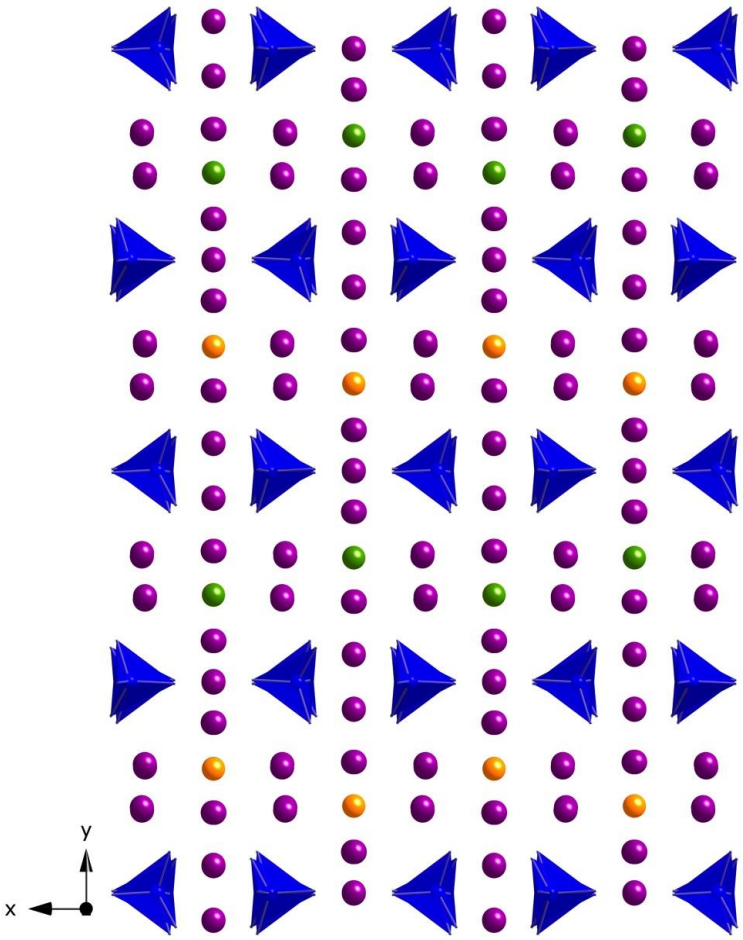

Figure A.3. Crystal structure of $Na_5Yb(OH)_6WO_4$, which is representative of the title compounds, where the isolated tungsten tetrahedra are shown down the *c* axis. Tungsten is shown in blue, *Ln*(1) is orange, *Ln*(2) is green, sodium is purple, and oxygen and hydrogen are omitted for clarity.

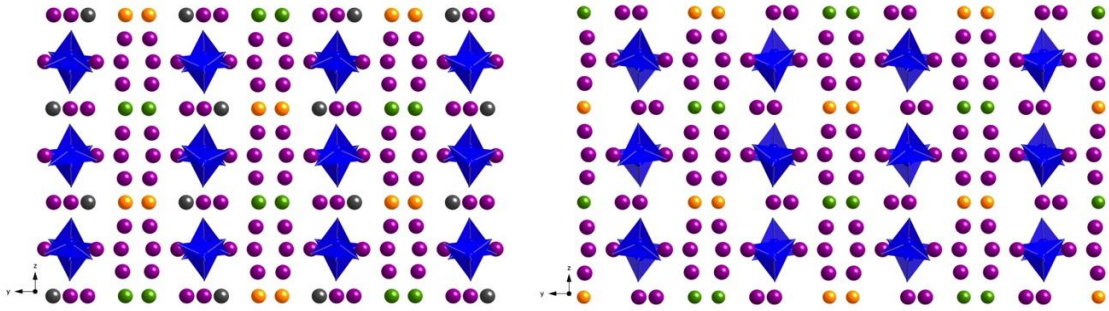

Figure A.4. Crystal structures of $Na_5Yb(OH)_6WO_4$ (left – also representative of the Tm analogue) and $Na_5Er(OH)_6WO_4$ (right). The surrounding of the tungsten atoms by sodium and lanthanide atoms is shown, along with the splitting of the Na(6) site to Na(6A) and Na(6B) in the Yb and Tm analogues. The Na(6B) site is shown in gray on the left image and in both images Na(1)-Na(6A) are shown in purple, *Ln*(1) is orange, *Ln*(2) is green, W(1) is blue, and oxygen and hydrogen are omitted for clarity.

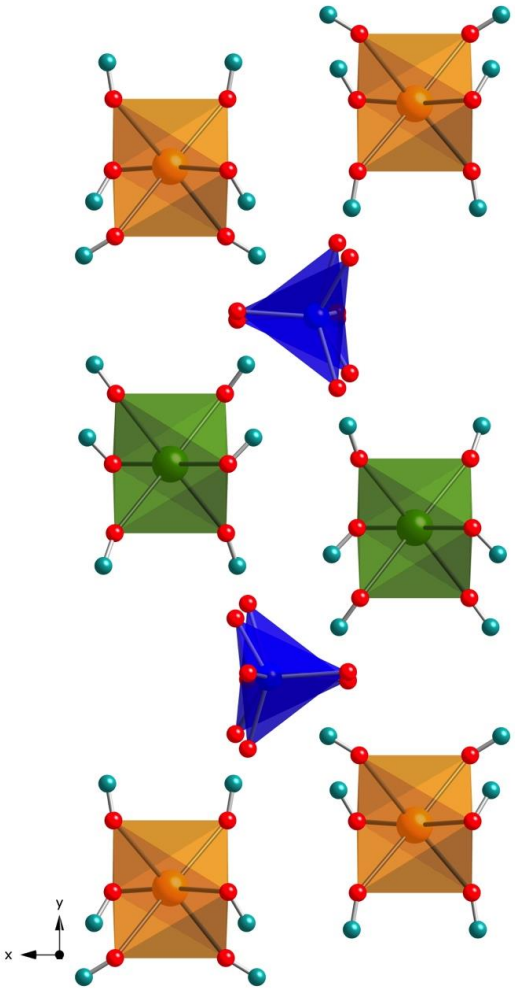

Figure A.5. Crystal structure of $Na_5Er(OH)_6WO_4$, which is representative of all analogues, where the hydroxide bonds on the *Ln*(1) and *Ln*(2) are shown in orange and green, respectively. The oxygen atoms are shown in red, the hydrogen in light blue, and the tungsten shown in dark blue.

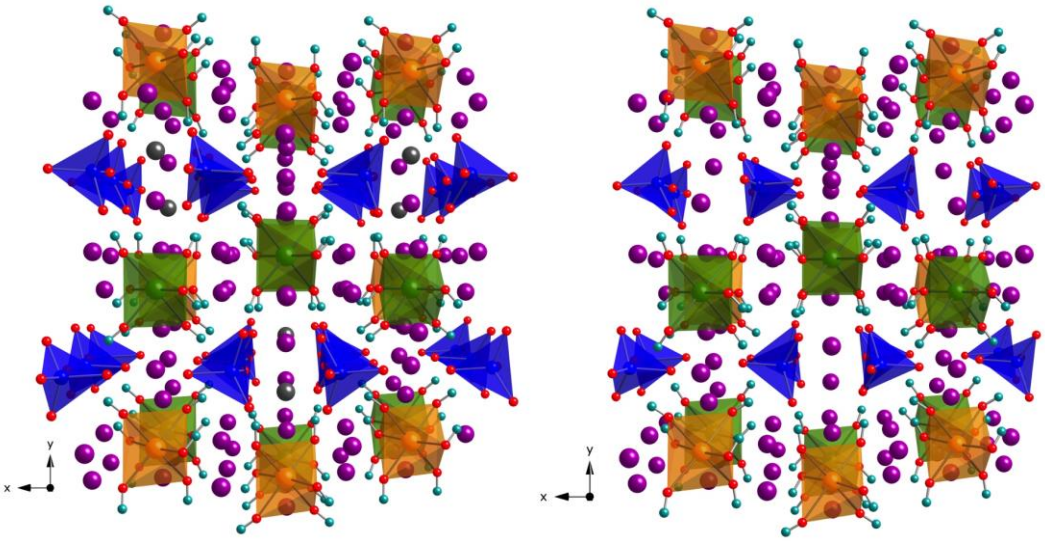

Figure A.6. Crystal structures of $Na_5Yb(OH)_6WO_4$ (left – also representative of Tm analogue) and $Na_5Er(OH)_6WO_4$ where the overall structure is shown down the *c* axis. *Ln*(1) is shown in orange, *Ln*(2) is green, tungsten is dark blue, Na(1)-Na(6A) are purple, Na(6B) is gray, oxygen is red, and hydrogen is light blue.

Appendix B

Permissions to Reprint

Chapter 2

American Chemical Society

Inorganic Chemistry

Chapters 3, 7, Appendix A

Elsevier

Solid State Sciences

As an author of an Elsevier journal, you retain certain rights detailed in this webpage:http://www.elsevier.com/authors/author-rights-and-responsibilities , provided that you properly acknowledge the original source of the material as follows: "Reproduced from *Authors name. Article title. Journal title year;volume number(issue number):first page-last page.* Copyright © *year [if applicable: name of learned society,* published by*]* Elsevier Masson SAS. All rights reserved."

If any part of the material to be used (for example, figures) has appeared in our publication with credit or acknowledgement to another source, permission must also be sought from that source (if such permission is not obtained then that material may not be included in your publication/copies).

Should the reuse you intend to make of your material be not included in such retained rights, please contact me directly with more details.

Yours sincerely,

Regina Lavanya Remigius

Senior Copyrights Coordinator – Global Rights

Elsevier

RELX India Pvt Ltd

(formerly Reed Elsevier India Private Limited)

Chapters 4, 5, and 9

CrystEngComm

Dear Allison

The Royal Society of Chemistry (RSC) hereby grants permission for the use of your paper(s) specified below in the printed and microfilm version of your thesis. You may also make available the PDF version of your paper(s) that the RSC sent to the corresponding author(s) of your paper(s) upon publication of the paper(s) in the following ways: in your thesis via any website that your university may have for the deposition of theses, via your university's Intranet or via your own personal website. We are however unable to grant you permission to include the PDF version of the paper(s) on its own in your institutional repository. The Royal Society of Chemistry is a signatory to the STM Guidelines on Permissions (available on request).

Please note that if the material specified below or any part of it appears with credit or acknowledgement to a third party then you must also secure permission from that third party before reproducing that material.

Please ensure that the thesis states the following:
Reproduced by permission of The Royal Society of Chemistry
and include a link to the paper on the Royal Society of Chemistry's website.

Please ensure that your co-authors are aware that you are including the paper in your thesis.

CrystEngComm, 2015,**17**, 4654-4661
DOI: 10.1039/C5CE00671F

CrystEngComm, 2015,**17**, 4691-4698
DOI: 10.1039/C5CE00630A

CrystEngComm, 2016,**18**, 2294-2302
DOI: 10.1039/C6CE00177G

Regards
Gill Cockhead

Gill Cockhead
Publishing Contracts & Copyright Executive
Royal Society of Chemistry,
Thomas Graham House,
Science Park, Milton Road,
Cambridge, CB4 0WF, UK
Tel +44 (0) 1223 432134

Chapter 8

Journal of Solid State Chemistry

ELSEVIER LICENSE
TERMS AND CONDITIONS
Apr 11, 2016

This is a License Agreement between Allison M Latshaw ("You") and Elsevier ("Elsevier") provided by Copyright Clearance Center ("CCC"). The license consists of your order details, the terms and conditions provided by Elsevier, and the payment terms and conditions.

All payments must be made in full to CCC. For payment instructions, please see information listed at the bottom of this form.

Supplier	Elsevier Limited The Boulevard,Langford Lane Kidlington,Oxford,OX5 1GB,UK
Registered Company Number	1982084
Customer name	Allison M Latshaw
License number	3845971094996
License date	Apr 11, 2016
Licensed content publisher	Elsevier
Licensed content publication	Journal of Solid State Chemistry
Licensed content title	Synthesis, structure, and polymorphism of A3LnSi2O7 (A=Na, K; Ln=Sm, Ho, Yb)
Licensed content author	Allison M. Latshaw,Jeongho Yeon,Mark D. Smith,Hans-Conrad zur Loye
Licensed content date	March 2016
Licensed content volume number	235
Licensed content issue number	n/a
Number of pages	7
Start Page	100

End Page	106
Type of Use	reuse in a thesis/dissertation
Intended publisher of new work	other
Portion	full article
Format	both print and electronic
Are you the author of this Elsevier article?	Yes
Will you be translating?	No
Title of your thesis/dissertation	Materials Discovery by Crystal Growth: Synthesis, Structure Determination, Magnetic, and Optical Properties of Complex Lanthanide Containing Oxides, Oxyhydroxides, and Oxyfluorides
Expected completion date	Aug 2016
Estimated size (number of pages)	200
Elsevier VAT number	GB 494 6272 12

Terms and Conditions

INTRODUCTION

1. The publisher for this copyrighted material is Elsevier. By clicking "accept" in connection with completing this licensing transaction, you agree that the following terms and conditions apply to this transaction (along with the Billing and Payment terms and conditions established by Copyright Clearance Center, Inc. ("CCC"), at the time that you opened your Rightslink account and that are available at any time at http://myaccount.copyright.com).

GENERAL TERMS

2. Elsevier hereby grants you permission to reproduce the aforementioned material subject to the terms and conditions indicated.

3. Acknowledgement: If any part of the material to be used (for example, figures) has appeared in our publication with credit or acknowledgement to another source, permission must also be sought from that source. If such permission is not obtained then that material may not be included in your publication/copies. Suitable acknowledgement to the source must be made, either as a footnote or in a reference list at the end of your publication, as follows:
"Reprinted from Publication title, Vol /edition number, Author(s), Title of article / title of chapter, Pages No., Copyright (Year), with permission from Elsevier [OR APPLICABLE SOCIETY COPYRIGHT OWNER]." Also Lancet special credit - "Reprinted from The Lancet, Vol. number, Author(s), Title of article, Pages No., Copyright (Year), with permission from Elsevier."

4. Reproduction of this material is confined to the purpose and/or media for which permission is hereby given.

5. Altering/Modifying Material: Not Permitted. However figures and illustrations may be altered/adapted minimally to serve your work. Any other abbreviations, additions, deletions and/or any other alterations shall be made only with prior written authorization of Elsevier Ltd. (Please contact Elsevier at permissions@elsevier.com)
6. If the permission fee for the requested use of our material is waived in this instance, please be advised that your future requests for Elsevier materials may attract a fee.
7. Reservation of Rights: Publisher reserves all rights not specifically granted in the combination of (i) the license details provided by you and accepted in the course of this licensing transaction, (ii) these terms and conditions and (iii) CCC's Billing and Payment terms and conditions.
8. License Contingent Upon Payment: While you may exercise the rights licensed immediately upon issuance of the license at the end of the licensing process for the transaction, provided that you have disclosed complete and accurate details of your proposed use, no license is finally effective unless and until full payment is received from you (either by publisher or by CCC) as provided in CCC's Billing and Payment terms and conditions. If full payment is not received on a timely basis, then any license preliminarily granted shall be deemed automatically revoked and shall be void as if never granted. Further, in the event that you breach any of these terms and conditions or any of CCC's Billing and Payment terms and conditions, the license is automatically revoked and shall be void as if never granted. Use of materials as described in a revoked license, as well as any use of the materials beyond the scope of an unrevoked license, may constitute copyright infringement and publisher reserves the right to take any and all action to protect its copyright in the materials.
9. Warranties: Publisher makes no representations or warranties with respect to the licensed material.
10. Indemnity: You hereby indemnify and agree to hold harmless publisher and CCC, and their respective officers, directors, employees and agents, from and against any and all claims arising out of your use of the licensed material other than as specifically authorized pursuant to this license.
11. No Transfer of License: This license is personal to you and may not be sublicensed, assigned, or transferred by you to any other person without publisher's written permission.
12. No Amendment Except in Writing: This license may not be amended except in a writing signed by both parties (or, in the case of publisher, by CCC on publisher's behalf).
13. Objection to Contrary Terms: Publisher hereby objects to any terms contained in any purchase order, acknowledgment, check endorsement or other writing prepared by you, which terms are inconsistent with these terms and conditions or CCC's Billing and Payment terms and conditions. These terms and conditions, together with CCC's Billing and Payment terms and conditions (which are incorporated herein), comprise the entire agreement between you and publisher (and CCC) concerning this licensing transaction. In the event of any conflict between your obligations established by these terms and conditions and those

established by CCC's Billing and Payment terms and conditions, these terms and conditions shall control.
14. Revocation: Elsevier or Copyright Clearance Center may deny the permissions described in this License at their sole discretion, for any reason or no reason, with a full refund payable to you. Notice of such denial will be made using the contact information provided by you. Failure to receive such notice will not alter or invalidate the denial. In no event will Elsevier or Copyright Clearance Center be responsible or liable for any costs, expenses or damage incurred by you as a result of a denial of your permission request, other than a refund of the amount(s) paid by you to Elsevier and/or Copyright Clearance Center for denied permissions.
LIMITED LICENSE
The following terms and conditions apply only to specific license types:
15. **Translation**: This permission is granted for non-exclusive world **English** rights only unless your license was granted for translation rights. If you licensed translation rights you may only translate this content into the languages you requested. A professional translator must perform all translations and reproduce the content word for word preserving the integrity of the article.
16. **Posting licensed content on any Website**: The following terms and conditions apply as follows: Licensing material from an Elsevier journal: All content posted to the web site must maintain the copyright information line on the bottom of each image; A hyper-text must be included to the Homepage of the journal from which you are licensing athttp://www.sciencedirect.com/science/journal/xxxxx or the Elsevier homepage for books athttp://www.elsevier.com; Central Storage: This license does not include permission for a scanned version of the material to be stored in a central repository such as that provided by Heron/XanEdu.
Licensing material from an Elsevier book: A hyper-text link must be included to the Elsevier homepage at http://www.elsevier.com . All content posted to the web site must maintain the copyright information line on the bottom of each image.

Posting licensed content on Electronic reserve: In addition to the above the following clauses are applicable: The web site must be password-protected and made available only to bona fide students registered on a relevant course. This permission is granted for 1 year only. You may obtain a new license for future website posting.
17. **For journal authors:** the following clauses are applicable in addition to the above:
Preprints:
A preprint is an author's own write-up of research results and analysis, it has not been peer-reviewed, nor has it had any other value added to it by a publisher (such as formatting, copyright, technical enhancement etc.).
Authors can share their preprints anywhere at any time. Preprints should not be added to or enhanced in any way in order to appear more like, or to substitute for, the final versions of articles however authors can update their preprints on arXiv or RePEc with their Accepted Author Manuscript (see below).
If accepted for publication, we encourage authors to link from the preprint to their

formal publication via its DOI. Millions of researchers have access to the formal publications on ScienceDirect, and so links will help users to find, access, cite and use the best available version. Please note that Cell Press, The Lancet and some society-owned have different preprint policies. Information on these policies is available on the journal homepage.

Accepted Author Manuscripts: An accepted author manuscript is the manuscript of an article that has been accepted for publication and which typically includes author-incorporated changes suggested during submission, peer review and editor-author communications.

Authors can share their accepted author manuscript:

- - immediately
    - via their non-commercial person homepage or blog
    - by updating a preprint in arXiv or RePEc with the accepted manuscript
    - via their research institute or institutional repository for internal institutional uses or as part of an invitation-only research collaboration work-group
    - directly by providing copies to their students or to research collaborators for their personal use
    - for private scholarly sharing as part of an invitation-only work group on commercial sites with which Elsevier has an agreement
- - after the embargo period
    - via non-commercial hosting platforms such as their institutional repository
    - via commercial sites with which Elsevier has an agreement

In all cases accepted manuscripts should:

- - link to the formal publication via its DOI
- - bear a CC-BY-NC-ND license - this is easy to do
- - if aggregated with other manuscripts, for example in a repository or other site, be shared in alignment with our hosting policy not be added to or enhanced in any way to appear more like, or to substitute for, the published journal article.

Published journal article (JPA): A published journal article (PJA) is the definitive final record of published research that appears or will appear in the journal and embodies all value-adding publishing activities including peer review co-ordination, copy-editing, formatting, (if relevant) pagination and online enrichment.

Policies for sharing publishing journal articles differ for subscription and gold open access articles:

Subscription Articles: If you are an author, please share a link to your article rather than the full-text. Millions of researchers have access to the formal publications on ScienceDirect, and so links will help your users to find, access, cite, and use the best available version.

Theses and dissertations which contain embedded PJAs as part of the formal submission can be posted publicly by the awarding institution with DOI links back to the formal publications on ScienceDirect.

If you are affiliated with a library that subscribes to ScienceDirect you have additional private sharing rights for others' research accessed under that agreement. This includes use for classroom teaching and internal training at the institution (including use in course packs and courseware programs), and inclusion of the article for grant funding purposes.

Gold Open Access Articles: May be shared according to the author-selected end-user license and should contain a CrossMark logo, the end user license, and a DOI link to the formal publication on ScienceDirect.

Please refer to Elsevier's posting policy for further information.

18. **For book authors** the following clauses are applicable in addition to the above: Authors are permitted to place a brief summary of their work online only. You are not allowed to download and post the published electronic version of your chapter, nor may you scan the printed edition to create an electronic version. **Posting to a repository:** Authors are permitted to post a summary of their chapter only in their institution's repository.

19. **Thesis/Dissertation**: If your license is for use in a thesis/dissertation your thesis may be submitted to your institution in either print or electronic form. Should your thesis be published commercially, please reapply for permission. These requirements include permission for the Library and Archives of Canada to supply single copies, on demand, of the complete thesis and include permission for Proquest/UMI to supply single copies, on demand, of the complete thesis. Should your thesis be published commercially, please reapply for permission. Theses and dissertations which contain embedded PJAs as part of the formal submission can be posted publicly by the awarding institution with DOI links back to the formal publications on ScienceDirect.

Elsevier Open Access Terms and Conditions

You can publish open access with Elsevier in hundreds of open access journals or in nearly 2000 established subscription journals that support open access publishing. Permitted third party re-use of these open access articles is defined by the author's choice of Creative Commons user license. See our open access license policy for more information.

Terms & Conditions applicable to all Open Access articles published with Elsevier:

Any reuse of the article must not represent the author as endorsing the adaptation of the article nor should the article be modified in such a way as to damage the author's honour or reputation. If any changes have been made, such changes must be clearly indicated.

The author(s) must be appropriately credited and we ask that you include the end user license and a DOI link to the formal publication on ScienceDirect.

If any part of the material to be used (for example, figures) has appeared in our publication with credit or acknowledgement to another source it is the responsibility of the user to ensure their reuse complies with the terms and conditions determined by the rights holder.

Additional Terms & Conditions applicable to each Creative Commons user license:

Chapter 6

ELSEVIER LICENSE
TERMS AND CONDITIONS
Jun 09, 2016

This Agreement between Allison M Latshaw ("You") and Elsevier ("Elsevier") consists of your license details and the terms and conditions provided by Elsevier and Copyright Clearance Center.

License Number: 3884960769129
License date: Jun 09, 2016
Licensed Content Publisher: Elsevier
Licensed Content Publication: Journal of Solid State Chemistry
Licensed Content Title: A5RE4X[TO4]4 crystal growth: Fluoride flux synthesis of Na5Ln4F[GeO4]4 (Ln=Pr, Nd), the first quaternary germanate oxyfluorides
Licensed Content Author: Allison M. Latshaw,Branford O. Wilkins,Gregory Morrison,Mark D. Smith,Hans-Conrad zur Loye
Licensed Content Date: July 2016
Licensed Content Volume Number: 239
Licensed Content Issue Number: n/a
Licensed Content Pages: 4
Start Page: 200
End Page: 203
Type of Use: reuse in a thesis/dissertation
Portion: full article
Format: both print and electronic
Are you the author of this Elsevier article? Yes
Will you be translating? No
Title of your thesis/dissertation: Materials Discovery by Crystal Growth: Synthesis, Structure Determination, Magnetic, and Optical Properties of Complex Lanthanide Containing Oxides, Oxyhydroxides, and Oxyfluorides
Expected completion date: Aug 2016
Estimated size (number of pages): 200
Elsevier VAT number: GB 494 6272 12

Terms and Conditions

INTRODUCTION

1. The publisher for this copyrighted material is Elsevier. By clicking "accept" in connection with completing this licensing transaction, you agree that the following terms and conditions apply to this transaction (along with the Billing and Payment terms and conditions established by Copyright Clearance Center, Inc. ("CCC"), at the time that you opened your Rightslink account and that are available at any time at http://myaccount.copyright.com).

GENERAL TERMS

2. Elsevier hereby grants you permission to reproduce the aforementioned material subject to the terms and conditions indicated.
3. Acknowledgement: If any part of the material to be used (for example, figures) has appeared in our publication with credit or acknowledgement to another source, permission must also be sought from that source. If such permission is not obtained then that material may not be included in your

publication/copies. Suitable acknowledgement to the source must be made, either as a footnote or in a reference list at the end of your publication, as follows:
"Reprinted from Publication title, Vol /edition number, Author(s), Title of article / title of chapter, Pages No., Copyright (Year), with permission from Elsevier [OR APPLICABLE SOCIETY COPYRIGHT OWNER]." Also Lancet special credit - "Reprinted from The Lancet, Vol. number, Author(s), Title of article, Pages No., Copyright (Year), with permission from Elsevier."
4. Reproduction of this material is confined to the purpose and/or media for which permission is hereby given.
5. Altering/Modifying Material: Not Permitted. However figures and illustrations may be altered/adapted minimally to serve your work. Any other abbreviations, additions, deletions and/or any other alterations shall be made only with prior written authorization of Elsevier Ltd. (Please contact Elsevier at permissions@elsevier.com)
6. If the permission fee for the requested use of our material is waived in this instance, please be advised that your future requests for Elsevier materials may attract a fee.
7. Reservation of Rights: Publisher reserves all rights not specifically granted in the combination of (i) the license details provided by you and accepted in the course of this licensing transaction, (ii) these terms and conditions and (iii) CCC's Billing and Payment terms and conditions.
8. License Contingent Upon Payment: While you may exercise the rights licensed immediately upon issuance of the license at the end of the licensing process for the transaction, provided that you have disclosed complete and accurate details of your proposed use, no license is finally effective unless and until full payment is received from you (either by publisher or by CCC) as provided in CCC's Billing and Payment terms and conditions. If full payment is not received on a timely basis, then any license preliminarily granted shall be deemed automatically revoked and shall be void as if never granted. Further, in the event that you breach any of these terms and conditions or any of CCC's Billing and Payment terms and conditions, the license is automatically revoked and shall be void as if never granted. Use of materials as described in a revoked license, as well as any use of the materials beyond the scope of an unrevoked license, may constitute copyright infringement and publisher reserves the right to take any and all action to protect its copyright in the materials.
9. Warranties: Publisher makes no representations or warranties with respect to the licensed material.
10. Indemnity: You hereby indemnify and agree to hold harmless publisher and CCC, and their respective officers, directors, employees and agents, from and against any and all claims arising out of your use of the licensed material other than as specifically authorized pursuant to this license.
11. No Transfer of License: This license is personal to you and may not be sublicensed, assigned, or transferred by you to any other person without publisher's written permission.
12. No Amendment Except in Writing: This license may not be amended except in a writing signed by both parties (or, in the case of publisher, by CCC on publisher's behalf).
13. Objection to Contrary Terms: Publisher hereby objects to any terms contained in any purchase order, acknowledgment, check endorsement or other writing prepared by you, which terms are inconsistent with these terms and conditions or CCC's Billing and Payment terms and conditions. These terms and conditions, together with CCC's Billing and Payment terms and conditions (which are incorporated herein), comprise the entire agreement between you and publisher (and CCC) concerning this licensing transaction. In the event of any conflict between your obligations established by these terms and conditions and those established by CCC's Billing and Payment terms and conditions, these terms and conditions shall control.
14. Revocation: Elsevier or Copyright Clearance Center may deny the permissions described in this License at their sole discretion, for any reason or no reason, with a full refund payable to you. Notice of such denial will be made using the contact information provided by you. Failure to receive such notice will not alter or invalidate the denial. In no event will Elsevier or Copyright Clearance Center be responsible or liable for any costs, expenses or damage incurred by you as a result of a denial of your permission request, other than a refund of the amount(s) paid by you to Elsevier and/or Copyright Clearance Center for denied permissions.

LIMITED LICENSE

The following terms and conditions apply only to specific license types:
15. **Translation**: This permission is granted for non-exclusive world **English** rights only unless your license was granted for translation rights. If you licensed translation rights you may only translate this

content into the languages you requested. A professional translator must perform all translations and reproduce the content word for word preserving the integrity of the article.
16. **Posting licensed content on any Website**: The following terms and conditions apply as follows: Licensing material from an Elsevier journal: All content posted to the web site must maintain the copyright information line on the bottom of each image; A hyper-text must be included to the Homepage of the journal from which you are licensing athttp://www.sciencedirect.com/science/journal/xxxxx or the Elsevier homepage for books athttp://www.elsevier.com; Central Storage: This license does not include permission for a scanned version of the material to be stored in a central repository such as that provided by Heron/XanEdu.
Licensing material from an Elsevier book: A hyper-text link must be included to the Elsevier homepage at http://www.elsevier.com . All content posted to the web site must maintain the copyright information line on the bottom of each image.

Posting licensed content on Electronic reserve: In addition to the above the following clauses are applicable: The web site must be password-protected and made available only to bona fide students registered on a relevant course. This permission is granted for 1 year only. You may obtain a new license for future website posting.
17. **For journal authors:** the following clauses are applicable in addition to the above:
Preprints:
A preprint is an author's own write-up of research results and analysis, it has not been peer-reviewed, nor has it had any other value added to it by a publisher (such as formatting, copyright, technical enhancement etc.).
Authors can share their preprints anywhere at any time. Preprints should not be added to or enhanced in any way in order to appear more like, or to substitute for, the final versions of articles however authors can update their preprints on arXiv or RePEc with their Accepted Author Manuscript (see below).
If accepted for publication, we encourage authors to link from the preprint to their formal publication via its DOI. Millions of researchers have access to the formal publications on ScienceDirect, and so links will help users to find, access, cite and use the best available version. Please note that Cell Press, The Lancet and some society-owned have different preprint policies. Information on these policies is available on the journal homepage.
Accepted Author Manuscripts: An accepted author manuscript is the manuscript of an article that has been accepted for publication and which typically includes author-incorporated changes suggested during submission, peer review and editor-author communications.
Authors can share their accepted author manuscript:

- – immediately
    - via their non-commercial person homepage or blog
    - by updating a preprint in arXiv or RePEc with the accepted manuscript
    - via their research institute or institutional repository for internal institutional uses or as part of an invitation-only research collaboration work-group
    - directly by providing copies to their students or to research collaborators for their personal use
    - for private scholarly sharing as part of an invitation-only work group on commercial sites with which Elsevier has an agreement
- – after the embargo period
    - via non-commercial hosting platforms such as their institutional repository
    - via commercial sites with which Elsevier has an agreement

In all cases accepted manuscripts should:

- – link to the formal publication via its DOI
- – bear a CC-BY-NC-ND license - this is easy to do
- – if aggregated with other manuscripts, for example in a repository or other site, be shared in alignment with our hosting policy not be added to or enhanced in any way to appear more like, or to substitute for, the published journal article.

Published journal article (JPA): A published journal article (PJA) is the definitive final record of published research that appears or will appear in the journal and embodies all value-adding publishing activities including peer review co-ordination, copy-editing, formatting, (if relevant) pagination and online enrichment.

Policies for sharing publishing journal articles differ for subscription and gold open access articles:
Subscription Articles: If you are an author, please share a link to your article rather than the full-text. Millions of researchers have access to the formal publications on ScienceDirect, and so links will help your users to find, access, cite, and use the best available version.
Theses and dissertations which contain embedded PJAs as part of the formal submission can be posted publicly by the awarding institution with DOI links back to the formal publications on ScienceDirect.
If you are affiliated with a library that subscribes to ScienceDirect you have additional private sharing rights for others' research accessed under that agreement. This includes use for classroom teaching and internal training at the institution (including use in course packs and courseware programs), and inclusion of the article for grant funding purposes.
Gold Open Access Articles: May be shared according to the author-selected end-user license and should contain a CrossMark logo, the end user license, and a DOI link to the formal publication on ScienceDirect.
Please refer to Elsevier's posting policy for further information.
18. **For book authors** the following clauses are applicable in addition to the above: Authors are permitted to place a brief summary of their work online only. You are not allowed to download and post the published electronic version of your chapter, nor may you scan the printed edition to create an electronic version. **Posting to a repository:** Authors are permitted to post a summary of their chapter only in their institution's repository.
19. **Thesis/Dissertation**: If your license is for use in a thesis/dissertation your thesis may be submitted to your institution in either print or electronic form. Should your thesis be published commercially, please reapply for permission. These requirements include permission for the Library and Archives of Canada to supply single copies, on demand, of the complete thesis and include permission for Proquest/UMI to supply single copies, on demand, of the complete thesis. Should your thesis be published commercially, please reapply for permission. Theses and dissertations which contain embedded PJAs as part of the formal submission can be posted publicly by the awarding institution with DOI links back to the formal publications on ScienceDirect.

Elsevier Open Access Terms and Conditions
You can publish open access with Elsevier in hundreds of open access journals or in nearly 2000 established subscription journals that support open access publishing. Permitted third party re-use of these open access articles is defined by the author's choice of Creative Commons user license. See our open access license policy for more information.
Terms & Conditions applicable to all Open Access articles published with Elsevier:
Any reuse of the article must not represent the author as endorsing the adaptation of the article nor should the article be modified in such a way as to damage the author's honour or reputation. If any changes have been made, such changes must be clearly indicated.
The author(s) must be appropriately credited and we ask that you include the end user license and a DOI link to the formal publication on ScienceDirect.
If any part of the material to be used (for example, figures) has appeared in our publication with credit or acknowledgement to another source it is the responsibility of the user to ensure their reuse complies with the terms and conditions determined by the rights holder.
Additional Terms & Conditions applicable to each Creative Commons user license:
CC BY: The CC-BY license allows users to copy, to create extracts, abstracts and new works from the Article, to alter and revise the Article and to make commercial use of the Article (including reuse and/or resale of the Article by commercial entities), provided the user gives appropriate credit (with a link to the formal publication through the relevant DOI), provides a link to the license, indicates if changes were made and the licensor is not represented as endorsing the use made of the work. The full details of the license are available at http://creativecommons.org/licenses/by/4.0.
CC BY NC SA: The CC BY-NC-SA license allows users to copy, to create extracts, abstracts and new works from the Article, to alter and revise the Article, provided this is not done for commercial purposes, and that the user gives appropriate credit (with a link to the formal publication through the relevant DOI), provides a link to the license, indicates if changes were made and the licensor is not represented as endorsing the use made of the work. Further, any new works must be made available on the same conditions. The full details of the license are available at http://creativecommons.org/licenses/by-nc-sa/4.0.
CC BY NC ND: The CC BY-NC-ND license allows users to copy and distribute the Article, provided this is not done for commercial purposes and further does not permit distribution of the Article if it is changed

Chapter 10

Springer

Journal of Chemical Crystallography

SPRINGER LICENSE
TERMS AND CONDITIONS

Apr 11, 2016

This is a License Agreement between Allison M Latshaw ("You") and Springer ("Springer") provided by Copyright Clearance Center ("CCC"). The license consists of your order details, the terms and conditions provided by Springer, and the payment terms and conditions.

All payments must be made in full to CCC. For payment instructions, please see information listed at the bottom of this form.

License Number	3845970565201
License date	Apr 11, 2016
Licensed content publisher	Springer
Licensed content publication	Journal of Chemical Crystallography
Licensed content title	Fluoride Flux Crystal Growth and Structure Determination of K5Sc2FSi4O13
Licensed content author	Allison M. Latshaw
Licensed content date	Jan 1, 2015
Volume number	45
Issue number	7
Type of Use	Book/Textbook
Requestor type	Publisher
Publisher	ProQuest
Portion	Full text
Format	Print and Electronic
Will you be translating?	No
Print run	2

Author of this Springer article	Yes and you are the sole author of the new work
Order reference number	None
Title of new book	Materials Discovery by Crystal Growth: Synthesis, Structure Determination, Magnetic, and Optical Properties of Complex Lanthanide Containing Oxides, Oxyhydroxides, and Oxyfluorides
Publisher	ProQuest
Author of new book	Allison M. Latshaw
Expected publication date of new book	Aug 2016
Estimated size of new book (pages)	200

Terms and Conditions

Introduction

The publisher for this copyrighted material is Springer. By clicking "accept" in connection with completing this licensing transaction, you agree that the following terms and conditions apply to this transaction (along with the Billing and Payment terms and conditions established by Copyright Clearance Center, Inc. ("CCC"), at the time that you opened your Rightslink account and that are available at any time at http://myaccount.copyright.com).

Limited License

With reference to your request to reuse material on which Springer controls the copyright, permission is granted for the use indicated in your enquiry under the following conditions:

- Licenses are for one-time use only with a maximum distribution equal to the number stated in your request.
- Springer material represents original material which does not carry references to other sources. If the material in question appears with a credit to another source, this permission is not valid and authorization has to be obtained from the original copyright holder.
- This permission
• is non-exclusive
• is only valid if no personal rights, trademarks, or competitive products are infringed.
• explicitly excludes the right for derivatives.
- Springer does not supply original artwork or content.
- According to the format which you have selected, the following conditions apply accordingly:
• **Print and Electronic:** This License include use in electronic form provided it is password protected, on intranet, or CD-Rom/DVD or E-book/E-journal. It may not be republished in electronic open access.
• **Print:** This License excludes use in electronic form.

• **Electronic:** This License only pertains to use in electronic form provided it is password protected, on intranet, or CD-Rom/DVD or E-book/E-journal. It may not be republished in electronic open access.
For any electronic use not mentioned, please contact Springer at permissions.springer@spi-global.com.
- Although Springer controls the copyright to the material and is entitled to negotiate on rights, this license is only valid subject to courtesy information to the author (address is given in the article/chapter).
- If you are an STM Signatory or your work will be published by an STM Signatory and you are requesting to reuse figures/tables/illustrations or single text extracts, permission is granted according to STM Permissions Guidelines: http://www.stm-assoc.org/permissions-guidelines/
For any electronic use not mentioned in the Guidelines, please contact Springer atpermissions.springer@spi-global.com. If you request to reuse more content than stipulated in the STM Permissions Guidelines, you will be charged a permission fee for the excess content.
Permission is valid upon payment of the fee as indicated in the licensing process. If permission is granted free of charge on this occasion, that does not prejudice any rights we might have to charge for reproduction of our copyrighted material in the future.
-If your request is for reuse in a Thesis, permission is granted free of charge under the following conditions:
This license is valid for one-time use only for the purpose of defending your thesis and with a maximum of 100 extra copies in paper. If the thesis is going to be published, permission needs to be reobtained.
- includes use in an electronic form, provided it is an author-created version of the thesis on his/her own website and his/her university's repository, including UMI (according to the definition on the Sherpa website: http://www.sherpa.ac.uk/romeo/);
- is subject to courtesy information to the co-author or corresponding author.
Geographic Rights: Scope
Licenses may be exercised anywhere in the world.
Altering/Modifying Material: Not Permitted
Figures, tables, and illustrations may be altered minimally to serve your work. You may not alter or modify text in any manner. Abbreviations, additions, deletions and/or any other alterations shall be made only with prior written authorization of the author(s).
Reservation of Rights
Springer reserves all rights not specifically granted in the combination of (i) the license details provided by you and accepted in the course of this licensing transaction and (ii) these terms and conditions and (iii) CCC's Billing and Payment terms and conditions.
License Contingent on Payment
While you may exercise the rights licensed immediately upon issuance of the license at the end of the licensing process for the transaction, provided that you have disclosed complete and accurate details of your proposed use, no license is finally effective unless and until full payment is received from you (either by Springer or by CCC) as provided in CCC's Billing and Payment terms and conditions. If full payment is not received by the date due, then any license preliminarily granted shall be deemed

automatically revoked and shall be void as if never granted. Further, in the event that you breach any of these terms and conditions or any of CCC's Billing and Payment terms and conditions, the license is automatically revoked and shall be void as if never granted. Use of materials as described in a revoked license, as well as any use of the materials beyond the scope of an unrevoked license, may constitute copyright infringement and Springer reserves the right to take any and all action to protect its copyright in the materials.

Copyright Notice: Disclaimer

You must include the following copyright and permission notice in connection with any reproduction of the licensed material:

"Springer book/journal title, chapter/article title, volume, year of publication, page, name(s) of author(s), (original copyright notice as given in the publication in which the material was originally published) "With permission of Springer"

In case of use of a graph or illustration, the caption of the graph or illustration must be included, as it is indicated in the original publication.

Warranties: None

Springer makes no representations or warranties with respect to the licensed material and adopts on its own behalf the limitations and disclaimers established by CCC on its behalf in its Billing and Payment terms and conditions for this licensing transaction.

Indemnity

You hereby indemnify and agree to hold harmless Springer and CCC, and their respective officers, directors, employees and agents, from and against any and all claims arising out of your use of the licensed material other than as specifically authorized pursuant to this license.

No Transfer of License

This license is personal to you and may not be sublicensed, assigned, or transferred by you without Springer's written permission.

No Amendment Except in Writing

This license may not be amended except in a writing signed by both parties (or, in the case of Springer, by CCC on Springer's behalf).

Objection to Contrary Terms

Springer hereby objects to any terms contained in any purchase order, acknowledgment, check endorsement or other writing prepared by you, which terms are inconsistent with these terms and conditions or CCC's Billing and Payment terms and conditions. These terms and conditions, together with CCC's Billing and Payment terms and conditions (which are incorporated herein), comprise the entire agreement between you and Springer (and CCC) concerning this licensing transaction. In the event of any conflict between your obligations established by these terms and conditions and those established by CCC's Billing and Payment terms and conditions, these terms and conditions shall control.

Jurisdiction

All disputes that may arise in connection with this present License, or the breach thereof, shall be settled exclusively by arbitration, to be held in the Federal Republic of Germany, in accordance with German law.

Other conditions:

V 12AUG2015

SPRINGER LICENSE
TERMS AND CONDITIONS

Apr 11, 2016

This is a License Agreement between Allison M Latshaw ("You") and Springer ("Springer") provided by Copyright Clearance Center ("CCC"). The license consists of your order details, the terms and conditions provided by Springer, and the payment terms and conditions.

All payments must be made in full to CCC. For payment instructions, please see information listed at the bottom of this form.

License Number	3845970881347
License date	Apr 11, 2016
Licensed content publisher	Springer
Licensed content publication	Journal of Chemical Crystallography
Licensed content title	Flux Crystal Growth and Structure Determination of K5Y2FSi4O13
Licensed content author	Allison M. Latshaw
Licensed content date	Jan 1, 2015
Volume number	45
Issue number	4
Type of Use	Book/Textbook
Requestor type	Publisher
Publisher	ProQuest
Portion	Full text
Format	Print and Electronic
Will you be translating?	No
Print run	2
Author of this Springer article	Yes and you are the sole author of the new work
Order reference number	None
Title of new book	Materials Discovery by Crystal Growth: Synthesis, Structure Determination,

	Magnetic, and Optical Properties of Complex Lanthanide Containing Oxides, Oxyhydroxides, and Oxyfluorides
Publisher	ProQuest
Author of new book	Allison M. Latshaw
Expected publication date of new book	Aug 2016
Estimated size of new book (pages)	200

Terms and Conditions

Introduction

The publisher for this copyrighted material is Springer. By clicking "accept" in connection with completing this licensing transaction, you agree that the following terms and conditions apply to this transaction (along with the Billing and Payment terms and conditions established by Copyright Clearance Center, Inc. ("CCC"), at the time that you opened your Rightslink account and that are available at any time at http://myaccount.copyright.com).

Limited License

With reference to your request to reuse material on which Springer controls the copyright, permission is granted for the use indicated in your enquiry under the following conditions:

- Licenses are for one-time use only with a maximum distribution equal to the number stated in your request.
- Springer material represents original material which does not carry references to other sources. If the material in question appears with a credit to another source, this permission is not valid and authorization has to be obtained from the original copyright holder.
- This permission
• is non-exclusive
• is only valid if no personal rights, trademarks, or competitive products are infringed.
• explicitly excludes the right for derivatives.
- Springer does not supply original artwork or content.
- According to the format which you have selected, the following conditions apply accordingly:
• **Print and Electronic:** This License include use in electronic form provided it is password protected, on intranet, or CD-Rom/DVD or E-book/E-journal. It may not be republished in electronic open access.
• **Print:** This License excludes use in electronic form.
• **Electronic:** This License only pertains to use in electronic form provided it is password protected, on intranet, or CD-Rom/DVD or E-book/E-journal. It may not be republished in electronic open access.

For any electronic use not mentioned, please contact Springer at

as if never granted. Further, in the event that you breach any of these terms and conditions or any of CCC's Billing and Payment terms and conditions, the license is automatically revoked and shall be void as if never granted. Use of materials as described in a revoked license, as well as any use of the materials beyond the scope of an unrevoked license, may constitute copyright infringement and Springer reserves the right to take any and all action to protect its copyright in the materials.

Copyright Notice: Disclaimer

You must include the following copyright and permission notice in connection with any reproduction of the licensed material:

"Springer book/journal title, chapter/article title, volume, year of publication, page, name(s) of author(s), (original copyright notice as given in the publication in which the material was originally published) "With permission of Springer"

In case of use of a graph or illustration, the caption of the graph or illustration must be included, as it is indicated in the original publication.

Warranties: None

Springer makes no representations or warranties with respect to the licensed material and adopts on its own behalf the limitations and disclaimers established by CCC on its behalf in its Billing and Payment terms and conditions for this licensing transaction.

Indemnity

You hereby indemnify and agree to hold harmless Springer and CCC, and their respective officers, directors, employees and agents, from and against any and all claims arising out of your use of the licensed material other than as specifically authorized pursuant to this license.

No Transfer of License

This license is personal to you and may not be sublicensed, assigned, or transferred by you without Springer's written permission.

No Amendment Except in Writing

This license may not be amended except in a writing signed by both parties (or, in the case of Springer, by CCC on Springer's behalf).

Objection to Contrary Terms

Springer hereby objects to any terms contained in any purchase order, acknowledgment, check endorsement or other writing prepared by you, which terms are inconsistent with these terms and conditions or CCC's Billing and Payment terms and conditions. These terms and conditions, together with CCC's Billing and Payment terms and conditions (which are incorporated herein), comprise the entire agreement between you and Springer (and CCC) concerning this licensing transaction. In the event of any conflict between your obligations established by these terms and conditions and those established by CCC's Billing and Payment terms and conditions, these terms and conditions shall control.

Jurisdiction

All disputes that may arise in connection with this present License, or the breach thereof, shall be settled exclusively by arbitration, to be held in the Federal Republic of Germany, in accordance with German law.

Other conditions: